



HAL
open science

Concepts for Wearable Technology in MR : Lightweight Flexible Radio Frequency Coils and Optical Wireless Communication

Lena Nohava

► **To cite this version:**

Lena Nohava. Concepts for Wearable Technology in MR : Lightweight Flexible Radio Frequency Coils and Optical Wireless Communication. Electromagnetism. Université Paris-Saclay, 2020. English. NNT : 2020UPAST069 . tel-03141307

HAL Id: tel-03141307

<https://theses.hal.science/tel-03141307v1>

Submitted on 15 Feb 2021

HAL is a multi-disciplinary open access archive for the deposit and dissemination of scientific research documents, whether they are published or not. The documents may come from teaching and research institutions in France or abroad, or from public or private research centers.

L'archive ouverte pluridisciplinaire **HAL**, est destinée au dépôt et à la diffusion de documents scientifiques de niveau recherche, publiés ou non, émanant des établissements d'enseignement et de recherche français ou étrangers, des laboratoires publics ou privés.

Concepts for Wearable Technology in MR: Lightweight Flexible Radio Frequency Coils and Optical Wireless Communication

Thèse de doctorat de l'université Paris-Saclay

École doctorale n° 575, Electrical, optics and bio :
physics and engineering (EOBE)

Spécialité de doctorat: Imagerie et physique médicale

Unité de recherche : Université Paris-Saclay, CEA, CNRS, Inserm, Laboratoire d'Imagerie
Biomédicale Multimodale Paris Saclay, 91401, Orsay, France

Référent : Faculté des sciences d'Orsay

**Thèse présentée et soutenue en visioconférence totale,
le 18.12.2020, par**

Lena NOHAVA

Composition du Jury

Maxim ZAITSEV

Professeur, Medical University of Vienna

Président

Irena ZIVKOVIC

Professeure assistante, Eindhoven University of Technology

Rapporteur & Examinatrice

Simon LAMBERT

Maître de conférences, HDR, Université Claude Bernard Lyon 1

Rapporteur & Examineur

Marie POIRIER-QUINOT

Professeure, Université Paris-Saclay

Examinatrice

Jacques FELBLINGER

Professeur, Université de Lorraine

Examineur

Andrew WEBB

Professeur, Leiden University

Examineur

Jean-Christophe GINEFRI

Maître de conférences, HDR, Université Paris-Saclay

Directeur de thèse

Elmar LAISTLER

Professeur associé, Medical University of Vienna

Co-encadrant & Examineur

Table of contents

PREFACE	v
Acknowledgements	vi
Abstract	viii
Résumé	ix
Acronyms and abbreviations	xi
Symbols	xiii
RESUME DE THESE	xv
Chapitre 1 : Introduction générale et motivation	xvi
Chapitre 2 : Contexte théorique	xx
Chapitre 3 : Instrumentation portable pour l'IRM	xxiii
Chapitre 4 : Développement d'antennes radiofréquences légères et flexibles	xxv
Chapitre 5 : Transmission de données sans fil en IRM	xxxiv
Chapitre 6 : Futur travail et conclusions	xxxviii
1. GENERAL INTRODUCTION	1
1.1 Motivation	2
1.2 Thesis Outline	5
2. THEORETICAL BACKGROUND	7
2.1 Magnetic Resonance Basics	8
2.1.1 The Nuclear Magnetic Resonance phenomenon	8
2.1.1.1 Nuclear spins and magnetic moment	8
2.1.1.2 Spins in a static magnetic field	9
2.1.1.3 Spins in a radio frequency field	12
2.1.1.4 Relaxation	13
2.1.1.5 Free Induction Decay	15
2.1.2 Magnetic Resonance Imaging	16
2.1.2.1 MR system components	16
2.1.2.2 Slice selection and spatial encoding	17
2.1.2.3 k-space	19
2.1.2.4 Imaging sequences	20
2.1.2.5 MR signal characteristics	22
2.1.2.5.1 Carrier frequency and receive bandwidth	22
2.1.2.5.2 Signal and noise	23
2.1.2.5.2.1 Reciprocity principle	23
2.1.2.5.2.2 Noise	24
2.1.2.5.2.3 Signal-to-noise ratio and coil sensitivity factor	26
2.1.2.5.2.4 Considerations for RF coil design	26
2.1.2.5.2.5 Dynamic range	29

2.2	Radio frequency coils	30
2.2.1	Transmission and reception	30
2.2.2	RLC circuits	31
2.2.2.1	Resonance in series and parallel RLC circuits	32
2.2.2.2	Q factor	33
2.2.2.3	Impedance matching	35
2.2.3	Coil types	36
2.2.3.1	Volume coils	36
2.2.3.2	Surface coils	37
2.2.3.2.1	Standard coils	38
2.2.3.2.2	Self-resonant structures	39
2.2.3.3	Coil arrays	42
2.2.4	Conventional interfacing to the MR scanner	44
2.2.4.1	Preamplifier	44
2.2.4.2	T/R switch	45
2.2.4.3	Common mode current traps	46
2.2.5	Coil performance characterization	47
2.2.5.1	S-parameters	47
2.2.5.2	Resonance frequency and Q factor measurements	48
2.2.5.3	B_1^+ mapping	49
2.2.5.4	Specific Absorption Rate	50
2.3	Numerical electromagnetic simulations	52
2.3.1	Basic principles	52
2.3.2	FDTD vs. FEM	53

3. WEARABLE MR TECHNOLOGY 55

3.1	Definition and motivation	56
3.2	Requirements for wearable MR devices	59
3.2.1	Flexibility	59
3.2.1.1	Flexible RF coil technology	59
3.2.1.1.1	Rigid anatomy-adapted RF coils	59
3.2.1.1.2	Semi-flexible/semi-rigid RF coils	60
3.2.1.1.3	Flexible RF coils	62
3.2.1.1.3.1	GE Healthcare AIR™ technology	62
3.2.1.1.3.2	Coaxial TLRs	63
3.2.1.1.3.3	Electro-textile ("E-textile")	64
3.2.1.1.4	Stretchable RF coils	64
3.2.1.1.4.1	Metal fibres	64
3.2.1.1.4.2	Liquid metal	65
3.2.1.1.4.3	Conductive elastomers	66
3.2.2	Removal of cabling	68
3.2.2.1	Optical fiber transmission	69
3.2.2.1.1	Analog optical fiber transmission	69
3.2.2.1.2	Digital optical fiber transmission	71
3.2.2.2	Wireless transmission	74
3.2.2.2.1	Analog wireless transmission	76
3.2.2.2.2	Digital wireless transmission	77
3.2.2.2.2.1	Optical wireless communication (OWC)	77
	Optical transmitters	81
	Optical receivers	86

3.2.2.3	Low power electronics	87
3.2.3	In vivo usability	89
3.2.3.1	Lightweight and ergonomics	89
3.2.3.2	Suitable materials	90
3.2.3.3	Safety	91
3.3	Conclusion	93
4.	STUDY I: FLEXIBLE RADIO FREQUENCY COILS	95
4.1	Prelude	96
4.2	<i>Article I</i> : Flexible multi-turn multi-gap coaxial RF coils: design concept and implementation for Magnetic Resonance Imaging at 3 and 7 T	96
4.3	Supplementary studies with flexible coaxial RF coils	113
4.3.1	Introduction	113
4.3.2	Design theory	114
4.3.2.1	Validation of the equivalent circuit model	114
4.3.2.2	Coaxial coil diameter ranges	118
4.3.2.3	Resonance behavior and interface component analysis	119
4.3.3	1T1G vs. MTMG coaxial coils	131
4.3.3.1	Comparison of same-size 1T1G- and MTMG-CCs at 3 T	131
4.3.3.1.1	Analytical calculations and EM simulations	131
4.3.3.1.2	Coil fabrication and bench measurements	135
4.3.3.1.3	MR experiments	138
4.3.3.1.4	Conclusion	141
4.3.3.2	Comparison of a 10 cm 1T1G- and 1TMG-CC at 7 T	142
4.3.3.2.1	Analytical calculations and bench measurements	142
4.3.3.2.2	Conclusion	143
4.3.4	MR experiments	144
4.3.4.1	Active detuning performance of 3 T SCs and CCs	144
4.3.4.2	SNR and transmit efficiency profile analysis	145
4.3.4.3	MR imaging with different types of fruit at 3 T	150
5.	STUDY II: WIRELESS DATA TRANSMISSION IN MR	155
5.1	Prelude	156
5.2	<i>Article II</i> : Perspectives in Wireless Radio Frequency Coil Development for Magnetic Resonance Imaging	156
5.3	Supplementary studies: MR compatible optical wireless data transmission	167
5.3.1	Introduction	167
5.3.2	Development of an OWC module prototype	168
5.3.2.1	Motivation	168
5.3.2.2	OWC module design	170
5.3.2.3	Component description	171
5.3.2.4	Experimental validation	174
5.3.2.5	Conclusion	180
5.3.3	OWC module use case simulation study	181
5.3.3.1	Module specifications	181
5.3.3.2	General set-up in the MR scanner	182
5.3.3.3	Alignment of OWC modules	183
5.3.3.4	Optical field-of-view simulation for different use cases	184

5.3.4	OWC module test summary	187
5.3.4.1	Outside of the MR scanner	187
5.3.4.2	Inside the MR bore	189
5.3.4.3	In vivo use	190
6.	OUTLOOK AND CONCLUSION	193
6.1	Future work	194
6.1.1	Flexible coaxial coils	194
6.1.2	Wireless data transmission in MR	195
6.2	Potential applications	198
6.2.1	MR mammography	198
6.2.2	Knee imaging	200
6.3	General conclusion	201
	APPENDIX	202
	LIST OF FIGURES	203
	LIST OF TABLES	207
	BIBLIOGRAPHY	208
	CURRICULUM VITAE	226
	LIST OF PUBLICATIONS	228

Preface

Acknowledgements

These past years as a PhD student were the possibility to learn more about RF coil engineering and MRI in general, to travel and to meet many great people. I want to express my sincere gratitude those who made my “PhD journey” this interesting and unforgettable.

My special thanks go to my supervisors Jean-Christophe Ginefri, Elmar Laistler and Roberta Frass-Kriegl. First of all, you were the ones who gave me the confidence to pursue a PhD, supported me in every step, encouraged me to participate in many conferences and taught me a lot about MRI and RF coils. I appreciate you giving me guidance and advice whenever I needed it but also for letting me work self-responsibly. You are not only excellent scientists but also genuinely nice people I really enjoy working with!

I want to thank my RF Lab colleagues: Sigrun Roat for helping me with her Matlab post-processing skills and time-consuming simulations which added significant value to this work. Raphaela Czerny for enthusiastically assisting me during late measurement sessions. Michael Obermann for letting me take part in his application oriented BRACOIL project and Jürgen Sieg for pub quiz evenings and a ridiculous amount of cake during coffee breaks. I appreciate all my other colleagues at the MR Center in Vienna (radiology and physics) for k-room chats, Christmas and summer parties and a pleasant work atmosphere that I do not take for granted. I also want to thank André Kühne for valuable scientific advice and for carrying out numerous coax coil simulations.

I want to thank my BioMaps colleagues: Georges Willoquet for his expertise in electronics, PCB design and willingness to experiment with sunglasses on. Marie Poirier-Quinot for always being amongst the ones showing interest in my work and the heartwarming laughs that can be heard across the hallway. Albine Pinseel for managing the French administration chaos, for organizing some of my trips and the memorable “séminaire annuel”. Laurène and Rose-Marie for letting me play around with the scanner and 3D printer and not to forget those with whom I spent some fun soirées in Paris, especially Isabelle, Sajad, Marylène, Gaëlle, Thomas and Charly.

I thank Luc Darrasse and Vincent Lebon for welcoming me at the SHFJ in this transitory period between IR4M and BioMaps.

To all my friends and family: You are the ones who pushed me to work harder but also encouraged me to take a step back when I needed it and, most importantly, to believe in me. Thank you for being there for me! I'm especially grateful for the love and constant support of my parents Christine and Martin as well as my "patchwork parents" Romana and Alois, the two power ladies I'm proud to call my grandmas and last but not least my awesome siblings Luca, Claus, Janis and Marlen. I wouldn't be where I am now without you.

I acknowledge financial support from the MESR (Ministère de l'Enseignement Supérieur et de la Recherche), funding my doctoral contract at the Université Paris-Saclay, the Austrian/French FWF/ANR grant Nr. I-3618, "BRACOIL", and Austrian/French OeAD WTZ grant FR 03/2018.

Abstract

Magnetic resonance imaging (MRI) has become a largely accessible non-invasive medical imaging modality in clinical diagnostics and is subject to lively research in various medical and technological fields. From a technological viewpoint, pursuing the goal of improving diagnostic value, shorter acquisitions and reduced complexity in patient handling together with improved image quality are setting the trend towards higher static magnetic field strength (B_0) and creative radio frequency (RF) coil designs.

Consequently, optimized RF hardware and electronics for **wearable MR technology** are currently emerging. Wearability implies lightweight, flexible, and wireless MR devices which improve patient comfort, safety, and usability. The adaptability to different body shapes and sizes yields significantly higher sensitivity.

In this work, **flexible** self-resonant coaxial transmission line resonators made from commercially available non-magnetic coaxial cables with introduced conductor gaps were investigated. The combination of coaxial coils with the multi-turn multi-gap principle increases the degrees in freedom in coil design and enables optimization of the coil size for a target application. This conformal coil design principle was studied *in silico* by analytical calculations and 3D electromagnetic simulations. Numerous prototypes were constructed, and their performance was tested both on the bench and on phantoms in MRI at 3 T and 7 T. It could be demonstrated that coaxial coils are robust against bending, have local specific absorption rate (SAR) similar to standard rigid copper coils and yield a signal-to-noise ratio (SNR) and transmit efficiency gain when form-fitted to the sample.

The second main aspect of this work are perspectives in **wireless** RF coil development. A comprehensive review of the state-of-the-art, an outline of hardware developments in the MR receive system, and an analysis of efficient wireless data transmission strategies including power supply and control signaling is given. Experimentally, an optical wireless communication module aiming at sensor data transmission, was shown to deliver 2 Mbps over 1.5 m using off-the-shelf optical components.

The successfully implemented coaxial coil design offers a versatile and robust alternative to rigid standard coils and combines the high sensitivity of conformal surface coils with the freedom to optimally set the coil size for a wide range of applications. Together with their low weight and flexibility, and in combination with wireless motion sensors, coaxial coils could be an ideal building block for wearable coil arrays with increased diagnostic value in breast, knee, or cardiac MRI.

Résumé

L'imagerie par résonance magnétique (IRM) est devenue une modalité d'imagerie médicale non invasive largement accessible dans les diagnostics cliniques et fait l'objet de recherches dynamiques dans divers domaines médicaux et technologiques. D'un point de vue technologique, la poursuite de l'objectif d'amélioration de la valeur diagnostique, d'acquisitions plus courtes et de réduction de la complexité de la prise en charge des patients, ainsi que l'amélioration de la qualité de l'image, donnent la tendance à une intensité de champ magnétique statique (B_0) plus élevée et à des conceptions créatives d'antennes radiofréquences (RF). Par conséquent, du matériel et des dispositifs électroniques RF optimisés pour **l'instrumentation portable en IRM** sont en train d'émerger. La portabilité implique des instruments d'IRM légers, flexibles et sans fil qui améliorent le confort des patients, la sécurité et la facilité d'utilisation. L'adaptabilité à différentes formes et tailles corporelles permet d'obtenir une sensibilité significativement plus élevée. Dans ce contexte, nous avons travaillé à l'étude et au développement d'antennes **flexibles** basées sur le principe des lignes de transmission à fentes auto-résonantes et fabriquées à partir de câbles coaxiaux commerciaux non magnétiques. La combinaison d'antennes à câbles coaxiaux avec le principe des résonateurs multi-tours multi-fentes augmente les degrés de liberté dans la conception des antennes et permet d'optimiser leurs tailles selon l'application visée. Ce nouveau type d'antennes a été étudié *in silico* par des calculs analytiques et des simulations électromagnétiques 3D. De nombreux prototypes ont été construits et leurs performances ont été testés à la fois sur banc et sur des fantômes en IRM à 3 et 7 T. Il a pu être démontré que les antennes coaxiales sont résistantes à la flexion, ont un taux d'absorption spécifique local (TAS) similaire aux antennes en cuivre rigides standards et permettent d'améliorer le rapport signal sur bruit (RSB) et l'efficacité de transmission lorsqu'elles sont adaptées à la forme de l'échantillon. Le deuxième aspect principal de ce travail concerne le développement d'antennes RF **sans fil**. Nous avons réalisé une revue complète de l'état de l'art et avons fourni un aperçu des récents développements instrumentaux des systèmes de transmission du signal en IRM ainsi qu'une analyse des stratégies de transmission sans fil des données IRM, de l'alimentation électrique et des signaux de commandes. Nous avons démontré expérimentalement, qu'un module de communication optique sans fil visant à transmettre les données des capteurs de mouvement, permettait d'atteindre 2 Mbps sur une distance de 1.5 m en utilisant des composants optiques disponibles dans le commerce.

L'étude approfondie du concept d'antennes coaxiales et leurs mises en œuvre effective réalisées dans ce travail ont montré qu'elles constituaient une alternative polyvalente et robuste aux antennes standards rigides et combinaient la haute sensibilité des antennes de surface flexibles avec la possibilité de choisir de manière optimale la taille de l'antenne pour un large éventail d'applications. Grâce à leur faible poids et à leur flexibilité, et en combinaison avec des capteurs de mouvement sans fil, les antennes coaxiales pourraient constituer un élément de base idéal pour les réseaux d'antennes portables avec une valeur diagnostique accrue en IRM du sein, du genou ou du cœur.

Acronyms and abbreviations

1T1G	single-turn single-gap
2D/3D	two-dimensional/three-dimensional
AC/DC	alternating current/direct current
ADC	analog-to-digital converter
AD	active detuning
APD	avalanche photodiode
Bd	Baud
bps	bits per second
CC	coaxial coil
CV_{Ref}	comparator reference voltage
DAC	digital-to-analog converter
DR	dynamic range
ECG	electrocardiogram
EM	electromagnetic
emf	electromotive force
FA	flip angle
FDA	Food and Drug Administration
FDTD	Finite Difference Time Domain
FEM	Finite Element Method
FID	Free Induction Decay
FLASH	fast low-angle-shot
FOV	field-of-view
FPGA	field programmable gate array
GRE	gradient echo
GUI	graphical user interface
iC	inner conductor
IEC	International Electrotechnical Commission
IF	intermediate frequency
IR	infrared
laser	light amplification by stimulated emission of radiation
LED	light-emitting diode
Li-Fi	Light Fidelity
LO	local oscillator
LOS	line-of-sight
MARMOT	MR compatible accelerometer for respiratory motion sensing
MIMO	multiple input multiple output
MIP	maximum intensity projection
MOSFET	metal-oxide-semiconductor field-effect transistor
MRI	Magnetic Resonance Imaging
MRS	Magnetic Resonance Spectroscopy
MTMG	multi-turn multi-gap

NF	noise figure [dB]
NLOS	non-line-of-sight
NMR	Nuclear Magnetic Resonance
NRZ	non-return-to-zero
O/E, E/O	optical-electrical, electrical-optical
<i>oCi</i>	outer conductor, inner surface
<i>oCo</i>	outer conductor, outer surface
OOK	on-off-keying
OWC	optical wireless communication
PCB	printed circuit board
PD	photodiode
PLL	phase-locked loop
RasPi	Raspberry Pi (single-board-computer)
RCLED	resonant cavity light-emitting diode
RF	radio frequency
RGB	red, green, blue
RIN	relative intensity noise
ROI	region of interest
Rx	receive(r)/reception
SAEC	signal analyzer and event controller
SAR	specific absorption rate [W/kg]
SC	standard coil
SE	mean SAR efficiency
SNR	signal-to-noise ratio
Sps	samples per second
T/R	Transmit/Receive
T_{acq}	acquisition time
T_E	echo time
TE	mean transmit efficiency
TIA	transimpedance amplifier
TL	transmission line
TLR	transmission line resonator
T_R	repetition time
TTL	transistor-transistor logic
Tx	transmit(ter)/transmission
UHF	ultra-high field
UV	ultraviolet
VCSEL	vertical-cavity surface-emitting laser
VNA	vector network analyzer
VOI	volume of interest
WDM	wavelength-division multiplexing
Wi-Fi	Wireless Fidelity

Symbols

B_1^+	radio frequency transmit field [T]
B_1^-	radio frequency receive field [T]
c_0	vacuum speed of light (299 792 458 m/s)
d_0	coil diameter [m]
f_0	self-resonance frequency [Hz]
f_L	Larmor frequency [Hz]
ϵ_0	vacuum permittivity ($8.8541878128(13) \cdot 10^{-12}$ F/m)
ϵ_r	relative dielectric permittivity
μ_0	permeability of free space ($4\pi \cdot 10^{-7}$ m·kg·s ⁻² ·A ⁻²)
μ_r	relative permeability
ρ_r	reflection coefficient [dB]
B_0	static magnetic field [T]
B_1	radio frequency field [T]
d_1	cable/conductor diameter [m]
E	electric field [V/m]
G	gradient field [T/m]
h	Planck's constant ($6.62607004 \cdot 10^{-34}$ m ² ·kg/s)
k	Boltzmann constant ($1.381 \cdot 10^{-23}$ J/K)
M	magnetization [A/m]
n_g	number of gaps
n_t	number of turns
P	power [W]
T	absolute temperature [K]
Z	impedance [Ω]
Z_0	characteristic impedance [Ω]
α	flip angle [°]
γ	gyromagnetic ratio [MHz/T]
δ	skin depth [m]
λ	wavelength [m]
ρ	resistivity [Ω m]
σ	electrical conductivity [S/m]
ω	angular resonance frequency [rad/s]

Résumé de thèse

Cette thèse est intitulée « *Concepts pour l'instrumentation portable en IRM: Développement d'antennes radiofréquences légères et flexibles et d'un système de transmission optique sans fil* ». Ce résumé donne un aperçu du manuscrit de la thèse qui est divisé en 6 chapitres : chaque chapitre sera brièvement résumé en langue française dans ce qui suit et le résumé sera complété par les figures les plus représentatives du contenu scientifique.

Chapitre 1 : Introduction générale et motivation

L'imagerie par résonance magnétique (IRM) est une technique d'imagerie médicale en constante évolution utilisée dans un large éventail d'applications et qui a gagné en accessibilité au cours des dernières décennies. L'IRM est couramment utilisée à des fins de diagnostic en routine clinique et dans le domaine de la recherche pour les études précliniques sur l'homme et l'animal.

Les principaux avantages de l'IRM par rapport à d'autres modalités d'imagerie sont sa non-invasivité, sa sécurité relative car aucun rayonnement ionisant n'est utilisé, son contraste exceptionnel des tissus mous et la polyvalence de la technique qui offre des informations structurelles, fonctionnelles (IRMf) et métaboliques (spectroscopie RM). L'imagerie du corps entier est possible avec les scanners RM cliniques standards à des résolutions de l'ordre du millimètre, tandis que les installations avancées permettent l'imagerie de petites structures avec des résolutions pouvant atteindre la dizaine de μm .

Le phénomène de résonance magnétique nucléaire (RMN) est exploité pour créer un signal provenant de moments magnétiques nucléaires excités ("spins") dans un tissu biologique placé dans un fort champ magnétique statique B_0 . L'instrument utilisé pour l'excitation des spins et la réception du signal réémis par ces mêmes spins est une structure résonnante, appelée antenne radiofréquence (RF). La fréquence de résonance de l'antenne RF est déterminée par l'intensité du champ B_0 et le rapport gyromagnétique du noyau imagé, classiquement ^1H . Des gradients de champ magnétique supplémentaires sont utilisés pour coder l'origine spatiale du signal.

La qualité des images en IRM dépend du rapport signal sur bruit (RSB) accessible. Par conséquent, plusieurs stratégies de développement liées à l'instrumentation, visant à améliorer le RSB, ont été poursuivies :

L'augmentation de l'intensité du champ magnétique statique B_0 (par exemple 7 T, [1–3]) permet de créer une aimantation nette plus élevée des tissus et, par conséquent, des amplitudes de signal détectables plus élevées. Le champ statique de référence pour l'imagerie clinique standard est de 3 T, mais un premier scanner clinique certifié à ultra-haute intensité de champ 7 T est déjà sur le marché.

Les axes de développement des gradients concernent l'amélioration de ses principales caractéristiques, c'est-à-dire la linéarité, l'intensité et la vitesse de commutation du gradient. L'augmentation de l'amplitude du gradient permet d'obtenir des résolutions spatiales plus élevées et des vitesses de commutation élevées permettent une imagerie plus rapide.

Un autre aspect important est l'optimisation des caractéristiques de transmission et de réception des antennes RF et le développement de réseaux d'antennes [4]. À 3 T, il est courant d'utiliser une grande antenne « corps entier » intégrée dans l'alésage du scanner pour créer un champ de transmission RF homogène. Cette grande antenne est ensuite souvent combinée avec de petites antennes de surface utilisées en réception seule avec une sensibilité accrue à proximité de la région du corps à imager. À 7 T, en raison des difficultés à produire un champ de transmission RF homogène lié aux effets de longueur d'onde, aucune antenne corps entier n'est intégrée et, par conséquent, des antennes de surface sont généralement utilisées en mode émission/réception (Tx/Rx). Un nombre plus élevé de canaux d'antennes permet l'imagerie parallèle [5–7] et les techniques de transmission parallèle [8], ce qui réduit considérablement les temps d'examen et, plus récemment, l'excitation RF plus homogène qui est particulièrement nécessaire à ultra haut champ. En outre, le développement d'antennes RF adaptées à la forme de la zone observée et flexibles, voire extensibles, a été particulièrement étudié. Ceci est motivé par un gain en signal et un confort accru pour le patient grâce à la conception d'antennes légères bien ajustées aux différentes anatomies. Une tendance à la construction d'instruments RF entièrement portables s'est dessinée au sein de la communauté scientifique ces dernières années. Un instrument RF portable se caractérise non seulement par sa flexibilité et la légèreté de ses matériaux, mais aussi par la suppression du câblage.

Cela implique une transmission sans fil des données RMN, de l'alimentation électrique et des signaux de contrôle.

L'intégration de capteurs supplémentaires ou de composants directement sur l'antenne RF pendant l'expérience d'IRM, par exemple pour la correction du mouvement ou le calage localisé, a gagné en intérêt car ils peuvent améliorer la qualité de l'image et la robustesse de l'acquisition. L'utilisation d'une électronique faible bruit et miniaturisée est un autre aspect de l'amélioration de la qualité des images d'IRM.

Ce travail vise à proposer des concepts et des démonstrations expérimentales pour le développement d'une instrumentation portable pour l'IRM.

Le premier objectif est le développement, la fabrication et la validation expérimentale d'antennes RF légères et flexibles pour un fonctionnement en réception uniquement à 3 T et en émission/réception à 7 T. Un nouveau concept d'antenne basé sur des résonateurs à ligne de transmission à plusieurs tours et plusieurs fentes fabriqués avec des câbles coaxiaux est introduit. Cette conception d'antenne permet un ajustement idéal de la forme de l'antenne et une plus grande liberté dans le choix de la taille de l'antenne. Cela élargit les possibilités de conception de l'antenne et permet d'optimiser le RSB et la profondeur de pénétration au regard de l'application anatomique visée. La conception d'antenne coaxiale proposée constitue une alternative fiable par rapport aux antennes rigides standards en fil de cuivre. Elle est particulièrement adaptée aux applications où les variabilités de la taille anatomique entre les patients sont importantes.

La rareté de la littérature disponible sur le sujet de la communication sans fil en IRM a été la motivation initiale pour le second objectif central de ce travail : une évaluation complète du statu quo dans le développement des antennes RF sans fil et l'analyse des développements liés à la transmission de données, à l'alimentation électrique et à la transmission des signaux de contrôle sans fil. Cela permet d'évaluer la faisabilité des antennes RF sans fil à l'avenir. L'accent a été plus particulièrement mis sur l'exploration de la communication optique sans fil pour une utilisation en IRM. La mise en œuvre pour la transmission de données de capteurs de mouvement a fait l'objet d'essais préliminaires avec un module personnalisé, ce qui constitue une première étape vers la future transmission optique sans fil des signaux RMN.

Cette thèse de doctorat a été réalisée dans le cadre d'un projet entre le Laboratoire d'imagerie biomédicale multimodale (BioMaps) de l'Université Paris-Saclay (Orsay, France) et le High Field MR Center du Center for Medical Physics and Biomedical Engineering de l'Université médicale de Vienne (Vienne, Autriche).

Deux publications scientifiques sont le résultat de ce projet de thèse :

1. « Antennes coaxiales multi-tours multi-fentes flexibles: conception et mise en œuvre pour l'IRM à 3 et à 7 Tesla » [9], publié dans *IEEE Transactions on Medical Imaging* et désigné *Article I* dans ce qui suit.
2. « Perspectives dans le développement d'antennes radiofréquences pour l'IRM » [10], publié dans *Frontiers in Physics* et désigné *Article II* dans ce qui suit.

Chapitre 2 : Contexte théorique

Ce chapitre décrit les concepts de base de la résonance magnétique nucléaire (RMN) et de l'imagerie par résonance magnétique (IRM). Il est suivi d'une introduction au contexte théorique concernant les antennes radiofréquences et les simulations électromagnétiques numériques.

Aujourd'hui, les scanners dédiés aux examens cliniques humains par RMN reposent sur la technologie supraconductrice pour la conception de l'aimant principal et fonctionnent généralement à des intensités de champ magnétique statique B_0 de 1.5 T ou 3 T. Au cours de la dernière décennie, les scanners IRM ultra haut champ (≥ 7 T) sont également devenus accessibles pour une utilisation clinique et de recherche haut de gamme. Le principe de la RMN est le suivant : un échantillon est composé d'un ensemble de moments magnétiques, qui dans leur état d'équilibre sont orientés de manière aléatoire. Sous l'influence de B_0 , les moments magnétiques sont alignés et forment une aimantation M_0 dont l'axe de précession est aligné selon B_0 et la fréquence angulaire dénotée fréquence de Larmor. Ce système peut être perturbé par un champ radiofréquence $B_1(t)$ perpendiculaire à B_0 et oscillant à la fréquence de Larmor. Le champ $B_1(t)$ décale les moments magnétiques de tous les spins pour les mettre en phase et crée une aimantation transversale détectable M_{xy} . L'excitation des spins repose sur le phénomène de "résonance magnétique nucléaire" qui ne se produit que lorsque l'on utilise une fréquence de résonance égale à la fréquence Larmor. Une antenne de réception RF peut détecter la magnétisation transversale tournante par l'induction d'une force électromotrice (*fem*). Des bobines de gradient sont utilisées pour générer des champs magnétiques variant le long des directions x , y et z , les gradients de champ magnétique. Les gradients de champ attribuent des informations spatiales au signal RMN détecté, de sorte que lors de la reconstruction de l'image, l'origine du signal détecté est connue.

Les antennes RF sont donc l'instrument utilisé pour l'excitation de l'ensemble des spins par l'émission d'impulsions RF de forte puissance et pour la réception du signal RM.

Le choix de la géométrie et du matériau de l'antenne est lié à des considérations relatives au signal et au bruit. En général, le diamètre d'une antenne de surface doit

être choisi en fonction de l'application cible : pour un RSB idéal à une profondeur de pénétration p , le diamètre de l'antenne d doit être environ égal à p . Les petites antennes de surface offrent une sensibilité supérieure à celui des antennes de volume. Il faut veiller à ce que le fonctionnement se fasse dans le régime dominé par le bruit de l'échantillon et non par le bruit de l'antenne ce qui impose une limite à la réduction de taille des antennes. De plus, les antennes de surface ont une distribution inhomogène de B_1 qui diminue fortement avec la distance dans l'échantillon. Il existe différents types d'antennes de surface : La construction peut être basée sur des éléments discrets, c'est-à-dire en utilisant des condensateurs discrets, formant un circuit RLC "standard". Une autre méthode pour réaliser une antenne RF est l'utilisation d'une capacité distribuée dans des structures auto-résonnantes.

Des résonateurs à ligne de transmission (TLR) de différentes formes ont été proposés. Ils résonnent sans utiliser de condensateurs discrets grâce à une capacité distribuée dans un substrat diélectrique séparant deux conducteurs inductifs. Les conducteurs sont coupés par des fentes à des positions diamétralement opposées. L'auto-résonance est déterminée par la géométrie de l'antenne et les propriétés du matériau. Bien que ce travail concerne les TLR à câbles coaxiaux (antennes coaxiales), d'autres variantes, par exemple les TLR à conducteurs parallèles, existent.

Les réseaux d'antennes de surface permettent de combiner des caractéristiques idéales : un champ de vue étendu et une grande sensibilité grâce à l'utilisation de petits éléments d'antennes. De plus, les réseaux d'antennes peuvent être utilisés pour l'imagerie parallèle ce qui permet l'acquisition accélérée d'images. Aussi, la transmission parallèle permet des temps d'examen encore plus courts, une excitation sélective et une homogénéisation du champ RF d'excitation. Néanmoins, le couplage mutuel entre plusieurs antennes à proximité immédiate entraîne une dégradation des performances des antennes. Deux méthodes de découplage courantes sont le découplage par chevauchement et le découplage par préamplificateur.

Outre les considérations de conception de l'antenne RF mentionnées ci-dessus, d'autres composants sont indispensables au bon fonctionnement de la chaîne d'excitation et de détection du signal MR lorsque l'on relie l'antenne à l'électronique du scanner IRM. Il est nécessaire d'accorder et d'adapter chaque antenne, de pré-amplifier le signal détecté, d'assurer la commutation émission/réception et de supprimer le mode commun dans les câbles.

Sur banc de mesure, la performance d'une antenne peut être caractérisée en utilisant un analyseur de réseau vectoriel pour mesurer la fréquence de résonance et le facteur de qualité à vide et en charge. Pour valider le fonctionnement de l'antenne dans l'IRM, des images peuvent être acquises avec des séquences d'écho de gradient pour déterminer le RSB. De plus, des cartes d'angle de basculement peuvent être mesurés en IRM et permettent le calcul de l'efficacité de transmission.

Les logiciels de simulations électromagnétiques 3D des antennes RF sont un outil efficace pour calculer la distribution de champ électromagnétique en résolvant les équations de Maxwell pour un espace de simulation discrétisé. Les deux méthodes de simulation très répandues pour la simulation d'antennes RF sont la méthode finite difference time domain (FDTD) et la méthode des éléments finis (FEM). Cette dernière est utilisée pour les simulations d'antennes coaxiales, car le maillage tétraédrique utilisé permet de résoudre efficacement les petites structures des antennes coaxiales (même celles inférieures à un millimètre) et les simulations dans le domaine fréquentiel permettent des temps de simulation plus courts. Il est particulièrement intéressant de simuler l'antenne en présence d'un échantillon pour obtenir des informations sur la distribution des champs E et B à l'intérieur du tissu. De plus, la densité de courant ainsi que la matrice des paramètres S de l'antenne peuvent être extraits des simulations électromagnétiques. Cela permet de calculer le taux d'absorption spécifique (TAS) maximal local (proportionnel à E^2), l'efficacité de transmission, le courant de surface et d'étudier différentes géométries en fonction de l'application visée.

Chapitre 3 : Instrumentation portable pour l'IRM

Dans ce chapitre, nous exposons la motivation pour le développement d'une instrumentation portable pour l'IRM. Les objectifs et les défis actuels associés au développement d'une instrumentation portable pour l'IRM sont liés à la flexibilité, la réduction ou la suppression du câblage et la facilité d'utilisation *in vivo*. Ces sujets sont abordés dans ce chapitre, avec des références à l'état de l'art qui établiront le lien contextuel entre les deux chapitres suivants (4 & 5).

La motivation pour le développement de solutions portables pour les appareils utilisés en IRM est principalement basée sur les arguments suivants :

- la facilité d'utilisation pour l'opérateur de l'appareil et la commodité pour le patient, c'est-à-dire un confort amélioré grâce à l'ergonomie, la légèreté, la flexibilité et la miniaturisation des composants ;
- l'accessibilité : le positionnement et la manipulation des antennes ne sont plus réservés à l'opérateur du scanner IRM, le patient peut mettre une antenne RF portable ;
- l'efficacité : le flux de travail et, par conséquent, le débit des patients peuvent être améliorés ;
- la sensibilité : pour les antennes RF, l'adaptation à la taille et à la forme du sujet et à l'anatomie spécifique signifie un couplage magnétique plus élevé et, par conséquent, une plus grande sensibilité de l'antenne.
- adaptabilité : L'adaptabilité joue un rôle important avec des tailles de sujet ou d'anatomie différentes comme mentionné ci-dessus. En outre, l'appareil peut être adapté pour accueillir des capteurs sans fil supplémentaires (par exemple sur une antenne RF) sans ajouter de câbles, de sorte que davantage d'informations sur les paramètres physiologiques et le mouvement peuvent être collectées en parallèle à l'IRM.
- sécurité : la réduction du poids et la suppression du câblage coaxial permet de réduire les risques, à la fois physiques et électriques.

Les différentes approches de conception d'antennes RF peuvent être systématiquement classées en fonction de leur degré d'adaptabilité au contour du

corps et au processus de fabrication, allant des antennes RF complètement rigides mais adaptées à l'anatomie aux antennes RF flexibles et extensibles.

Différentes alternatives à la transmission de signaux RMN par câble coaxial existent. En général, le signal RMN peut être codé dans le domaine numérique ou analogique et transmis à l'aide de techniques de transmission par fibre optique ou sans fil. Comparé aux signaux analogiques, les signaux numériques sont transmis sans fil de manière plus fiable sur de longues distances et éliminent les problèmes de plage dynamique ou de stabilité du signal. Cependant, les exigences en matière de largeur de bande pour les signaux RMN, en particulier si l'on considère les données RMN issues de réseau d'antennes directement numérisées, atteignent les limites de la technologie Wi-Fi actuelle. La communication optique sans fil est une nouvelle alternative au Wi-Fi qui utilise la lumière dans la gamme des infrarouges (IR), du visible ou des ultraviolets (UV) comme support d'information. Avec des solutions technologiques sophistiquées, les liaisons optiques sans fil sont capables de transmettre des données à un débit de plusieurs Gbps. Un résumé et une discussion des différentes approches proposées pour la transmission sans fil de différents signaux en IRM sont donnés dans l'*Article II*. La communication optique numérique sans fil sera détaillée dans le chapitre 3 car cette approche de communication a été utilisée dans le développement d'un module dédié à la transmission optique sans fil de données de capteurs de mouvement.

Outre les aspects technologiques mentionnés ci-dessus, d'autres aspects importants pour l'utilisation d'un appareil portable en IRM in vivo, concernant la sécurité du patient, le confort ou la certification des antennes sont également discutés.

Deux aspects principaux ont été identifiés comme faisant partie des avancées technologiques indispensables à l'émergence de l'instrumentation portable pour l'IRM :

- Le développement d'antennes RF légères et flexibles et de réseaux de d'antennes.
- Les stratégies de transmission de signaux et d'énergie sans fil dans l'environnement RM.

Les chapitres suivants se concentrent chacun sur l'étude d'un des aspects mentionnés ci-dessus.

Chapitre 4 : Développement d'antennes radiofréquences légères et flexibles

Ce chapitre décrit le « Développement d'antennes RF coaxiales multi-tours et multi-fentes (MTMF) flexibles : conception et validation expérimentale pour l'imagerie par résonance magnétique à 3 et 7 Tesla » [9] (*Article 1*). De même, il comprend une série d'études supplémentaires résultant de calculs analytiques, de simulations électromagnétiques et de tests sur banc expérimental et en IRM avec des antennes coaxiales flexibles.

L'utilisation de câbles coaxiaux pour la fabrication d'antennes radiofréquences auto-résonantes basées sur le principe des TLR permet de réaliser des antennes flexibles et légères, particulièrement intéressantes pour développer des réseaux à haute densité de parallélisme. Toutefois, le concept proposé pour des structures à un seul tour et une seule fente sur les conducteurs du câble coaxial limite les possibilités en termes de taille d'antenne. Dans ce cas, la taille de l'antenne ne peut pas être optimisée pour une application clinique donnée car les diamètres possibles sont limités par la fréquence de résonance visée (f_0) d'une part et par les propriétés du câble coaxial utilisé, i.e. diamètre extérieur (d_1), permittivité (ϵ_r), impédance (Z_0), d'autre part. Dans le but d'augmenter les degrés de liberté pour la conception et l'optimisation de la géométrie des antennes, nous avons élargi le concept initial en le combinant avec le principe des résonateurs MTMF.

Ce nouveau concept est étudié par calculs analytiques de la fréquence de résonance basée sur un circuit électrique équivalent, par simulations électromagnétiques, et par mesures sur table (analyseur de réseau) pour différentes configurations d'antennes coaxiales. Le fonctionnement de ces antennes coaxiales a ensuite été validé en IRM.

Principe des antennes coaxiales MTMF

La Figure 1 présente le principe de fonctionnement des antennes coaxiales MTMF étudiées dans ce travail. Dans la Figure 1a des exemples de positionnement de fentes avec 1-3 tours et 1-3 fentes sont exposés. La Figure 1b présente les paramètres du câble coaxial alors que le circuit équivalent pour un nombre arbitraire de tours est représenté sur la Figure 1c. Les paramètres des antennes coaxiales sont listés dans ce qui suit : n_g , n_t ... nombre de fentes et de tours, d_0 ... diamètre de l'antenne, l ... longueur

d'un embout coaxial, d_1 ... diamètre extérieur du conducteur du câble coaxial, d_2 ... diamètre du conducteur intérieur, ϵ_r ... permittivité relative, Z_0 ... impédance caractéristique du câble (Ω), X_{shield} ... réactance inductive de la surface extérieure du blindage coaxial, X_{TL} ... réactance d'un stub coaxial (capacitif à la résonance), R ... résistance (pertes ohmiques de l'antenne).

Le port de l'antenne est toujours situé à une fente du conducteur intérieur et est représenté comme une source de tension en (a). À l'aide du schéma électrique équivalent (c) nous avons établi la condition de résonance des antennes MTMF en fonction de leurs caractéristiques (équations 1-3).

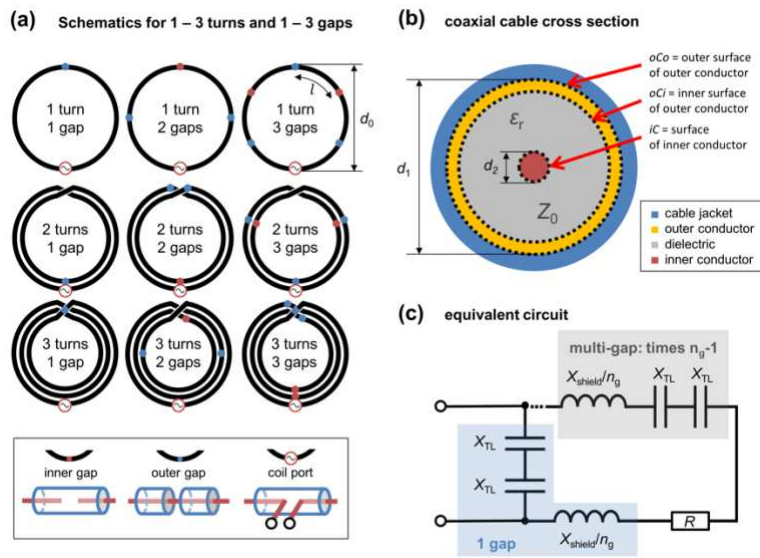


Figure 1 : Principe des antennes coaxiales MTMF et schéma électrique équivalent

$$X_{\text{shield}}(\omega) = n_t^2 \omega \mu_0 \frac{d_0}{2} \left[\ln \left(\frac{8d_0}{d_1} \right) - 2 \right] \quad (1)$$

$$X_{\text{TL}}(\omega) = -Z_0 \cot \left(\frac{\omega l \sqrt{\epsilon_r}}{c_0} \right) \quad (2)$$

$$Z_{\text{tot}}(\omega) = R + i(X_{\text{shield}} + 2n_g X_{\text{TL}}) \quad (3)$$

Pour illustrer l'extension du diamètre réalisable des antennes auto-résonantes en utilisant le concept MTMF par rapport aux antennes mono-tour mono-fente (1T1F), les diamètres d_0 des antennes coaxiales ont été calculés dans Matlab en utilisant des plages de valeurs réalistes pour tous les paramètres (ϵ_r , d_1 , Z_0 , n_t , n_g , B_0). La Figure 2 montre que, par rapport à une antenne coaxiale 1T1F, l'utilisation de plusieurs tours

permet d'obtenir des diamètres d'antennes plus petits et l'utilisation de plusieurs fentes permet d'obtenir des diamètres plus grands.

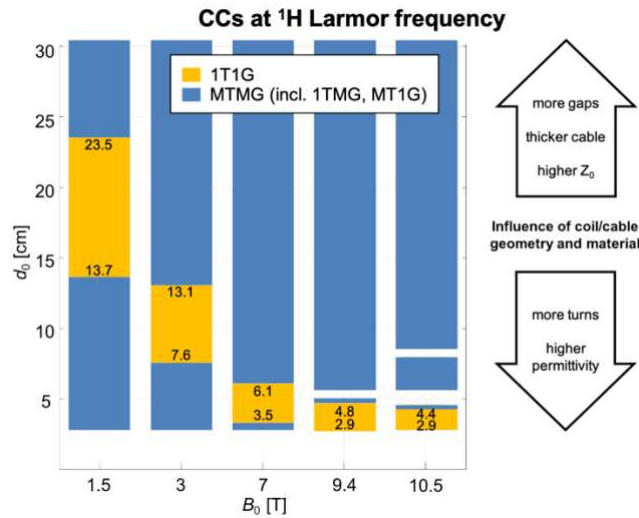


Figure 2 : Relation entre B_0 et d_0 ; résultats calculés montrant la gamme des diamètres d'antenne réalisable avec des antennes coaxiales MTMF comparé à des antennes 1T1F

Fabrication d'antennes

Plusieurs configurations d'antennes coaxiales ont ensuite été fabriquées ainsi que des antennes standards en cuivre de même taille pour comparaison. Les quatre diamètres d'antenne suivants (d_0), avec leurs applications biomédicales respectives possibles, ont été choisis :

- 4 cm (peau, main, poignet),
- 7 cm (coude, cheville, sein, tête),
- 10 cm (sein, tête, genou) et
- 15 cm (cœur, abdomen).

Dans cette étude, des antennes pour l'IRM à 3 T en mode réception et pour l'IRM à 7 T en mode émission/réception ont été fabriquées. 5 types de câbles coaxiaux non magnétiques disponibles dans le commerce ont été sélectionnés pour la fabrication des antennes coaxiales. Nous avons retenu des configurations, en fonction du type de câble, du nombre de tours et de fentes, pour lesquelles la fréquence de résonance propre calculée était proche de la fréquence de Larmor ($\pm 10\%$). Un nombre de tours et de fentes minimal a été visé pour réduire le bruit de l'antenne et pour assurer sa flexibilité. Au total, huit antennes coaxiales ont été fabriquées, avec un nombre de tours maximal $n_{t,\max} = 2$ et un nombre de fentes maximal $n_{g,\max} = 5$. La Figure 3 montre

les antennes coaxiales fabriquées pour l'IRM à 3 T (a) et à 7 T (b) et leur circuit d'interface pour l'adaptation et l'accord de l'antenne.

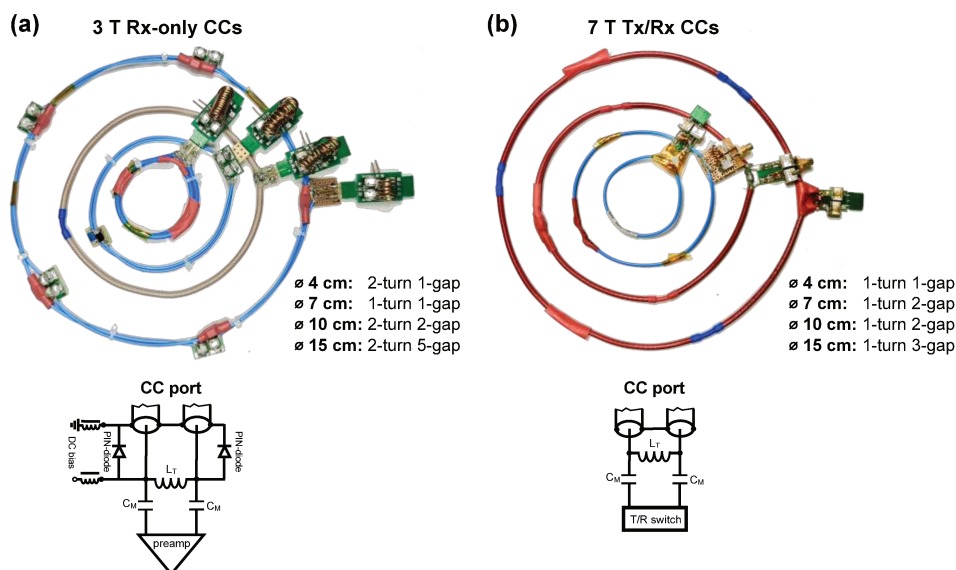


Figure 3 : Antennes coaxiales fabriquées pour l'IRM à 3 T en mode réception et l'IRM à 7 T en mode émission/réception

À titre de comparaison, des antennes standard rigides (SC) de mêmes diamètres ont été fabriquées à partir de fil de cuivre de 1 mm pour l'utilisation à 3 et à 7 T.

Simulations électromagnétiques

Pour les simulations d'antennes coaxiales, la méthode FEM implémentée dans le logiciel de simulation CST Studio Suite 2020 (Dassault Systèmes, Paris, France) a été utilisée. Des paramètres tels que le champ E , le champ B et la densité de courant de surface $K = dl/dl$ ainsi que la matrice des paramètres S de l'antenne ont été extraits des simulations. Le courant de surface sur les conducteurs coaxiaux de l'antenne, l'efficacité de transmission (B_1^+/\sqrt{P}), l'efficacité du TAS ($B_1^+/\sqrt{\max. 10g \text{ TAS}}$) et le 10g-TAS local pour les antennes utilisées en émission (à 7 T) ont été calculés en post-traitement. Pour les simulations des champs E et B , un échantillon cubique a été placé à une distance de 0.5 mm de l'antenne. Les dimensions de la base carrée du fantôme sont $4d_0 \times 4d_0$ ($d_0 =$ diamètre de l'antenne), la hauteur du fantôme est de 250 mm, la conductivité est de 0.6 S/m et la permittivité ϵ_r de 80.

La Figure 4 montre les résultats de simulation de la densité de courant de surface $K = dl/dl$ et du courant de surface $|I|$ d'une antenne 1T1F (a) et d'une antenne 2T5F (b)

à leurs fréquences de résonance propres respectives f_0 . Le comportement typique des lignes de transmission peut être observé pour le conducteur intérieur iC et la surface intérieure du conducteur extérieur oCi : le courant sur iC est le courant miroir du courant sur oCi , avec un maximum de la densité de courant à chaque fente extérieure et un zéro à chaque fente intérieure. Cependant, le courant sur oCo , qui correspond au courant effectif vu à distance de l'antenne, est plutôt constant le long du conducteur.

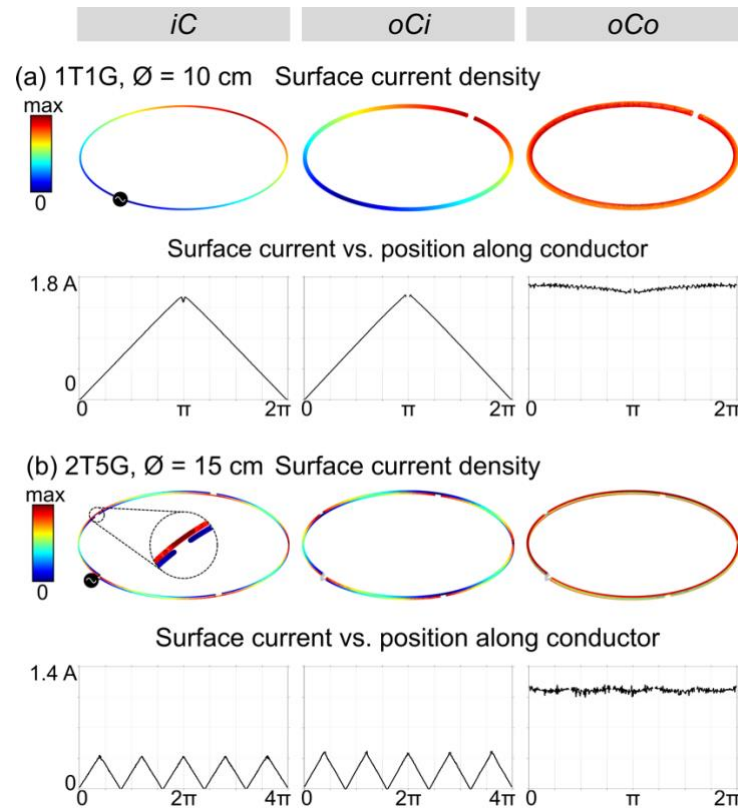


Figure 4 : Résultats de simulation de la densité de courant de surface $K = dI/dl$ et du courant de surface $|I|$ pour deux exemples représentatifs d'antennes coaxiales : (a) 1T1F et (b) MTMF.

Les calculs de cartes TAS basées sur les simulations de champ E normalisé à la puissance acceptée par l'antenne ont révélé des cartes de TAS ponctuel ainsi que des cartes d'efficacité TAS ($B_1^+ / \sqrt{\max. 10g \text{ TAS}}$) comparables pour les antennes coaxiales et les antennes standards. Cela démontre que les antennes coaxiales utilisées à 7 T en émission/réception ont des performances similaires à celles des antennes standards mais offrent l'avantage de la flexibilité. La Figure 5 montre l'exemple d'une comparaison entre une antenne coaxiale et une antenne standard en termes de TAS ponctuel (projection d'intensité maximale) et efficacité TAS qui est représentatif pour l'ensemble des simulations.

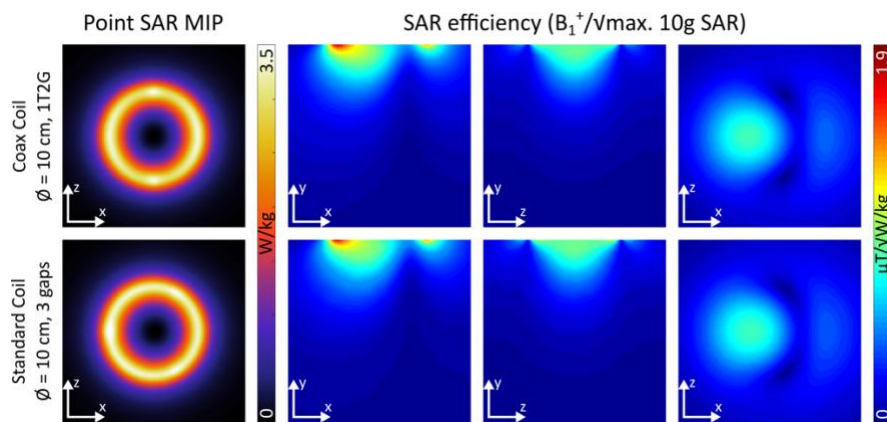


Figure 5 : Comparaison entre le TAS local (projection d'intensité maximale) et cartes d'efficacité TAS pour une antenne coaxiale et une antenne standard à 7 T.

Validation expérimentale

Toutes les antennes ont été testées sur banc expérimental. Pour les antennes coaxiales, la déviation maximum entre la fréquence de résonance propre mesurée et calculée est de $\pm 13.9\%$ ce qui valide le modèle électrique équivalent et la formule analytique de résonance des antennes coaxiales MTMF. La caractérisation des facteurs de qualité des antennes à vide et en condition de charge par un fantôme mimant les tissus biologiques (conductivité ≈ 0.2 S/m) a montré que le rapport Q_u/Q_l est généralement plus faible pour les antennes coaxiales que pour les antennes standards. À 3 et 7 T, pour les deux types d'antennes ainsi que pour les différents positionnements d'antennes (plat, courbé) et les différents volumes de fantômes (conteneur, ballons), les rapports Q_u/Q_l ont toujours été supérieurs à 2, ce qui démontre le fonctionnement des antennes dans un régime dominé par le bruit de l'échantillon. Lors de la flexion des antennes coaxiales, les niveaux d'adaptation en puissance, à la fréquence de Larmor, sont dégradés. Par conséquent, pour certaines antennes coaxiales, une réadaptation à l'état courbé était indispensable.

La Figure 6 montre des résultats acquis en IRM à 3 T révélant un découplage insuffisant entre l'antenne de réception et l'antenne d'émission corps entier avec des changements relatifs de l'angle de basculement de plus de 60 %, comme le montre la Figure 6b. Ce scénario peut se produire avec une antenne coaxiale 2T5F utilisant un circuit de découplage actif (DA) composé de diodes PIN court-circuitant le conducteur interne et externe uniquement au niveau du port de l'antenne. Avec un réseau de DA composé d'un ensemble de diodes PIN placées à chaque fente et d'un piège RF reliant les fentes extérieurs (Figure 6a), l'efficacité du DA est assurée car les résonances résiduelles sont éliminées (Figure 6c). Comme le montre la Figure 6d, avec l'antenne

positionnée à plat sur un conteneur, le RSB moyen dans une région d'intérêt circulaire est inférieur pour les antennes coaxiales par rapport aux antennes standards. L'utilisation d'une antenne coaxiale courbée sur un fantôme (ballon) par rapport à une antenne standard à plat se traduit par un gain en RSB modéré ou un RSB légèrement inférieur dans la même région d'intérêt (-2.3 %, +10.8 %, +7.0 % et -5.7 % pour les antennes coaxiales de 4, 7, 10 et 15 cm, respectivement).

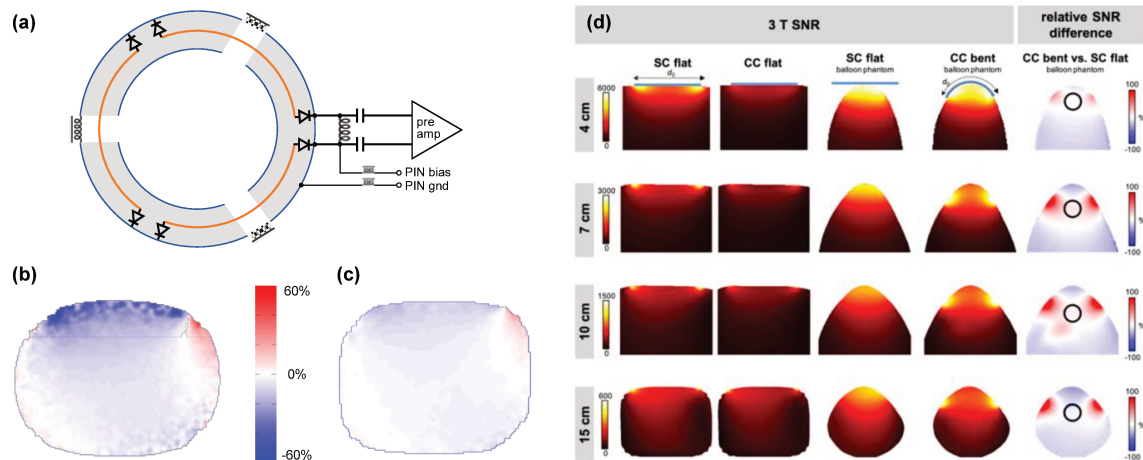


Figure 6 : (a) Circuit de découplage requis pour les antennes multi-fentes utilisées à 3 T. Changements relatifs de l'angle de basculement (b) sans ou (c) avec circuit de découplage actif à chaque fente. (d) Cartes calculées du RSB.

Une étude supplémentaire a été menée à 3 T pour évaluer les performances en imagerie des antennes coaxiales sur différents types de fruits avec une séquence 2D d'écho de gradient. Les images acquises sont présentées à la Figure 7.

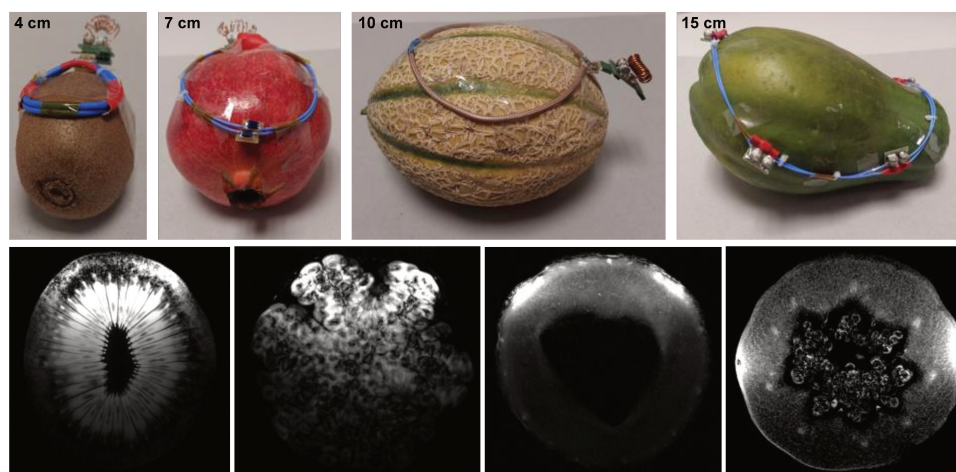


Figure 7 : IRM à 3 T avec les antennes coaxiales placées sur des différents fruits

À 7 T, les cartes d'efficacité de transmission B_1^+/\sqrt{P} présentées à la Figure 8a montrent une bonne comparabilité des antennes standards et des antennes coaxiales

à plat. La configuration courbée des antennes coaxiales a montré une efficacité de transmission plus élevée que celle des antennes standards plates avec un gain d'efficacité de +17.1 %, +14.8 %, +9.1 % et +21.9 % pour les antennes coaxiales de 4, 7, 10 et 15 cm, respectivement. Les cartes de RSB calculées (Figure 8b) montrent un gain important du RSB moyen dans une région d'intérêt circulaire avec une antenne coaxiale courbée (+40.5 %, +18.0 %, +11.1 % et +10.6 % pour les antennes coaxiales de 4, 7, 10 et 15 cm, respectivement).

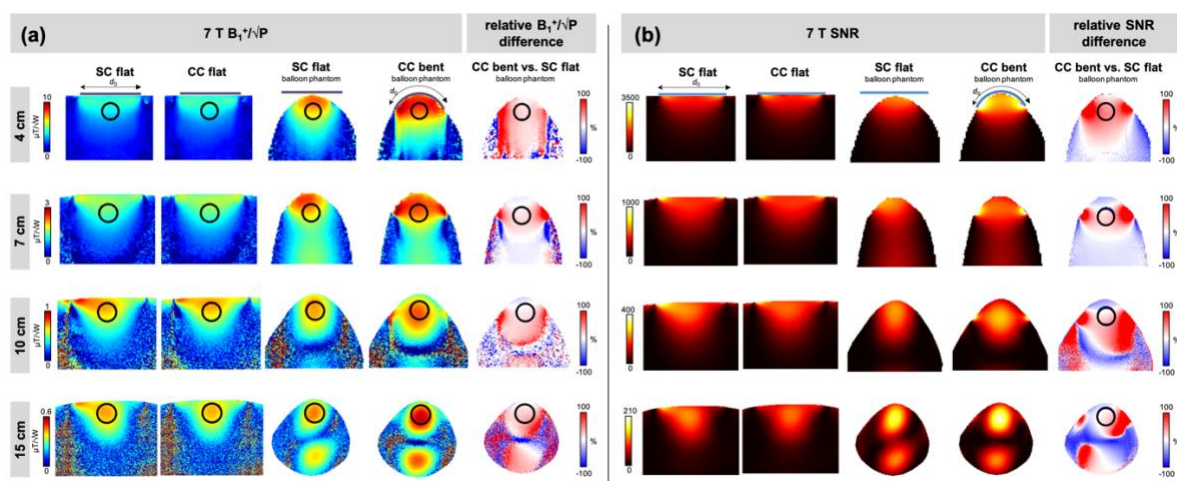


Figure 8 : (a) Cartes d'efficacité de transmission (B_1^+/\sqrt{P}) et (b) de RSB pour les antennes standards et coaxiales utilisées à 7 T.

Conclusion

Nous avons proposé un nouveau concept d'antennes combinant le principe des structures auto-résonantes à câbles coaxiaux avec celui des lignes de transmission multi-tours multi-fentes. Un circuit équivalent a été proposé et des solutions analytiques pour le diamètre possible des antennes MTMF ont été calculées pour cinq intensités de champ B_0 . Des simulations de densité de courant de surface ont été effectuées pour analyser les trois parties conductrices distinctes d'une antenne coaxiale. L'étude s'est concentrée sur une preuve de concept de l'utilisation des antennes coaxiales MTMF en mode réception à 3 T et en mode émission/réception à 7 T. Des antennes de 4, 7, 10 et 15 cm de diamètre ont été fabriquées à partir de câbles coaxiaux non magnétiques. Au cours des tests sur banc expérimental et en IRM, les antennes coaxiales ont démontré leur robustesse à la flexion ainsi que l'amélioration du B_1^+/\sqrt{P} et du RSB (7 T) ou l'absence de réduction significative du RSB (3 T)

lorsqu'elles sont courbées sur un échantillon par rapport à l'utilisation des antennes standards en cuivre à plat.

L'atout majeur des antennes coaxiales MTMF présentées dans cette étude est leur faible poids, leur flexibilité et le fait que la taille de l'antenne peut être choisie (presque) librement pour différentes intensités de champ B_0 . En appliquant le principe des résonateurs MTMF, la restriction de taille des antennes 1T1F peut être surmontée, et les antennes coaxiales peuvent être optimisées en taille pour une large gamme d'applications anatomiques. La grande flexibilité des antennes coaxiales est particulièrement avantageuse pour les applications où la variabilité entre sujets est forte (sein, abdomen, articulations, cœur, etc.) où les antennes rigides standards seraient généralement placées loin de la zone anatomique concernée. En outre, le faible poids et la flexibilité permettent la fabrication d'antennes "portables", ce qui augmente le confort du patient.

Chapitre 5 : Transmission de données sans fil en IRM

Ce chapitre résume l'intégralité de l'article publié dans *Frontiers in Physics* qui aborde les « Perspectives de développement d'antennes radiofréquences sans fil pour l'imagerie par résonance magnétique » [10] (*Article II*). Les études supplémentaires présentées dans ce chapitre portent sur le développement d'un module prototype de communication optique sans fil, des simulations du champ de vue optique dans l'imageur et un résumé du protocole de tests pour l'utilisation future des modules OWC (*angl.*, optical wireless communication) en IRM.

Perspectives des antennes RF sans fil pour l'IRM

L'*Article II* traite des défis scientifiques et technologiques liés au développement d'antennes radiofréquences (RF) sans fil pour l'IRM basée sur la littérature, ainsi que sur l'interprétation des auteurs. Les principales exigences et stratégies possibles pour la mise en œuvre d'un système sans fil pour les trois sous-systèmes importants dans la chaîne de réception en IRM sont présentés et discutés. La Figure 9 illustre ces trois sous-systèmes : signaux RMN de réception, signaux de contrôle et alimentation électrique sans fil. Pour les signaux RF des installations IRM modernes, par exemple à un champ statique de 3 T et en utilisant un réseau d'antenne de réception de 64 canaux, avec une numérisation du signal RMN au plus près de l'antenne et des méthodes avancées pour une compression de gamme dynamique (souvent plus de 16 bits) et du débit de données, des débits > 500 Mbps seront nécessaires. Pour la transmission de données sans fil à haut débit, les technologies WiGig opérant à 60 GHz et la communication optique sans fil semblent être des stratégies prometteuses. Toutefois, la fonctionnalité de ces systèmes intégrés à l'antenne pendant les examens IRM reste à vérifier. Outre les signaux RF, les signaux de contrôle pour les composants, pour assurer par exemple le découplage actif, la synchronisation avec le système IRM et l'ajustement fin de B_0 , doivent être gérés. L'alimentation électrique sans fil est également une question importante, en particulier pour un grand nombre de composants supplémentaires embarqués sur l'antenne. Des systèmes de transfert d'énergie sans fil (plus de 10 W) semblent être une solution intéressante par rapport à l'utilisation de batteries. À notre avis, les antennes RF sans fil deviendront finalement réalisables à l'avenir en combinant les stratégies efficaces disponibles issues des récentes avancées scientifiques. Des innovations sont

spécifiquement nécessaires en ce qui concerne les technologies de transmission sans fil, la compatibilité IRM et l'alimentation électrique sans fil.

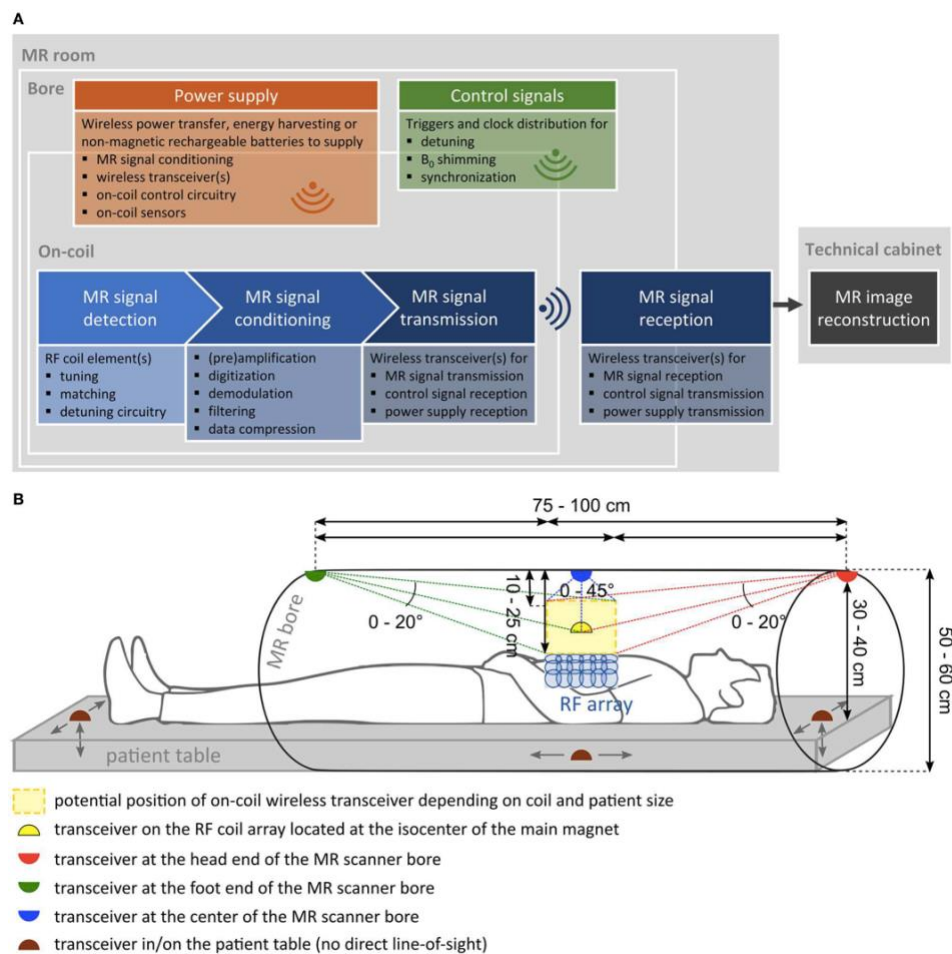


Figure 9 : Schéma fonctionnel d'une chaîne de réception IRM sans fil comprenant trois sous-systèmes principaux : signaux RMN de réception (bleu), signaux de contrôle (vert), et alimentation électrique (orange) sans fil. (B) Vue latérale des variantes de positionnement de l'émetteur-récepteur sans fil, y compris des estimations de la distance et de l'angle de transmission. Figure publiée dans l'Article II, [10].

Développement d'un système de transmission optique sans fil

La possibilité théorique d'utiliser une approche de communication optique sans fil pour le transfert de données à haut débit dans les réseaux de récepteurs RF sans fil à l'avenir a été examinée dans l'Article II. Des études supplémentaires étaient menées afin d'explorer le développement d'un module OWC. Afin d'alléger les exigences en termes de débit de données (≈ 1 Mbd) pour le développement du prototype de communication optique sans fil, un accéléromètre compatible IRM pour la détection des mouvements respiratoires, ou "MARMOT"[11], a été choisi comme exemple de

capteur portable qui pourrait bénéficier d'une chaîne de transmission de données sans fil.

L'objectif était d'abord de caractériser les performances d'un module composé d'un émetteur et d'un récepteur optiques et de circuits électroniques Tx et Rx environnants comme le montre la Figure 10.



Figure 10 : Vue d'ensemble des modules de transmission optique sans fil

Comme la communication bidirectionnelle (semi-duplex) est ciblée pour les capteurs de mouvement, chaque module devrait être équipé de composants Rx et Tx, c'est-à-dire de photodiode et de DEL, dans la version finale. Pour les premiers essais, au lieu d'interfacer directement les modules à une sortie MARMOT, un Raspberry Pi (ordinateur mono-carte) a été connecté à chaque module OWC via ses broches d'entrée/sortie polyvalentes (GPIO). Les cartes Tx et Rx fabriquées sur lesquelles ont été conduits les tests sont présentées en Figure 11.

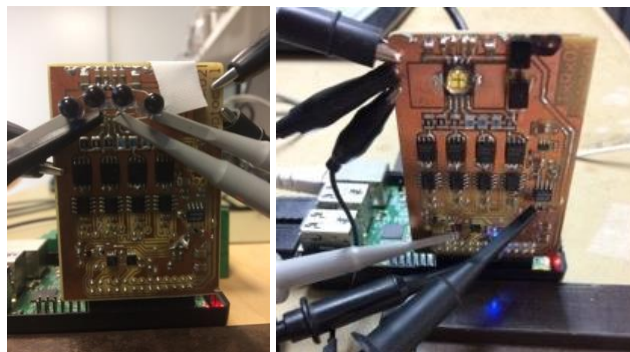


Figure 11 : Carte émettrice (à gauche) et réceptrice (à droite). Les DEL entourées d'une lentille sphérique sur la carte Rx ne sont pas utilisées et pourraient être remplacées par des DEL IR comme sur la carte Tx pour des tests bidirectionnels.

Les tests préliminaires ont révélé que les modules prototypes conçus permettent de réaliser la communication optique sans fil à courte (0.3 m) et à longue (1.5 m) portée. Le débit de données maximum réalisable pour une transmission fiable est de 2 MBd. La Figure 12 montre l'exemple d'une transmission réussie du message « Hello world » à 2 MBd avec une distance de 1.5 m entre les deux modules, avec deux DEL actives et une puissance totale des DEL de 2.28 W. Dans la capture d'écran de l'oscilloscope, les traces jaunes correspondent au signal émis par les DEL, les traces vertes au signal reçu par les photodiodes après amplification, et les traces roses au signal reçu après

le comparateur. L'amplitude de la tension de référence (utilisée par le comparateur) est représentée par la trace violette.

test	number of active LEDs	P_{LED} [W]	distance [m]	data rate [MBd]	message	status
2	2	2.28	1.5	2	"Hello world"	OK



Figure 12 : Capture d'écran de l'oscilloscope, montrant la transmission d'une série de bits à un débit de 2 MBd et les paramètres mentionnés dans le tableau en dessus de la figure.

Cette performance à 2 MBd permettrait même la transmission optique sans fil des signaux multiplexés de deux MARMOTs. Les distances de transmission possibles permettraient de s'adapter à différents scénarios de positionnement des modules dans l'IRM comme illustré dans la Figure 9.

Un avantage de cette configuration de module optique est le fonctionnement avec des émetteurs produisant de la lumière dans la gamme proche infrarouge, qui n'est pas visible pour l'œil humain et peut donc avoir des puissances élevées sans être perçue comme "trop lumineuse". Néanmoins, une solution avec des composants dans le domaine visible pourrait également être intéressante car elle pourrait être utilisée en même temps à des fins d'éclairage. Pour le détecteur IR, la lumière ambiante dans le domaine visible n'a aucune influence sur les performances de la transmission de données, car un filtre bloquant la lumière du jour est intégré dans le boîtier de la photodiode.

Les améliorations possibles et les orientations des travaux futurs concernant principalement l'adaptation du module OWC pour une utilisation en IRM seront examinées dans le chapitre 6.

Chapitre 6 : Futur travail et conclusions

Les travaux présentés sur le développement d'antennes coaxiales légères et flexibles, les perspectives des antennes RF sans fil ainsi que le développement d'un système de communication optique sans fil révèlent plusieurs aspects qui peuvent être pris en compte pour des futurs travaux.

La comparaison entre les antennes coaxiales 1T1F et MTMF présentée seulement pour certains cas à 3 et 7 T demande une étude plus systématique et plus approfondie de la différence entre l'utilisation d'une antenne ayant une résonance proche de la fréquence de Larmor et une antenne ayant une résonance inférieure ou supérieure à la fréquence de Larmor. Par ailleurs, la conception d'une antenne coaxiale à double accord, c'est-à-dire adaptée à un fonctionnement à différentes fréquences, pourrait être intéressante. À cette fin, mais aussi de manière plus générale, les composants d'accord et d'adaptation devraient également être intégrés dans les simulations électromagnétiques pour tenir compte des pertes dans l'interface de l'antenne. Les configurations de réseaux avec des antennes coaxiales pourraient être intéressantes car le RSB élevé des antennes de surface souple peut être exploité sur un champ de vue étendu. Les études pourraient se concentrer sur les performances d'imagerie parallèle et de transmission parallèle d'un tel réseau. Un autre aspect particulièrement important pour les réseaux coaxiaux flexibles utilisés en mode émission/réception dédiés à l'imagerie in vivo à 7 T est une étude approfondie du TAS local et global en utilisant des simulations EM et différents scénarios de flexion de l'antenne, car la superposition des champs électriques est influencée par la position des antennes.

Le prototype de système optique sans fil décrit est la première étape vers le développement d'un système compatible avec l'environnement IRM. Afin d'obtenir un système entièrement compatible IRM, certains composants devront être remplacés par une version non magnétique appropriée. En outre, les composants qui n'ont pas montré d'attraction significative par un aimant puissant sur banc de tests devraient, dans une prochaine étape, être testés sur fantôme dans l'IRM. Des améliorations sont possibles concernant les adaptations manuelles nécessaires pour le réglage de la tension de référence et de l'alimentation des DEL. Cela nécessite

l'automatisation du contrôle de ces paramètres, par exemple par un circuit de contrôle automatique du gain pour adapter l'amplitude de la tension reçue en fonction de la distance entre l'émetteur et le récepteur. Dès que l'objectif principal mentionné ci-dessus, à savoir la mise en œuvre d'un module entièrement compatible avec l'IRM, sera atteint, l'accent sera donc mis sur la recherche d'une configuration de module avec des exigences minimales en matière de puissance.

Comme la motivation initiale est la transmission sans fil du signal d'un capteur de mouvement, la version finale du module compatible IRM et optimisée en puissance sera interfacée avec un capteur de mouvement. Les performances de la liaison sans fil seront caractérisées au cours d'une expérience d'imagerie réaliste avec une correction rétrospective du mouvement basée sur les données de l'accéléromètre acquises via la liaison optique sans fil. Une perspective à long terme est l'étude de la manière d'augmenter le débit de données numérisées. Très probablement, cela nécessitera un circuit et des composants optiques de commutation plus rapide et des mécanismes d'alignement.

Le but ultime pour l'avenir des antennes de réception et des réseaux d'antennes serait de fusionner les développements des antennes flexibles et de la transmission de signaux sans fil. Dans le contexte plus large de la future mise en œuvre des antennes de réception flexibles sans fil, nous devons prendre en compte toutes les différentes parties du système de réception : transmission du signal RMN, alimentation électrique et signaux de commande sans fil. Les principaux défis restants sont liés à la recherche de composants de numérisation et d'alimentation entièrement compatibles IRM, et d'émetteurs-récepteurs sans fil à haut débit de données. Les besoins élevés en énergie peuvent rapidement devenir un challenge. À notre connaissance, une chaîne RF de réception entièrement sans fil consistant en une antenne numérique interfacée à un émetteur-récepteur sans fil, qui est alimenté et contrôlé sans fil, même pour un seul élément d'antenne, n'a pas encore été développée.

Il existe diverses applications imaginables pour des antennes RF flexibles sans fil. Pour les deux applications potentielles suivantes, elles pourraient avoir un impact considérable sur un grand nombre d'exams en clinique et sur une large cohorte de patients.

- **Mammographie par IRM**

Actuellement, la mammographie par IRM est réalisée avec une antenne intégrée dans deux moules rigides en forme de coupe et la patiente en position face contre terre (en décubitus ventral). En fonction de la taille des seins, la charge de l'antenne peut être sous-optimale, par exemple pour les petits seins, ce qui entraîne une pénalité de RSB. Pour les seins de plus grosse taille, le positionnement est compliqué et, en général, la position n'est pas confortable pour la patiente. Cela souligne la nécessité de progrès technologiques pour améliorer le confort du patient et la qualité de l'image. Une solution polyvalente serait le développement d'un gilet d'antennes léger et flexible qui pourrait être porté comme un soutien-gorge de sport. En utilisant des éléments d'antenne coaxiale, le poids total d'un réseau d'antennes pourrait être maintenu très bas (≈ 1.5 kg).

- **Imagerie du genou**

Les blessures au genou peuvent impliquer différentes parties de l'articulation qui peuvent être efficacement identifiées en IRM, en particulier à très haut champ. Une antenne de genou flexible permettrait la flexion de l'articulation d'une acquisition d'image statique à l'autre et l'imagerie cinématique du genou.

En conclusion, ce travail de thèse présente le développement et la mise en œuvre d'antennes RF coaxiales flexibles basées sur le principe des résonateurs à ligne de transmission pour l'IRM à 3 T en mode réception et l'IRM à 7 T en mode émission/réception. Le concept repose sur l'extension à de multiples tours et/ou fentes dans le câble coaxial permettant la construction d'antennes de forme adaptée et de taille optimale pour une profondeur de pénétration donnée en fonction de l'application anatomique visée. La flexibilité permet d'obtenir une sensibilité et une efficacité de transmission optimales des antennes lorsqu'elles sont conformées à une forme courbée ce qui pourrait être exploitée dans une configuration de réseau à l'avenir. Ce travail comprend également un examen complet des perspectives de développement d'antennes de radiofréquence sans fil pour l'IRM et donne un aperçu de la future mise en œuvre d'un système de communication optique sans fil pour les données de capteurs de mouvement dans l'environnement IRM.

1. General Introduction

1.1 Motivation

Magnetic resonance imaging (MRI) is a constantly developing medical imaging technique for a wide range of applications which has gained accessibility over the last few decades. MRI is routinely used for diagnostic purposes in clinical routine and in the research domain for pre-clinical human and animal studies.

The major advantages of MRI over other imaging modalities are its non-invasiveness and relative safety as no ionizing radiation is used, its outstanding soft-tissue contrast, and the versatility of the technique offering structural, functional (fMRI), and metabolic (MR spectroscopy) information. Whole-body imaging is feasible with standard clinical MR scanners at resolutions in the mm range, while advanced setups allow imaging of small structures down to tens of μm .

The nuclear magnetic resonance (NMR) phenomenon is exploited to create a signal originating from excited nuclear moments (“spins”) in a biological tissue, located in a strong static magnetic field B_0 . The instrument used for spin excitation and signal reception is a resonating structure, the so-called radio frequency (RF) coil. The RF coil’s operation frequency is determined by the B_0 field strength and the gyromagnetic ratio of the nucleus under investigation. Additional magnetic field gradients spatially encode the signal.

The MR image quality depends on the achievable signal-to-noise ratio (SNR). Therefore, several development strategies related to hardware, aiming for signal enhancement have been pursued:

The increase in static magnetic B_0 field strength (e.g. 7 T, [1–3]) to create higher net tissue magnetization and, therefore, higher detectable signal amplitudes. The benchmark for standard clinical imaging is 3 T while a first certified clinical ultra-high field (UHF) 7 T MR scanner is already on the market.

Gradient hardware development is focused on improving its main performance characteristics, i.e. linearity, gradient strength and gradient slew rate. With increased gradient amplitude, higher image resolutions can be obtained, and high slew rates allow for high-speed imaging.

Another main aspect is the optimization of transmit and receive characteristics of RF coils and the development of coil arrays [4]. At 3 T, it is common to use a large body coil integrated in the scanner bore for homogeneous RF transmit field creation in combination with small receive-only surface coils with enhanced sensitivity close to the body region to be imaged. At 7 T, due to the difficulties in producing a homogeneous RF transmit field related to wavelength effects, no such body coil is integrated and, therefore, typically surface coils are used in transmit/receive (Tx/Rx) mode. Higher coil channel counts allow for parallel imaging [5–7] and parallel transmission techniques [8] resulting in drastically shorter examination times, and, more recently, more homogeneous, RF excitation which is especially required at UHF. In addition, the development of form-fitting and flexible or even stretchable RF coils has been emphasized. This is motivated by signal gain and increased patient comfort with close-fitting lightweight coil design and the adaptability to different anatomies. A trend towards construction of fully wearable MR devices has been noticeable within the research community in recent years. A wearable MR device is not only characterized by flexibility and lightweight material but also by the removal of cabling. This implies wireless MR data transmission, wireless power supply, and transmission of control signals in the MR environment.

The integration of additional sensors or on-coil components during the MRI process, e.g. for motion correction or localized shimming, have gained interest as they can improve image quality and robustness of the acquisition. The use of low-noise and miniaturized electronics are further aspects in the improvement of MR data quality.

This work aims at proposing concepts and proofs-of-concept for the development of wearable technology in MR.

The first goal was the development, fabrication, and experimental validation of flexible lightweight RF coils for Rx-only operation at 3 T and Tx/Rx operation at 7 T. A novel coil concept based on auto-resonant multi-turn multi-gap coaxial transmission line resonators is introduced. This coil design enables ideal form-fitting and the choice of arbitrary coil sizes which results in an expansion of possible coaxial coil design parameters and optimal SNR and penetration depth depending on the target anatomical application. The proposed coaxial coil (CC) design presents a reliable alternative compared to rigid standard copper wire coils (SCs). It is especially

suitable for applications where inter-patient variability of anatomy size is large and a conformal “one-size-fits-all” coil yields optimum SNR for the majority of patients.

The sparse available literature reviewing the topic of wireless communication in MR was the initial motivation for the second central goal of this work: a comprehensive evaluation of the status quo in wireless RF coil development and analysis of developments related to wireless data transmission, wireless power supply, and wireless control signaling. This provides an outlook on the feasibility of wireless RF coils in the future. The focus is further put on the exploration of optical wireless communication (OWC) for use in MR. The implementation for motion sensor data transmission is the aim of preliminary tests with a custom-built OWC module which is a first step towards future OWC signal transmission in the MR.

1.2 Thesis Outline

This PhD thesis was conducted in the frame of a project between the Laboratoire d'imagerie biomédicale multimodale (BioMaps) at the Université Paris-Saclay (Orsay, France) and the High Field MR Center at the Center for Medical Physics and Biomedical Engineering at the Medical University of Vienna (Vienna, Austria).

This thesis manuscript is divided into six chapters:

In the present *chapter 1*, a general introduction of the context, the main objectives and an overview over the following chapters are given.

In *chapter 2*, the theoretical background and physics related to the thesis work will be thoroughly explained. A focus will be put on MR fundamentals, RF coils, and electromagnetic (EM) simulation basics.

In *chapter 3*, several interrelated aspects important for wearable MR devices are discussed based on the motivation for wearable devices, the state-of-the-art, and challenges in their development. This chapter will establish the contextual link between the two subsequent chapters 4 and 5 and explain why two main aspects have to be considered for the development of wearable MR technology: flexible radio frequency coils (*Study I*) and the wireless data transmission in MR (*Study II*).

Chapter 4 briefly introduces the specific thematic of flexible RF coils and includes the integrality of an article on “Flexible multi-turn multi-gap coaxial RF coils: design concept and implementation for Magnetic Resonance Imaging at 3 and 7 Tesla”, published in *IEEE Transactions on Medical Imaging* [9]. The following sub-section is dedicated to various supplementary studies regarding flexible coaxial radio frequency coils and is concerned with the design concept validation and additional experimental studies and simulations.

In *chapter 5*, the wireless RF coil thematic is shortly introduced, followed by the published *Frontiers in Physics* article “Perspectives in Wireless Radio Frequency Coil Development for Magnetic Resonance Imaging” [10] which comprises a summary and

analysis of the status quo of wireless RF coils, suggesting the option of optical wireless RF coils for the future. The “supplementary studies” section focuses on the description of the development of a custom-built OWC module for optical wireless data transmission of motion sensor signals. Furthermore, an optical field-of-view (FOV) simulation study and an OWC test summary are presented.

In *chapter 6*, an outlook on required future work and potential applications will be given. This will then be ultimately followed by a general conclusion of this thesis work.

The overall thesis structure is depicted in Figure 1.1, listing the chapters and main contents depending on their specificity and chronological appearance in the manuscript. Dark purple boxes indicate studies (*Study I/II*) that led to article publication in scientific journals.

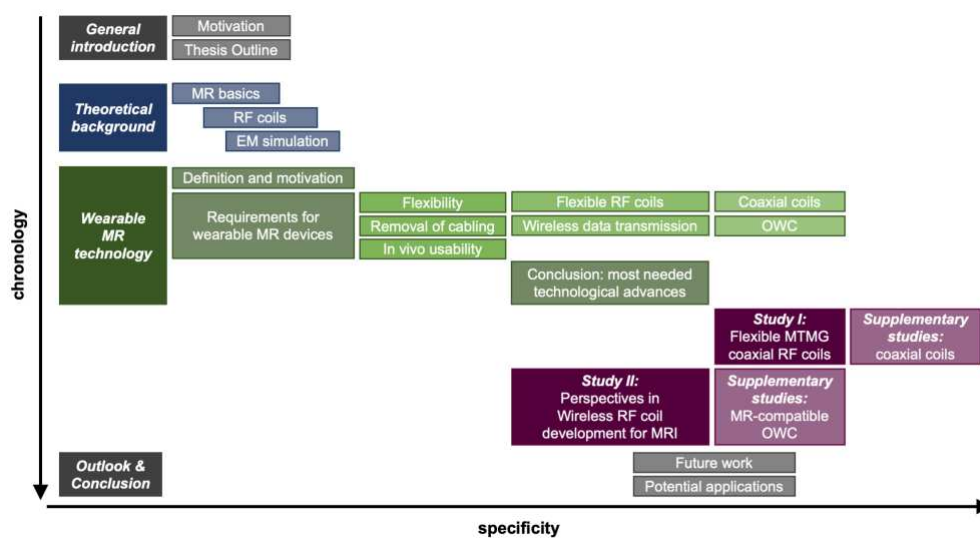


Figure 1.1: Thesis structure overview. The chart shows a “chronology” axis, spanning over all 6 thesis chapters. Chapter content is then classified along the “specificity” axis, ranging from general to the most detailed explanations and studies.

2. Theoretical Background

This chapter starts with the description of the basic concepts of nuclear magnetic resonance physics and magnetic resonance imaging (2.1). This will be followed by an introduction to the theoretical background concerning radio frequency (RF) coils (2.2) and numerical electromagnetic simulations (2.3).

2.1 Magnetic Resonance Basics

NMR physical principles can only be explained in depth using quantum mechanics which is beyond the scope of this thesis. For a basic understanding, the classical view with some quantum mechanical elements gives a sufficiently accurate approach for the description of most relevant phenomena. The mentioned principles, equations and conclusions are summarized based on sources [12–15] unless otherwise stated.

2.1.1 The Nuclear Magnetic Resonance phenomenon

2.1.1.1 Nuclear spins and magnetic moment

Atomic nuclei possess a quantum mechanical property called nuclear spin I with a discretized magnitude $|I|$ given by

$$|I| = \hbar\sqrt{I(I+1)} \quad \text{Eq. 2.1}$$

$$I = 0, \frac{1}{2}, 1, \frac{3}{2}, \dots \quad \text{Eq. 2.2}$$

where I denotes the spin quantum number and \hbar is the reduced Planck constant ($h/2\pi$).

The intrinsic angular momentum vector, or spin, I is linearly related to a moving charge's magnetic dipole moment μ via the gyromagnetic ratio γ which depends on the nucleus.

$$\mu = \gamma \cdot I \quad \text{Eq. 2.3}$$

$$\gamma = \frac{\mu_N g_n}{\hbar} \quad \text{Eq. 2.4}$$

μ_N is the nuclear magneton and g_n is the nuclear g -factor.

In general, all nuclei with a net spin $I \neq 0$ create a magnetic moment and can therefore be employed in NMR experiments. The ^1H (hydrogen) nucleus, consisting of one

proton with a spin quantum number of $I = \frac{1}{2}$, is the most targeted nucleus in biomedical NMR applications as it has a high natural abundance and high occurrence in human tissue compounds. There are other NMR-relevant nuclei, depending on the target biomedical application, among which the most commonly used are listed in Table 2.1. ^{31}P is used to study the energy metabolism in cells. ^{13}C and ^{23}Na are used to investigate changes in metabolic and physiologic processes which can be an indicator for a variety of diseases e.g. of cancerous nature or due to cardiovascular disfunction.

nucleus	nuclear spin I	gyromagnetic ratio $\gamma/2\pi$ [MHz/T]	natural abundance [%]	f_L [MHz] @ $B_0 = 3$ T
^1H	1/2	42.58	99.985	127.7
^{13}C	1/2	10.71	1.10	32.1
^{23}Na	3/2	11.26	100	33.8
^{31}P	1/2	17.24	100	51.7

Table 2.1: NMR relevant nuclei

2.1.1.2 Spins in a static magnetic field

In absence of magnetic fields, the magnetic moments of a spin system within a sample, e.g. the human body, are randomly orientated. As soon as an external static magnetic field (\mathbf{B}_0) is applied, conventionally along the z-direction, the magnetic moments align either parallel or antiparallel to the static magnetic field direction. I_z describes the component of the angular momentum vector \mathbf{I} along \mathbf{B}_0 and is quantized to:

$$I_z = \hbar \cdot m_I \quad \text{Eq. 2.5}$$

where m_I denotes the magnetic quantum number which is limited to $2I + 1$ values.

$$m_I = -I, -I + 1, \dots, I - 1, I \quad \text{Eq. 2.6}$$

Using Eq. 2.3 the z-component of the magnetic moment μ_z can be derived.

$$\mu_z = \gamma \cdot \hbar \cdot m_I \quad \text{Eq. 2.7}$$

For the example of a ^1H nucleus where $m_I = \pm \frac{1}{2}$, μ_z has two possible states.

$$\mu_z = \begin{cases} +\frac{1}{2}\gamma \cdot \hbar \\ -\frac{1}{2}\gamma \cdot \hbar \end{cases} \quad \text{Eq. 2.8}$$

The phenomenon of distinct split energy levels of magnetic moments under the influence of a static magnetic field is called the “Nuclear Zeeman effect” and is

schematically depicted in Figure 2.1. It is shown that spins aligned antiparallel to the B_0 field ($m_l = -\frac{1}{2}$) have higher potential energy E than spins aligned in parallel to B_0 ($m_l = +\frac{1}{2}$).

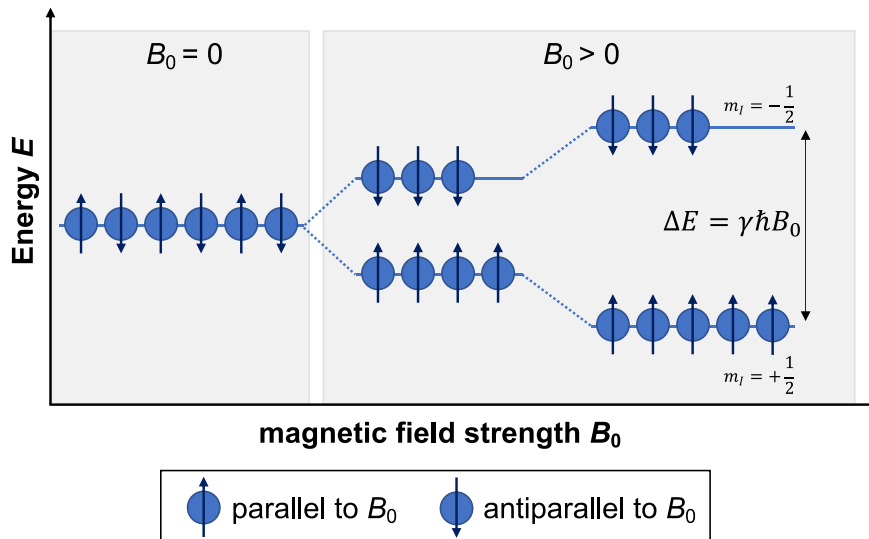


Figure 2.1: Illustration of the Zeeman splitting effect and corresponding potential energy of the spins aligned parallel or antiparallel to the B_0 field.

The potential energy E of the magnetic moment in presence of a B_0 field is given by

$$E = -\mu_z \cdot B_0 = \pm \frac{1}{2} \gamma \cdot \hbar \cdot B_0 \quad \text{Eq. 2.9}$$

For the ^1H nucleus, this results in an energy difference or energy necessary for the transition between energy states ΔE which linearly increases with B_0 as given in Eq. 2.10. In other words, by emission or absorption of photons with energy $\hbar \cdot \omega_L = h \cdot f_L$ (with $\omega = 2\pi f$ and $\hbar = \frac{h}{2\pi}$), the transition between energy states is possible.

$$\Delta E = \gamma \cdot \hbar \cdot B_0 = \hbar \cdot \omega_L = h \cdot f_L \quad \text{Eq. 2.10}$$

The angular frequency ω_L (Eq. 2.11) is the so-called Larmor frequency which increases with magnetic field strength and depends on the gyromagnetic ratio in $\text{rad} \cdot \text{s}^{-1} \cdot \text{T}^{-1}$. For practical reasons, often the factor $\frac{\gamma}{2\pi}$ is given in $\text{MHz} \cdot \text{T}^{-1}$ for ordinary Larmor frequency f_L calculations in MHz depending on the B_0 field strength (Eq. 2.12). Some examples for Larmor frequencies assuming that $B_0 = 3 \text{ T}$ are given in Table 2.1.

$$\omega_L = \gamma B_0 \quad \text{Eq. 2.11}$$

$$f_L = \frac{\gamma}{2\pi} B_0 \quad \text{Eq. 2.12}$$

Boltzmann statistics allow for the prediction of the number of spins in each energy level, N_- indicating the number of spins in the antiparallel (high) energy state and N_+ indicating the number of spins in the parallel (low) energy state. The ratio of spin numbers in thermal equilibrium is given by

$$\frac{N_+}{N_-} = e^{\frac{\Delta E}{kT}} = e^{\frac{\gamma \hbar B_0}{kT}} \quad \text{Eq. 2.13}$$

where k is the Boltzmann constant and T the absolute temperature in Kelvin. Usually, the number of excess of spins parallel to B_0 (N_+) is very small but still results in a net magnetization \mathbf{M} which can be written as the vector sum of individual magnetic moments of the total number $N = N_+ + N_-$ of spins.

$$\mathbf{M} = \sum_{i=0}^N \boldsymbol{\mu}_i \quad \text{Eq. 2.14}$$

Using Eq. 2.13, the number of excess spins ΔN in parallel to B_0 ($N_+ - N_-$) can be approximated taking into account that, typically, the thermal energy kT is much larger than the magnetic energy $\gamma \hbar B_0$.

$$\Delta N = N \cdot \tanh \frac{\gamma \hbar B_0}{2kT} \approx N \cdot \frac{\gamma \hbar B_0}{2kT} \quad \text{Eq. 2.15}$$

When combining Eq. 2.14 and Eq. 2.15, this results in the expression given in Eq. 2.16. This equation establishes the linear relationship between the equilibrium magnetization M_0 in a static magnetic field B_0 and the total number of spins N as well as the angular momentum μ_z . This means that for a spin ensemble, the net magnetization in a static magnetic field can be increased by increasing the B_0 magnetic field strength which is the trend followed by major MR system vendors.

$$M_0 = \Delta N \cdot \mu_z \approx N \cdot \mu_z \cdot \frac{\gamma \hbar B_0}{2kT} \quad \text{Eq. 2.16}$$

The macroscopic measure of a net magnetization vector \mathbf{M} is practical for the description of a spin ensemble as thereby, classical physics can be used to formulate equations of motion for the magnetization \mathbf{M} .

According to classical mechanics, one can consider that magnetic moments in a static magnetic field experience a torque \mathbf{T} that strives for the minimization of potential energy, and therefore the alignment to the external B_0 field.

$$\mathbf{T} = \frac{d\mathbf{I}}{dt} = \boldsymbol{\mu} \times \mathbf{B}_0 \quad \text{Eq. 2.17}$$

Using Eq. 2.3 and Eq. 2.17, the following relationship can be found:

$$\frac{d\boldsymbol{\mu}}{dt} = \boldsymbol{\mu} \times \gamma \mathbf{B}_0 = \boldsymbol{\mu} \times \boldsymbol{\omega}_L \quad \text{Eq. 2.18}$$

Further substituting the individual magnetic moment by the macroscopic magnetization for a spin ensemble according to Eq. 2.14 yields

$$\frac{d\mathbf{M}}{dt} = (\mathbf{M} \times \gamma \mathbf{B}_0) = \mathbf{M} \times \boldsymbol{\omega}_L \quad \text{Eq. 2.19}$$

The above-derived equation of motion for the magnetization (Eq. 2.19) describes a precession of \mathbf{M} around \mathbf{B}_0 (or the z-axis) at the Larmor frequency ω_L . As the precessing spins are largely out of phase, there exists no detectable net transverse component of \mathbf{M} in the x- or y-direction but only along z. This is sketched in Figure 2.2a.

2.1.1.3 Spins in a radio frequency field

The spin system is in its equilibrium state under the influence of \mathbf{B}_0 only and can be disturbed using a time-dependent RF field $\mathbf{B}_1(t)$, oscillating at the Larmor frequency. With an RF coil employed for the emission of such a B_1 field perpendicular to the B_0 field direction, the RF field shifts the magnetic moments of all spins to precess in phase and creates a, now detectable, transverse magnetization component M_{xy} . The spin excitation relies on the “nuclear magnetic resonance” phenomenon which only occurs when using a resonance frequency that equals ω_L . A receive RF coil can detect the transverse rotating magnetization by induction of an electromotive force (*emf*). Under the presence of an RF field, the magnetization precesses around the sum of the \mathbf{B}_0 and $\mathbf{B}_1(t)$ field which is given by

$$\mathbf{B}(t) = \mathbf{B}_0 + \mathbf{B}_1(t) = \begin{pmatrix} B_1 \cdot \cos(\omega_L t) \\ B_1 \cdot \sin(\omega_L t) \\ B_0 \end{pmatrix} \quad \text{Eq. 2.20}$$

The equation of motion for the magnetization taken from Eq. 2.19 therefore becomes

$$\frac{d\mathbf{M}}{dt} = \mathbf{M} \times \gamma \mathbf{B}(t) \quad \text{Eq. 2.21}$$

As illustrated in Figure 2.2a, in the laboratory frame of reference (x, y, z) , under the influence of a static magnetic field only, the equilibrium magnetization \mathbf{M}_0 precesses at ω_L around the z -direction (\mathbf{B}_0). The trajectory followed by the magnetization in the laboratory frame under the application of a \mathbf{B}_1 field is more complex and resembles a helix. It is more convenient to visualize and describe this motion in the rotating frame of reference (x', y', z') , with a rotating frequency equal to ω_L around z which is shown in Figure 2.2b. For an observer in the rotating frame, \mathbf{M}_0 appears stationary and is tilted towards the xy -plane resulting in a magnetization \mathbf{M} with a net transverse (M_{xy}) and longitudinal component (M_z), when a \mathbf{B}_1 field is applied along the x' -direction.

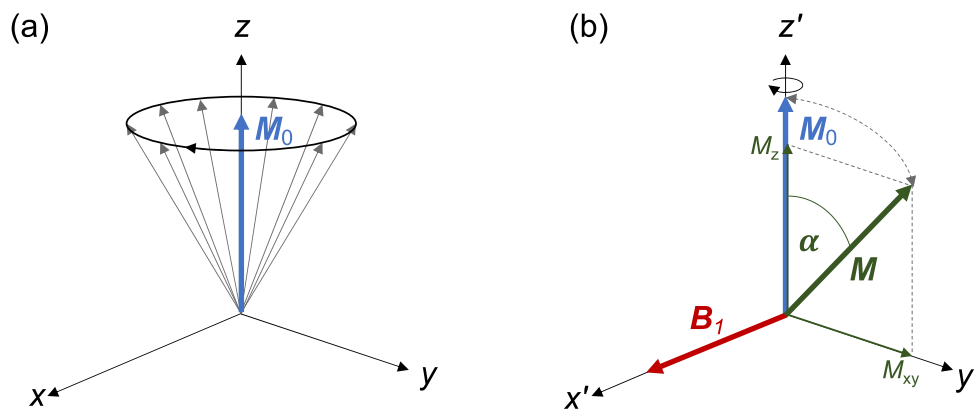


Figure 2.2: (a) Equilibrium magnetization \mathbf{M}_0 in the laboratory frame, spins precess around the z -direction (which is also the \mathbf{B}_0 direction), (b) illustration of tilted magnetization towards the transverse plane in the rotating frame during \mathbf{B}_1 transmission.

The tilting of the magnetization towards the xy -plane is quantized by the flip angle α . Over a certain volume, the flip angle distribution $\alpha(\mathbf{x})$ results from the application of an RF field with the spatial distribution $B_1(\mathbf{x})$ produced by a pulse of shape $\mathbf{b}(t)$ for a certain pulse duration T_{pulse} .

$$\alpha(\mathbf{x}) = \gamma B_1(\mathbf{x}) \int_0^{T_{\text{pulse}}} \mathbf{b}(t) dt \quad \text{Eq. 2.22}$$

For a rectangular pulse, the flip angle distribution can be simplified to

$$\alpha(\mathbf{x}) = \gamma B_1(\mathbf{x}) T_{\text{pulse}} \quad \text{Eq. 2.23}$$

2.1.1.4 Relaxation

After spin polarization by a static magnetic B_0 field and spin excitation by an RF (B_1) field, the spin system will return to its equilibrium state, i.e. to the initial

magnetization M_0 . This process is called “relaxation” and one can differentiate between two mechanisms: longitudinal (spin-lattice) and transversal (spin-spin) relaxation which are characterized by the time constants T_1 and T_2 , respectively. Figure 2.3 illustrates the processes of longitudinal (a) and transversal (b) relaxation.

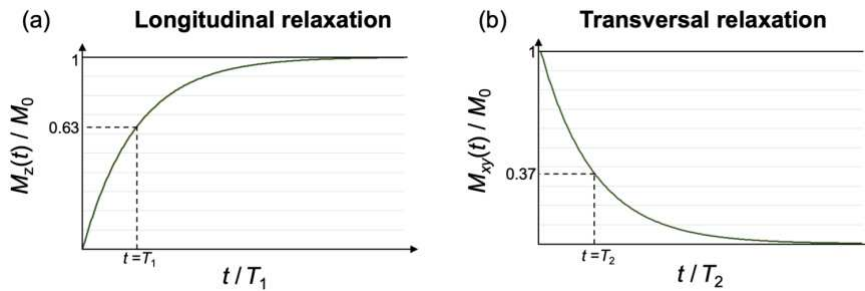


Figure 2.3: Time variation of the (a) longitudinal and (b) transversal magnetization component during spin relaxation.

The longitudinal magnetization component M_z recovers to its initial amplitude M_0 based on the interaction of spins with their surrounding molecular lattice. M_z regains amplitude at a rate given by

$$\frac{dM_z}{dt} = \frac{1}{T_1} (M_0 - M_z(t)) \quad \text{Eq. 2.24}$$

The solution to this differential equation is the exponential recovery process of the longitudinal magnetization (Eq. 2.25) which is plotted in Figure 2.3a. T_1 characterizes the time at which M_z has regained $\approx 63\%$ of its initial amplitude.

$$M_z(t) = M_z(0) \cdot (1 - e^{-\frac{t}{T_1}}) \quad \text{Eq. 2.25}$$

Transversal or T_2 relaxation refers to the decay of transversal magnetization M_{xy} with time which is caused by interactions between spins and the resulting loss of spin phase coherence. The decay is characterized by the time constant T_2 indicating when M_{xy} has decreased to $\approx 37\%$ of its initial amplitude. This is illustrated in Figure 2.3b.

$$\frac{dM_{xy}}{dt} = -\frac{1}{T_2} M_{xy}(t) \quad \text{Eq. 2.26}$$

$$M_{xy}(t) = M_{xy}(0) \cdot e^{-\frac{t}{T_2}} \quad \text{Eq. 2.27}$$

The differences in T_1 and T_2 times are used in MRI to create contrast between different tissue types. Considering ^1H NMR in biological tissues, the T_2 relaxation times (10–300 ms) are typically much shorter than the T_1 relaxation times (500–3000 ms) [15].

The expressions found for T_1 and T_2 relaxation can be included in the equation of motion for the magnetization in Eq. 2.21. This yields the well-known complete Bloch equations (Eq. 2.28 - Eq. 2.30) describing the dynamics of a magnetization $\mathbf{M} = (M_x, M_y, M_z)^T$ in the laboratory frame, accounting for the Larmor precession of \mathbf{M} in a static \mathbf{B}_0 field and rotation of \mathbf{M} by an RF field \mathbf{B}_1 , which combined determine the total \mathbf{B} field given by $\mathbf{B} = (B_{1x}, B_{1y}, B_0)^T$. An additional term describes the dependence of \mathbf{M} on relaxation phenomena.

$$\frac{dM_x(t)}{dt} = \gamma(M_y(t)B_0 - M_z(t)B_{1y}(t)) - \frac{M_x(t)}{T_2} \quad \text{Eq. 2.28}$$

$$\frac{dM_y(t)}{dt} = \gamma(M_z(t)B_{1x}(t) - M_x(t)B_0) - \frac{M_y(t)}{T_2} \quad \text{Eq. 2.29}$$

$$\frac{dM_z(t)}{dt} = \gamma(M_x(t)B_{1y}(t) - M_y(t)B_{1x}(t)) - \frac{M_z(t) - M_0}{T_1} \quad \text{Eq. 2.30}$$

2.1.1.5 Free Induction Decay

The most basic NMR experiment consists of the generation of a free induction decay (FID) using an RF coil which is placed close to a sample in a B_0 field, creating a B_1 -field oriented in the transverse plane (perpendicular to B_0). After spin excitation by RF transmission, the net magnetization vector rotates around the transverse plane and a weak *emf* is induced in the RF coil. The amplitude of the detected NMR signal oscillating at the Larmor frequency decays when the RF excitation is switched off and spins start losing their coherent phase. In practice, the dephasing is accelerated by external field inhomogeneities which results in a decay with a time constant T_2^* much shorter than T_2 . T_2' in Eq. 2.31 indicates the influence of the B_0 field inhomogeneity (e.g. due to susceptibility differences or technical reasons) on the total decay time T_2^* .

$$\frac{1}{T_2^*} = \frac{1}{T_2} + \frac{1}{T_2'} \quad \text{Eq. 2.31}$$

The signal decaying with time constant T_2^* is the FID shown in Figure 2.4.

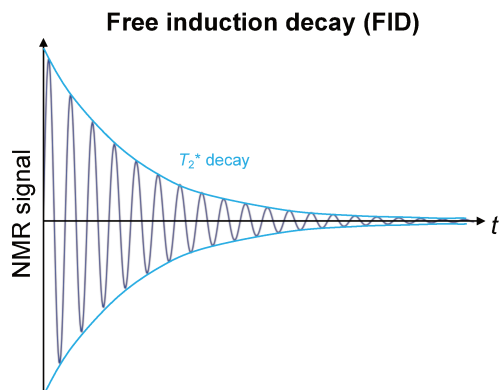


Figure 2.4: Free induction decay

2.1.2 Magnetic Resonance Imaging

2.1.2.1 MR system components

The main components of an MR system are listed in Table 2.2. The main magnet, gradient coils and RF coils generate different static or oscillating (electro)magnetic fields with distinct functions which ultimately enable the reconstruction of an image. Without a doubt, other peripheral elements, e.g. the image reconstruction computer, shim coils, B_0 shielding elements, the cooling system or patient monitoring devices are indispensable for the functioning of the whole system and for image quality optimization but will not be explained in detail here.

component	created field	function
main magnet	static magnetic field B_0	spin polarization
gradient coils	gradient fields G_x, G_y, G_z	spatial localization
radio frequency coils	radio frequency field B_1	spin excitation and signal reception

Table 2.2: Main components of an MRI system

In early years, main magnet technology was based on permanent or resistive electromagnet systems [16]. Nowadays, large bore scanners dedicated to human clinical MR examinations rely on superconductor technology for main magnet design and typically operate at B_0 static magnetic field strengths of 1.5 T or 3 T. Over the last decade, also UHF 7 T MR scanners became accessible for high-end clinical examinations and research. This trend towards higher static magnetic field strengths

can be explained by the aim to create higher detectable nuclear magnetization and, therefore, MR signal amplitudes. This aspect will be detailed in section 2.1.2.5.2 (*Signal and noise*).

Gradient coils are used to generate time-varying magnetic fields along the x , y and z -direction. Magnetic gradient fields assign spatial information, in the form of slightly varying frequency and phase, to the detected MR signal so that during image reconstruction the origin of the detected acquired signal is known.

RF coils are the instrument which can create a B_1 field and are used for spin ensemble excitation by emission of high-power RF pulses and for MR signal reception. Typically, in clinical 3 T MR scanners, a whole-body coil is integrated in the scanner for RF transmission sometimes also used for reception if not replaced with receive-only coil arrays. However, at UHF, the integration of a body coil gets more complicated due to reduced wavelength effects and space constraints. Therefore, smaller volume or local surface coils are usually used for RF transmission and reception.

2.1.2.2 Slice selection and spatial encoding

The sample to be imaged can be divided into small volumes, so-called voxels, with a three-dimensional spatial location \mathbf{x} . In order to reconstruct an MR image, magnetic field gradients in all three orthogonal directions (G_x , G_y , G_z) are necessary to map the signals originating from each of these voxels onto a specific location in image space. The total gradient field is composed of gradients in x -, y - and z -direction with linearly varying magnetic fields.

$$\mathbf{G}(t) = G_x(t)\hat{\mathbf{x}} + G_y(t)\hat{\mathbf{y}} + G_z(t)\hat{\mathbf{z}} \quad \text{Eq. 2.32}$$

$\mathbf{G}(t)$ superimposes the main magnetic field B_0 yielding a total magnetic field of

$$B(\mathbf{x}, t) = B_0 + \mathbf{G}(t) \cdot \mathbf{x} \quad \text{Eq. 2.33}$$

which results in a different precessional frequency and phase of the spins, depending on their spatial location \mathbf{x} . As schematically drawn in Figure 2.5, in MRI, three different gradients fields are used for slice selection (in z -direction), frequency encoding (in x -direction) and phase encoding (in y -direction).

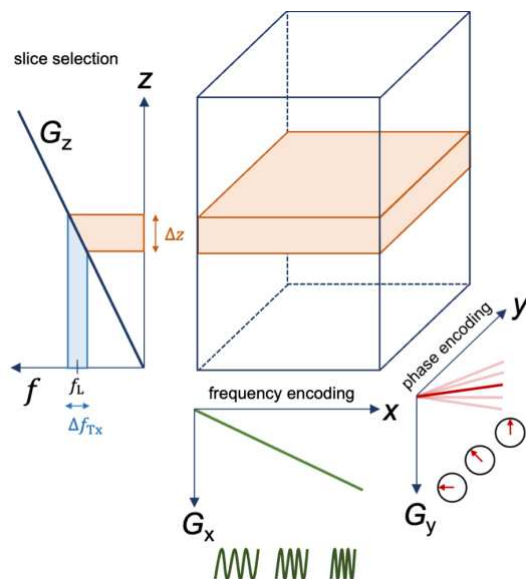


Figure 2.5: Slice selection and spatial encoding in MRI

If the z -axis is chosen as slice selection axis, a gradient G_z applied at the same time as the RF pulse transmission changes the magnetic field strength and therefore the precessional frequency of the magnetic moments along z . The Larmor frequency becomes a function of spatial location z .

$$\omega(z) = \omega_L + \gamma G_z \cdot z \quad \text{Eq. 2.34}$$

The selective excitation of a slice parallel to the xy -plane is done with an RF transmit pulse that has a certain bandwidth Δf_{TX} which determines the thickness Δz of the selected slice according to the following relationship:

$$\Delta z = \frac{\Delta f_{TX}}{\gamma G_z} \quad \text{Eq. 2.35}$$

where G_z is the gradient strength (usually given in mT/m). The slice thickness can be modified by the gradient slope and the RF transmit bandwidth Δf_{TX} (see Figure 2.5). Ideally, transverse magnetization is only created in the targeted slice, which is determined by the RF excitation pulse shape in the time domain. The pulse shape can be chosen such as to achieve the desired slice excitation profile in the frequency domain. As time and frequency domain are related via Fourier transformation, a sinc-shaped RF pulse is commonly employed in MRI for rectangular slice profile excitation. In addition to slice selection, spatial encoding in the x - and y -direction is performed by frequency and phase encoding. A frequency encoding “readout” gradient in x -

direction, denoted G_x , is switched on during data acquisition (readout). As a consequence, the Larmor frequencies vary depending on their x -location and this information can be used to identify the spatial origin of signals in x -direction.

$$\omega(x) = \omega_L + \gamma G_x \cdot x \quad \text{Eq. 2.36}$$

The third spatial dimension (y) is encoded by the G_y gradient introducing a certain phase shift shortly before data readout. This is referred to as phase encoding and to fully encode a 2D image, a phase encoding gradient of different amplitude, as schematically indicated in Figure 2.5, has to be repeated for every readout (frequency encoding) step. The number of times the phase encoding gradient is applied determines the duration of image acquisition.

The frequency and phase variation in the received MR signal depending on the x - and y - direction for 2D imaging can be translated into spatial information using Fourier transforms during image reconstruction.

2.1.2.3 k-space

During each MR experiment, the signal acquired in the presence of a gradients for slice excitation, frequency and phase encoding is stored in a matrix which is known as spatial frequency space or k -space. Depending on the timing of RF pulses and gradients, the k -space matrix is filled in line by line. Conventionally, and as mentioned above, the x -direction is referred to as frequency encoding and the y -direction as phase encoding direction. The k -space trajectory covered during image readout after RF excitation ($t = 0$) is determined by the gradient waveforms and given by

$$\mathbf{k}(t) = \gamma \int_0^t \mathbf{G}(t') dt' \quad \text{Eq. 2.37}$$

The resulting signal can be written as

$$S(\mathbf{k}(t)) = \int_{\text{sample}} \rho(\mathbf{x}) e^{-i\mathbf{k}(t) \cdot \mathbf{x}} d\mathbf{x}. \quad \text{Eq. 2.38}$$

Eq. 2.38 reveals that the spatial spin density distribution $\rho(\mathbf{x})$ over the sample, i.e. the image, and the signal distribution in k -space $S(\mathbf{k})$, i.e. the spatial frequency domain, are related via Fourier transformation (FT) as shown in Figure 2.6.

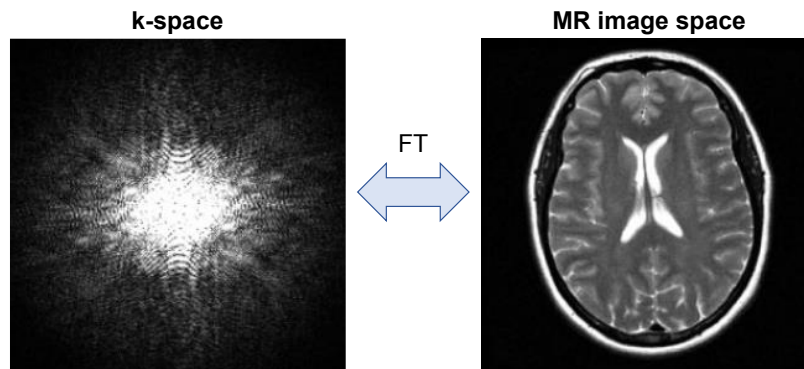


Figure 2.6: *k*-space and image domain, adapted from [17]

The center of the *k*-space contains low spatial frequency information mainly responsible for basic image shape, contrast and brightness. The periphery of the *k*-space corresponds to high frequencies which define sharp edges and image details.

2.1.2.4 Imaging sequences

In MRI, different techniques for image formation, i.e. sequences determining the timing and amplitude of RF pulses and gradients, exist. As the FID decays very rapidly (with time constant T_2^*), an echo generated by refocusing of the transverse magnetization by a spin or gradient echo is used in basic imaging sequences, shortly described in the following.

A spin echo sequence is illustrated in a diagram for one frequency-encoding line in Figure 2.7. First, a 90° flip angle RF pulse is applied, creating a transverse magnetization component and a measurable FID. The spins start to dephase but a 180° “refocusing” pulse reverses the dephasing process and due to the rephasing, a spin echo is detectable after the echo time T_E . When applying multiple 180° pulses, a spin echo appears after each T_E and their amplitudes decay with time constant T_2 . The slice selection gradient G_z is switched simultaneously with the 90° RF pulse, followed by a gradient of opposite polarity and half the duration to rephase spins along the slice thickness. Also, during the 180° RF pulse, G_z is switched on again. The phase encoding gradient G_y is switched on shortly between slice excitation and spin echo. For a *k*-space matrix of size 256×256 ($k_x \times k_y$), the phase-encoding gradient is switched on 256 times with different amplitudes and with repetition time T_R (time interval between two 90° pulses). The frequency-encoding gradient is marked by G_x and is active during the spin echo readout. To avoid full dephasing of the spins

precessing in the frequency encoding direction during the echo time T_E , another G_x gradient is applied before the 180° pulse. This leads to a rephasing of the spins so that at the center of the readout interval and the maximum of the spin echo, they are in phase again.

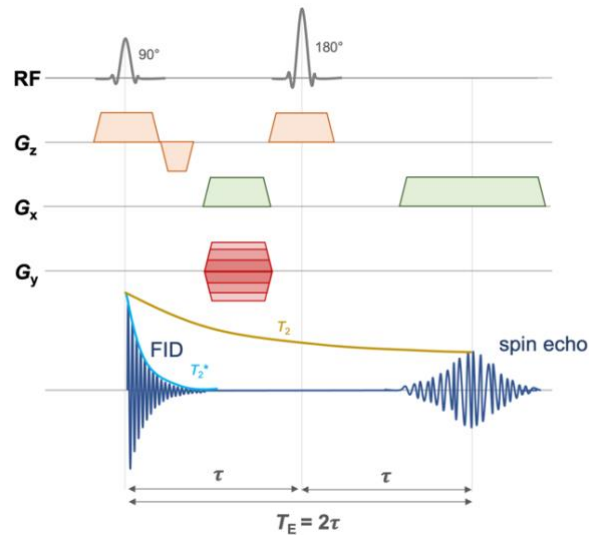


Figure 2.7: Spin echo sequence diagram, adapted from [18]

A gradient echo (GRE) sequence produces an echo based on the application of a gradient pulse which artificially dephases the spins so that the FID decays more quickly than at T_2^* . By reversing the polarity of the gradient, the spins are rephased again and an echo is measurable after T_E , as shown in Figure 2.8. The T_E of gradient echoes is much shorter than for spin echoes as the echo creation has to fit within the T_2^* decay. This is the reason why the GRE is faster than the spin echo imaging technique.

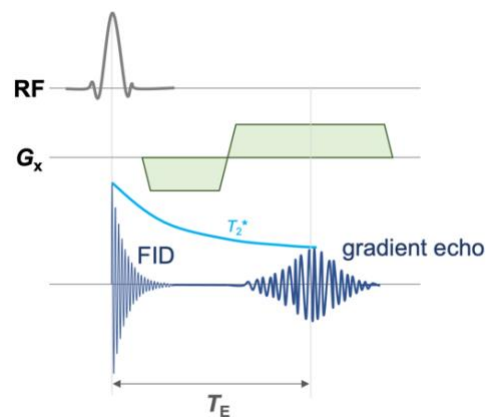


Figure 2.8: Gradient echo formation, adapted from [18]

2.1.2.5 MR signal characteristics

The above-mentioned basics explaining the origin of MR signals and image formation allow for a summary of MR signal properties which will strongly influence further signal processing stages, e.g. preamplification, down-sampling and analog-to-digital conversion in the MR receive chain. This will be complemented with additional considerations on the achievable signal amplitude and noise mechanisms in MR.

2.1.2.5.1 Carrier frequency and receive bandwidth

For most clinical MRI scenarios, the RF carrier frequency of MR signals lies between 64 and 300 MHz (following Eq. 2.12) or speaking in terms of B_0 field strengths, the range is from approximately 1.5 to 7 T. The bandwidth of the received MR signal Δf_{Rx} is given by the frequency range that readout gradients map the spatial locations onto. It is directly proportional to the maximum gradient strength and the FOV size, which is illustrated in Figure 2.9.

$$\Delta f_{\text{Rx}} = \gamma \cdot G_x \cdot \text{FOV} \quad \text{Eq. 2.39}$$

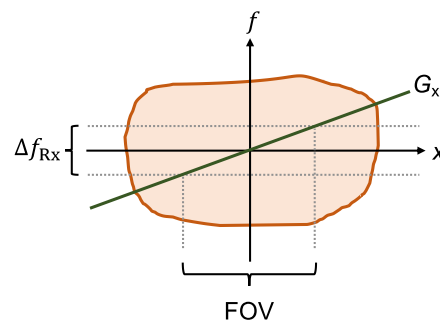


Figure 2.9: MR receive bandwidth depending on the gradient strength and FOV, adapted from [19]

In some scenarios, the receive bandwidth Δf_{Rx} can reach more than 1 MHz. This is the case with strong gradients (e.g. $G_x = 80$ mT/m) and a large FOV (e.g. $\text{FOV} = 30$ cm) but typical receive bandwidths are in the range of hundreds of kHz or only a few kHz for MR spectroscopy (MRS). Note that here, one speaks of receive bandwidth whereas for slice excitation, the transmission bandwidth of the excitation pulse is decisive to determine the slice profile (see Figure 2.5).

The RF carrier frequency and receive signal bandwidth will in general have an effect on the signal digitization approach used in the RF receive chain, i.e. the sampling frequency of the analog-to-digital converter (ADC) that has to be chosen to correctly

represent the analog MR signal in the digital domain. Figure 2.10 illustrates the basic functioning principle of an ADC. In a first step the received signal is sampled at a given rate f_s controlled by a clock. In a second step, the ADC assigns each sample one of the available 2^b discrete amplitude quantization levels, determined by the ADC bit resolution b . In traditional MR systems, the ADC is located in the technical cabinet or in the MR room and coaxial cables are commonly used to transfer the analog RF signal to the digitization stage. In modern systems, the ADC is located directly on-coil and in this case, often optical fibers are employed for further signal transmission in the MR environment. More details on different digitization and data transmission approaches for the MR signal will be provided in section 3.2.2 of this manuscript and in *Article II* (section 5.2).

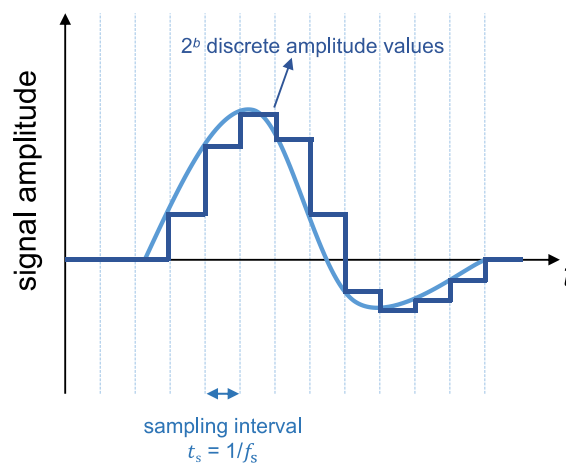


Figure 2.10: Analog-to-digital conversion

2.1.2.5.2 Signal and noise

Besides its carrier frequency and receive signal bandwidth, the MR signal is characterized by the largest and smallest detected signal amplitude, determined by the induced emf and the noise floor.

2.1.2.5.2.1 Reciprocity principle

The principle of reciprocity establishes a link between the transmit field and the receive sensitivity of an RF coil [20,21]. The exact derivation for NMR signal amplitude calculations based on fundamental equations in electromagnetic theory, i.e. Ampère's and Faraday's law describing the magnetic field produced by an alternating current passing through a coil and the emf induced by a time-dependent

rotating magnetic field in the RF coil, respectively, can be found in reference [20]. The central aspect stated by D.I. Hoult is that the *emf* induced in a receive coil by the precessing spins is proportional to the hypothetical magnetic field produced by the coil when applying unit current, assuming that the transverse component of the B_1 field, $B_{1,xy}$, is homogeneous over the whole voxel volume V (which is realistic for small voxels in the mm^3 range). This fact can be used to estimate the coil's receive sensitivity based on its transmit performance. The induced *emf* is given by

$$emf = \omega_L(B_{1,xy}/I)M_0V\cos(\omega_L t) \quad \text{Eq. 2.40}$$

where $B_{1,xy}/I$ is the magnetic coupling coefficient which describes the ability of the RF coil to produce a magnetic field $B_{1,xy}$ per unit current I .

As $\omega_L \propto B_0$ (Eq. 2.11) and $M_0 \propto B_0$ (Eq. 2.16), the following relationship is found:

$$emf \propto B_0^2 \quad \text{Eq. 2.41}$$

The induced *emf* generates current flow in the coil conductor and a detectable voltage at the coil terminal (also called "coil port"). The maximum received signal voltage (V_{max}) can reach the tens of mV range for 3D imaging at high B_0 fields (neglecting relaxation effects) but is usually even weaker and rather situated in the hundreds of μV range [15,22,23].

2.1.2.5.2.2 Noise

The minimum voltage of the MR signal that can be detected is limited by the thermal noise and is typically in the nV range [22]. Therefore, a difference of up to six orders of magnitude between highest and lowest detected signal voltage is possible in MR. According to Johnson-Nyquist's theorem, the thermal noise is determined by

$$V_{\text{noise}} = \sqrt{4kT_{\text{eq}}R_{\text{eq}}\Delta f_{\text{Rx}}} \quad \text{Eq. 2.42}$$

where k is the Boltzmann constant and Δf_{Rx} the receiver bandwidth. $T_{\text{eq}}R_{\text{eq}}$ denotes the equivalent temperature-weighted sum of resistances according to respective dissipation rates and local temperatures in different media [24]. The two principal noise sources contributing to R_{eq} in MRI are the coil resistance (R_c) and sample resistance (R_s).

Ohmic losses in the coil conductor are responsible for coil noise. Due to the skin effect, the cross-sectional area A in the coil conductor for AC current passing is reduced at high frequencies. Considering a skin depth $\delta = \sqrt{2\rho/\omega_L\mu}$ and the formula for the resistance $R_c = \frac{\rho}{A \cdot l}$ (ρ denotes the resistivity in $\Omega \cdot \text{m}$ and l the conductor length in m), for a conductor with a diameter of $d_1 \gg 2\delta$, one can approximate for the cross-sectional area $A \propto \delta \propto 1/\sqrt{\omega_L} \propto 1/R_c$. From this relationship one can see that

$$R_c \propto \sqrt{B_0} \tag{Eq. 2.43}$$

Coil noise can be minimized e.g. by using highly conductive conductor material, by reducing the number and size of solder joints or by employing cooled or superconducting coils.

Sample noise arises mainly due to the magnetic coupling with the RF coil to the sample, depending on its conductivity (e.g. $\approx 0.77 \text{ S/m}$ for muscle tissue at 300 MHz [25]) and temperature. The associated magnetically coupled noise originates from the thermal excitation of charges in the sample in presence of the RF excitation field. Circular components of the Brownian motion of these electrical charges induce a voltage in the RF coil at the same time of MR signal induction which results in random fluctuation of the measured signal, detected as noise.

Another factor contributing to sample noise is capacitive coupling due to stray capacitances between the coil and the sample. Electric potential differences along the coil conductor create E fields that reach the sample surface and induce dielectric losses. As a consequence, noise is coupled to the coil by thermal fluctuation of these electric dipoles distributed at the surface of the sample. This noise effect can be limited for example by distributed series capacitors along the coil loop that equilibrate the electric potential distribution.

Spin noise is the third noise mechanism contributing to sample noise, originating from fluctuations of transverse magnetic moments. This is not a major factor for MRI with high receive bandwidths but can be limiting in MRS with high spectral resolution [24].

When dielectric losses are limited, magnetic coupling between the coil and the sample is the main contribution to sample noise. In this case, the noise voltage induced in the

coil increases linearly with frequency. Therefore, the power dissipation in the sample is proportional to the square of the frequency, resulting in the following relationship for the effective sample resistance [24,26]:

$$R_s \propto B_0^2 \quad \text{Eq. 2.44}$$

2.1.2.5.2.3 Signal-to-noise ratio and coil sensitivity factor

Two important measures to characterize the signal and noise in MR experiments are the signal-to-noise ratio (SNR) and the coil sensitivity factor S_{RF} . The SNR can be derived using the above-mentioned equations for the *emf* (Eq. 2.40) and noise voltage V_{noise} (Eq. 2.42) and can be complemented with imaging parameter and system design dependencies to obtain Eq. 2.45.

$$\text{SNR} \approx F^{-\frac{1}{2}} \frac{emf}{V_{noise}} \sqrt{T_{acq}} \approx F^{-1/2} \frac{\omega_L(B_{1,xy}/I)}{\sqrt{4kT_{eq}R_{eq}\Delta f_{Rx}}} VM_{xy} \sqrt{T_{acq}} \quad \text{Eq. 2.45}$$

where F is the total noise factor accounting for noise introduced by additional scanner electronics such as preamplifiers, T_{acq} is the total acquisition time and M_{xy} is the transverse magnetization component in a voxel volume V . As it can be observed, this SNR formula depends on the imaging parameters used.

The coil's contribution to the SNR, independent of the imaging parameters, is given by the RF sensitivity factor

$$S_{RF} = \frac{\omega_L(B_{1,xy}/I)}{\sqrt{4kT_{eq}R_{eq}}} \quad \text{Eq. 2.46}$$

which represents the time-domain SNR achievable with an RF coil per unit of magnetic moment and unit receive bandwidth.

2.1.2.5.2.4 Considerations for RF coil design

In RF coil design, the focus lies on the improvement of the sensitivity factor S_{RF} . For a given ω_L this can be achieved by increasing the magnetic coupling factor or by reducing the noise.

Using Biot-Savart's law to establish a relationship between the magnetic coupling coefficient, the coil radius r_0 of a circular surface coil and the distance a from the coil along the central axis yields:

$$\frac{B_{1,xy}}{I} = \frac{\mu_0}{2} \frac{r_0^2}{(r_0^2 + a^2)^{3/2}} \quad \text{Eq. 2.47}$$

It can be seen that very close to the coil ($a = 0$) the magnetic coupling coefficient and therefore the SNR is inversely proportional to the coil radius.

$$\frac{B_{1,xy}}{I} = \frac{\mu_0}{2r_0} \quad \text{Eq. 2.48}$$

Hence, for same applied current, smaller coils produce higher $B_{1,xy}$ than large coils. The drawback of using small coil is that their magnetic coupling coefficient decreases more rapidly in depth and these coils therefore only allow for imaging of superficial areas.

In the case of a circular, lossless loop positioned at the surface of a uniformly conductive sample, optimal SNR at a certain penetration depth p inside the sample is achieved when the coil diameter d equals approximately the desired penetration depth [27–29].

$$d = \frac{2p}{\sqrt{5}} \approx p \quad \text{Eq. 2.49}$$

Eq. 2.49 can be taken as an initial guideline assuming sample noise dominance and no coil losses. In practice, as investigated by Kumar *et al.* [30], including coil losses and depending on the B_0 field strength and target depth, the optimum coil diameter differs from the one calculated for the case without coil losses. Furthermore, the distance between coil and the sample influences the achievable SNR in a certain depth inside the sample [24].

Assuming a constant $B_{1,xy}/I$ over the sample volume V_s , S_{RF} can be rewritten into [24]

$$S_{\text{RF}} \approx \sqrt{\frac{\mu_0 \omega_L \eta Q}{4kT_{\text{eq}} V_s}} \quad \text{Eq. 2.50}$$

The filling factor η represents the geometrical relationship between the RF coil and the sample and is defined as the ratio of the magnetic field energy stored inside the sample volume V_s to the total magnetic energy stored by the RF coil [21]. The electrical quality factor Q indicates the contribution of power loss mechanisms and is given by

$$Q = \frac{L_{\text{eq}} \omega_L}{R_{\text{eq}}} \quad \text{Eq. 2.51}$$

where the equivalent self-inductance L_{eq} represents the total magnetic energy stored per unit current in the coil conductor. The factor $\sqrt{\eta Q}$ proportional to S_{RF} indicates the amount of magnetic energy the RF coil can store in the sample volume per input power. This factor should ideally be maximized by placing the coil very close to the sample and by aiming for high Q factors which is achieved when reducing the noise R_{eq} .

With the goal of relating the achievable SNR to the B_0 field strength, equations Eq. 2.41 and Eq. 2.43 describing the dependencies of different noise sources on B_0 , and the expression for the SNR in Eq. 2.45 can be used to derive

$$SNR \propto \frac{B_0^2}{\sqrt{B_0^2 + \alpha\sqrt{B_0}}} \quad \text{Eq. 2.52}$$

where the factor α depends on the ratio between coil and sample noise R_c/R_s .

Ideally, in an MR experiment, the SNR is only limited by noise originating from magnetic coupling to the sample, dominating over coil noise ($R_s \gg R_c$). In this case, the SNR scales with B_0 . If coil noise takes over as the dominant noise source ($R_c > R_s$), SNR scales with $\sqrt[4]{B_0^7}$. At low static magnetic fields with small coils or small samples, the coil noise usually dominates. For a given B_0 field strength, the coil size has to be larger than a defined critical value to reach the sample noise domain. With increasing B_0 field, this critical coil size decreases [24]. Therefore, high B_0 field strength does not only bring the advantage of higher induced signal (Eq. 2.41) but also offers the possibility to use miniature RF coils while still operating in the sample noise domain.

The scaling rules for the Q factor, SNR and RF sensitivity factor for the two different noise domains are summarized in Table 2.3 [24]. In the case of non-conductive samples, the noise stems solely from coil losses whereas with conductive samples it is assumed that noise originates only from the sample.

	Non-conductive sample	Conductive sample
Quality factor Q	$\omega^{1/2}d$	$\omega^{-1}d^{-2}$
S_{RF}	$\omega^{3/4}d^{-1}$ *	$d^{-5/2}$
SNR	$\omega^{7/4}d^2$ *†	$\omega d^{1/2}$ †

 Table 2.3: Scaling rules for the Q factor, RF sensitivity factor and SNR

2.1.2.5.2.5 Dynamic range

To sum this up, different MR system, imaging and RF coil design parameters influence the minimum and maximum detected NMR signal. The ratio between the maximum and minimum signal amplitude is defined as the dynamic range (DR) usually given in dB.

$$\text{DR} = 20\log_{10}\left(\frac{2V_{\text{max}}}{V_{\text{noise}}}\right) \quad \text{Eq. 2.53}$$

The factor 2 in Eq. 2.53 accounts for positive and negative amplitudes of the oscillating signal. For MRI, the DR is typically around 90 dB but can also reach more than 120 dB for example in the case of high-resolution 3D acquisitions at ultra-high field [31,32], i.e. when the signal ranges from nV to mV. The MRI noise floor and signal peak, i.e. the whole DR, must fit within the ADC dynamic range given by the ADC bit resolution. Therefore, to correctly represent the MR signal in the digital domain, a suitable ADC bit resolution b has to be chosen according to the following criterion

$$\text{DR} = 20\log_{10}(2^b) \rightarrow b = \frac{\text{DR}}{6.02} \quad \text{Eq. 2.54}$$

It can be concluded that besides a high static B_0 field strength, a major aspect for high achievable SNR is the choice of ideal RF transmitters and receivers, i.e. RF coils. The functioning principle of RF coils based on RLC circuit technology, different coil types, the components needed for coil interfacing to the MR scanner and coil performance characteristics will be discussed more in detail in the next section.

* Assuming a constant filling factor η .

† Assuming a linear increase of the transverse magnetization with frequency and a constant ratio between the voxel volume V and the sample volume V_s .

2.2 Radio frequency coils

2.2.1 Transmission and reception

An RF coil can have different functions during MRI. It can act as a transceiver of an electromagnetic field in the RF range, i.e. be used for transmission and reception. Else, an RF coil can be used for transmission or reception only. At clinical field strengths, e.g. 1.5 or 3 T it is very common to use Rx-only coils because a transmit coil (the body coil) is typically incorporated in the scanner bore. At 7 T it is more common to use transceiver coils as large body coils are often not included in the MR scanner system by default.

Based on Ampère's law, a current flow in the RF coil creates a magnetic field \mathbf{B}_1 that has to be perpendicular to the main magnet field \mathbf{B}_0 and oscillating at an RF frequency equal to the Larmor frequency to excite the magnetic moments in the sample and, as a consequence, tilt the net magnetization to the transverse plane. Following Faraday's law, the oscillating transverse magnetization induces an *emf* in the RF coil which is the received signal.

The linearly polarized \mathbf{B}_1 field produced by an RF coil can be decomposed into two circularly polarized counter-rotating components denoted as B_1^+ and B_1^- . Only the component rotating in the same direction as the nuclear precession (by convention B_1^+) contributes to spin excitation. The receive signal is proportional to the B_1^- component rotating in the opposite direction.

$$B_1^+ = \frac{B_{1,x} + iB_{1,y}}{2} \quad \text{Eq. 2.55}$$

$$B_1^- = \frac{(B_{1,x} - iB_{1,y})^*}{2} \quad \text{Eq. 2.56}$$

where * denotes the complex conjugate.

It has to be noted that especially at high magnetic field strengths, the B_1^+ and B_1^- field's spatial distribution strongly depends on the electrical properties of the sample, i.e. the relative permittivity and conductivity. The characteristic $|B_1^+|$ and $|B_1^-|$ asymmetry observed with conductive samples at UHF is explained more in detail and graphically shown in reference [33]. This asymmetry has to be taken into account when tailoring the B_1^+ and B_1^- field at UHF depending on the coil type used and the specific anatomical target application.

2.2.2 RLC circuits

In its most basic form, an RF coil can be described as a resonant circuit consisting of an inductance (L) determined by the conductor geometry, a resistance (R) proportional to both coil and sample losses, and a capacitance (C) determined by capacitors placed at conductor intersections. The RLC circuit, i.e. the RF coil, can interact with the precessing magnetization and is sensitive to signal induction by the rotating magnetization, only if it is designed so that its B_1 field vector and coil area is oriented perpendicular to B_0 and if it has a resonance frequency ω_0 which is equal to the Larmor frequency ω_L depending on the B_0 field strength and the nucleus under investigation. This process of resonance frequency adjustment is called “tuning”. Having a closer look at series and parallel resonant circuits, depending on how R , L and C are assembled, allows for the derivation of the resonance condition for ω_0 calculations. A basic representation of an RF coil, forming a series or parallel RLC circuit, is shown in Figure 2.11a and b, respectively. The inductance L is determined by geometrical properties of the coil (a circular loop in this example). The coil conductor material has a certain resistance R . Lossy capacitors and inductors will also contribute to the effective R . C_T denotes the tuning capacitor.

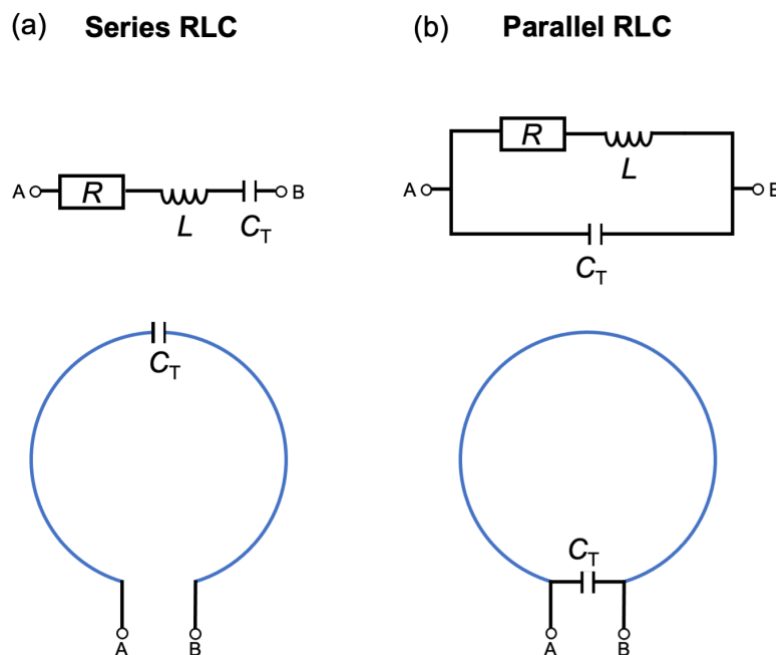


Figure 2.11: Basic representation of an RF coil forming either a series (a) or parallel RLC circuit (b)

2.2.2.1 Resonance in series and parallel RLC circuits

The impedance of an AC circuit is given by

$$Z = R + iX \quad \text{Eq. 2.57}$$

where the real part $\text{Re}(Z)$ is the resistance R and the imaginary part $\text{Im}(Z)$ is the reactance X .

In case of a series RLC circuit configuration, the total coil impedance across the coil port indicated by the terminals A and B in Figure 2.11a, is the sum of individual components' impedances.

$$Z_{\text{coil,series}} = R + i\left(\omega L - \frac{1}{\omega C_T}\right) \quad \text{Eq. 2.58}$$

The resonance occurs when the imaginary part is zero ($\text{Im}(Z) = 0$), i.e. when the capacitive equals the inductive reactance. This means that the energy in the RLC circuit is exchanged back and forth between capacitor (electric energy) and inductor (magnetic energy) and is dissipated in the resistance R . The resonance frequency ω_0 is therefore given by

$$\omega_{0,\text{series}} = \sqrt{\frac{1}{LC_T}} \quad \text{Eq. 2.59}$$

As can be seen in Figure 2.12a, the impedance is at a minimum on resonance and equal to the resistance.

$$|Z_{\text{coil,series}}(\omega_0)| = \text{Re}(Z) = R \quad \text{Eq. 2.60}$$

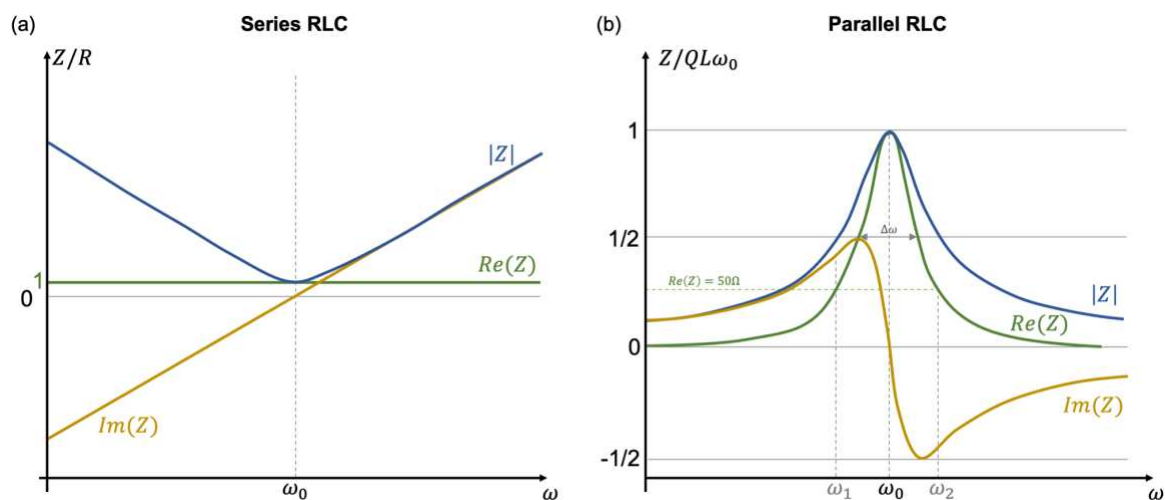


Figure 2.12: Impedance plots (magnitude, real and imaginary part) for a series (a) and parallel RLC (b)

In case of a parallel resonant circuit, as sketched in Figure 2.11b, the total coil impedance across the port (AB) is given by

$$\frac{1}{Z_{\text{coil,parallel}}} = \frac{1}{R + i\omega L} + i\omega C_T \quad \text{Eq. 2.61}$$

When defining the resonance condition the same way as for series RLCs ($\text{Im}(Z) = 0$), it can be derived [34] that

$$\omega_{0,\text{parallel}} = \sqrt{\frac{1}{LC_T} - \frac{R^2}{L^2}} \approx \omega_{0,\text{series}} \quad \text{Eq. 2.62}$$

Typically, L is much larger than R ($\propto 1/Q$) and the parallel resonance frequency differs less than 1 % [34] from the series resonance frequency (Eq. 2.59).

On resonance, the impedance magnitude equals

$$|Z_{\text{coil,parallel}}(\omega_0)| \approx \text{Re}(Z) \approx \frac{L^2 \omega_0^2}{R} \approx QL\omega_0 \quad \text{Eq. 2.63}$$

and is at a maximum, as can be observed in Figure 2.12b. With typical values for the inductive reactance $L\omega_0$ (100 Ω) and assuming $L \gg R$, the impedance can reach a value of 10 k Ω [34].

2.2.2.2 Q factor

As illustrated in Figure 2.12b, $\Delta\omega$ is defined as the bandwidth at half height of the real part of Z , i.e. the -3 dB bandwidth. The ratio between the resonance frequency and the bandwidth yields the expression for the Q factor.

$$Q = \frac{\omega_0}{\Delta\omega} \quad \text{Eq. 2.64}$$

The higher the Q factor, i.e. the sharpest the resonance peak, the more frequency selective the coil. Complementarily, the Q factor is a parameter that also indicates how much energy is stored and dissipated in the RF coil (or the coil and the sample).

$$Q = 2\pi \frac{\text{energy stored}}{\text{energy dissipated per cycle}} = \frac{L\omega_0}{R} \quad \text{Eq. 2.65}$$

When examining the coil only, the loss mechanism responsible for setting a limit to the achievable Q factor, called the unloaded Q factor (Q_u), is coil loss R_c .

$$Q_u = \frac{\omega_0 L}{R_c} \quad \text{Eq. 2.66}$$

In presence of a sample, i.e. in loaded coil configuration, the loaded Q factor (Q_l) will be limited due to the addition of sample losses R_s arising from magnetic coupling.

$$Q_l = \frac{\omega_0 L}{R_c + R_s} \quad \text{Eq. 2.67}$$

In coil design, the goal is to achieve a ratio between unloaded and loaded Q factor which is larger or at least equal to 2. Following the relationship in Eq. 2.68 this indicates that sample noise dominates over coil noise ($R_s \geq R_c$) which is the desirable operating regime for RF coils.

$$\frac{Q_u}{Q_l} = \frac{R_c + R_s}{R_c} = 1 + \frac{R_s}{R_c} \quad \text{Eq. 2.68}$$

When coil sizes get smaller, the sample noise (magnetic coupling) decreases and as soon as $R_s < R_c$, i.e. the coil noise is dominant, either this noise source has to be reduced, for instance by cooling the RF coil, using less resistive material or less lossy capacitors, or the coil diameter has to be increased again.

From the above-described, one can understand that one goal in RF coil design is the maximization of the unloaded Q factor, i.e. the reduction of R_c . As already stated in section 2.1.2.5 (*Signal and noise*), one way to achieve a reduction of sample losses stemming from dielectric losses (capacitive coupling to the sample) is the use of distributed capacitors along the coil conductor. Figure 2.13 shows the comparison of a non-segmented coil loop with an inhomogeneous current distribution (a) and a capacitively segmented loop with a homogeneous current distribution (b).

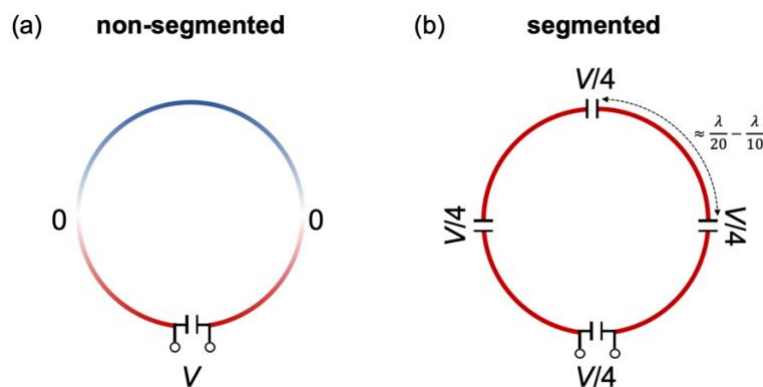


Figure 2.13: Current distribution in a non-segmented (a) and capacitively segmented (b) loop coil

The distributed capacitors equilibrate E fields as the voltage across one capacitor is reduced. This is advantageous as high E fields can lead to heating and cause dielectric losses. As the energy stored in the electric field is proportional to $E^2 \propto V^2$, a reduction of the voltage and resulting E field by a factor of 4 divides the energy loss by a factor of 16. Further, homogeneous current along the loop as shown in Figure 2.13b leads to a uniform B_1 field distribution whereas for the non-segmented case shown in Figure 2.13a, a B_1 cancellation in the center of the coil will occur. As a rule of thumb, ideally the segment length between capacitors should be between $\lambda/20$ and $\lambda/10$ [34], where λ denotes the wavelength in free space.

2.2.2.3 Impedance matching

An RF coil tuned to the target Larmor frequency and ideally equipped with distributed tuning capacitors has to undergo an impedance matching process before it can be connected to the MR scanner's RF Tx and Rx chain. By convention, all components are optimized to work in a 50Ω system. For efficient power transfer in this system, the coil impedance and impedance of other devices and cables has to be matched to 50Ω . If the impedance is off, this results in reflected power which in the case of transmit coils for example results in only a fraction of the power transferred by the amplifier available the coil. As shown in Figure 2.12b, the parallel RLC has a resistance $\text{Re}(Z)$ that is frequency dependent and equals 50Ω at two resonance frequencies ω_1 and ω_2 . In contrast to the resonance ω_0 , where $\text{Im}(Z) = 0$, at ω_1 an inductive and at ω_2 a capacitive imaginary part of the impedance remains. This reactance can be cancelled by a series capacitance (at ω_1) or inductance (at ω_2). In practice, as shown in Figure 2.14a, impedance matching is mostly done by a series capacitor C_M as they are less lossy than inductors [15,34]. C_M cancels the remaining inductive reactance and shifts the resulting resonance frequency to ω_1 . In addition to capacitive segmentation along the loop, the implementation of balanced matching capacitors as depicted in Figure 2.14b is advantageous to limit the E field near the coil and thereby dielectric losses. To do so, the matching interface consisting of one capacitor C_M in unbalanced configuration has to be modified so that the capacitors are split into two series capacitors, i.e. the capacitor value has to be doubled to $2C_M$. Further, balanced matching provides an electrical symmetry with respect to the ground which reduces

common mode currents in the coil winding. Often, a capacitor C_{TM} is used which not only influences the matching but also the tuning.

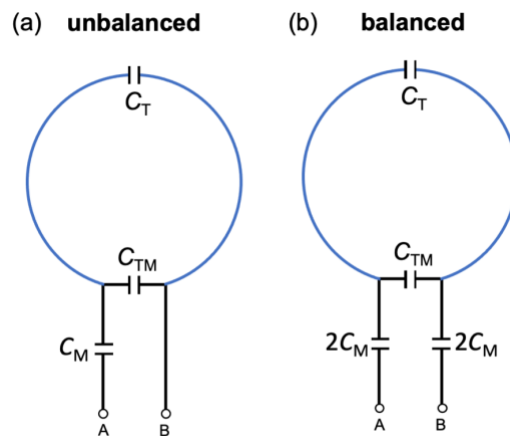


Figure 2.14: Unbalanced (a) and balanced (b) capacitive matching

2.2.3 Coil types

Geometrical shapes of commonly used coil types are shown in Figure 2.15. They can be grouped into volume and surface coils which will be described in the next sections.

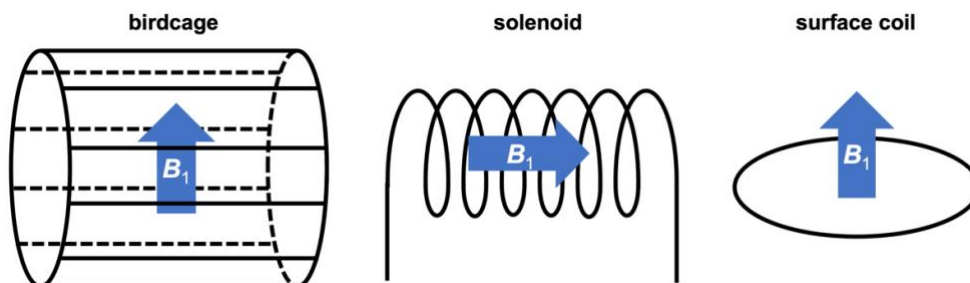


Figure 2.15: Volume coils (birdcage and solenoid) and surface coil

2.2.3.1 Volume coils

Two examples of volume coils are shown in Figure 2.15: a birdcage coil and a solenoid coil. For RF transmission, the goal is to create a strong, homogeneous B_1 field, perpendicular to the B_0 field direction. For this purpose, large volume coils that fit around different patient anatomies have been designed over the years. One prominent example is the cylindrical birdcage coil [35,36] which can be employed for head and knee but also whole-body imaging. A number of conductor legs, typically between 12 and 24, connects the end rings (top, bottom) of the coil. Tuning capacitors

can be positioned either on the legs (low pass birdcage) or on end rings between the legs (high pass birdcage). The band pass birdcage is a combination of the two. As a birdcage resonator creates a B_1 field which is perpendicular to the legs, i.e. the coil axis, the coil can be inserted in the scanner bore along its axis which facilitates positing of the head or knee inside the coil. In contrast, a solenoid volume coils produces a B_1 field which is parallel to its axis (see Figure 2.15) and therefore has to be placed perpendicular to the B_0 field direction. For large anatomies, the use of such coils is clearly impractical but solenoid coils have shown to yield very homogeneous and high B_1 fields suitable for microscopic and for human finger imaging [37].

For reception, the volume coil type is often a suboptimal solution as in various cases, the coil conductors are placed far away from the sample, i.e. the filling factor is low. Further, large coil elements that cover a wide FOV do not allow to achieve highest possible SNR. As a consequence, birdcage coils are often used for RF transmission in combination with small surface coils or coil arrays for reception.

2.2.3.2 Surface coils

The choice of the surface coil geometry and material is linked to signal and noise considerations discussed more in detail in section 2.1.2.5 (*Signal and noise*). In general, the surface coil diameter should be chosen according to the target application. As a rule of thumb, for ideal SNR in a penetration depth p , the coil diameter d should approximately equal p (Eq. 2.49). Small surface coils provide high sensitivity, but care has to be taken to ensure operation in the sample noise dominated regime. Also, surface coils have an inherently inhomogeneous B_1 distribution which decreases strongly with distance from the coil conductor. Different types of surface coils exist: Coil construction can be based on lumped elements, i.e. discrete capacitors, forming a “standard” RLC circuit as shown in Figure 2.14. Another method is the use of distributed capacitance and inductance in self-resonant structures to build an RF coil. Both coil types will be described below (2.2.3.2.1 and 2.2.3.2.2).

As mentioned above, small Rx-only surface coils are often combined with large Tx coils to benefit from the advantages of each distinct coil design. During RF transmission, it is indispensable to avoid coupling between Tx and Rx coil as both coils are designed to resonate at the same frequency ω_L . Coupling of high RF transmit

power to the Rx coil can become a safety issue as concentrated E fields risk patient burns. Furthermore, the preamplifier might be damaged due to high induced currents which can also lead to B_1^+ distortion resulting in MR imaging artifacts. This implies the necessity of implementing a mechanism in the surface coil to switch it off during RF transmission. This is often realized by an active detuning (AD) trap circuit which will be discussed for the case of a “standard” coil below. For self-resonant coils, i.e. coaxial Rx-only coils described in this work, AD doesn’t rely on a trap circuit but on creating a short between the conductors responsible for the resonant behavior of the coil. This will be discussed more in detail in chapter 4. It shall be mentioned here that, in addition to AD, further safety measures for sufficient decoupling are commonly implemented in Rx-only coils, e.g. passive detuning by two crosses diodes or fuses that intersect the RF coil conductor if high currents are induced.

2.2.3.2.1 Standard coils

For standard surface coils, the choice of suitable inductors with a low resistivity is important. Mostly copper or silver is employed in wire or tape form, and sometimes printed or etched on a circuit board. Capacitors and other components in the circuitry should have a high Q and be suited for use in MRI, i.e. not contain any ferro- or strongly paramagnetic parts. A typical example of a standard Rx-only coil is shown in Figure 2.16. The addition of a PIN diode-controlled AD trap circuit, consisting of the inductor L_{AD} , the capacitor C_{AD} and the PIN diode tuned to resonate at the Larmor frequency (by C_{AD} and L_{AD}) is effective in suppressing coupling and detuning the Rx coil during RF Tx. Actively controlled by the MR system and timed according to the sequence, the PIN diode is forward biased (12 V at 100 mA for Siemens systems) during RF transmission so that the trap circuit intentionally couples with the RF coil and splits the resonance peak. During RF reception, the diode is reverse biased (-30 V for Siemens systems) so that it appears as an “open” and the RF coil is tuned again.

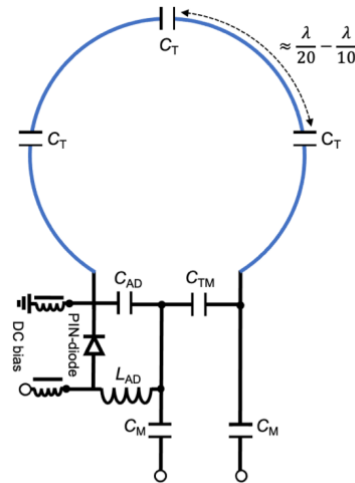


Figure 2.16: Receive-only standard loop coil

2.2.3.2.2 Self-resonant structures

Another method to fabricate an RF coil is the use of self-resonant structures. Transmission line resonators (TLRs) in different forms are currently employed in MRI. They resonate without the use of discrete capacitors, but a capacitance which is continuously distributed in a dielectric substrate separating the inductor paths. The inductors are intersected by gaps, typically placed at diametrically opposite positions, such as to create an external magnetic field. The self-resonance is determined by the coil geometry, material properties and number of gaps. As for standard surface coils, the choice of materials with low resistivity for conductors and low dielectric losses for the substrate is important. This section will be focused on a description of the basic functioning principle of TLRs. Different implementations and the advantages in terms of flexibility will be discussed in the next chapter and in *Article I*. While this work is concerned with coaxial TLRs, other variants, e.g. parallel-plate TLRs exist.

In Figure 2.17, schematic drawings of both TLR types are shown. For both structures, the fabrication can be done using a flexible or rigid dielectric substrate. Further, single-turn single-gap (1T1G), single-turn multi-gap (1TMG), multi-turn single-gap (MT1G) or multi-turn multi-gap (MTMG) variants are possible. For a target Larmor frequency, multiple gaps allow for larger coil diameters and multiple turns for smaller coils as compared to the 1T1G coil. For parallel-plate TLRs, every configuration has successfully been designed or implemented in MRI [38–47]. The design of coaxial coils for MR was largely inspired by previous publications introducing “shielded” loop

resonators or coaxial TLRs [48–52] which are also employed for other applications than MRI e.g. for wireless power transfer [53,54]. For MR imaging, coaxial coils (CCs) have only been used in 1T1G configuration, e.g. in references [52,55] and one special 1TMG configuration with arbitrarily arranged gaps in [56]. Furthermore, MT1G [51] or 1TMG [57,58] coaxial coils have been suggested in patents or publications but not tested in MRI so far. In Figure 2.17, an example of a 1T1G and 1T2G (double-gap) TLR is shown for the parallel-plate and coaxial configuration.

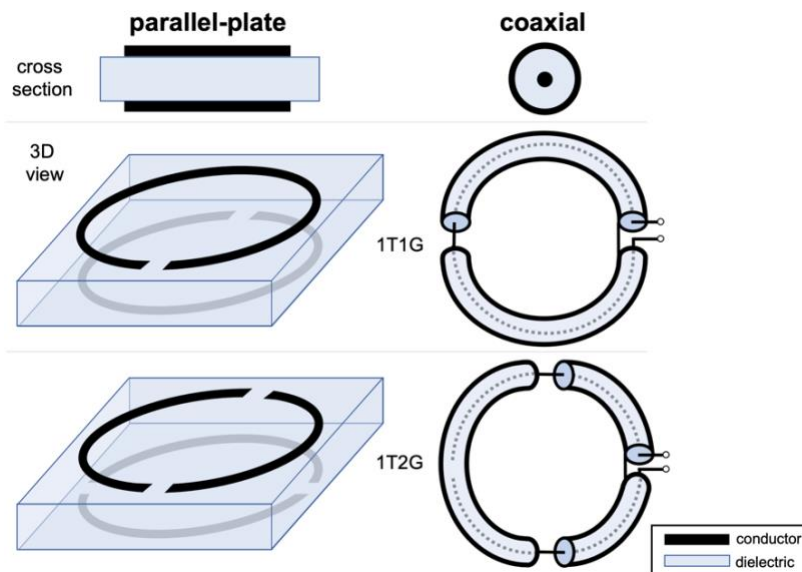


Figure 2.17: Parallel plate and coaxial transmission line resonators. The coil port is indicated for coaxial TLRs as this structure will be explained more in detail, using an equivalent circuit scheme, in the next figure (Figure 2.18)

The transmission line (TL) is either formed by the top and bottom conductor in case of the parallel-plate TLR and for the coaxial structure, the TL is given by the inner conductor and the inner surface of the outer conductor. Differential mode currents in the transmission line have opposed phase and equal amplitudes and therefore do not create a magnetic field outside of the transmission line [34]. By gap introduction, the differential mode is disturbed and allows the common mode current to flow. Thus, due to the common mode current, an external magnetic field is created outside of the transmission line. This current can be considered constant along the transmission line for large wavelengths compared to the conductor length [34]. For the case of a coaxial structure, when the skin depth is inferior to the thickness of the outer transmission line conductor, i.e. at high frequencies, three conductor paths can be distinguished: the inner conductor and the inner surface of the outer conductor (i.e. the transmission

line parts), and the outer surface of the shield which carries the current creating the magnetic field.

As already mentioned, the main difference to “standard” wired coils is that the resonance is given by the distributed inductance and capacitance rather than by discrete elements. For parallel-plate TLRs, an exact derivation of the analytical model and resonance condition can be found in reference [59]. The self-resonance frequency ω_0 can be numerically calculated using the following equation:

$$\frac{L_{\text{tot}}\omega_0}{4n_g Z_0} \tan\left(\frac{\omega_0\sqrt{\varepsilon_r}l}{4n_g c_0}\right) = 1 \quad \text{Eq. 2.69}$$

where L_{tot} is the sum of the individual inductances of all n_t conductor turns and their respective mutual inductances. n_g is the number of gaps, ε_r is the relative permittivity of the substrate, l is the total length of the conductor on one side of the substrate (including gaps) and c_0 is the vacuum speed of light. The characteristic transmission line impedance Z_0 can be derived using semi-empirical models and the corresponding equation can be found in [40].

For coaxial TLRs, a resonance condition for 1T1G configurations has been proposed in reference [55]. For sake of completeness, the resonance condition for frequency calculations found for the most general case of MTMG structures will be given here. This is an anticipation of what will be explained in *Article I* and examined more in detail in the supplementary study section 4.3.2. The total reactance X_{tot} of a coaxial coil which equals zero at resonance is given by

$$\begin{aligned} X_{\text{tot}}(\omega_0) &= X_{\text{shield}}(\omega_0) + 2n_g X_{\text{TL}}(\omega_0) \\ &= n_t^2 \omega_0 \mu_0 \frac{d_0}{2} \left[\ln\left(\frac{8d_0}{d_1}\right) - 2 \right] - 2n_g Z_0 \cot\left(\frac{\omega_0 l \sqrt{\varepsilon_r}}{c_0}\right) = 0 \end{aligned} \quad \text{Eq. 2.70}$$

where X_{TL} describes the coaxial stub reactance and X_{shield} the outer shield reactance. d_0 is the coil diameter of a circular loop coil and d_1 the outer coaxial conductor (shield) diameter. Z_0 is the characteristic transmission line impedance which is usually 50 Ω or 75 Ω for commercial coaxial cables. An approximation for Z_0 when using non-standardized coaxial structures is given in *Article I*. l denotes the length of one coaxial stub which depends on the number of turns n_t and gaps n_g , and the gap

width. The schematic representation of a 1-gap, 2-gap and 3-gap coaxial coil and the corresponding equivalent circuit is shown in Figure 2.18. Open-circuited coaxial stubs act as a capacitor if their length is inferior to $< \lambda/4$ (where λ denotes the wavelength in the coaxial line). The coaxial stubs are in series and interconnected via the coaxial shield, i.e. the inductance of the outer conductor. If the coil diameter is assumed to stay constant for the examples shown in Figure 2.18 and the same coaxial structure is used, the increase in number of gaps will lead to a higher resonance frequency. This is due to the fact that the coaxial stubs (= capacitors) in series decrease the total capacitance. Among other aspects, the implications of using multiple turns and/or gaps in coaxial coils, the investigation of coil flexibility, and the discussion of the equivalent circuit model will be central topics of chapter 4.

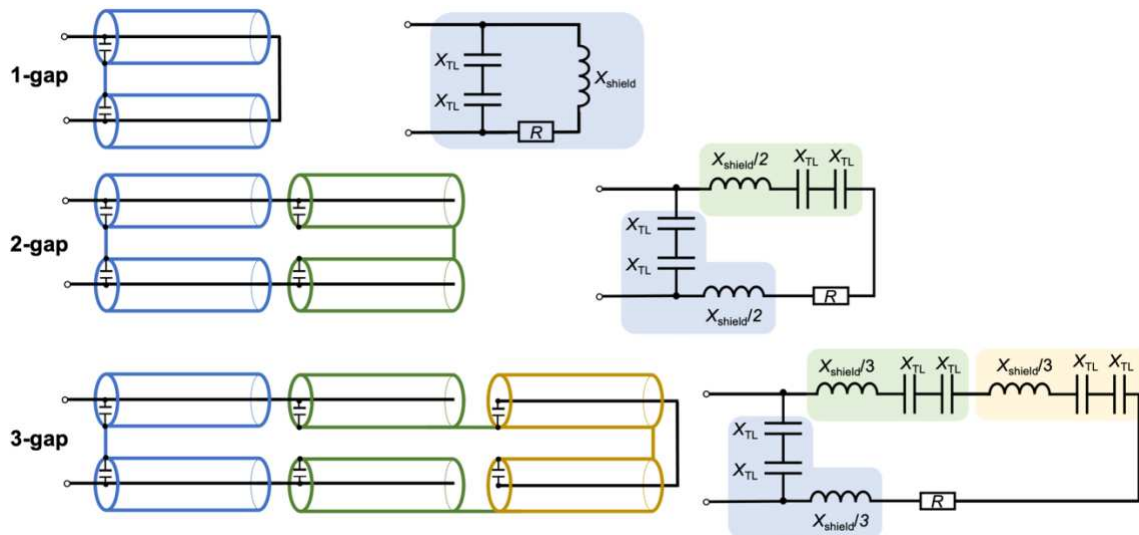


Figure 2.18: Schematic representation of a 1-gap, 2-gap and 3-gap coaxial TLR with corresponding equivalent circuit diagram

2.2.3.3 Coil arrays

The arrangement of single surface coil elements in array configuration allows to combine large FOV coverage and high sensitivity by using small coil elements. Furthermore, coil arrays can be employed in parallel imaging [5–7] which allows for the accelerated acquisition of MR images. Also, parallel transmission [8] (pTx) enables spatially selective excitation with short pulses and transmit field homogenization (shimming). Nevertheless, with the use of multiple coils in close vicinity, mutual inductive coupling between elements is an issue that needs to be

addressed as it leads to resonance peak splitting resulting in sensitivity reduction at the Larmor frequency and therefore an overall coil performance degradation. Mutual coupling can be described by the shared magnetic flux between two magnetically linked coils which is proportional to the current in a coil and the mutual inductance between coils. Two common methods to ensure decoupling between elements which are often jointly applied in arrays are overlap and preamplifier decoupling. They are sketched in Figure 2.19 and were introduced (amongst other aspects) in a fundamental paper by Roemer *et al.* on the “NMR phased array” [4].

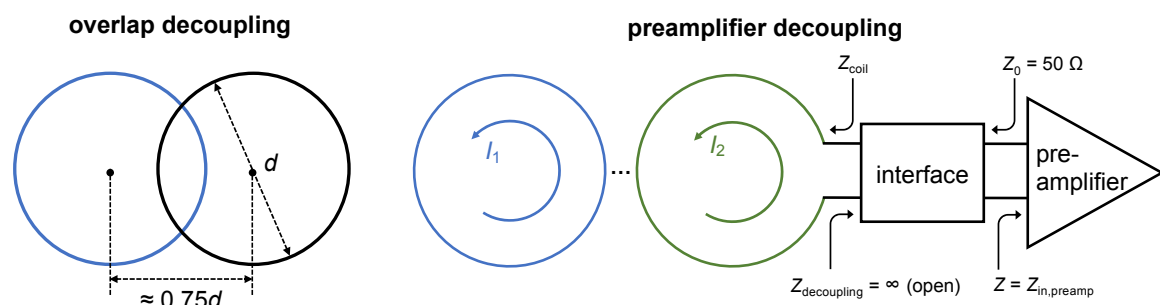


Figure 2.19: Decoupling techniques for coil arrays: overlap and preamplifier decoupling

Overlap decoupling targets the cancellation of mutual inductance between adjacent coil elements by arranging them with an overlap so that the net magnetic flux shared by the two coils is zero. In theory, for circular coils this can be achieved when the distance between coil centers spans approximately 0.75 times the coil diameter as indicated in Figure 2.19. In practice, the optimal overlap deviates from this theoretical guideline and has to be determined on the bench depending on the coil geometry and conductor properties. Other techniques to eliminate mutual inductance are based on shared inductors or capacitors between elements, decoupling annexes [43] or decoupling rings [42]. While overlap decoupling only works for nearest neighbor coil elements, coupling to the next-nearest neighbor coil element might still be strong and needs to be suppressed by complementary techniques.

Preamplifier decoupling is commonly used to minimize the current I in each coil and therefore also the common magnetic flux, in addition to methods used for the cancellation of mutual inductance (e.g. overlap decoupling). As indicated in Figure 2.19, the basic principle to reduce the current I_2 in the coil relies on the transformation of the preamplifier input impedance to a high impedance (open) at

the coil port. As a consequence, the current flow through the coil is suppressed, leading to minimized coupling with other coils while the MR signal is still detectable as a potential difference, i.e. voltage at the coil port. Note that the schematic drawn in Figure 2.19 applies to standard coils. With coaxial coils, “reverse preamplifier decoupling” is employed. Inversely to SCs, with CCs, the preamplifier impedance is transformed to a low impedance (short) at the coil port, as proposed by Zhang *et al.* [55].

2.2.4 Conventional interfacing to the MR scanner

In addition to RF coil design considerations mentioned above, when relating the coil to the MR scanner’s electronics, some other key hardware components are indispensable for the proper functioning of the MR signal excitation and detection chain. They will be shortly explained below.

2.2.4.1 Preamplifier

While in the transmit chain, signal voltages are very high and power matching (2.2.2.3) has to be considered, the received MR signal is weak (usually in the mV range [15,22,23]) and needs to be pre-amplified before further linking it to the MR scanner receive chain. After the RF coil, the preamplifier is one of the devices in the receive chain which adds noise to the signal which is indicated by the noise factor F_{preamp} (Eq. 2.71). This noise factor is minimized for a specified input impedance $Z_{\text{opt,in}}$ which can be equal to $Z_0 = 50 \Omega$ (see Figure 2.19). Therefore, the coil impedance has to be transformed to $Z_{\text{opt,in}}$ in order to achieve minimal noise factor. This process is called noise matching. The SNR output depends on the preamplifier noise figure NF (in dB) given by

$$\text{NF} = 10\log_{10}(F_{\text{preamp}}) = 20\log_{10}\left(\frac{\text{SNR}_{\text{in}}}{\text{SNR}_{\text{out}}}\right) \quad \text{Eq. 2.71}$$

which should ideally be 0 but is typically in the range of 0.5 dB, also for the preamplifier used during measurements in this work (Hi-Q.A. Inc., Carleton Place, Ontario, Canada). It is advantageous to place the preamplifier as close as possible to the coil’s signal output as long cable connections also add unwanted noise to the receive signal. Friis’ formula [60] states that the noise factors in the receive chain are

scaled according to the amount of amplification in the preceding stages. The total noise factor F_{tot} is given by:

$$F_{\text{tot}} = F_1 + \frac{F_2 - 1}{G_1} + \frac{F_3 - 1}{G_1 G_2} + \frac{F_4 - 1}{G_1 G_2 G_3} + \dots \quad \text{Eq. 2.72}$$

where the index labels the noise factor (F_n) and gain (G_n) of the n^{th} amplification component. Therefore, the preamplifier must have lowest possible noise figure (≤ 0.5 dB) and high enough gain (typically around 30 dB) so that additional components have minimized influence on the total receive chain's noise figure.

2.2.4.2 T/R switch

If a coil is used for both transmission and reception, the signal paths have to be carefully separated and during the imaging sequence, switching between both coil functions has to be performed. A transmit/receive (T/R) switch is used for exactly this purpose. An active T/R switching circuitry is shown in Figure 2.20. It consists of PIN diodes which are activated by an external DC control unit. A $\lambda/4$ transmission line terminated in a short has high input impedance (open) and therefore directs the transmitter power to the RF coil. If desired, the $\lambda/4$ isolating elements can be multiplied to improve the receiver protection. As the timing between Tx and Rx state is controlled via the DC supply, RF choke and DC blocking capacitors are required to separate AC from DC paths. During reception, the diodes are reverse biased (open), therefore directing the received MR signal to the Rx chain of the scanner.

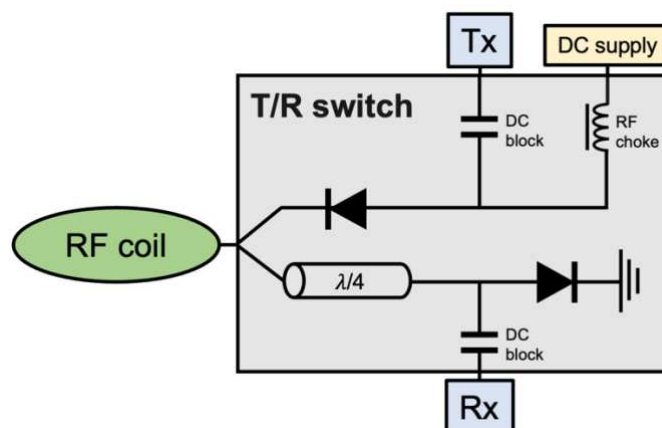


Figure 2.20: Basic schematic of a T/R switch, adapted from [34]

2.2.4.3 Common mode current traps

In conventional MR systems, coaxial cables are used for MR signal transmission from the coil to the coil plug inside the MR bore. The outer conductor of coaxial cable (shield) is prone to common mode current induction due to the RF transmit field which can lead to local heating. Common mode currents can also lead to undesired crosstalk between cables and image artifacts. These facts motivate the development of wireless RF coils, which will be partly discussed in chapter 3 and emphasized in chapter 5, especially in *Article II*.

If an RF coil, an electrically balanced circuit, is connected to a coaxial cable which is an unbalanced line, a “balanced to unbalanced” transformer, i.e. a balun is needed to ensure that no currents are flowing on the outer shield of the coaxial cable. One possibility to efficiently protect the circuit against common modes is a trap balun shown in Figure 2.21. It is designed to suppress currents on the outer conductor of the cable by a high impedance which is produced by forming a loop with the coaxial cable and by tuning the corresponding inductance to the Larmor frequency with a capacitor C_T . A more versatile solution is the “floating” cable trap [61] schematically shown in Figure 2.21. It is not connected or soldered to the cable and can be designed to fit over a strand of cables. The floating trap is a transmission line formed of two concentric cylinders covered with conductive foil, separated by a low loss dielectric and tuned by capacitors soldered at one end between the inner and outer cylinder surface. The coaxial cable that carries the common mode current acts as the central conductor of a transmission line formed with the inner cylinder of the floating trap. As a consequence, the unwanted common mode currents on the coaxial cable shield are blocked by the floating trap. When the cylinder is separated into two parts, the gap distance between half-cylinders allows for fine-tuning of the trap. Also, this facilitates measuring the trap and placing it on the cable assembly.

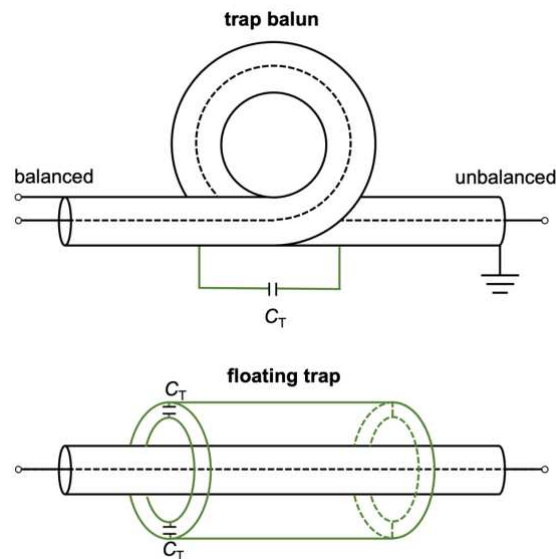


Figure 2.21: Trap balun and floating cable trap for common mode current suppression

2.2.5 Coil performance characterization

On the bench and during MRI experiments, several methods and tools are used to characterize the performance of an RF coil. In the following, basic concepts will be introduced which should help to understand the examination process of RF coils described in chapter 4.

2.2.5.1 S-parameters

A vector network analyzer (VNA) is a tool that consists of a signal generator which can be connected to a network under test. The VNA can measure amplitude and phase as a function of frequency and capture, subsequently process and display the signal influenced by the connected network under test. The VNA enables the measurement of so-called scattering (S -) parameters on the bench. S -parameters are used to describe the relationship between incident, reflected and transmitted waves of a 2-port network under test, as shown in Figure 2.22. The vector \mathbf{a} stands for the incident wave (Eq. 2.73) whereas \mathbf{b} denotes the outgoing wave (Eq. 2.74) and they depend on the voltage, the characteristic impedance and resulting current in this network.

$$a_1 = \frac{V_1 + Z_0 I_1}{2\sqrt{Z_0}} \quad a_2 = \frac{V_2 - Z_0 I_2}{2\sqrt{Z_0}} \quad \text{Eq. 2.73}$$

$$b_1 = \frac{V_1 - Z_0 I_1}{2\sqrt{Z_0}} \quad b_2 = \frac{V_2 + Z_0 I_2}{2\sqrt{Z_0}} \quad \text{Eq. 2.74}$$



Figure 2.22: 2-port network

When port 1 is used for transmission ($a_2 = 0$), S_{11} and S_{21} (in dB) are the reflection and transmission S-parameters (or coefficients), respectively, and given by:

$$S_{11} = 10\log\left(\frac{b_1}{a_1}\right)^2 = 20\log\left(\frac{b_1}{a_1}\right) \quad \text{Eq. 2.75}$$

$$S_{21} = S_{12} = 10\log\left(\frac{b_2}{a_1}\right)^2 = 20\log\left(\frac{b_2}{a_1}\right) \quad \text{Eq. 2.76}$$

S_{11} is also often denoted as the reflection coefficient ρ_r .

Displayed on a logarithmic scale on the network analyzer, the S-parameters are commonly used for resonance frequency and Q factor measurements and impedance matching.

The RF coil can either be directly related to one port of the VNA via a 50 Ω connection to carry out a S_{11} measurement. The S_{11} parameter gives information about the resonance, i.e. at which frequency (ideally) none of the energy is reflected ($S_{11} = -\infty$ dB). In practice, the S_{11} curve will show a dip at the resonance and levels of < -20 dB are desirable as this corresponds to only 1 % of reflected power. The transmission coefficient S_{21} can be used to measure coupling from port 1 to port 2 (or coil 1 to coil 2). If $S_{21} = 0$ dB this scenario would imply that all of the power emitted by coil 1 ends up in coil 2, i.e. the coils strongly couple. Ideally, in coil arrays, S_{21} should be minimized.

2.2.5.2 Resonance frequency and Q factor measurements

Probes connected to the VNA which are used for RF coil resonance frequency f_0 and Q factor measurements on the bench are commonly called “sniffer loops”, “loop probes” or “pick-up probes”. These probes allow for characterization of the RF coil via

inductive coupling, also when the coil is not directly connected to the one of the VNA ports.

The double-loop probe method [62] uses two identical loops geometrically decoupled from each other. When the probe is placed close to the RF coil to be investigated, a transmission measurement with each of the sniffer loops connected to a VNA port is carried out. The signal is transmitted through one sniffer loop and induces a signal in the RF coil which is picked up again by the second sniffer loop. The resonance frequency f_0 can be derived from the maximum of the resulting S_{21} curve and the Q factor can be measured using the -3 dB bandwidth method (Eq. 2.64) which is typically an integrated VNA function. It has to be considered that probe loops should be small compared to the RF coil and placed far enough from the coil, else it could perturb the B_1 field and lead to measurement inaccuracy. The coupling between the dual-loop probe and the RF coil should not be too strong because this would lead to added noise (equivalent resistance) and an erroneous measured Q factor. In practice, S_{21} should be below -40 dB and the lowest detectable signal is determined by the baseline value (usually -80 dB) indicating the noise from coupling between the sniffer loops.

With a single-loop probe method [63], reflection measurements are performed. To achieve a measurement of the coil's properties only, two separate measurements of the reflection coefficient need to be performed consecutively: one with the loop probe alone in free space ($\rho_{r,0}$) and the other one with the RF coil placed close to the loop probe ($\rho_{r,c}$). By subtraction of the environmental influence from the measurement with coil, this yields a compensated reflection coefficient measurement ($\rho_{r,comp} = \rho_{r,c} - \rho_{r,0}$). Similarly to the double-loop probe method, from this compensated S_{11} ($\rho_{r,comp}$) curve, f_0 and the Q factor can be determined on the VNA.

2.2.5.3 B_1^+ mapping

It is interesting to investigate the RF transmit field (B_1^+) distribution and transmit efficiency, i.e. the B_1^+ amplitude per square root of input power (B_1^+/\sqrt{P}), created by an RF coil to tailor the B_1 field for a specific application, optimize the coil design and compare different designs or geometries. This can be done in MRI experiments or using electromagnetic simulations. The latter will be detailed in section 2.3.

With MR imaging methods, the flip angle (FA) distribution can be measured and this information together with knowledge about the duration, voltage amplitude and shape of the applied RF transmit pulse can be used to calculate the transmit efficiency. The general relationship between FA distribution $\alpha(\mathbf{x})$, the transmit field distribution $B_1^+(\mathbf{x})$, the pulse shape and pulse duration T_{pulse} is given in Eq. 2.22. For a rectangular pulse voltage amplitude V_{pulse} , and assuming a $Z_0 = 50 \Omega$ system, the transmit efficiency can be calculated pixel- or voxel-wise using a measured FA map.

$$B_1^+(\mathbf{x})/\sqrt{P} = \frac{\alpha(\mathbf{x})\sqrt{Z_0}}{\gamma T_{\text{pulse}} V_{\text{pulse}}} \quad \text{Eq. 2.77}$$

Commonly, also the transmit efficiency (TE) averaged over a certain region of interest (ROI) or volume of interest (VOI) is given as a measure for coil performance.

$$\text{TE} = \text{mean}(B_1^+)/\sqrt{P} \quad \text{Eq. 2.78}$$

In this work, the saturated turbo fast low-angle-shot (FLASH) method was used for FA mapping [64].

It is based on two image acquisitions: a proton density weighted image for normalization with the signal intensity $S_0(\mathbf{x})$, and an image acquired directly after a slice-selective saturation RF pulse with signal intensity $S_{\text{sat}}(\mathbf{x})$. A Turbo FLASH sequence is used for readout. Ultimately, the flip angle can be calculated by [64]:

$$\alpha(\mathbf{x}) = \arccos\left(\frac{S_{\text{sat}}(\mathbf{x})}{S_0(\mathbf{x})}\right) \quad \text{Eq. 2.79}$$

2.2.5.4 Specific Absorption Rate

The specific absorption rate (SAR) in W/kg is defined as the time-averaged dissipated RF energy in a certain body region per mass unit m due to an applied RF field and thereby created electric field $\mathbf{E}(\mathbf{x})$. The SAR in the volume of interest V can be obtained from the E field, the mass density $\rho(\mathbf{x})$ and the electrical conductivity $\sigma(\mathbf{x})$.

$$\text{SAR} = \int_V \frac{\sigma(\mathbf{x})}{2\rho(\mathbf{x})} |\mathbf{E}(\mathbf{x})|^2 d\mathbf{x} \quad \text{Eq. 2.80}$$

It is important to determine the E field pattern which can be the superposition of multiple RF transmit channels' E fields as locally concentrated E fields, or so-called SAR hotspots, can cause patient burns. Local SAR must not exceeded certain limits defined in the IEC (International Electrotechnical Commission) standard 60601-2-

33 [65]. This becomes especially challenging at higher B_0 field strengths as the SAR scales with $|E|^2$. Local SAR limits in the IEC norm [65] are given for an averaging volume of 10 g body mass. Furthermore, in addition to spatial averaging, temporal averaging is required as SAR limits are either given for 6 min or 10 s averaging time (see Table 2.4). This can be done by adding the temporal weighting factor τ/T_{avg} in Eq. 2.80, indicating the RF duty cycle, i.e. the time τ the RF pulse is applied during the total averaging time. In Table 2.4. the defined 10 g SAR limits for local transmit coils as published in the IEC standards [65], are listed. The normal operating mode corresponds to the “mode of operation of the MR equipment in which none of the outputs have a value that can cause physiological stress to patients” [65].

averaging time	6 min		
body region	head	trunk	extremities
normal operating mode	10 W/kg	10 W/kg	20 W/kg
short duration SAR	10 s averaging time: SAR limits should not exceed two times the stated value.		

Table 2.4: Excerpt from the SAR limits set for the “normal operating mode” in the IEC standard, [65].

According to Pennes’ bioheat equations [66], as long as heat conduction and perfusion is negligible, the SAR can be directly related to the temperature increase ΔT in tissue over a duration Δt . The heat capacity constant of the tissue is denoted as c .

$$c \frac{\Delta T}{\Delta t} = \text{SAR} \quad \text{Eq. 2.81}$$

However, in reality, perfusion, thermal conduction and the heat generated by the subject are not negligible and need to be considered for temperature simulations.

For RF coil characterization, the SAR efficiency (SE) can be formulated, indicating how much transmit field is produced on average over a certain ROI or VOI per square root of the maximum local 10 g SAR.

$$\text{SE} = \text{mean}(B_1^+) / \sqrt{\max(\text{SAR}_{10\text{g}})} \quad \text{Eq. 2.82}$$

EM simulations are a helpful tool to obtain a SAR estimation using simulated E field data. The basics of EM simulations and comparison of two simulation methods will be presented in the next section.

2.3 Numerical electromagnetic simulations

2.3.1 Basic principles

Full wave 3D electromagnetic simulations of RF coils are commonly used to calculate their EM field distribution by solving Maxwell's equations for a discretized simulation space. It is especially interesting to simulate the coil in the presence of a sample to obtain knowledge about the E and B field distribution inside the tissue. This can be done prior to actual coil fabrication to investigate different geometries with respect to the target application. Most common RF simulation tools provide the possibility to model the geometry of the RF coil conductor and the sample with CAD tools and to assign them electrical properties (ϵ_r , σ). In some cases, even segmented realistic whole-body models are available, consisting of a variety of different tissue types.

In simulations of RF coils employed at UHF, some specific effects can be observed as the wavelength in tissue decreases with frequency and depends mainly on the dielectric permittivity ϵ_r (which is also frequency-dependent, [25]).

$$\lambda = \frac{\lambda_0}{\sqrt{\mu_r \epsilon_r}} \approx \frac{\lambda_0}{\sqrt{\epsilon_r}} \approx \frac{c_0}{f_L \sqrt{\epsilon_r}} \quad \text{Eq. 2.83}$$

For 7 T (≈ 300 MHz) and assuming a relative permeability $\mu_r \approx 1$ and a relative permittivity of $\epsilon_r \approx 80$ for a biological sample, this leads to a shortened EM wavelength in tissue of only ≈ 11 cm, which is comparable to the dimensions of human body parts, e.g. the head. As a consequence, for large volume coils, as used e.g. in head imaging, this can lead to EM field interferences that create an inhomogeneous B_1^+ distribution causing a “central brightening” effect [33,67]. In advanced designs, the field distribution can be optimized using static or dynamic B_1 shimming, or parallel transmission.

Furthermore, the square dependency of the E (and B_1) field on the field strength poses constraints on the SAR when using coils in Tx mode. This needs careful investigation and is also possible with EM simulations. Full wave EM simulation of a coil including a body or phantom model as well as a dedicated post-processing workflow allow for the calculation of e.g. B_1^+/\sqrt{P} and SAR maps from simulated fields. In the following, two wide-spread simulation methods for RF coil simulation, the finite difference time domain (FDTD) [68] and finite element method (FEM) [69] are shortly introduced and compared with respect to the application of coaxial coil simulations.

2.3.2 FDTD vs. FEM

FDTD is based on the discretization of Maxwell's equations directly in the time domain using their partial differential form. The propagation of the EM field is approximated in a grid of rectangular cuboid cells, the "Yee cells" [68]. This allows for the simulation of complex and inhomogeneous simulation spaces with cuboid meshing. Many anatomical numerical body models are available, e.g. the "Virtual family" models consisting of more than 80 different tissue types [70]. A possible simulation workflow for the design of form-fitting transceiver coils at UHF using the "XFDTD" simulation software by Remcom (State College, PA, USA) in combination with a circuit co-simulation approach [71] and a realistic body model is described in-depth in reference [72]. A disadvantage of the FDTD method is that not only the structure under test but also the surrounding simulation space is discretized. In this surrounding space, wave propagation can be limited by suitable boundary conditions. Nonetheless, this simulation approach is time-consuming. Usually, for large simulation spaces and complicated geometries, convergence is only reached after a large amount of simulated time steps. The required memory and computation time scale proportionally to the geometry, the frequency and the size of the surrounding space. The simulation mesh has to be composed of cuboid cells which results in problems encountered when curved structures have to be modelled. This applies to the concrete case of circular coaxial coils consisting of sub-mm structures, i.e. with an inner and outer coaxial conductor thickness of typically only ≈ 0.2 mm and an overall cable diameter of $\approx 1-2$ mm. FDTD meshing can result in a too coarse staircase-type mesh, meaning that the grid cell size is too big to yield accurate simulation results. Finely resolving the coil conductors with many small grid cells leads to an accurate representation of the coaxial coil but the fine mesh – an example is shown in Figure 2.23 – results in very long computation times, not feasible for coaxial coil simulations in practice.

The Finite Elements Method is based on a numerical solution of Maxwell's equations in the frequency domain. This can be done for a single frequency at a time or a number of frequency samples in the course of a frequency sweep. The simulation space is typically composed of finite elements using a tetrahedral mesh. This way, small (even

sub-mm) coaxial coil structures can be efficiently resolved, and the resolution can be adapted to the geometry, i.e. larger mesh cells can be used for surrounding free space. An example of a coaxial coil's FEM mesh is shown in Figure 2.23. Further, this simulation method is time efficient due the fact that a narrow band, i.e. single frequency simulation is possible.

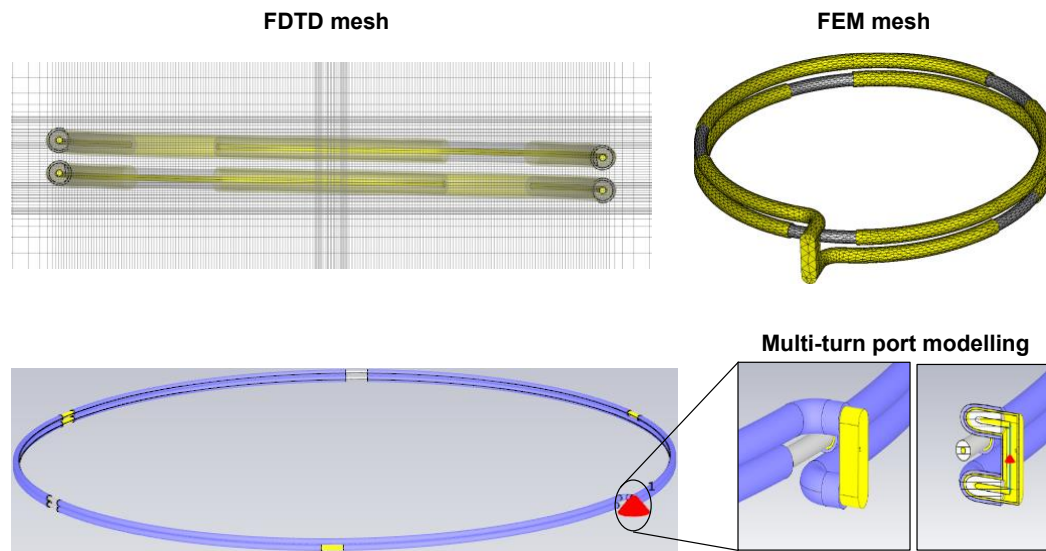


Figure 2.23: Comparison between FDTD and FEM mesh and example of multi-turn CC port modelling in CST

For the above-explained reasons, for coaxial coil simulations carried out in the frame of this thesis (presented in chapter 4) the FEM solver implemented in the simulation software CST Studio Suite 2020 (Dassault Systèmes, Paris, France) was used. Parameters like the E field, B field and surface current density as well as the coil's S -parameter matrix can be extracted from CST simulations. For E and B field simulations, a cuboid sample was placed at a distance of 0.5 mm from the coil. Multi-turn coils were modelled as helical structures and the coil feed port was placed as depicted in the bottom part of Figure 2.23. Calculations of the surface current on all three coaxial coil conductors, of the transmit efficiency, the SAR efficiency and local 10 g SAR were carried out in post-processing. The exact sample properties as well as the post-processing workflow are described more in detail in *Article I* (4.2).

3. Wearable MR technology

After the introduction of the general theoretical background, including magnetic resonance, RF coils and EM simulation, in this chapter the focus will be shifted to the specific topic of “wearable technology” (WT) in MR hardware development. First, the question “Why wearable and what does it mean?” is answered, i.e. a definition of the term and the motivation for smart wearable electronics in MR is discussed. Secondly, the different requirements for wearable MR devices are presented which is followed by a conclusion on the most needed technological advances.

3.1 Definition and motivation

Following the definition of Godfrey *et al.* [73] “*Wearable technology (WT, or wearable computing) encapsulates a plethora of devices worn directly on or loosely attached to a person*”. Obviously, WT is a quite vast term comprising devices that can be classified by applications, e.g. fitness, healthcare, lifestyle, infotainment, industry or military use. Smart wearable electronic components used in those devices range from microcontrollers, memories, batteries, sensors, audio equipment, and displays to cameras and can be worn on different body parts e.g. the eye, wrist, foot, neck, chest or the whole body.

The principle building material for wearable technologies that are not wearable gadgets (e.g. fitness bracelets) but “smart garments” [74] is a textile with a certain function, differing from the functions of a simple textile, thus also called “smart textile”. According to Langenhove *et al.* [75], this can be explained as follows: “*Smart textiles are textiles that are able to sense stimuli from the environment, to react to them and adapt to them by integration of functionality in the textile structure. The stimulus and response can have an electrical, thermal, chemical, magnetic or other origin.*”. For MR signals, the stimulus is of magnetic origin, i.e. the smart textile “senses” a current being induced by magnetic coupling in a conductive textile structure. The “reaction” to this stimulus can be the simple electrical transmission of the MR signal to some outlet where it would then be further transmitted to the MR scanner. In more sophisticated smart wearables, for example the automatic resonance frequency adaptation of flexible receive coils by an integrated retuning system as published by Mehmman *et al.* [76] could be enabled. The textile itself can be either used as a carrier material and be adapted to integrate off-the-shelf rigid electronics or to embed

traditional but flexible electronics, or the textile can replace parts of the electronics (e.g. cabling can be replaced by conductive yarns or braids) and in the most extreme case the textile takes over all electronics' functions.

Nowadays, wearable technology is largely used in daily life (e.g. smartwatches, fitness trackers) but also in other not MR-related fields the technological development is advanced. An example is energy harvesting with smart wearables based on the photovoltaic [77] or piezoelectric [78] principle. For health and well-being applications, smart wearables mostly target the improvement of physiological monitoring with textile-embedded sensors, e.g. ECG (electrocardiogram) electrodes in T-shirts [79,80]. There is a subtle nuance between the meaning of "portable" compared to "wearable" because a device can be a handheld, wireless and small so that it can be stored in a pocket or bag, and thus portable, but not directly fabricated of a textile or always worn on-body. One portable device example from the medical imaging sector is a handheld wireless ultrasound scanner [81], controlled via an application that can run on any portable device (smartphone, tablet). Unlike for ultrasound devices, for conventional high-field MR scanners relying on superconductive magnet technology, it is impossible to transform the whole system into a portable device. Nevertheless, some recent developments demonstrate the feasibility and advantages of low-field portable, or so-called "tabletop", MR scanners based on permanent or resistive magnets [82–84] for point-of-care imaging and diagnosis.

As a consequence, for high-end clinical scanners (> 3 T), the development of wearable MRI-related technology is focused on sensors and detectors used in the MR system, e.g. for the MR signal detection or patient monitoring. Some recent examples for wearable MR technology - other than flexible RF coils which will be discussed in section 3.2.1.1. - are a Bluetooth sensor for patient monitoring (heart rate, blood oxygen saturation, surface temperature and humidity) during MRI scans developed by Vogt *et al.* [85] or a 2.4 GHz wireless miniature motion sensor developed by Van Niekerk *et al.* [86] that can be placed on the subject's nose and is employed for prospective motion correction.

The motivation for the development of wearable solutions for MR devices is mainly based on the following arguments:

- convenience: for the device operator and the subject, i.e. improved comfort because of ergonomics, lightweight, flexibility and miniaturization of components;
- usability: changes in posture (e.g. flexion of joints) for dynamic imaging or changes in patient position in between scans can be more easily done;
- efficiency: the workflow and, therefore, patient throughput can be increased;
- accessibility: the patient can put on a wearable coil in the changing room, i.e. the coil positioning and handling is not restricted to the MR scanner operator only;
- sensitivity: for RF coils the adjustment to subject size and shape of target anatomy means higher magnetic coupling and, therefore, sensitivity. Less variation in coil loading leads to more stable inter-subject performance;
- adaptability: to each subject size or anatomy. Further, RF coils and electronics can be adapted so that they can hold additional, ideally wireless, sensors collecting more information about physiological parameters and motion in parallel to MRI;
- safety: reduced weight and removal of coaxial cabling.

3.2 Requirements for wearable MR devices

This sub-chapter analyzes the most important requirements for wearability, specifically focused on MR devices. The current goals and challenges in the development of wearable MR devices are flexibility, reduction or removal of cabling and in vivo usability. These topics are discussed in the following sections, supported by references to the state-of-the art.

3.2.1 Flexibility

One of the central keywords of this thesis is “flexibility”. A paradigm shift from rigid to flexible assemblies in the context of MR hardware has clearly been noticeable within the last decade. The goal is to make MR devices more versatile, handling around the patient and the MR bore easier, and to find the ideal balance between flexibility and robustness of the designed hardware for clinical routine use.

3.2.1.1 Flexible RF coil technology

Especially for RF coil and coil array technology the benefits of flexibility are convincing: An RF coil ideally closely adapted to the patient anatomy yields constant filling factor and strong magnetic coupling to the target imaging FOV. This leads to signal enhancement, performance stability and increased patient comfort, especially when combined with lightweight design, in the confined space of the MR bore where conventional bulky rigid coils are often perceived as intimidating and heavy.

An overview over the current flexible RF coil development is given in the introduction section of *Article I* but this chapter leaves more room for details and discussions. In the following, different approaches for RF coil design are systematically categorized depending on their degree of adaptability to the body contour and the manufacturing process, ranging from completely rigid to flexible and stretchable RF coils.

3.2.1.1.1 Rigid anatomy-adapted RF coils

The most commonly used coils in conventional MR set-ups are fabricated of copper wires or copper traces with high conductivity on a rigid printed circuit board (PCB). These coils are tuned and matched using lumped components, encapsulated in a rigid (often injection-molded or 3D-printed) housing that is form-fitted to the average or

often largest possible anatomy of the target body region. Birdcage coils for example can be used for all kinds of anatomies, e.g. the knee or the head, but for small patients the coil-sample distance is often too large to achieve satisfying receive sensitivity whereas the produced Tx field is ideally homogeneous over the whole FOV. Therefore, in addition to a large local birdcage coil or the body coil (the birdcage coil integrated in the scanner bore) used for transmission, a rigid but anatomy-adapted RF coil or coil array is used for signal reception. At UHF (≥ 7 T), mostly the same anatomy-adapted coil is used in Tx/Rx mode since there is no body coil integrated in the MR scanner.

Examples for anatomy shaped rigid coils exist for various body parts, such as a tight-fitting helmet for the head [87,88], cup-shaped formers for the breast [89], half-cylinders for the calf [90,91] or a cylinder for a single finger [37].“ A recent paper discusses the relevance of novel “3D plasmonics” technologies for the fabrication of tailored, multifunctional MRI coils [92].

3.2.1.1.2 Semi-flexible/semi-rigid RF coils

Taking a step towards flexibility but keeping rigid parts of the coil, several mechanically adjustable, size-adaptable – “semi-flexible” or “semi-rigid” – coils have been developed over the years. These coils are restricted to bending or size-adjusting in one direction at a time only. Below, a selective list of interesting work, sorted in chronological order, is presented.

Kwok *et al.* [93] built a volume-adjustable 4-channel phased array specifically for hip imaging at 1.5 T, consisting of a dual anterior and posterior “clamp-like” copper wire array on a Plexiglas support with an adjustable distance between the two parts by a hinge on one side.

Hardy *et al.* [94] designed a 128-channel coil combining one 64-channel flexible anterior coil array with a fixed 64-channel array in the patient table and demonstrate high acceleration factors with parallel imaging and improved SNR per unit time compared to a 32-element array for body MRI.

Adriany *et al.* [95] proposed a 16-channel geometrically adjustable transceiver array system for parallel imaging of the human head at 7 T. Holder mechanics allow the rapid change in position of transmission line coil elements around the head and a

tunable decoupling capacitor ensures decoupling of neighboring elements with varying inter-element distance.

Nordmeyer-Massner *et al.* [96] constructed a wrist array for proton MRI at 3 T with 8 trapezoidal surface coil elements of 7 cm length arranged around the wrist in a truncated cone shape with a mechanism for modifiable coil inclination, i.e. cone opening, and can therefore be fitted to the individual wrist anatomy.

Mager *et al.* [97] demonstrated that inkjet printing of coil conductors and in-line capacitors was possible with ink containing silver that was sintered after printing. Flexible polyimide (Kapton) foil was used as a substrate (or dielectric for the capacitor) and experiments conducted with a coil operating at 400 MHz.

Wu *et al.* [98] presented a flexible microstrip array with parallel imaging capability (16 coils on Teflon, attached onto a soft canvas former) designed to be wrapped around the human anatomy for various applications (liver, torso, head, knee, palm) at 7 T.

Zhang *et al.* [99] published their work on a semi-flexible 32-channel anterior coil with three hinge axes and a rigid 32-channel posterior coil (64-channels in total) Rx-only coil array which has shown to facilitate pediatric body MRI at 3T.

Hancu *et al.* [100] demonstrate the advantages of using a semi-flexible 31-channel breast array with two flexible “flaps” holding coil elements and electronics (the whole integrated in a rigid former) over the use of a completely rigid 16-channel coil at 3 T in prone patient position.

Corea *et al.* [101] transferred conductive ink onto a transparent flexible polyethylene terephthalate film by a screen-printing process. Using dielectric ink, or the substrate as dielectric, also capacitors are printed in this design and the usability was demonstrated for cervical spine and knee imaging at 3 T. Furthermore, a 12-channel screen-printed coil array designed for pediatric applications has been shown to yield similar performance to a commercial 32-channel cardiac array and to improve acceptance of parents and caretakers as well as comfort for patients [102,103].

Frass-Kriegl *et al.* [104] used combined rigid/flexible PCBs in a versatile 23-channel Rx-only coil array dedicated to high resolution imaging of various body parts (e.g. the ankle, elbow, occipital cortex or shoulder) at 3 T.

Kriegl *et al.* and Hosseinnezhadian *et al.* [42,43] employed TLR technology for the fabrication of a 4- or 12-channel array using flexible substrate for TLR fabrication

combined with rigid PCBs for lumped components. Both arrays implement novel decoupling techniques (annexes or rings) and can be used for high resolution imaging at 7 T, the 12-channel array specifically targets cardiac applications. The TLR fabrication approach used in the cited work above is related to previous publications on flexible double-sided (parallel-plate) TLRs printed on thin polymer film, e.g. Teflon or Kapton, [44–46]. The similarities of these double-sided TLRs on a flexible dielectric to an approach using two wires with a gap surrounded by a dielectric (GE Healthcare AIR™ technology) will be explained together with other flexible coil approaches below.

Rios *et al.* [105] designed a pneumatic-based size-adjustable 13-channel Rx copper wire array that can physically adapt to infant head dimensions for neonate imaging at 3 T.

Zhang *et al.* [106] developed a trellis structure for tailored size-adaptable surface coil arrays which can expand and contract and outperform dedicated commercial coils with similar coverage.

Iwasawa *et al.* [107] claimed that with their size-adaptable 8-channel prototype RF receiver, the inter-element distance can be changed with negligible SNR degradation at 3 T because of the use of a high blocking impedance in the preamplifier decoupling circuit.

3.2.1.1.3 Flexible RF coils

In contrast to semi-rigid or semi-flexible coils of various forms as listed above, those described as completely flexible can be bent in all three spatial dimensions. Therefore, limitations to bending occur only because of concerns regarding mechanical robustness. The following manufacturing processes or flexible coil technologies have been identified:

3.2.1.1.3.1 GE Healthcare AIR™ technology

In 2016, General Electric (GE) Healthcare introduced a lightweight AIR™ (Adaptive Image Receive) coil technology [108], highly robust against coil overlap variations [109–111], that is commercialized in a blanket-like array design with miniaturized interface boxes. The exact coil type and fabrication process has not been disclosed in scientific publications but the coils presented on the GE website and in publications

demonstrating the applications show a lot of similarities with the patent published by Stormont *et al.* in 2019 [112] where the cross section of a loop coil is depicted as two parallel (stranded) wires, encapsulated in a flexible dielectric. It is mentioned that at least one gap is introduced in the conductors, also named “INCA” conductors, thereby forming a transmission line with a distributed capacitance in the dielectric and the resulting coil element weighs only approximately 10 g.

The use of AIR™ coils has been proposed for many different applications at 3 T, e.g. a 16-channel (4 x 4 channel) [113] or a 22-channel array for head and neck imaging [114] used to improve workflow in radiation therapy treatment planning based on 3 T MR images. Other applications include MR neurography of the brachial plexus with a tight-fitting 24-channel vest array [115] or prostate, pelvis and rectal imaging with a 50-channel array consisting of a central and two lateral flaps [116]. Furthermore, the design was used in a 16-channel head coil in an open “ski-mask” design for neuroimaging [117].

3.2.1.1.3.2 Coaxial TLRs

In comparison to screen-printing or custom-made conductor assemblies, the use of commercially available non-magnetic coaxial cables to form a self-resonant TLR means less complicated manufacturing while still resulting in a lightweight, ultra-flexible coil solution. Different forms of transmission line resonators, i.e. parallel-plate and coaxial TLRs have been discussed in section 2.2.3.2 (Theoretical Background), and the state-of-the art, advantages of coaxial TLRs (or “coaxial coils”, CCs) as well as functioning (e.g. the high impedance behavior and current distribution) will be more extensively explained in *Article I* and supplementary studies in section 4.3. The novelty presented in *Article I* is to combine the coaxial TLR principle [55,58] with the multi-turn multi-gap principle [118], previously only employed with parallel-plate TLRs [41]. Multi-turn multi-gap coaxial coils are used in Rx-only mode at 3 T and Tx/Rx mode at 7 T and compared to standard copper wire coils.

Coaxial coil elements can be woven into and/or sewn onto some textile and conformed to a curved surface e.g. as demonstrated in a 3-channel design for 3 T MRI by Obermann *et al.* [119], using single-turn single gap coaxial coils. Recent publications showed the usability of single-turn single-gap coaxial coils in array configuration (Rx-only at 1.5 T, Rx-only at 3 T and Tx/Rx at 7 T) [55,120–124] for

applications including in vivo human pelvis, neck, hand and knee imaging or ex vivo sample imaging with the coil elements attached to some flexible support.

3.2.1.1.3.3 Electro-textile ("E-textile")

Zhang *et al.* [125] used conductive cloth (no specifications given) with high conductivity which was laser cut to the desired coil shape and attached to a cotton-like support designed to fit around the human neck. In a cadaver study they showed the SNR gain over a standard coil and in principle, this coil fabrication technique could also be used with stretchable textiles.

3.2.1.1.4 Stretchable RF coils

Clearly, stretchable coil designs offer the highest degree of flexibility but in addition to bending the coil, also stretching can influence the coil's performance or mechanical robustness. Different manufacturing techniques for stretchable coil conductors exist:

3.2.1.1.4.1 Metal fibres

Nordmeyer-Massner *et al.* [126] fabricated a stretchable 8-channel knee array out of a 5-mm copper fiber braid which was stitched onto a medical bandage. Depending on the stretching (up to 30 %), the coil geometry changes and therefore also the conductor length and wire configuration, resulting in resonance frequency and impedance changes which degrade the SNR performance and preamplifier decoupling as well as overlap decoupling when the distance between coil elements varies. Directly comparing the stretchable array to a commercial rigid 8-channel array in phantom imaging at 3 T revealed a 20 % SNR penalty.

Similarly, Port *et al.* [127] used 5-mm copper braid to construct a 4-channel wrist array, combined with on-coil digitization and optical fiber MR signal transmission at 3 T.

Agir *et al.* [128] experimented with conductive silver thread and elastic fibers to fabricate a single coil element of 4 cm width targeting breast MRI at 3 T.

Vincent *et al.* [129,130] used conductive thread stitched in a zigzag pattern onto a polyester support material, with coil diameters of approximately 7 cm for the fabrication of a flexible 2-channel breast coil array that can be attached to the

subject's sports bra. In single-element phantom experiments, an SNR decrease was experienced with the stretchable coil compared to the use of a standard surface coil at the same coil-sample distance.

Gruber *et al.* [131] constructed a 6-channel knee array for 1.5 T MRI with metal wires mounted onto an elastic substrate in a meandered way. The array consisted of two rigid and four stretchable elements and demonstrated considerable SNR gain compared to a geometrically identical completely rigid coil array.

3.2.1.1.4.2 Liquid metal

Already in 1986 and 1990, Malko *et al.* [132] and Rousseau *et al.* [133] explored the possibility of filling liquid metal (mercury) in elastic tubes and used this manufacturing technique for “versatile” surface coils in 0.5 T MRI with the main drawback of high toxicity of mercury.

Port *et al.* [134] recently published their approach to developing a stretchable wearable receiver coil based on eutectic Gallium Indium (eGaIn), which is liquid at room temperature, filled in silicone tubes and sealed with a copper contact.

The advantages of eGaIn are its high electrical conductivity and low toxicity. The resistivity of eGaIn ($\rho_{\text{eGaIn}} = 29.4 \mu\Omega \cdot \text{cm}$) is 17 times higher than the one of copper ($\rho_{\text{copper}} = 1.68 \mu\Omega \cdot \text{cm}$) but at approximately 128 MHz, the skin depth δ (Eq. 3.1) in eGaIn and therefore the cross-sectional current area A is 4 times larger than the one of copper and for conductors where $d_1 \gg 2\delta$, the effective resistance $R = \frac{\rho}{A \cdot l}$ is only 4 times larger as compared to copper.

$$\delta = \sqrt{\frac{\rho}{\pi f_0 \mu_r \mu_0}} \quad \text{Eq. 3.1}$$

Under strain (up to 60 %), the unloaded Q decreases moderately and the larger the cylindrical phantom, the more the SNR of the liquid metal coil formed to the phantom approaches the SNR of a reference copper coil. Liquid coil elements can be sewn onto a knee bandage [135] or for an even more convenient solution, two layers of textile with embedded electronics and pouches for the coil conductors were used. Using this coil concept, a 4-channel array was constructed for kinematic knee imaging. Still, the potential danger of leakage and patient contact with toxic liquid metal is one drawback of these coils.

Varga *et al.* [136] and Mehmman *et al.* [137] investigated coils made of liquid metal stencil-printed onto neoprene foam, where the liquid metal was not encapsulated and therefore not directly patient-use friendly. Due to the higher resistivity compared to copper, a 34 % lower SNR was reported for liquid metal coils. An automated re-tuning system [76] attached to the coil port can help achieve more stable coil performance with strong bending and stretching.

3.2.1.1.4.3 Conductive elastomers

To circumvent the potential leakage of toxic liquid metals, an interesting alternative is the use of a conductive elastomer consisting of a fully washable polymer exhibiting elasticity with added conductive wires, fibers, carbon nanotubes, flakes or particles. Port *et al.* [138] presented a study using an elastomer with a resistivity of $\rho_{\text{elastomer}} = 700 \mu\Omega \cdot \text{cm}$ and therefore 417 times higher than for copper but again, due to the skin effect at 128 MHz, this is reduced to a factor of approximately 20 for the effective resistance. Under strain, the unloaded Q is reduced and recovers when strain is released and after some initial measurement cycles, the Q -value stabilizes for the remaining measurements. A 14 % lower SNR was observed in the phantom center for elastomer coils as compared to the copper reference coil and in a comparable set-up as used with liquid metal coils, the proof-of-concept of employing this coil concept for knee MRI was successfully demonstrated.

With flexible and stretchable designs, coils can be ideally conformed to the body part to be imaged but this entails different technical challenges which can be summarized in the following bullet points:

- fabrication process: trade-off between conductivity and flexibility or stretchability;
- mechanical robustness: has to be ensured for usage in clinical routine and stable coil performance;
- influence of bending and stretching: geometrical changes of the coil itself or the arrangement in an array result in resonance frequency shifts and coil impedance changes which can degrade device performance in terms of impedance matching, preamplifier decoupling, and overlap decoupling;

- weight and bulkiness: miniaturization of integrated electronics and removal of lumped components is required;
- safety issues: heating and electrical contact to the patient has to be avoided;
- performance reliability: anatomy or body position must not influence the coil performance in daily clinical use.

In practice, it is the central goal to find a suitable coil design for a defined target application yielding high SNR, patient safety and comfort but also robustness. Whereas standard coils can be adapted to the average anatomy, they are often placed in a rigid housing and bending of copper wires used for standard coil construction is not easily reversible from one anatomy size or application to another. Also, solder joints along the coil are prone to breaking with bending. Since the coil geometry and distance between coil and sample is the main factor to be considered for optimal SNR, the design of body-conforming rigid coils can be quite restrictive to some anatomy sizes, often the largest possible. The more conformal a rigid coil is, the smaller the percentage for which the shape is fitting. Furthermore, rigid coils are often more cumbersome and heavier than flexible alternatives. For flexible coils which are perfectly fitted to the anatomy, the difficulty lies in finding a suitable conductor material with high conductivity which - in exchange for high flexibility and lightweight - doesn't introduce too much penalty on SNR when used in MRI. Furthermore, the design of flexible and robust housings for the clinical usage of flexible coils is a challenging task. The benefits and disadvantages of different coil designs have to be carefully evaluated before using them on a larger scale, e.g. for clinical applications.

3.2.2 Removal of cabling

Another requirement which has to be taken into account when aiming for wearable MR technology is the removal of cabling, e.g. DC power cables, coaxial cables, or DC control lines. For all in-bore electronics (e.g. sensors and power supply solutions) but especially for Rx-only coils in MRI it is advantageous to get rid of galvanic cable connections. The reasons, especially concerning patient safety and device functioning and the central goal of providing wearability are detailed in the introduction section of *Article II*. In the following sections 3.2.2.1 and 3.2.2.2, an emphasis is put on the discussion of different alternatives to coaxial cable MR signal transmission. This will also be the occasion to explain the basics of digital optical wireless communication as this approach was used in the development of an OWC module for motion sensor data transmission in the frame of this thesis. Section 3.2.2.2, highlights the importance of low power electronics for wearable MR technology.

As the overview in Table 3.1 illustrates, the MR signal, encoded either in the digital or analog domain, can be transmitted using optical fiber or wireless transmission methods, each presenting specific advantages and disadvantages as compared to the use of simple coaxial cabling for each Rx coil channel.

encoding	transmission	
	optical fiber	wireless (RF/optical)
analog	<ul style="list-style-type: none"> + simple low-cost implementation + minimum of additional on-coil components + no interference with RF measurement - performance limited by laser's RIN, trade-off between NF and dynamic range - laser dissipates much power - LED has low modulation speed 	<ul style="list-style-type: none"> + no need for digital electronics - high RF transmit power can potentially interrupt data transmission or lead to antenna damage - phase instability and channel fading (e.g. due to patient motion) - requires analog frequency multiplexing with multiple channels - synchronization is challenging
digital	<ul style="list-style-type: none"> + use standard optical links (e.g. RCLED transceivers) + no RF spectrum/bandwidth limits + no fading due to patient motion - AD conversion, processing requires several chips (on-coil), power 	<ul style="list-style-type: none"> + most flexible option + bandwidth efficiency using diversity schemes (e.g. MIMO) - data rate pushes the limits of current wireless technology (e.g. Wi-Fi, Li-Fi)

Table 3.1: Alternative MR signal transmission methods, adapted from [139], RIN... relative intensity noise, NF...noise figure, LED...light-emitting diode, RCLED...Resonant Cavity LEDs, MIMO... multiple input multiple output, Wi-Fi...Wireless Fidelity, Li-Fi...Light Fidelity

3.2.2.1 Optical fiber transmission

The schematics shown in Figure 3.1 and Figure 3.2 represent different strategies for analog or digital optical fiber signal transmission and were completed with the possibility of optical wireless data transmission (indicated by the dashed line) instead of optical fibers, which will be discussed in the next sub-section (3.2.2.2).

3.2.2.1.1 Analog optical fiber transmission

Two main strategies for analog optical fiber signal transmission exist which are shown in Figure 3.1: (a) direct and (b) external optical modulation.

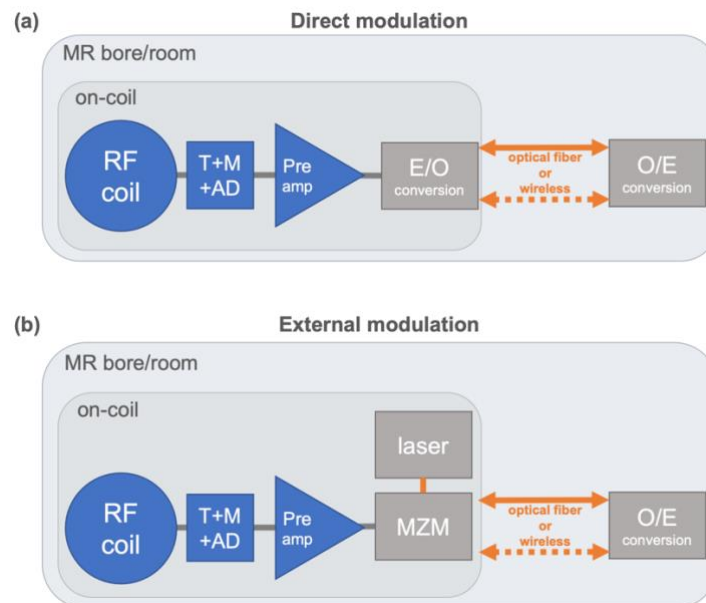


Figure 3.1: Schematic representation of analog optical fiber or optical wireless transmission strategies: (a) direct modulation or (b) external modulation. Additional filtering and amplification stages that might be necessary for signal conditioning are not shown. T+M...tune & match, AD...active detuning, E/O...electro-optical, MZM...Mach-Zehnder modulator (E/O converter), OWC...optical wireless communication.

In the following, examples of published work for both approaches will be given and shortly explained:

(a) Direct modulation

The simplest method is the direct intensity modulation of a laser or LED (light-emitting diode) current with the advantage of the optical fibers being immune to interaction with the RF Tx field and therefore eliminating the risk of heating due to EM coupling.

Yuan *et al.* [140–142] report that the laser relative intensity noise (RIN), photodiode (PD) shot noise and thermal noise and laser or amplifier nonlinearities limit the dynamic range of the optical link, which is often inferior to the required DR in high-field MR examinations [32,143]. Du *et al.* [144] experimented with different analog optical transmitters and found that a vertical-cavity surface-emitting laser (VCSEL) was the best choice for direct modulation in MRI applications because of its small size, low power consumption (low threshold current) and wide temperature range. Fandrey *et al.* [145] used a photovoltaic power converter to drive a VCSEL, directly modulated with the RF signal for the design of a 1.5 T miniature catheter coil without any galvanic connections. Biber *et al.* [146] used a complex analog time division multiplexing and analog signal compression system to be able to transmit the signal of 4 RF channels via a single optical fiber link.

(b) External modulation

With an external modulator, e.g. a Mach-Zehnder modulator (MZM) as used by Koste *et al.* [147], the electro-optical signal conversion happens in the modulator consisting of electro-optic material that receives a continuous wave laser signal which is then intensity modulated by the RF signal. Aydé *et al.* demonstrated that an electro-optic crystal in bulk [148] or in waveguide format [149] can be employed as a laser polarization state modulator (based on the Pockels effect [150]) to sense the RF magnetic field. External modulation methods are often more complex, more expensive, involve a higher component count but can achieve higher DR than direct modulation methods [149].

Independently of or together with analog RF signal transmission over optical fibers, active optical detuning has been implemented in several works [143,151,152] with a laser controlled circuitry to create PIN bias current, either by a battery power supply or photodiode current.

3.2.2.1.2 Digital optical fiber transmission

Prerequisite for the transmission of digital signals via optical fibers is a digitization step, e.g. on-coil for the MR signal, to convert analog into digital electrical signals using an ADC. Several publications demonstrate the successful implementation of optical fibers for the transmission of digitized MR signals [127,134,153–156]. The different existing digitization strategies as well as benefits and challenges related to each method are discussed more in detail in *Article II* but shall be schematically sketched in Figure 3.2.

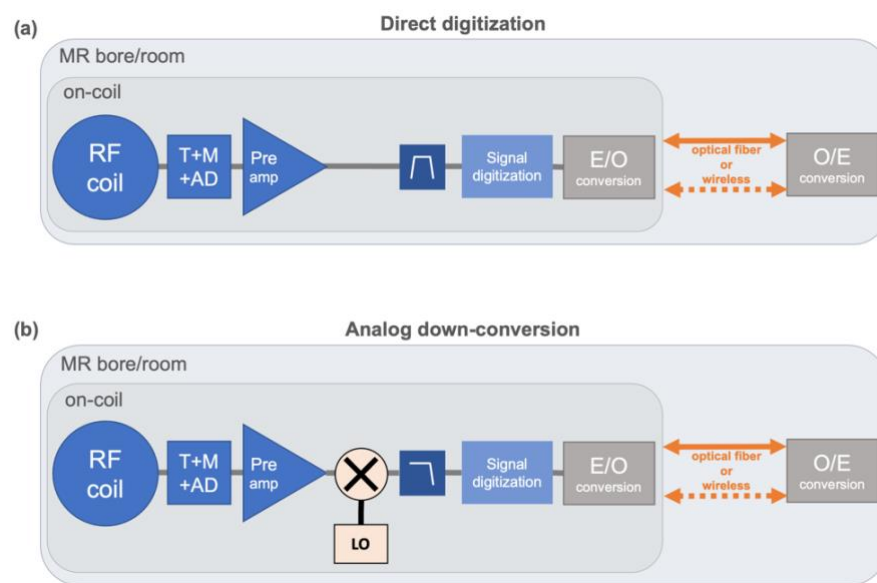


Figure 3.2: Schematic representation of digital optical fiber or optical wireless transmission strategies: (a) direct digitization or (b) analog down-conversion. Additional filtering and amplification stages that might be necessary for signal conditioning are not shown. T+M...tune & match, AD...active detuning, LO... local oscillator, E/O...electro-optical, OWC...optical wireless communication.

The two main possible strategies are (a) direct digitization or (b) analog down-conversion prior to digitization, also listed in Figure 2 of *Article II*:

(a) Direct digitization

With RF Larmor frequencies up to 300 MHz, direct sampling at the Nyquist rate is not the most reasonable option as ADC requirements then become more stringent, i.e. high sampling frequencies according to the Nyquist theorem $f_s > 2f_{\max}$ and high precision > 16 -bit would be required and resulting data rates very high. This would also impose high demands on subsequent digital

processing stages. Using a direct sub-sampling approach, with rates of several tens of MHz (below the Nyquist rate), a band-pass filter designed to operate at the carrier frequency is needed to avoid signal aliasing which restricts the use to a specific B_0 field [157].

(b) Analog down-conversion

Another method is analog down-conversion prior to digitization using a mixer which performs a multiplication of the RF input with a local oscillator (LO) signal, shifting the MR signal to an intermediate frequency (IF) or to baseband (around 0 Hz), followed by a low-pass filter. Nyquist-Shannon's theorem states that the sampling frequency only has to be at least twice the maximum information bandwidth so assuming a band-limited signal with a Δf_{Rx} of ± 1 MHz, a sampling rate of at least 2 MSps would be sufficient. As the LO frequency can be modified, this method is more easily adaptable to other field strengths [157]. Quadrature (I/Q) demodulation will only be shortly mentioned here and is explained more in detail in references [22,139,157,158]. In modern MR receiver architectures, sampling is often done in complex mode with a reduced rate of $f_s > \Delta f_{\text{Rx}}$, by so-called I(in-phase)/Q(quadrature) demodulation collecting both real and imaginary data for each sampling point to eliminate signal ambiguities. This is done with a second LO mixer shifted by 90° , yielding I and Q components which are interpreted as parts of a complex baseband signal.

It should be noted here that the conversion and digitization steps do not necessarily need to happen in this order. In "mixed" approaches, for example analog demodulation to an IF can be followed by digital down-conversion to baseband after the ADC.

Some selected ADC examples suitable for on-coil use, i.e. where the data sheet explicitly mentioned a non-magnetic package available for use in MRI, are listed in Table 3.2. Concerning the ADC choice, a trade-off between different criteria has to be found:

- Ideally, the ADC supports a high number of input channels (to connect more than one RF Rx channel),
- high precision (> 16-bit for high DR), has a
- low power consumption per channel and the
- output is in a high-speed serial format (for example JESD204B, commonly used in combination with optical fiber data transmission) to avoid the need for an additional serializer on-coil.
- The output format and data rate, e.g. JESD204B which supports up to 12.5 Gbps lane rate, should also be compatible with the FPGA (field programmable gate array) and the optical fiber or wireless transmission approach used.

Out of the commercially available options, the ADS52J65 would be a good candidate to perform on-coil digitization for example using a direct undersampling approach in order to minimize the form factor of discrete on-coil components.

ADC	# ch.	bits	power (mW/ch.)	max. sampling rate (MSps)	output format
ADS52J65 [159]	8	16	70	125	JESD204B
AD9656 [160]	4		197	125	JESD204B
ADS5263 [161]	4		355	100	Serial LVDS

Table 3.2: Non-magnetic ADC examples, LVDS...low voltage differential signaling

As also mentioned in *Article II*, it can be advantageous to perform some kind of data compression to alleviate data rate and storage requirements.

The primary objective is to reduce the data rate on-coil before optical fiber or especially before wireless transmission. This can be done by ADC-integrated decimation features or some other digital operations controlled by an FPGA, e.g. by coil-wise or “dynamic” demodulation on a per-channel basis or DR compression [139,162].

The secondary objective is data compression before storage and post-processing that takes place out-of-bore, again using an FPGA, for example. One way to reduce the amount of data used in processing is to exploit the redundancy of the signal from different coils through coil compression. By combining the original coil data into a

new, reduced set of virtual coils, the amount of data is decreased by several factors, which reduces the computational burden for reconstruction [163,164].

The on-coil FPGA could also ensure stable synchronization between the MR system and digital wireless or optical fiber transmission system (e.g. via a phase-locked loop, PLL) and handle the interfacing between ADC(s) and wireless/optical fiber transceiver(s). As for ADCs, MR compatibility, a small form factor and low power consumption is crucial for the FPGA. An example, suitable for in-bore real-time signal processing as demonstrated by Reber *et al.* [156], is the Artix-7 (Xilinx, San Jose, CA, USA).

According to literature, optical transceivers coupled to optical fibers that were employed in the MR environment are either non-magnetic commercial options or custom-made. Aggarwal *et al.* [165] report using a Firecomms 1 Gbps LC (Lucent Connector) transmitter and receiver and a plastic optical fiber connection. Vogt *et al.* [166] developed a custom non-magnetic micro-optical module using a VCSEL laser transmitter and PD receiver that can operate at speeds higher than 1 Gbps over glass fiber which was then used in connection with a wearable in-field MRI receiver. Out-of-bore [167] or in-bore [156] digital optical fiber transmission experiments were conducted with standard small form-factor pluggable (SFP) or similar transceivers that can achieve data rates of several Gbps but presumably contain some ferro- or paramagnetic parts (e.g. housing). A thorough component search identified solutions dedicated for use in MRI are proposed by Firecomms and Molex [168,169]. Non-magnetic transceivers based on RCLED (Resonant Cavity Light-Emitting Diode) transmitter technology are available for data rates up to 250 Mbps.

3.2.2.2 Wireless transmission

Even if optical fibers can be assembled to thinner bundles than coaxial cables and do not need common mode traps as they are not conductive, they still limit handling and do not allow for a truly wearable MR device solution. Therefore, the goal of implementing wireless data transfer in MR seems evident.

In Figure 3.3 an exemplary wireless MRI set-up is sketched. The spatial location of different building blocks that play a role for the development of wireless RF coils - wireless MR signals, control signals and power supply - is indicated. An ideally flexible

receive-only coil array is placed on the patient, as close as possible to the organ to be imaged. The patient is moved inside the bore and during MRI, the MR signal is acquired and pre-processed before it is wirelessly transmitted. It is necessary to send some control signals to the coil, for example for active detuning of the receive coil elements during RF transmission, and some on-coil components must be supplied with electrical power, ideally also wirelessly. The transmitted MR signal will be sent via free space to a wireless receiver, that can be located at different positions in the MR room or in the bore which is shown in *Article II* (Figure 1B), implying different required transmission distances. Ideally, the connection between the MR signal receiver and the technical cabinet, where the post-processing and MR image reconstruction takes place, is realized with optical fibers (white lines) to ensure immunity to EM interference.

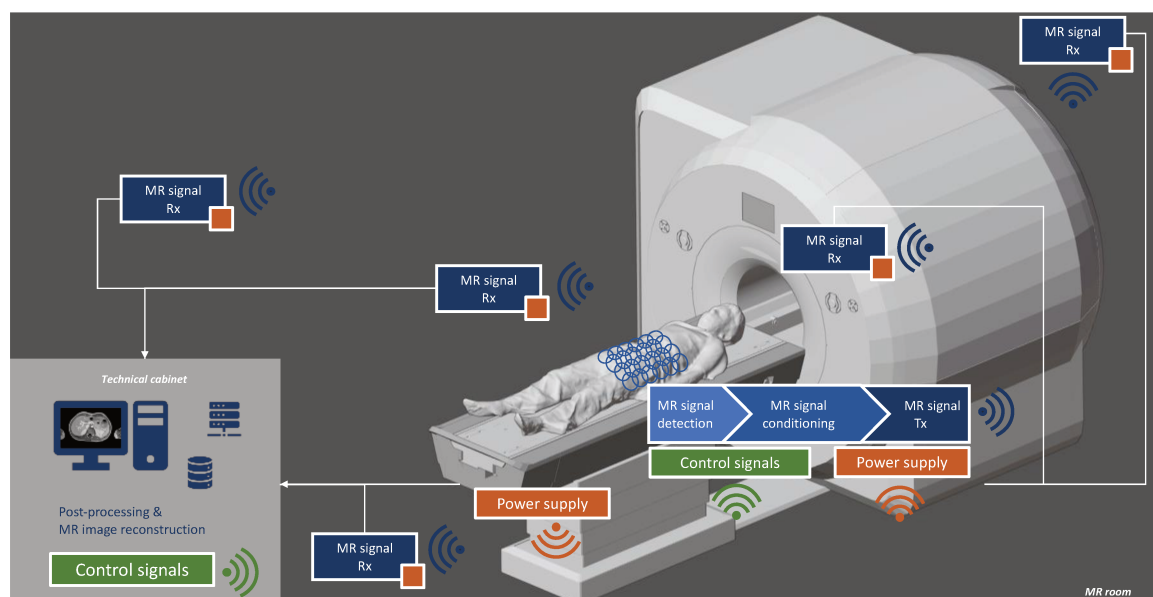


Figure 3.3: Wireless MR signal Rx chain overview

To cover all different possible variants of wireless transmission, i.e. analog or digital and RF wireless or OWC, the E/O (electrical-optical) and O/E (optical-electrical) conversion steps in Figure 3.1 and Figure 3.2 can be replaced by generic wireless transceivers. In *Article II*, several different digital wireless technologies, operating at Wi-Fi (Wireless Fidelity) frequencies (2.4-60 GHz carriers) or with OWC (THz carriers), and their suitability for MR signal transmission are discussed. In this section, at first some early publications on analog wireless MR signal transmission are revised to complement digital strategies discussed in *Article II*. Besides “flexibility”,

the keyword “optical wireless communication” is central in this thesis as this approach is proposed as a high-speed alternative to Wi-Fi for the future development of wireless RF coils. Furthermore, a prototype OWC module is presented in section 5.3.2. Therefore, the basics of optical wireless communication with digital signals and the relevance for wearable MRI will be explained more in detail.

3.2.2.2.1 Analog wireless transmission

In literature, inductively coupled coils [170] or RF field concentrators based on metamaterials [171,172] are sometimes presented as “wireless” coils. Although in principle this is correct as there is no direct wired connection from the RF coil or field concentrator to the MR scanner input, in case of inductive coupling, the sniffer loop is usually placed very close to the RF coil for high coupling efficiency and is related to the MR scanner input via coaxial cables. In case of using a metamaterial placed close to the ROI, the MR signal reception still has to be performed by the RF coil, conventionally with a tethered connection to the scanner. As a consequence, the whole set-up cannot be considered as a truly wireless solution.

Approaches where the MR signal itself is modulated or upconverted with an analog carrier of higher frequency, in the microwave (mostly low GHz) range, will be considered as analog wireless MR signal transmission methods here. In a US patent from 2003, Boskamp [173] describes the possibility of transmitting multiplexed analog MR signals with a 900 MHz carrier over free space. Heid *et al.* [174] and Martius *et al.* [175] use a microwave antenna array with parametric upconverters to establish a single frequency multiple input multiple output (MIMO) microwave link between a multi-channel coil and the MR scanner’s receiver electronics. Work by Scott *et al.* [176] or Riffe [177] using amplitude (AM) or single-sideband (SSB) modulation demonstrates the feasibility of analog wireless transmission at carriers from 800 MHz to 2.5 GHz but also underlines possible system issues. Analog modulation and multiplexing of analog Rx channels is challenging while keeping synchronicity to the MR system reference frequency and without interferences between channels. Furthermore, signal cancellations or phase shifts can occur due to patient motion or wireless antenna electronics can potentially be interrupted by locally induced electromagnetic fields during the application of high power RF

transmit pulses [139,178]. Compared to digital system implementations, an analog wireless system could possibly be advantageous for power, size, weight, and costs. Compared to the use of optical fibers and analog wireless Tx in the GHz range, optical analog free space transmission in the THz range could be more easily deployable than RF antennas and brings the advantage of immunity against RF interference. The use of a VCSEL and avalanche photodiode (APD) as analog OWC components combined with lenses is shown in [179] for the time-multiplexed analog signals of an MR compatible positron emission tomography detector front-end over 2 m distance. According to Refai *et al.* [180], an analog optical wireless signal chain can perform comparably to analog fiber transmission over short distances with a line-of-sight (LOS) between optical modules.

3.2.2.2.2 Digital wireless transmission

Digital wireless signals are more reliably transmitted over long distances and eliminate DR or signal stability concerns. However, bandwidth requirements for MR signals, especially considering directly digitized array data, push the limits of current Wi-Fi technology. A summary and discussion of different digital wireless approaches proposed for the free space transmission of MR signals, partially tested in-bore, are given in *Article II*.

3.2.2.2.2.1 Optical wireless communication (OWC)

An emerging alternative to Wi-Fi is the use of light in the infrared (IR), visible or ultraviolet (UV) range as information carrier [181,182]. Li-Fi (Light Fidelity) [183,184] has been introduced as a novel OWC high-speed networking approach, potentially replacing the currently wide-spread use of Wi-Fi in various underwater, space or terrestrial (indoor or outdoor) applications in the future.

For daily-life wireless networks, e.g. in offices, homes, public spaces, the advantage of Li-Fi in comparison to Wi-Fi is the possibility of integration in existing lighting infrastructure and as light does not penetrate walls, full data security is given as access is only possible within the coverage of the Li-Fi network. Also, the optical spectrum offers a large license-free bandwidth which is five orders of magnitude (100 000 times) wider than the entire RF spectrum, as indicated in Figure 3.4.

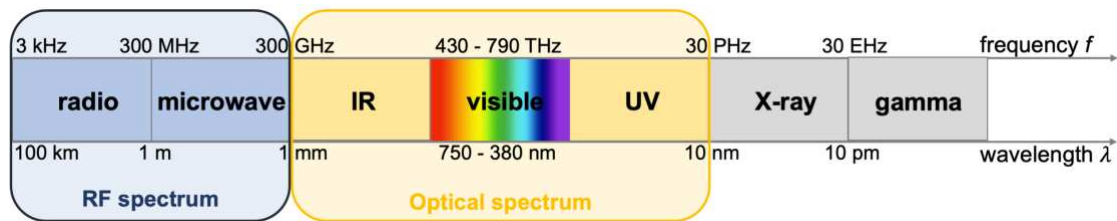


Figure 3.4: The electromagnetic spectrum. Note that the axis is not proportional.

Current Wi-Fi standards allow for data rates of up to multiple Gbps, e.g. using mm wave (60 GHz) technology and complex modulation schemes [165,185–187]. However, typical Wi-Fi technologies rather operate in the tens or hundreds of Mbps range. To cite some recent OWC data rate examples, Faulwaßer *et al.* [188] can be mentioned as they designed a short-range 10 Gbps bi-directional Li-Fi link with 850 nm near-IR lasers, clearly outperforming current Wi-Fi standards. In the visible light range, using 680 nm wavelength VSCEL transmitters, OWC over a distance of more than 10 m was demonstrated at a 2 Gbps rate with APDs [189] or up to 3 Gbps with a single PIN photodiode receiver [190]. With a single 400 nm micro LED, almost 8 Gbps were reached [191]. Tsonev *et al.* [192] transmitted data at more than 3 Gbps with an RGB (red, green, blue) laser triplet generating white light and discuss the feasibility of more than 100 Gbps performance. In the UV spectrum, a 260 nm micro-LED has been shown to be suitable for 1 Gbps link design [193]. Commercially available Li-Fi solutions exist but are in a rather early stage of being implemented for wireless networking in offices or for industrial use [194–197] and outdoor long distance laser communication links [198,199].

For MR signals, digital optical fiber signal transmission has already been demonstrated but OWC has not been implemented in-bore yet although it has been proposed in a US patent by Bulumulla *et al.* in 2007 [200]. A relevant advantage of OWC specifically for MR hardware is the fact that the THz frequency range does not overlap with the RF band and the data channel is therefore immune to interferences. Furthermore, OWC approaches rely on small low-power components, e.g. LEDs and PDs, to transmit signals over free space which is practical for on-coil integration. Achievable high data rates are interesting, especially for multi-channel applications with on-coil digitization of the MR signal. With OWC data rates, even the transmission of directly digitized data without on-coil data compression would be imaginable. While OWC transceivers could also be integrated in the MR room's lighting

infrastructure, the establishment of an often required LOS between transmitter and receiver for high-speed data transfer can become a challenge.

Comparable to RF wireless (Wi-Fi) networking, Haas *et al.* [182] proposed a model for the different communication system layers of OWC networks and list required technologies. This model is shown in Figure 3.5 and the outermost layers, “networking and protocols”, “interference mitigation and mobility support” and “medium access control” are the same as for Wi-Fi approaches as described in reference [182] but for the remaining layers, specific solutions for OWC exist. Some key concepts will be shortly explained below.

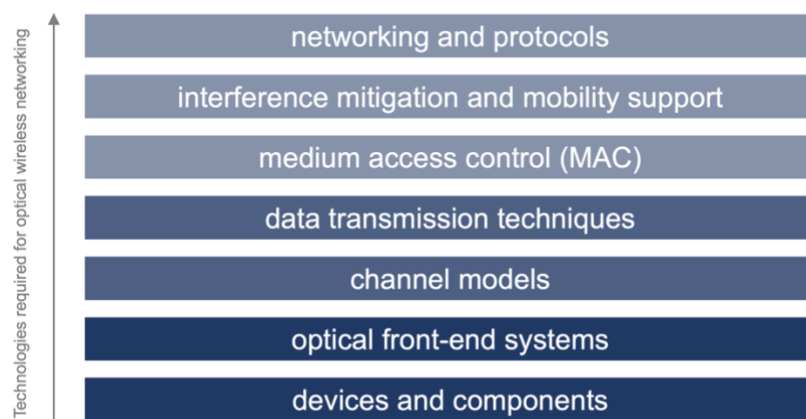


Figure 3.5: Required technologies for optical wireless networking, adapted from [182,201]

The “**data transmission techniques**” layer concerns encoding schemes and multiplexing strategies. For OWC systems, data is often encoded using simple non-return-to-zero (NRZ) on-off-keying (OOK), where the presence of the carrier for a certain duration represents a binary “1” and the absence for the same duration a binary “0”. As shown in Figure 3.6, with NRZ, only one transition between bits is required. Using Manchester encoding, a transition at the middle of each bit width is needed, which can be advantageous as the bit stream inherently contains clock data to synchronize receiver and transmitter. With NRZ encoding and long data transmissions of the same binary symbol, the recovery of the clock is not possible at all times.

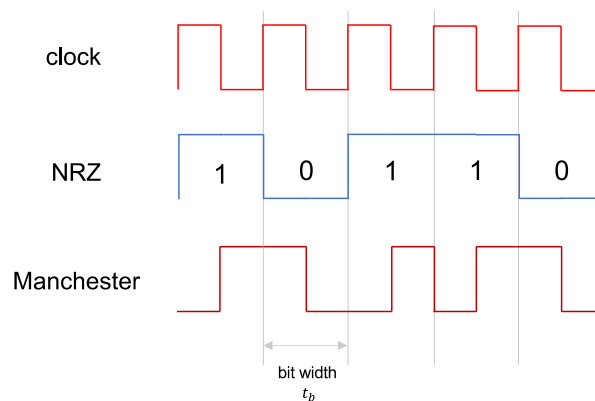


Figure 3.6: Encoding schemes

To overcome data rate limitations, multiplexing strategies can be implemented in an OWC system, either in the time, wavelength or spatial domain. As mentioned above for RGB LEDs, also RGB LEDs can be used as separate wavelength-division multiplexed (WDM) channels to increase achievable data rates as compared to the use of a single LED [202]. In the spatial domain, by properly setting the beam width and detection field of view, MIMO techniques using optical transmitter and detector arrays can be employed.

The “**channel models**” aspect describes the light propagation channel between transmitter and receiver. Channel models can be divided into direct LOS and non-line-of-sight (NLOS) approaches, the latter using one or multiple reflections of diffuse or focused light beams. With NLOS scenarios, reported possible transmission distances (depending on optical power at the receiver) and achievable data rates are lower than with LOS approaches [203].

“**Optical front-end systems**” can be employed in combination with the optical transmitter and receiver with the goal to optimize the OWC link characteristics, e.g. the spatial range or eye-safety. The optical equipment can help to form beam divergence or convergence with a concave or convex lens in the most basic set-up. Furthermore, dedicated optical wavelength filters can be employed to eliminate the influence of daylight or limit multi-channel interference.

OWC transceiver design considerations usually start with the choice of adequate “**devices and components**”. The optical transmitter and receiver as well as surrounding circuitry determine the achievable OWC data rate and transmission distance. Therefore, in the following, functioning principles and characteristics of

optical sources and detectors will be explained based on references [204–207] unless otherwise stated.

Optical transmitters

Semiconductor-based optical transmitters which take over the role of E/O conversion in OWC systems consist of a p-n junction, i.e. a p- and n-type semiconductor brought into contact. When a p-n junction is forward biased by an applied voltage, the diffusion of electrons and holes across the junction creates a current flow. In the depletion region (around the p-n junction), the electrons and electron holes can recombine through spontaneous or stimulated emission and emit photons, i.e. generate light. During recombination, electrons in the conduction band transition to the valence band and emit electromagnetic energy in the form of photons. The wavelength λ of the emitted light is a function of the band gap energy E_g which depends on the semiconductor materials used, given by

$$E_g = h\nu = \frac{hc_0}{\lambda} \quad \text{Eq. 3.2}$$

where h is Planck's constant, ν the photon frequency and c_0 the vacuum speed of light.

As illustrated in Figure 3.7, light emission can occur due to spontaneous emission as it is the case for LEDs, emitting incoherent light. Lasers are equipped with some optical gain medium and optical feedback method, e.g. an optical cavity, which leads to the stimulated emission of coherent light.

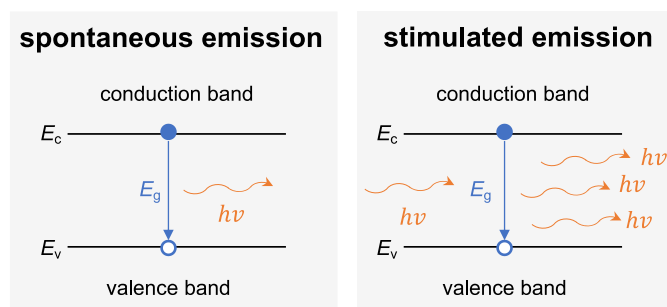


Figure 3.7: LED and laser functioning principle based on spontaneous and stimulated light emission

A comparison of aspects that are relevant for OWC and differentiate LEDs from semiconductor lasers is given in Table 3.3.

parameter	LED	laser
output power	low	high
radiant angle	wide	narrow
modulation bandwidth/speed	moderate	fast
power consumption	low-moderate	high
linearity	high	low
eye safety concerns	low	high
reliability/lifetime	high	moderate
cost	low	moderate-high

Table 3.3: Typical characteristics comparison between an LED and a semiconductor laser

Stimulated emission in lasers leads to higher **output power**, a narrow **radiant angle** as the beam is focused and it is therefore more suitable for wide-distance free space data transmission. In general, the intensity of a point light source approximately decreases with the square of the transmission distance, and the angular dependency of radiant sensitivity is often indicated by the angle of half intensity in optical transmitter data sheets.

Depending on the LED type used for OWC, the **modulation bandwidth**, i.e. the possible switching speed can vary. Generally, the LED frequency response is a function of the carrier lifetime t_c which describes the recombination dynamics of a semiconductor diode and depends on the LED type (surface- or edge-emitting), material and doping level of the semiconductor used. The modulation bandwidth, i.e. the 3 dB cut-off frequency at which the electrical power is half or reduced by 3 dB and at which the ratio of input to output current or input or output voltage drops by a factor of $\sqrt{0.5} = 0.707$, is determined by

$$f_{3\text{dB}} = \frac{1}{2\pi t_c} \quad \text{Eq. 3.3}$$

For component choice, usually not the carrier lifetime t_c but the rise t_r and fall time t_f of LEDs and PDs are indicated in data sheets and can be taken as a “conservative guideline” [204] for achievable modulation frequency and bit rate calculations in the design of OWC systems. The rise time t_r is defined as the time during which the response increases from 10 % to 90 % of its final output value when the input is changed abruptly. For LEDs, t_r is the time over which the emitted optical power builds up from 10 % to 90 % of its final value when the incident current is changed abruptly. For PDs, t_r is the time over which the current builds up from 10 % to 90 % of its final

value when the incident optical power is changed abruptly. Conversely, fall times describe the time for the transition from 90 % to 10 %.

The inverse relationship between the bandwidth and the rise/fall time $t_{r/f}$ can be explained by considering a simple RC circuit as a suitable equivalent model for the optical component. The time constant $\tau = RC$ of this system has the following relation to the component's rise time:

$$t_r = (\ln 9)\tau \quad \text{Eq. 3.4}$$

From the above-mentioned equation for the 3 dB cut-off frequency (Eq. 3.3), one can approximate:

$$f_{3\text{dB}} = \frac{1}{2\pi\tau} = \frac{\ln 9}{2\pi\tau} \approx \frac{0.35}{t_{r/f}} \text{ or } \approx \frac{0.7}{(t_r+t_f)} \text{ (assuming } t_r = t_f) \quad \text{Eq. 3.5}$$

The upper limit for the achievable bit rate ($B = \frac{1}{t_b}$, [bps]) depends on the encoding scheme used (examples are given in Figure 3.6) and the modulation frequency or rise/fall time characteristics (Eq. 3.5). For NRZ encoding, as the pulse width which is needed to represent one bit equals the bit width (see Figure 3.6), the criterion for the required rise/fall time is:

$$t_{r/f} \leq 0.7t_b \text{ or } t_{r/f} \leq \frac{0.7}{B} \quad \text{Eq. 3.6}$$

If t_r equals t_f , this means that $B = 2 \cdot f_{3\text{dB}}$.

With Manchester encoding, due to one transition at the middle of each bit width, some pulse widths are reduced to half the length ($t_b/2$) as with NRZ encoding. Therefore, the required rise/fall time is:

$$t_{r/f} \leq 0.35t_b \text{ or } t_{r/f} \leq \frac{0.35}{B} \quad \text{Eq. 3.7}$$

With equal rise and fall time, $B = f_{3\text{dB}}$. In short, this means that for specific rise/fall time characteristics of an optical transmission system, the effective data rate achievable with Manchester encoding is half compared to the one that can be reached with NRZ.

Typically, "direct emission" LEDs emitting light directly from the diode junction can have a rise/fall time of a few ns. Most common LED switching speeds do not exceed tens to hundreds of MHz [182,204]. Indirect emission LEDs, e.g. white phosphor LEDs, transform the LEDs monochromatic light into a broader spectrum by excitation of phosphors. Due to needed time for excitation, achievable switching speeds are lower.

RGB LEDs are therefore often preferred in the visible light spectrum as they have faster modulation speeds, allow for WDM and create white light that can be used for illumination purposes. Some special-purpose LEDs, e.g. RCLEDs allow for the emission of even shorter pulses.

The 3 dB modulation frequency or bit rate calculation based only on the LED or PD rise time is an overestimation as other factors than the LED's or PD's inherent characteristics can lower the optical system's switching speed. The total system rise time can be increased by the transmitting and receiving circuitry, e.g. due to the inductance of long traces or parasitic capacitances. Temperature or drive-current dependent non-linearities of various components in the signal chain (LEDs, amplifier, PDs) and high needed forward voltages of the LED can also decrease the achievable speed in practice. IR LEDs typically have the lowest forward voltages, and thus, are suitable for high-speed applications.

The system rise time t_{system} is calculated by the square root of sum of squares of individual components' rise/fall times. For simplicity, t is used instead of $t_{r/f}$. The indices are "Txc" for transmitter circuitry, "Tx" for transmitter (LED or laser), "Rx" for receiver (PD), "Rxc" for receiver circuitry (e.g. amplifiers, comparators). The index "OWC" expresses the optical wireless link influence on the achievable data rate which can suffer from attenuation, ambient light noise, multi-path propagation and dispersion causing inter-symbol interference [208].

$$t_{\text{system}} = \sqrt{t_{\text{Txc}}^2 + t_{\text{Tx}}^2 + t_{\text{Rx}}^2 + t_{\text{Rxc}}^2 + t_{\text{OWC}}^2} \quad \text{Eq. 3.8}$$

Lasers can be modulated at higher frequencies (GHz range) because of short recombination times associated with the stimulated light emission. Therefore, lasers are used in applications where high data rates are required. As shown in the graph in Figure 3.8, the laser threshold current ($I_{\text{threshold}}$) and therefore **power consumption** is higher than LED drive currents. LEDs provide higher **linearity** over a large range of drive currents than lasers which in practice show linear behavior only in a limited range above their threshold current. Usually, heating will also lead to non-linear behavior of LEDs and laser diodes. Amongst a large variety of different laser types, the VCSEL is interesting for OWC in general but also for use in MRI. A VCSEL emits light in a direction perpendicular to the active-layer plane. It is a high-speed optical transmitter option that has a small form factor, and low power requirements.

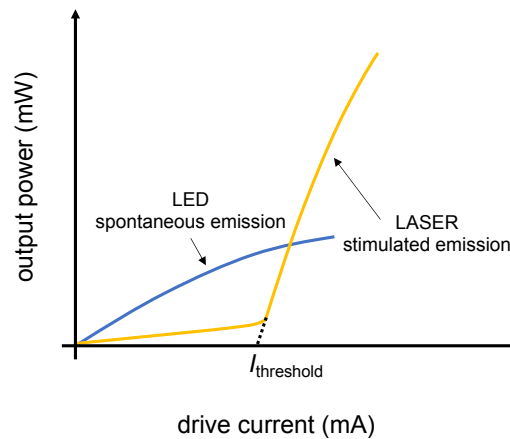


Figure 3.8: LED vs. laser linearity and output power depending on drive current, adapted from [206]

The aspect of **eye-safety** is important considering that focused light on the retina of the human eye can cause local heating and permanent damage. Eye safety concerns for laser light are higher than for same power LED light [209,210] because collimated laser beams make small spots with higher light intensity possible. The human eye can see wavelengths (perceived as different colors) approximately between 400 and 700 nm but is also transparent to light in the IR range. IR wavelengths < 1400 nm can pass through the cornea and lens of the eye while wavelengths > 1400 nm are absorbed [211]. This means that e.g. IR lasers in the 1550 nm range can operate at much higher intensities for far-range and high data rate communication in comparison to other IR lasers near 800 nm.

For reliable, economical OWC systems, the **lifetime and cost** of optical components is decisive. Due to the more complex laser structure, higher operating currents and possible heating which can require active cooling (e.g. with thermoelectric elements), lasers tend to be less robust, they have a shorter lifetime and are usually more expensive than LEDs.

Optical receivers

Optical receivers are the second main component in an OWC system, responsible for O/E conversion, i.e. for the detection of light intensity changes. Photodetectors which consist of a reverse biased p-n semiconductor junction in their most basic form convert light into electrical current based on optical absorption, sketched in Figure 3.9.

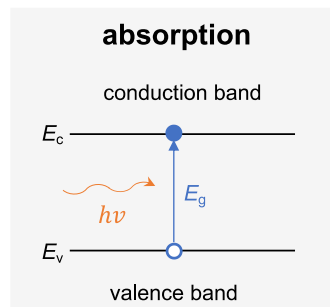


Figure 3.9: Photodiode functioning principle based on optical absorption

If the energy of absorbed photons ($h\nu$) in the depletion region is higher than the bandgap energy, an electron-hole pair is generated. Consequently, due to the creation of an electric field, electrons and holes move across the semiconductor resulting in a current flow, i.e. the photocurrent I_p . Typically, photocurrents are low and require amplification. I_p is directly proportional to the incident optical power P_{opt} . The ratio between I_p and P_{opt} is the photodiode's responsivity in A/W.

Besides the responsivity, typical PD characteristics include the wavelength of peak sensitivity which depends on the PD material and should be matched to the transmitter's peak wavelength. Further, the radiant characteristics should be in accordance with the needs of the OWC system, i.e. when a divergent light beam is used, the radiant sensitivity of the PD ideally is large. By the application of a reverse bias voltage, the PD is operated in photoconductive mode, which results in faster response times but also a dark current, i.e. a current generated through the diode without light applied (usually in the nA range) which sets a lower limit for the detectable optical power. The PD's frequency response time depending on its rise and fall time and the role for the system rise time have been discussed together with LED switching speeds above.

Photodiodes with an additional intrinsic, undoped i-layer in between p- and n-type semiconductor (PIN diodes) are commonly used as photodetectors as they have a

larger depletion region and therefore increase the responsivity and the frequency response. APDs generate multiple electron-hole pairs per photon due to the avalanche effect. Therefore, APDs have an even higher responsivity than a PIN photodiode. However, APDs require a higher reverse bias voltage and usually come at higher cost. This condensed summary of OWC fundamentals will serve as a basis for describing the prototype OWC transceiver design in section 5.3 and for further discussions on the implementation of OWC in MRI.

3.2.2.3 Low power electronics

Besides the development of flexible and wireless MR hardware solutions, the difficulty of providing wireless power supply for this hardware is of major concern for the future of wearable MR devices. In *Article II*, the issues with DC cables or battery power in MR are discussed and some alternative wireless strategies are mentioned alongside with exemplary wireless RF coil power budget calculations. To limit the needed power for wearable MR devices in the first place, the choice of implemented electronics has to be carefully made. For wireless RF coils this especially concerns:

- the preamplifier (e.g. 70 mW, Hi-Q.A. Inc. Carleton Place, Ontario, Canada),
- the ADC architecture (e.g. 70 mW/channel, ADS52J65, [159]),
- the FPGA (e.g. 210 mW, Artix-7, Xilinx, San Jose, CA, USA, [212]),
- detuning switches with negligible power consumption (e.g. low voltage-controlled GaN FETs (Gallium nitride field effect transistors) instead of PIN diodes, [213]),
- a PLL for synchronization (e.g. 35 mW, [155]),
- the wireless transceivers and surrounding circuitry. An ambitious 200-250 mW/channel, comparable to values reported for commercial high-speed optical fiber transceivers [168,169] is assumed. Custom-built solutions could yield lower power consumptions < 100 mW [156,166] but for OWC, probably the needed optical power and therefore total power consumption increases.

Omitting additional gain stages or additional components that might be needed for example for clocking circuitry or when using other MR receiver architectures, the total estimated power consumption easily adds up to more than 0.5-1 W per channel.

Often, for on-coil electronics integration in MR, a trade-off between high performance and power consumption has to be found. For example, a suitable alternative to readily available large power consuming Wi-Fi antennas has been proposed for short distances using a 60 GHz mm wave link [165]. Another sophisticated low-power option is the receiver integrated circuit published by Sporrer *et al.* [155], consuming less than 240 mW/channel for signal down-conversion, digitization and components dedicated to synchronization but doesn't include optical or wireless transceiver power consumption. In the design of an in-bore receiver described by Reber *et al.* [156], a higher required power consumption of ≈ 1.5 W/channel was reported (including optical fiber transceiver) which can lead to very high power demands if this receiver solution is scaled up to be used with 64 coil channels (resulting in 96 W).

Also, the amount of additional sensors that can be employed in parallel with MRI or the duration of sensor operation, e.g. for motion detection and correction (30-40 mW/sensor [11,214]), depends on the available wireless power capacity.

The main challenges for the removal of cabling, applicable to all wearable MR devices and concerning data transmission or power supply, can be summarized in the aspects listed below and are further discussed in *Article II*:

- correct representation and transfer of data (MR signal, sensor signals) with other methods than conventional coaxial cables (analog/digital, optical fiber/OWC or RF wireless),
- limited availability of MR compatible components,
- the need for wireless power solutions and low power electronics,
- potential interference of multiple wireless devices in parallel to MR, e.g the RF coil, sensors, power supply and B_0 shim or detuning control.

3.2.3 In vivo usability

In addition to the above-mentioned technological aspects, some other important aspects concerning patient safety, comfort, or medical product certification have to be taken into account for the usage of an ideally wearable, i.e. flexible and wireless MR device in vivo.

3.2.3.1 Lightweight and ergonomics

The motivation for developing lightweight ergonomic MR devices is the improvement of patient comfort and ease of handling. For RF coils, ergonomic design can be achieved by miniaturization of the coil electronics and adaptation of the shape of the flexible coil to the one of normal clothing. The arrangement of RF coil elements on flexible or stretchable support materials has been demonstrated for a knee bandage or athletic pants [134,138], a sports bra [129], a patient cloth-like shirt [115] or gloves [55,122]. Ergonomic design facilitates handling for the coil operator but could also render the MR workflow more efficient if the patient is able to safely put on the coil in the changing room without assistance. Individual coil sizes could further improve comfort and optimize form-fitting for applications where patient anatomy size varies strongly.

While small sensors used in MR usually have negligible weight, the RF coil weight can vary largely. Conventional large multi-channel arrays with rigid housing and many on-coil electronics, e.g. the preamplifier located as close as possible to the coil's output and cable traps, are bulky and heavy. Some MR scanner vendors propose flexible lightweight coil arrays. One widely used example is the Siemens 4-channel "flex coil" [215] which is commercialized in a "small" and "large" version. The latter is dedicated to shoulder, knee or hip imaging, has the dimensions 51.6 cm x 22.4 cm and weighs 550 g in total (4.8 kg/m²) for the coil only, i.e. the weight on the patient without cable and coil plug connector.

Another flexible lightweight coil array is currently under development at the Medical University of Vienna using single-turn single-gap coaxial coils with miniaturized PCB layout and components [216]. In the final array version, coils will be similarly arranged as in the previously published 3-channel array [119] with overlapping 8 cm diameter coils. The extrapolated total weight of a 28-channel coaxial coil array

version with the interface PCB enclosed in a custom 3D-printed housing, cable traps, fixation straps, different textile layers and estimated maximum dimensions of 60 cm x 30 cm is only ≈ 1.3 kg (7.2 kg/m²). Cable connections to the coil plug, again equipped with some cable traps, will add weight but not necessarily on-patient as these cables are located at one end of the coil and routed along the patient bed.

With a flexible but not wireless coil as described above, i.e. with conventional coaxial cable MR signal transmission, there is still room for improvement in terms of weight reduction. Commonly used cable traps encapsulated in bulky 3D printed housing could be replaced by novel approaches for lighter and more flexible cable trap construction, e.g. the “caterpillar trap” [217] or miniaturized “inverted cable traps” [218].

Challenges with lightweight and flexible materials can be encountered when attaching the coils to the support material so that a rather stable coil position is ensured with regard to overlap while still providing full flexibility. Further, the coil’s mechanical robustness and performance with different bending scenarios have to be investigated, even more carefully when the goal is that the coil is not only handled by the coil operator but also patients.

3.2.3.2 Suitable materials

The choice of coil support and fabrication materials has an effect on overall coil flexibility, weight, safety and hygiene for *in vivo* use.

Suitable materials can either be a thin layer of flexible substrate (e.g. for screen-printed coils) or stretchable textile (e.g. for liquid metal or coaxial coils). The support material should offer the desired flexibility and stretchability with respect to the target application but also account for the coil’s robustness upon bending or stretching. The coils can be fixed at certain positions to their support material, e.g. for strain relief to prevent mechanical damage of soldering upon bending.

To contain the coils and provide electrical isolation, for flexible coils, different layers of thin stretchable or flexible material can be sewn together. One approach is to create textile pouches to insert the coils as has been shown for liquid metal or conductive elastomer coils [134,138]. Coaxial coils can be sewn onto or woven into some padding layer, as shown by Obermann *et al.* [119] and, for *in vivo* use, the coil array should additionally be surrounded by surface material that is easily cleanable and splash-

water resistant, e.g. synthetic medical leather. Semi-flexible coils can be combined with small rigid 3D-printed housing parts (e.g. biocompatible polyamide, [104]) to protect electronics and are then assembled with flexible materials to allow for form-fitting to the patient's anatomy. For medical products and in vivo use, the used materials must be in conformity with applicable standards imposed by the IEC but also the United States Food and Drug Administration (FDA) and the EU regulation 2017/745 on medical devices. Example requirements are biocompatibility, non-inflammability and resistance to disinfectants. For routine use, materials should also ideally be tearproof and have a long lifetime.

3.2.3.3 Safety

With both, rigid or wearable MR technology, the patient safety aspect is of great importance for in vivo use. While in general, MRI can be considered as a safe imaging modality, some risks remain. A recently published 10-year FDA report on adverse events that occurred in the MR environment [219] analyzed approximately 1550 event reports in total. Out of all reported MRI-related adverse events, 59 % were of thermal, 11 % of mechanical and 9 % of projectile nature. Within the thermal events that were produced due to "contact with an object", MRI coils and cables were cited in the first place (54 %) for the cause of burn injuries. ECG electrodes or leads, patient clothing and pulse oximeters are other examples of objects that can be involved in thermal events. Detailed event descriptions mention that burn injuries were caused when (third party or vendor) coils were routed over the patient, when there was direct contact between patients and coil cables or baluns, or when only thin sheets or blankets were used for padding. SAR and heating issues and IEC/FDA limits were discussed in the theoretical background section 2.2.5.4. To prevent potential thermal events, it has to be ensured that legal limits and regulations for medical devices are respected [65,220]. This can become challenging with flexible coil design as E fields superimpose depending on the coil position and, therefore, the SAR distribution has to be investigated for different coil positioning and bending scenarios. Furthermore, additional electronics on-coil, e.g. wireless transceivers, digitization components or physiological sensors, could potentially heat up during long operation or lead to local heating induced by RF transmission. Coupling between the RF transmit field and the Rx coil elements or cables has to be suppressed by

detuning circuits and cable traps. Electrical contact of wearable electronics and cables with the patient has to be avoided and, obviously, moving or loose ferromagnetic parts that could lead to “projectile” effects must not be part of a wearable MR device.

3.3 Conclusion

To conclude this chapter, two main aspects were identified to be amongst the most needed technological advances, indispensable for the emergence of wearable MR technology:

- The development of flexible lightweight RF coils and coil arrays.
- Strategies for wireless signal and power transmission in the MR environment.

The following chapters of this thesis each focus on the study of one of the above-mentioned aspects:

Study I: Flexible radio frequency coils

This study describes “Flexible multi-turn multi-gap coaxial RF coils: design concept and implementation for Magnetic Resonance Imaging at 3 and 7 Tesla” (*Article I*) published in *IEEE Transactions on Medical Imaging* [9]. A supplementary studies chapter includes additional results from analytical calculations, EM simulations, bench tests and MR imaging with coaxial coils.

Study II: Wireless Data Transmission in MR

A published article (*Article II*) in *Frontiers in Physics* elucidates the “Perspectives in Wireless Radio Frequency Coil Development for Magnetic Resonance Imaging” [10] and supplementary studies are concerned with the development of an OWC module prototype, optical FOV simulations and a test summary for OWC modules in MR.

4. Study I: Flexible radio frequency coils

4.1 Prelude

The outline of different flexible and stretchable RF coil fabrication techniques has demonstrated the growing interest in conformal RF coils and coil arrays in the MR hardware research community. Amongst recent publications, especially the investigation of coaxial cables as flexible coil conductors stands out.

While the basic design concept of coaxial transmission line resonators has been introduced in some early MRI-related publications [51,52], only in 2018 Zhang *et al.* [55] presented the benefits of a multi-channel MRI glove coil constructed out of single-turn single-gap coaxial loops in comparison to rigid standard coil arrays. The aim was to explore and understand the characteristics and the performance of coils fabricated of non-magnetic coaxial cables more deeply. More specifically, the focus of this work was to extend the possible coil dimensions and overcome the limits encountered with single-turn single-gap CCs. The overall goal of the study presented in *Article I* was to investigate multi-turn multi-gap (MTMG) coaxial coils. To this end, an equivalent circuit has been modelled and the coil behavior has been examined using EM simulations. It has been investigated whether coaxial coils offer a competitive alternative to standard rigid coils in terms of SNR, transmit efficiency and local SAR. This resulted in a proof-of-concept of employing MTMG-CCs as flexible RF coil elements in 3 T and 7 T MRI.

4.2 ***Article I: Flexible multi-turn multi-gap coaxial RF coils: design concept and implementation for Magnetic Resonance Imaging at 3 and 7 T***

This chapter is an exact replica of the article entitled “Flexible multi-turn multi-gap coaxial RF coils: design concept and implementation for Magnetic Resonance Imaging at 3 and 7 Tesla” [9], accepted for publication in *IEEE Transactions on Medical Imaging* (early access version published on January 13th, 2021). This work is licensed under a Creative Commons Attribution 4.0 License (<https://creativecommons.org/licenses/by/4.0/>).

Citation information: DOI 10.1109/TMI.2021.3051390

Flexible Multi-Turn Multi-Gap Coaxial RF Coils: Design Concept and Implementation for Magnetic Resonance Imaging at 3 and 7 Tesla

Lena Nohava¹, Associate Member, IEEE, Raphaela Czerny, Sigrun Roat², Michael Obermann, Andre Kuehne, Roberta Frass-Kriegl, Jacques Felblinger³, Member, IEEE, Jean-Christophe Ginefri, and Elmar Laistler⁴

Abstract—Magnetic resonance has become a backbone of medical imaging but suffers from inherently low sensitivity. This can be alleviated by improved radio frequency (RF) coils. Multi-turn multi-gap coaxial coils (MTMG-CCs) introduced in this work are flexible, form-fitting RF coils extending the concept of the single-turn single-gap CC by introducing multiple cable turns and/or gaps. It is demonstrated that this enables free choice of the coil diameter, and thus, optimizing it for the application to a certain anatomical site, while operating at the self-resonance frequency. An equivalent circuit for MTMG-CCs is modeled to predict their resonance frequency. Possible configurations regarding size, number of turns and gaps, and cable types for different B_0 field strengths are calculated. Standard copper wire loop coils (SCs) and flexible CCs made from commercial coaxial cable were fabricated as receive-only coils for 3 T and transmit/receive coils at 7 T with diameters

between 4 and 15 cm. Electromagnetic simulations are used to investigate the currents on MTMG-CCs, and demonstrate comparable specific absorption rate of 7 T CCs and SCs. Signal-to-noise ratio (SNR), transmit efficiency, and active detuning performance of CCs were compared in bench tests and MR experiments. For the form-fitted receive-only CCs at 3 T no significant SNR degradation was found as compared to flat SCs on a balloon phantom. Form-fitted transmit/receive CCs at 7 T showed higher transmit efficiency and SNR. MTMG-CCs can be sized to optimize sensitivity, are flexible and lightweight, and could therefore enable the fabrication of wearable coils with improved patient comfort.

Index Terms—Coaxial cable, flexibility, magnetic resonance imaging (MRI), MR physics, radio frequency (RF) coils, transmission line resonator (TLR).

Manuscript received October 14, 2020; revised November 21, 2020; accepted January 9, 2021. This work was supported in part by the Agence Nationale de Recherche (ANR) and Austrian Science Fund (FWF): I-3618 and in part by the Austrian/French OeAD/MAEE Project WTZ/PHC Amadée under Grant FR03/2018. (Corresponding author: Elmar Laistler.)

Lena Nohava is with the High Field MR Center, Center for Medical Physics and Biomedical Engineering, Medical University of Vienna, 1090 Vienna, Austria, and also with the Laboratoire d'Imagerie Biomédicale Multimodale Paris Saclay (BioMaps), CEA, CNRS, Inserm, Université Paris-Saclay, 91401 Orsay, France (e-mail: lena.nohava@meduniwien.ac.at).

Raphaela Czerny, Sigrun Roat, Michael Obermann, Roberta Frass-Kriegl, and Elmar Laistler are with the High Field MR Center, Center for Medical Physics and Biomedical Engineering, Medical University of Vienna, 1090 Vienna, Austria (e-mail: raphaela.czerny@gmail.com; sigrun.roat@meduniwien.ac.at; michael.obermann@meduniwien.ac.at; roberta.frass@meduniwien.ac.at; elmar.laistler@meduniwien.ac.at).

Andre Kuehne is with MRI.TOOLS GmbH, 13125 Berlin, Germany (e-mail: kuehne@mritools.de).

Jacques Felblinger is with the Inserm, IADI, Université de Lorraine, 54000 Nancy, France (e-mail: j.felblinger@chru-nancy.fr).

Jean-Christophe Ginefri is with the Laboratoire d'Imagerie Biomédicale Multimodale Paris Saclay (BioMaps), CEA, CNRS, Inserm, Université Paris-Saclay, 91401 Orsay, France (e-mail: jean-christophe.ginefri@universite-paris-saclay.fr).

This article has supplementary material provided by the authors and color versions of one or more figures available at <https://doi.org/10.1109/TMI.2021.3051390>.

Digital Object Identifier 10.1109/TMI.2021.3051390

I. INTRODUCTION

IN MAGNETIC resonance imaging (MRI), radio frequency (RF) coils are used to excite the nuclear magnetic moments, and to receive the MR signal at the Larmor frequency (f_{Larmor}) which is proportional to the static magnetic field (B_0). RF coils can be operated in receive-only mode if a separate transmit coil is available. For clinical MRI systems up to 3 T, this is a high-power body coil incorporated in the scanner bore. At ultra-high field (UHF, ≥ 7 T) [1]–[3], no such whole-body transmit coils are available. Therefore, transmit/receive (Tx/Rx) coils are often employed at UHF. In general, the target field of view (FOV) and penetration depth p determine the optimal coil size to be chosen for a certain biomedical application. Assuming a lossless circular coil, the coil diameter d_0 should equal $\frac{2p}{\sqrt{5}} \approx p$ to achieve optimal SNR in depth p inside a uniformly conductive sample [4]. Proximity to the target tissue is key for high magnetic coupling, resulting in high receive sensitivity and transmit efficiency. A high filling factor with the RF coil placed close to the sample results in less variation in coil performance due to varying loading conditions between different subjects and/or applications. Coils form-fitted to the average anatomy, e.g. for the human head, breast, calf or finger [5]–[8], have already been implemented with rigid

housings. However, weight, size and flexibility restrictions as well as suboptimal form-fitting in some cases are the drawbacks of these coils.

Flexible and stretchable RF coils are of great interest, as they can be closely fitted to the anatomy. The degree of flexibility depends on the respective design approach. Some investigations focused on coils with mechanically adjustable rigid or semi-flexible housing parts that can be wrapped around a 2D curved body contour [9]–[16]. Further improvement in flexibility was reached with printed and stitched coils on flexible substrate or even elastic textile. Screen-printed MRI coils [17] developed by Corea *et al.* have shown to be a reliable alternative to bulky conventional coils with comparable SNR, suitable especially for pediatric imaging [18]. Stretchable Rx coils produced with copper braids [19], [20], meandered conductors [21], liquid metal printed into neoprene support material [22], liquid metal filled tubes [23], [24] or conductive elastomers [25] mostly target wrist or knee imaging and offer a truly wearable solution.

In other studies targeting the fabrication of flexible RF coils, transmission line resonator (TLR) technology has been extensively employed [26]–[38]. All these approaches have in common that they are formed by at least two transmission line segments separated by gaps in one of the conductors. The TLR self-resonance is determined by the coil geometry and material properties (loop diameter, wire and substrate width, number of conductor turns and gaps, dielectric permittivity, etc.). In contrast to printed or braided copper structures, the advantage of self-resonant TLRs is that, ideally, e.g. when inductively matched and used in Tx/Rx mode, no lumped components with solder joints adding rigidity and losses are required. With capacitive matching and cabled connection to the MR system and depending on the coil function (Tx/Rx or Rx-only), still, some lumped components, e.g. for active detuning, are required either at the coil feed port or along the coil conductor. Initial MRI experiments with single parallel-plate TLR elements by Gonord *et al.* were conducted using a rigid dielectric substrate with a single-turn single-gap (1T1G) conductor deposited on both sides of the dielectric [39]. This was continued by the introduction of single-turn multi-gap (1TMG) TLR design to allow for larger coil diameters at UHF and multi-turn single-gap (MT1G) TLR design for small coils at UHF [40], [41]. So far, different flexible implementations of parallel-plate TLRs have been proposed: Ginefri *et al.* used small implantable multi-turn single-gap TLRs printed on a polymeric layer for rat brain MRI at 7 T [31]. Frass-Kriegl *et al.* extended the design to multi-turn multi-gap (MTMG) TLRs (MTMG-TLRs) which considerably increased the degree of freedom in parallel-plate TLR design [32]. Flexible coil arrays for 7 T were fabricated with single-turn multi-gap TLRs [13], [16]. Recently, a TLR structure of two parallel wire conductors encapsulated in a thin loop of dielectric material was proposed by Stormont *et al.*, which can be employed in blanket-like arrays [37].

Coaxial cable TLRs – with inner and outer conductor (cable shield) separated by a dielectric and gaps intersecting both conductors on opposite sides as for parallel-plate TLRs – have

already been proposed as self-resonant RF coils by Zabel *et al.* for 1.5 T and Haziza *et al.* for low field [26], [27] and have recently been patented [33]. Equally as the embedded parallel-line TLRs in [37], coaxial coils (CCs) provide higher flexibility than parallel-plate TLRs; since they can be bent along a 3D curved body contour and therefore ideally form-fitted to the anatomy of interest, even with large inter-subject variability. Further, lightweight wearable array design and imaging of moving body parts becomes possible. CCs are especially interesting as some of the challenges arising in flexible coil development seem to be alleviated: they demonstrate robustness against coil deformation, load variation and inter-element coupling (overlap change) in an array configuration [29], [34], [38]. The re-occurring research interest in coaxial coil design has clearly been inspired by previous work on “shielded loop” (surface) [42], [43] and “coaxial cavity” (volume) resonators [44].

In 2018, Zhang *et al.* proposed 1T1G – “high impedance” – surface CCs to fabricate a wearable glove receive-array for 3 T MRI [34]. As the self-resonance frequency of a 1T1G-CC is given by the coil diameter and the properties of the chosen coaxial structure, the coil design is limited to one specific coil diameter in order to tune the self-resonance of the CC to the desired Larmor frequency. In the supplementary material of [34], the possibility to slightly vary the coil diameter with different cable properties, i.e. the dielectric constant of the substrate, cable thickness and characteristic cable impedance (depending on the ratio between outer and inner conductor thickness) is shortly discussed. No strict criteria to maintain flexibility were applied, i.e. also rigid dielectrics and cable thicknesses > 1 cm were considered, but still, the range of accessible diameters was very limited and not necessarily the optimum for a given anatomical application. With 1T1G-CCs, e.g. ^1H MRI of the breast can be realized at 3 T with a required coil diameter of approximately 8-10 cm to achieve the desired penetration depth. However, at 7 T, the 1T1G-CC diameter is restricted to a maximum of around 4-6 cm which can be suitable for human wrist/hand MRI or ex-vivo small animal imaging [30], [36] whereas at 1.5 T, the 1T1G-CC diameter is constrained to a minimum of 14-23 cm, only suitable e.g. for abdomen or pelvis imaging [35].

The purpose of this work is to explore the size limits of 1T1G-CCs and introduce and examine the extended design concept of coaxial coils with more than one gap and/or cable turns – multi-turn multi-gap CCs (MTMG-CCs) – as proposed by Laistler and Moser [45]. Some publications have suggested [46] or proven [29] the feasibility of introducing multiple gaps (at arbitrary positions) in the coaxial coil conductor to tune the surface coil to a desired resonance frequency. However, to the knowledge of the authors, this approach has never been investigated more systematically. Based on parallel-plate MTMG-TLRs [32], the goal is to increase the degrees of freedom in coaxial coil design, i.e. to allow for free choice of the CC diameter at any B_0 field to optimize the coil elements for the target application, which is not possible with 1T1G-CCs.

II. MATERIALS AND METHODS

A. MTMG-CC Design Theory

In Fig. 1a, examples of CC layouts showing equidistant inner and outer gap positioning with one or multiple turns and/or gaps are given. The coil and cable parameters are specified in Fig. 1b and the equivalent circuit of a CC with an arbitrary number of turns and gaps is sketched in Fig. 1c.

In order to design and fabricate a CC, self-resonant at the target Larmor frequency, it is useful to formulate the resonance condition based on an equivalent circuit model. In measurements, the self-resonance can be determined inductively with a pick-up probe; in that case the CC can be seen as a series resonant circuit consisting of the impedances of the transmission line segments, and the inductance and resistance of the outer surface of the coax shield.

It is noteworthy that in a CC three distinct conductor parts can be identified, as illustrated in Fig. 1b: iC , the surface of the inner conductor; oCi , the inner surface of the outer conductor, and oCo , the outer surface of the outer conductor. The latter two are separated due to the skin effect at high frequencies and are only connected at the outer gaps. This way, the CC can be seen as transmission line segments formed by iC and oCi , interconnected via the inductance represented by oCo .

The total impedance Z_{tot} can, therefore, be estimated by the following equations:

$$X_{\text{shield}}(\omega) = n_t^2 \omega \mu_0 \frac{d_0}{2} \left[\ln \left(\frac{8d_0}{d_1} \right) - 2 \right] \quad (1)$$

$$X_{\text{TL}}(\omega) = -Z_0 \cot \left(\frac{\omega l \sqrt{\epsilon_r}}{c_0} \right) \quad (2)$$

$$Z_{\text{tot}}(\omega) = R + i (X_{\text{shield}}(\omega) + 2n_g X_{\text{TL}}(\omega)) \quad (3)$$

The inductive reactance X_{shield} is the classical approximation of the inductance of a conductive loop of the same diameter and thickness as oCo and is proportional to the squared number of turns (n_t) of the coaxial cable. The reactance X_{TL} of each transmission line segment is calculated with the classical formula for a lossless open-ended coaxial stub. The imaginary part of the total impedance Z_{tot} is the sum of the reactances of the outer shield and $2n_g$ (twice the number of gaps) transmission line segments in series. The resonance condition is met, when the imaginary part of Z_{tot} disappears. Multiple resonances occur as the coaxial stub reactance alternates periodically with $\lambda/4$ between capacitive and inductive. In this work, only coils operated close to their first self-resonant mode f_0 are considered. The motivation to do so will be explained based on electromagnetic simulations in results section C.

From equations (1)-(3), the resonance frequency of the CC can be calculated in dependence of the coil diameter d_0 , the number of turns n_t and gaps n_g , and the cable properties ϵ_r , d_1 , and Z_0 . The characteristic impedance Z_0 of a coaxial structure can be approximated and depends on the diameters of inner (d_2) and outer (d_1) conductor and the dielectric properties:

$$Z_0 = \frac{1}{2\pi} \sqrt{\frac{\mu_0}{\epsilon_0 \epsilon_r}} \ln \left(\frac{d_1}{d_2} \right) \quad (4)$$

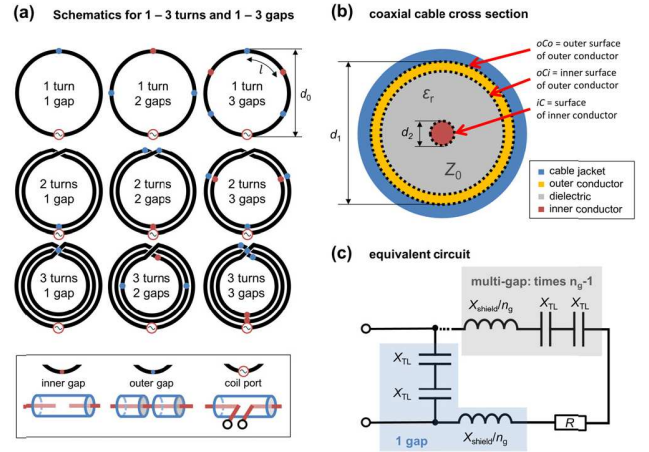


Fig. 1. Examples of gap positioning with 1-3 turns and 1-3 gaps (a), coaxial cable parameters (b), equivalent circuit model for an arbitrary number of turns (c), n_g , n_t ...number of gaps and turns, d_0 ...coil diameter, l ...length of one coaxial stub, d_1 ...outer diameter of outer conductor of coaxial cable, d_2 ...diameter of inner conductor, ϵ_r ...relative permittivity, Z_0 ...characteristic cable impedance (Ω), X_{shield} ...inductive reactance of the outer surface of the coax shield, X_{TL} ...reactance of one coaxial stub (capacitive at resonance), R ...resistance (ohmic coil losses). Although positioning of the port, depicted as a voltage source in (a), at the inner or outer gap would be equivalent in theory, it was always placed at inner gaps due to engineering considerations.

where μ_0 is the permeability of free space and ϵ_0 is the vacuum permittivity. For calculations in this work, Z_0 values given in the coaxial cable's data sheets were used and gap widths of 5 mm were taken into account for coaxial stub lengths. The high impedance of the CC (c.f. "high impedance coil (HIC)", Zhang *et al.* [34]) appears if the inner conductors at an inner gap are viewed as the coil port, since the first two coaxial stubs are then connected in parallel to the port and a parallel resonant circuit is formed (see also the schematic in Fig. 1c).

Since the electric and magnetic fields of a coaxial transmission line are confined to its inside, the part of the CC interacting with the environment is the outer surface of the shield, oCo . In the receive case, voltage is induced on the shield and, therefore, across the outer gap. In the transmit case, the excitation voltage at the CC port produces a current flow on the shield, which in turn creates the B_1^+ field.

B. Extension of Achievable Coil Diameter Range

To illustrate the extension of the achievable coil diameter range with MTMG-CCs as compared to 1T1G-CCs, the achievable coil diameters d_0 with self-resonant CCs were calculated using realistic value ranges for all coil and cable parameters (ϵ_r , d_1 , Z_0 , n_t , n_g , B_0). The reasoning for the limits for each parameter is detailed in Table I.

Using equations (1)-(3), numerical forward calculation of the resonance frequency f_0 was done in Matlab 2017b (The Mathworks, Inc., Natick, MA, USA). The parameter ranges from Table I were discretized for the calculations: the coil diameter range was sampled in 0.5 mm steps from 28.5 to 300 mm, resulting in 544 diameters. Five different cable

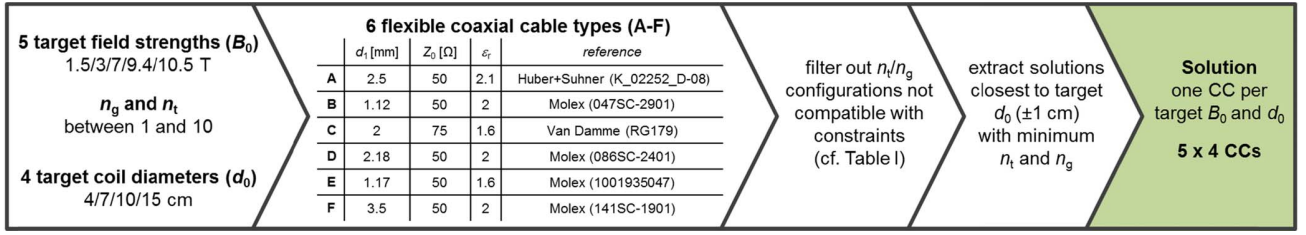


Fig. 2. MTMG-CC selection with commercial coaxial cables, specifying cable parameters (Z_0 , d_1 , ϵ_r) and references.

TABLE I

PARAMETER SPACE AND INEQUALITY CONSTRAINTS CONSIDERED IN THE CALCULATION OF THE ACHIEVABLE COIL DIAMETER RANGE FOR MTMG-CC VS. 1T1G-CCS

Parameter	Investigated range	Reasoning for limits
B_0 [T]	1.5, 3, 7, 9.4, 10.5	Common field strengths in MR
Characteristic impedance of coaxial cable Z_0 [Ω]	50, 75	Industry standards
Relative permittivity of cable dielectric ϵ_r	$1.2 \leq \epsilon_r \leq 3.5$	Literature research on dielectric materials in commercially available flexible coaxial cables (min: foamed polyethylene, max: silicone rubber or polyvinyl chloride (PVC)). The maximum dielectric diameter is approx. the diameter of the widely used RG58 cable, which was considered as the thickest cable that allows for sufficient flexibility. The minimum was determined by practical feasibility of gap construction and thin nonmagnetic cable availability.
Dielectric diameter d_1 [mm]	$1 \text{ mm} \leq d_1 \leq 3.5 \text{ mm}$	The minimum coil diameter is dictated by the minimum required length of cable segment to enable easy and reproducible fabrication of the gaps (experimentally determined: 9 cm) and $n_g = 1$, $n_t = 1$. The maximum was chosen to be 30 cm to possibly allow for the use as a transmit coil with a large FOV.
Coil diameter d_0 [cm]	$d_{0,\min} = \frac{9 \text{ cm}}{\pi}$ $d_{0,\min} \leq d_0 \leq 30 \text{ cm}$	
Number of turns n_t	$1 \leq n_t \leq 10$ (integer) $n_t \leq \frac{d_0}{\delta \cdot d_1}$	Experimentally found constraint for flexibility, depending on coil diameter and cable thickness
Number of gaps n_g	$1 \leq n_g \leq 10$ (integer) $n_g \leq \frac{d_0}{d_{0,\min}} \cdot n_t$	Limited by shortest possible cable segment (see "coil diameter").

parameter sets (each determined by ϵ_r , d_1 , Z_0) were defined: two of these parameter sets were chosen to yield the minimum and maximum coil diameter, respectively, and three other cable parameter sets were added with intermediate parameter values. All 100 combinations of $n_t \leq 10$ and $n_g \leq 10$ were used. From the resulting $544 \times 5 \times 10 \times 10 = 272\,000$ coil variants, only the solutions obeying the inequality constraints regarding n_t and n_g from Table I, and those with resonance frequencies close to one of the five target Larmor frequencies (maximum $\pm 1\%$ deviation) were retained. The result of this theoretical approach is a range of possible coil diameters d_0 for each n_t/n_g CC configuration and B_0 field strength.

C. Realistic Coil Designs and Fabrication

In a second step, a more practical approach was pursued to select and fabricate CCs that are useful for different applications, and feasible in terms of non-magnetic flexible coaxial cable availability and geometry. The process to extract suitable CC solutions from the many calculations described in section B is summarized in Fig. 2.

For RF coils in the sample dominated noise regime, the SNR-optimum for a target penetration depth p is obtained with a d_0 approximately equal to p [4], the following four target coil diameters with respective possible biomedical applications were chosen: 4 cm (skin, hand, wrist), 7 cm (elbow, ankle, breast, head), 10 cm (breast, head, knee) and 15 cm (heart, abdomen). Further, 6 non-magnetic commercially available

coaxial cable types were selected. For all cables, the outer conductor (shield) is thick enough to separate the currents on oCi and oCo over a frequency range from 50-500 MHz. The skin depth is always at least a factor of 10 smaller than the shield thickness. The steps to calculate d_0 for each target Larmor frequency, within a parameter space given by the cable types and n_g/n_t configurations, were the same as described in section B. Solutions with ± 1 cm maximum d_0 deviation from the target value and self-resonance frequency deviating $\pm 10\%$ from f_{Larmor} were kept. From these, the designs with the least number of gaps and turns were selected, since each gap is a potential breaking point even if covered with heat shrink tubing. Also, flexibility is reduced by soldering of the shield at inner gaps, heat shrink tubing, and by the number of turns. As a result, for each target field strength B_0 and target coil diameter d_0 , one CC design was found that could be fabricated out of one of the 6 coaxial cable types, accepting the mentioned slight deviations between f_{Larmor} and the calculated f_0 .

In this study, the 3 and 7 T ^1H coils from this design set were fabricated. The resulting eight (MTMG-)CCs had diameters of 4, 7, 10 and 15 cm, $n_{t,\max} = 2$ and $n_{g,\max} = 5$, and were fabricated from five different coaxial cables. Exact CC configurations and used cable types are detailed in results section B. For comparison, rigid standard coils (SCs) fabricated out of 1 mm copper wire and the same coil diameters as the CCs were constructed. All coils were tested on the bench and in MRI. For 3 T, Rx-only coils and for 7 T Tx/Rx coils were constructed.

Photographs and respective interface schematics of all fabricated coils are shown in Fig. 3. The interfacing circuitry at the coil port includes components for fine-tuning, matching and active detuning (AD) with PIN diodes (DH80106-10N, Cobham, Wimborne, UK) to decouple the 3 T Rx-only coils during transmission. A low-noise preamplifier (Hi-Q.A. Inc., Carleton Place, Ontario, Canada) was placed directly after the matching network of 3 T Rx-only coils. At 7 T, a transmit/receive (T/R) switch (Stark Contrast, Erlangen, Germany) with integrated low-noise preamplifier (Siemens Healthcare, Erlangen, Germany) was used to interface the coil to the scanner.

Rx-only CC interfaces were designed with a tuning inductor L_T which shifts the resonance to a higher frequency. In the loaded case, self-resonances f_0 of the CCs were generally lower than f_{Larmor} and a residual capacitive imaginary part of the impedance appeared at resonance that could be compensated with an inductor, as also explained in [34].

TABLE II
POSSIBLE CC CONFIGURATION ($n_t T n_g G$) AND CABLE TYPE (IN PARENTHESIS, SEE FIG. 2) PER B_0 AND COIL DIAMETER d_0

d_0 [cm]	B_0 [T]										
						3			7		
	1.5	3	7	9.4	10.5	$f_{0,meas}$ [MHz]	$f_{0,calc}$ [MHz]	$f_{0,sim}$ [MHz]	$f_{0,meas}$ [MHz]	$f_{0,calc}$ [MHz]	$f_{0,sim}$ [MHz]
	CC configuration (cable type)										
4	3T1G (E)	2T1G (D)	1T1G (B)	1T1G (C)	1T1G (C)	111.0	118.0 (+6.3 %)	111.0 (+0.0 %)	286.2	303.0 (+5.9 %)	287.3 (+0.4 %)
7	2T1G (A)	2T2G (E)	1T2G (B)	1T2G (F)	1T2G (C)	126.8	122.4 (-3.5 %)	125.6 (-1.0 %)	298.5	326.7 (+9.4 %)	309.2 (+3.6 %)
10	3T2G (C)	1T1G (A)	1T2G (C)	1T3G (F)	1T3G (C)	108.5	114.7 (+5.8 %)	109.0 (+0.5 %)	258.5	294.4 (+13.9 %)	276.2 (+6.9 %)
15	1T1G (B)	2T5G (B)	1T3G (C)	1T5G (A)	1T5G (C)	123.2	124.3 (+0.9 %)	115.6 (-6.2 %)	261.5	282.0 (+7.8 %)	263.4 (+0.7 %)

Fabricated and tested CCs are marked in light blue. On the right side of the table, f_0 measurements with the double-loop probe ($f_{0,meas}$) are compared to numerical calculations based on the equivalent circuit model ($f_{0,calc}$) and EM simulations ($f_{0,sim}$). Percentages in parenthesis indicate the respective relative deviation from $f_{0,meas}$.

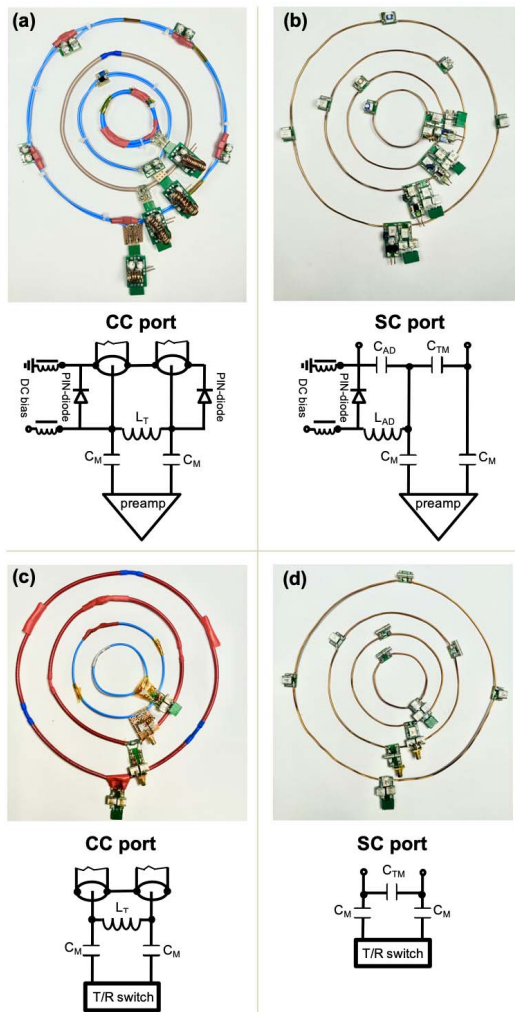


Fig. 3. Photographs of fabricated Rx-only CCs (a) and SCs (b) for 3 T and Tx/Rx CCs (c) and SCs (d) for 7 T and respective interface circuit schematics for tuning, matching and active detuning (only at 3 T). Note that the coils are only placed inside each other for the photograph, they are operated separately.

A tuning capacitor C_T instead of L_T would add to the coaxial stub capacitance (X_{TL}) and could therefore be used to lower the frequency if the self-resonance was higher than the target f_{Larmor} . Note that in work of Ruytenberg *et al.* [28], [38],

purely capacitive tuning and matching is used for 10 cm Tx/Rx CCs with a first self-resonance of ≈ 110 MHz (see simulated and calculated values shown in Table II for a 10 cm 1T1G, cable A). For this coil example, with a tuning capacitor across the coil port (Fig. 1), the first parallel resonance mode measured across the port shifts to tens of MHz, whereas the second resonance mode shifts closer to the desired Larmor frequency, i.e. around 300 MHz. Therefore, due to the multiple resonances of a CC originating from the coaxial stub impedance behavior, the 1T1G-CC with a self-resonance $f_0 < f_{Larmor}$ used in [28], [38] can still be tuned and matched to 297.2 MHz with only capacitive components. To compare coil designs and motivate the use of a coil with an f_0 as close as possible to f_{Larmor} , the current distribution and amplitude along the oCo , depending on the coil geometry and operation frequency, was analyzed using electromagnetic simulation of the above-mentioned example of a 10 cm 1T1G-CC ($f_0 < f_{Larmor}$) compared to a 1T2G-CC used in this study ($f_0 \approx f_{Larmor}$), for $f_{Larmor} = 297.2$ MHz.

The determination of values for L_T and matching capacitors (C_M) for all CCs relied on S_{11} measurements of the unmatched and untuned loaded CC at the coil port using a vector network analyzer (VNA, E5071C, Agilent, Santa Clara, CA, USA). S_{11} measurements were exported for circuit simulation in ADS (Keysight Technologies Inc., Santa Rosa, CA, USA) where tuning (to f_{Larmor}) and matching (< -40 dB) components were determined. Inner gaps were constructed by cutting out ≈ 5 mm length of the inner conductor and to keep stability and a round coil shape, either heat shrink tubing was placed over the inner conductors close to the gap position or the inner conductors were bent away from the coil (with their isolating layer, especially with thin cables) and the outer conductors were soldered back together. Then again, heat shrink tubing was placed over the soldered outer conductor. Heat shrink tubing was also placed over the outer gaps for electrical insulation and mechanical stability. In CCs with multiple turns, insulating tape was wrapped around all cable turns to prevent f_0 shifts due to changes in the relative position of the individual cable turns.

The copper wire SCs were capacitively tuned (C_{TM}) and matched (C_M) and segmented by tuning capacitors along the loop at a length of maximum $\approx \lambda/10$ to limit losses due to high electric fields [47].

D. Electromagnetic Simulations

Simulations of all implemented CCs were performed using the finite element solver of CST Studio Suite 2020 (Dassault Systèmes, Paris, France). Curved surfaces were approximated using second order finite elements. For accurate results, adaptive mesh refinement was used, with the S-parameter convergence criterion set to 0.001. Broadband results were generated using the general-purpose broadband sweep method of CST with a maximum S-parameter interpolation error of 0.001, which allowed to extract a broadband response between 50 and 500 MHz using approximately 10 frequency samples. In a first simulation run, the self-resonances f_0 of the unloaded coax loops were determined by finding the first local maximum of $|Z|$. In a second run, 3D current monitors were placed at these frequencies in addition to monitors covering the respective target Larmor frequency. Subsequently, surface current density ($K = dI/dl$) as well as S-matrices were exported for further analysis. Forward power was set to 0.5 W. Multi-turn coils were modeled as helical structures, where outbound wires at the start and end were used in order to close the coil without crossing the coaxial line in between (Fig. 6b). Further, CCs and SCs designed for Tx/Rx use at 7 T were simulated in loaded configuration. The box-shaped phantom dimensions were adapted depending on the coil diameter ($4d_0$ cm \times $4d_0$ cm \times 25 cm), electrical properties set to a conductivity of $\sigma = 0.6$ S/m and permittivity of $\epsilon_r = 80$ and the phantom placed at 0.5 cm from the coil.

Post-processing of the simulated data was performed with Matlab 2017b. Simulations were scaled to 1 W accepted input power (P_{acc}), taking into account the respective reflection coefficients (S_{11}) from simulation. The surface current density K was analyzed on the three mentioned conductor parts iC , oCi , and oCo . The surface current I was derived by integrating K over volumes along the structures of a length of 1 mm. Multiplication with the respective conductor diameter yields the surface current I . The outbound wires for the multi-turn CCs were excluded from the surface current evaluation. Specific absorption rate (SAR) was calculated pointwise and 10 g averaged from simulated E -field data over the whole phantom. Maximum intensity projections (MIPs) of the point SAR in the coronal plane, i.e. parallel to the coil plane, and SAR efficiency ($B_1^+/\sqrt{\max. 10g SAR}$) maps in all planes (sagittal and transversal through the coil's center, coronal at a distance $d_0/4$ from the coil) were calculated for 7 T CCs and SCs. Maximum 10 g and point SAR values per 1 W P_{acc} were extracted and mean transmit efficiency (mean B_1^+/\sqrt{P}) as well as mean SAR efficiency (mean $B_1^+/\sqrt{\max. 10g SAR}$) were calculated in a half-spherical volume of interest with its center at the coil center, and a diameter equal to d_0 to yield quantitative measures for comparison between CCs and SCs.

E. Bench Measurements

Phantoms used in bench tests and MRI experiments are shown in Fig. 4. A 5- or 25-liter container phantom (Fig. 4a) was used for measurements where the coils were placed in a flat configuration on the phantom surface. Measurements with bent coils were performed using a 3D-printed holder-set

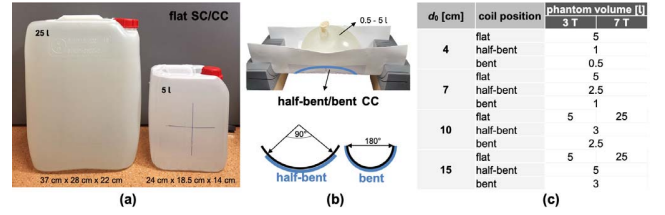


Fig. 4. Bench and MR measurement set-up: container phantoms used for flat measurements (a), holders with PTFE plate and balloon phantom to simulate two bending scenarios (b), phantom volumes used per coil size and coil position (c).

up with slits to place a bent polytetrafluoroethylene (PTFE) sheet and balloon phantoms of different sizes depending on the target application and bending radius (Fig. 4b). The average bending case (“half-bent”) was defined as opposite coil conductor ends spanning a 90° angle and in the maximum assumed bending case (“bent”), coil ends span a 180° angle in the cross-section, as shown in Fig. 4b.

All phantoms were filled with saline solution (1.6 g NaCl/l deionized water) with a DC conductivity of 0.2 S/m, and doped with 1 ml/l Gd-based contrast agent to shorten acquisition time. For 3 T measurements, all coils were directly placed on or under the phantom. The same applies for 7 T measurements, except for the 15 cm coils, which were placed at 1 cm distance from the sample using a foam spacer, in order to reduce loading.

Bench tests were performed using the VNA. First, the self-resonance frequency of CCs was measured inductively with a decoupled double-loop probe (baseline value < -80 dB) [48] without interface. SCs were tuned by distributed capacitors. Inductive measurements were performed with SCs and CCs in flat position and CCs in half-bent and bent position. For these coil setups, the unloaded and loaded resonance frequency ($f_{0,u}$ and $f_{0,l}$) and quality factor ($Q_{0,u}$ and $Q_{0,l}$), respectively, were determined. Copper wire SCs cannot be reversibly bent, therefore, only CCs were investigated in bent configuration.

Coils with interfaces were connected to the VNA via their 50Ω matching circuit and using a custom-built test rig to mimic the MR scanner's coil connectors including DC supply to switch either the AD circuit or the transmit/receive switch. All coils were initially tuned and matched in flat position on the container phantom with a volume listed in Fig. 4c. S-parameter measurements (S_{11} in dB) of the matching level at f_{Larmor} were carried out to track changes during CC bending and characterize the behavior in two different bending scenarios with different balloon phantom sizes, also measuring $f_{0,l}$ and Q_l . In a next step, the coils were re-tuned and re-matched to be used in either flat position (SC) or bent position (CC) on a balloon phantom (see Fig. 4b). Again, the matching level at f_{Larmor} and Q_{loaded} was measured. With the test rig, the functioning of AD components in the Rx-only coils was verified: for SCs the AD circuit was tuned to f_{Larmor} to efficiently block currents at this frequency and for CCs, the switching of all PIN diodes between tuned and detuned state was checked.

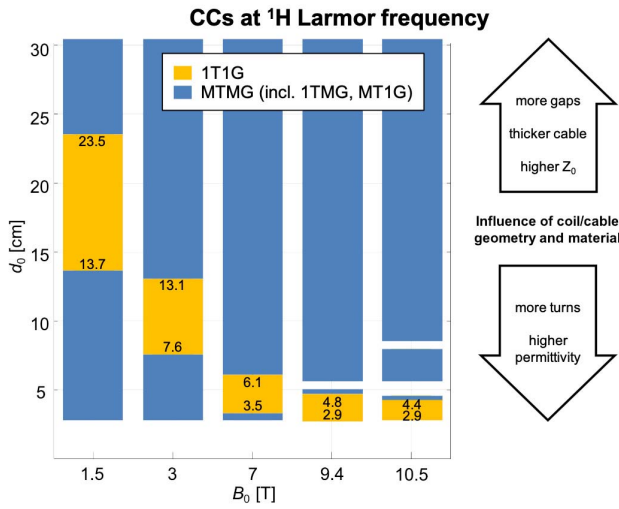


Fig. 5. Possible CC diameters (d_0) at the ^1H Larmor frequency for 5 different common field strengths using realistic coil and cable parameters (see Table I). The diameters that can be achieved with 1T1G coils are marked in yellow, the diameters only accessible with multiple turns and/or gaps are marked in blue. Due to the discrete nature of some of the parameters, small voids in the diameter ranges at 9.4 and 10.5 T can be observed.

F. MRI Experiments

MRI experiments were carried out on a 3 T and a 7 T MR scanner (Prisma Fit and 7 T Magnetom, Siemens Healthineers, Erlangen, Germany) in the following setups: SCs and CCs in flat position on a container phantom, and SCs in flat and CCs in bent position on a balloon phantom. The aim was to compare CCs and SCs in terms of SNR performance (3 T and 7 T), and evaluate transmit efficiency (7 T only).

At 3 T, gradient-echo (GRE) images were acquired in a transversal slice through the coil center (scan parameters: $T_R/T_E = 50/10$ ms, $\text{FOV} = 290 \times 290$ mm 2 , 0.6×0.6 mm 2 in-plane resolution, 6.5 mm slice thickness). Data from GRE scans were used to calculate SNR maps and to evaluate SNR in a circular ROI with diameter $d_0/4$ centered underneath the coil. The distance D between coil and ROI center was 1, 2.5, 4 and 5.5 cm for the 4, 7, 10 and 15 cm coil, respectively. Relative SNR difference maps for the CC vs. the SC on a balloon phantom were calculated as $\text{SNR}_{\text{CC}}/\text{SNR}_{\text{SC}} - 1$.

To determine the reliability of AD circuits in CCs and SCs, we performed flip angle mapping with and without the Rx coil present in flat position, using the body coil for Tx/Rx. From these data, the relative flip angle difference maps with vs. without Rx coil were calculated. Efficient decoupling from the body coil in Rx-only CCs has already been demonstrated in single-gap CCs [34]. To test this for coils with multiple gaps, measurements of the flip angle distribution (saturated Turbo FLASH [49]) with and without the detuned MTMG coil present were performed. The transmission decoupling performance of the coil with the highest number of gaps in the study (2T5G-CC) with only one pair of detuning PIN diodes at the coil port, was compared to another one with a pair of PIN diodes at each of the inner gaps. In the latter case, at every outer gap an RF choke (1812CS, Coilcraft, Cumberland, UK)

was placed to provide the DC connection for biasing the PIN diodes (see photograph in Fig. 3a).

At 7 T, flip angle maps in the central sagittal slice were acquired, using the saturated Turbo FLASH method [49]. The excitation pulse amplitude V_{ref} was adjusted to achieve an average flip angle of 90° in a ROI with diameter $d_0/4$ and the ROI center at a distance D from the coil center in flat position ($D = 1, 2, 2.2, 2.7$ cm for the 4, 7, 10 and 15 cm coil, respectively). For the balloon phantom and the SC in flat or the CC in bent position, the pulse amplitude V_{ref} was again adjusted to obtain a 90° flip angle in the same ROI. B_1^+/\sqrt{P} maps, i.e. the RF transmit field normalized to the input power, indicating the transmit efficiency, were calculated from flip angle maps and the respective pulse parameters. GRE images were also acquired in the central sagittal slice (scan parameters: $T_R/T_E = 50/4.8$ ms, in-plane resolution 0.5×0.5 mm 2 , $\text{FOV} = 256 \times 256$ mm 2 , 3 mm slice thickness). As the flip angle in the ROI was kept constant for each coil setup, SNR evaluation in the same ROI allows comparison of the coil's receive sensitivity contribution only. Relative SNR and B_1^+/\sqrt{P} difference maps for the CC versus the SC on a balloon phantom were calculated.

III. RESULTS

A. Extension of Achievable Coil Diameter Range

Fig. 5 illustrates the possible coil size ranges for 1T1G (yellow) versus MTMG-CCs (blue) within the chosen parameter space detailed in Table I. As can be seen, 1T1G-CCs are limited to large coils at low field and small coils at high field. Allowing for multiple turns and/or gaps, the possible diameter range starts at approximately 3 cm for all B_0 field strengths. The range is almost continuous up to 30 cm in diameter and discontinuities only appear at ultra-high field. In practice, commercially available coaxial cables only cover the assumed continuous range for permittivity and cable diameter discretely, and therefore obviously leading to discrete achievable CC diameters. These, however, still offer sufficient freedom in choice of the coil size to obtain results close to the target coil size. On the right side of Fig. 5, the arrows indicate how coil and cable parameters influence the coil size.

B. Realistic Coil Designs

In Table II, realistic design parameters for the fabrication of CCs made from non-magnetic commercially available flexible coaxial cable types are listed for different B_0 fields and target d_0 with their self-resonance as close as possible to the target f_{Larmor} . The deviations from the measured resonance frequency are $< 13.9\%$ for calculated and $< 6.9\%$ for the simulated values. Note that the values for $f_{0,\text{meas}}$ here differ from the unloaded values in supplementary Table I,¹ since they were obtained without AD components or interface connector on the coil.

¹Supplementary materials are available in the supporting documents /multimedia tab.

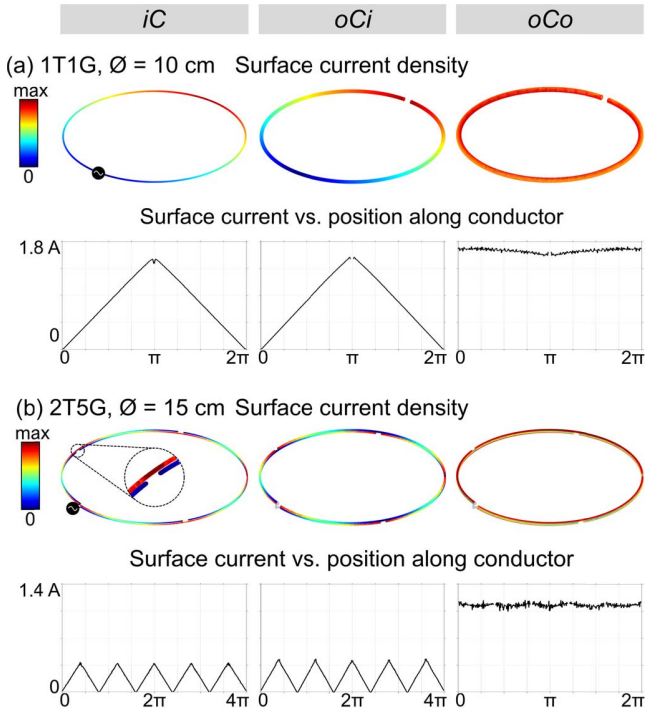


Fig. 6. Surface current density and surface current simulation results. Two representative simulation results are shown to depict the coaxial coils' behavior for (a) single turn single gap, (1T1G, $d_0 = 10$ cm, $f_0 = 109$ MHz) and (b) a multi turn multi gap (2T5G, $d_0 = 15$ cm, $f_0 = 115.6$ MHz) at their respective self-resonances f_0 . The surface current densities K at f_0 are depicted as 3D plots for iC , oCi , and oCo , scaled to their individual maximum. The corresponding magnitudes of the surface currents $|I|$ along the coil windings are shown as line plots, starting from 0 at the feed point to $n_t \times 2\pi$ in the case of iC and oCi . The current on oCo has opposite direction to its mirror-current on iC . For oCo , the surface current was integrated over all turns, since this represents the effective current seen at distance from the coil, and the plot only goes to 2π . The feeding and necessary connecting structures to avoid self-intersection of the geometry are depicted in grey/black.

C. Electromagnetic Simulations

Fig. 6 shows simulation results of a 1T1G (a) and a MTMG (b) CC at their respective self-resonances f_0 . Results for all investigated coils (blue area in [Table II](#)) at their target Larmor frequency f_{Larmor} are shown in supplementary Fig. 1¹. The typical transmission line behavior can be observed for iC and oCi , where the current on iC is the mirror-current of the current on oCi , with a maximum in current density magnitude at each outer gap and a zero at each inner gap. However, the current along oCo , which corresponds to the effective current seen at distance from the coil, is rather constant along the conductor.

The motivation to use a CC with a first self-resonance as close as possible to the Larmor frequency which is the case for all MTMG-CCs employed in this work, is illustrated with the example shown in [Fig. 7](#). Both coils have a diameter of 10 cm and are simulated at a Larmor frequency of 297.2 MHz. The 1T1G-CC geometry was chosen according to details given in [38] (cable A) and has a simulated $f_{0,\text{sim}}$ of 109.0 MHz. The 1T2G-CC used in this work has an $f_{0,\text{sim}}$ of 276.2 MHz (see [Table II](#)). Simulation results of the surface current density and surface current I in [Fig. 7](#) are in agreement with the ones

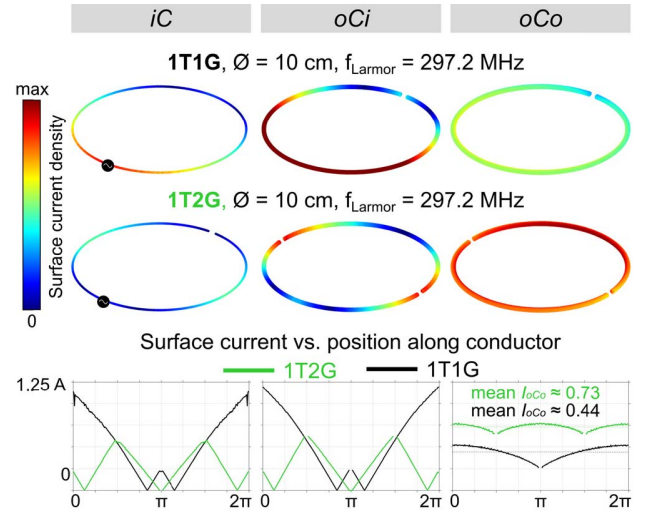


Fig. 7. Surface current density and surface current simulation results for a 10 cm 1T1G-CC compared to a 1T2G-CC of same size.

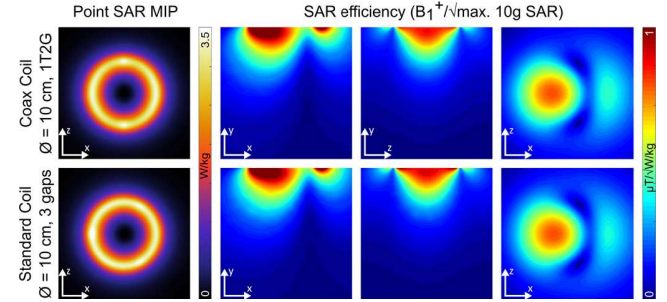


Fig. 8. Point SAR MIPs (W/kg) and SAR efficiency (B_1^+/\sqrt{W} /kg) maps calculated from EM simulation results for a 10 cm CC and SC used at 7 T.

shown for the 1T1G-CC in [38] and demonstrate that, scaled to 1 W accepted power, I along the oCo is higher in amplitude and more homogeneous for the 1T2G-CC.

SAR simulations targeted the comparison between SCs and CCs used in Tx/Rx mode at 7 T. [Fig. 8](#) shows a representative simulation result for a 10 cm CC and SC, i.e. SAR MIPs in the coronal (xz) plane and SAR efficiency maps in a transversal and sagittal slice through the coil center as well as in a coronal slice (at a distance of 2.5 cm from the coil). The coaxial coil in this example has two gaps and the standard coil is segmented by three capacitor “gaps”. In supplementary Fig. 2¹, SAR simulation results for all CCs and SCs (8 in total) are presented. [Table III](#) summarizes maximum local 10 g SAR, maximum point SAR, mean transmit (TE) and mean SAR (SE) efficiency values for all 7 T CC and SCs. All maps and parameters are very similar for the 7, 10 and 15 cm SCs and CCs. The 4 cm SC has slightly lower maximum local 10 g SAR and higher mean TE, i.e. also higher SE than the CC, although still comparable in performance (see supplementary Fig. 2¹).

D. Bench Measurements

Bench measurement results for 3 T and 7 T SCs and CCs without and with interface, different coil positions, and tuning and matching configurations are summarized in supplementary

TABLE III
7 T SIMULATION RESULTS FOR ALL CCs AND SCs

d_0 [cm]	max. 10 g SAR	max. point SAR	mean TE	mean SE	
coil type	W/kg per 1 W P_{acc}	W/kg per 1 W P_{acc}	$\mu T/\sqrt{W}$	$\mu T/\sqrt{W/kg}$	
4	CC	5.04	17.05	4.33	1.93
	SC	4.69	15.61	4.53	2.09
7	CC	2.85	6.56	1.56	0.92
	SC	2.87	6.84	1.58	0.93
10	CC	1.81	3.43	0.84	0.62
	SC	1.81	3.78	0.86	0.64
15	CC	1.03	1.89	0.45	0.44
	SC	1.01	2.14	0.46	0.46

Table I¹. For Rx-only CCs at 3 T with multiple gaps (7 and 15 cm CCs), AD PIN diodes lead to a relatively low Q_u due to added ohmic losses but CCs still operate in the sample noise dominated domain. From Q_u and Q_l values measured for CCs in flat position without interface, we can conclude that the frequency-normalized coil losses R_C scale with $d_0 n_l^2$ and the frequency-normalized sample losses R_S scale with $d_0^3 n_l^2$ in accordance with equations 8 and 9 given in [50]. Generally, Q_u of CCs is comparable or lower as for SCs and Q_l of CCs is comparable or higher as for SCs. Therefore, the Q -ratio (Q_u/Q_l) is mostly lower for CCs than for SCs. At both 3 and 7 T, for both coil types, different coil setups (flat, half-bent, bent) and phantom volumes (container, balloons) the Q -ratios were always superior to 2, demonstrating coil operation in a sample noise dominated regime.

In flat and loaded coil configuration, SCs and CCs with their interfaces were tuned to the respective f_{Larmor} and matched to a level better than -18.4 dB. During CC bending, either to half-bent or bent position, $f_{0,1}$ increases. Thus, matching at f_{Larmor} is degraded. The higher Q_l and the higher $\Delta f_{0,1}$, the stronger the observed degradation in matching. For some CCs, re-tuning and re-matching to the balloon phantom is indispensable. The CCs with 15 cm diameter at 3 T and the ones with 7, 10, and 15 cm at 7 T were acceptably matched even during strong bending (assuming a threshold of -8 dB/15 % reflected power). During re-tuning and re-matching of SCs in flat and CCs in bent position on the balloon phantom, matching levels better than -15 dB were reached.

E. MRI Experiments

At 3 T, flip angle mapping results with a 2T5G-CC using an AD circuitry consisting of PIN-diodes shorting inner and outer conductor only at the coil port (see circuit scheme in Fig. 3a) reveal non-sufficient decoupling of Rx and body coil with relative flip angle changes of over 60 % shown in Fig. 9b. With an AD network consisting of a set of PIN diodes at every inner gap and RF chokes connecting the outer gaps (Fig. 9a), reliable AD is ensured as any residual resonances are eliminated (Fig. 9c). For all SCs and CCs used in this study, the relative flip angle difference without vs. with Rx coil present is $< 10 - 20$ % over the whole phantom.

3 T SNR maps are presented in Fig. 10. All images shown in Fig. 10 and Fig. 11 were cropped to the respective coil size. In flat position, the average SNR in a circular ROI is lower for CCs as compared to SCs (-48.6 %, -33.9 %, -28.2 %

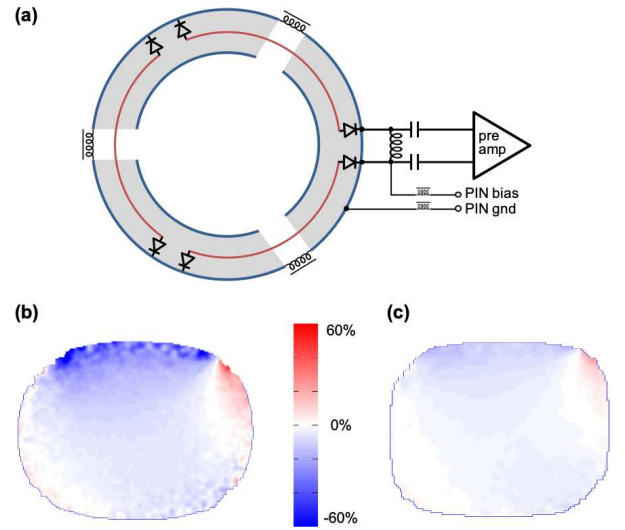


Fig. 9. Active detuning components with multiple gaps (arbitrary nt): (a) inner gaps need to be shorted by PIN diodes and outer gaps connected by RF chokes. Relative flip angle difference maps for a 2T5G 15 cm diameter CC at 3 T (b) detuned only at the port or (c) at every inner gap.

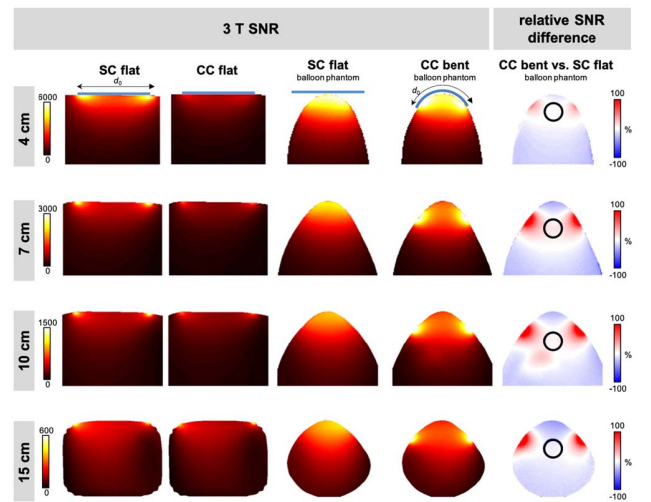


Fig. 10. 3 T MRI results, SNR maps in the central transversal slice for the 4, 7, 10 and 15 cm SC and CC in flat position on a container phantom and the SC in flat and the CC in bent position on a balloon phantom, relative SNR difference maps.

and -17.1 % for the 4, 7, 10 and 15 cm CC, respectively). Using the CC bent to the balloon phantom compared to a flat SC results in a moderate SNR gain or slightly lower SNR in the ROI (-2.3 %, $+10.8$ %, $+7.0$ % and -5.7 % for the 4, 7, 10 and 15 cm CC, respectively), as also shown in relative SNR difference maps in Fig. 10.

At 7 T, transmit efficiency B_1^+/\sqrt{P} maps presented in Fig. 11a show good comparability of SCs and CCs in flat measurements as the same pulse amplitude was needed for SCs and CCs to achieve a 90° average flip angle in the circular ROI ($V_{ref} = 25, 63, 130$ and 200 V for the 4, 7, 10 and 15 cm coils, respectively). B_1^+/\sqrt{P} between CC and SC only slightly differs by $+2.5$ % (4 cm), $+3.2$ % (7 cm), -0.8 % (10 cm) and -2.4 % (15 cm). On the balloon phantom, with the SC in flat position and the CC bent to the balloon, lower V_{ref}

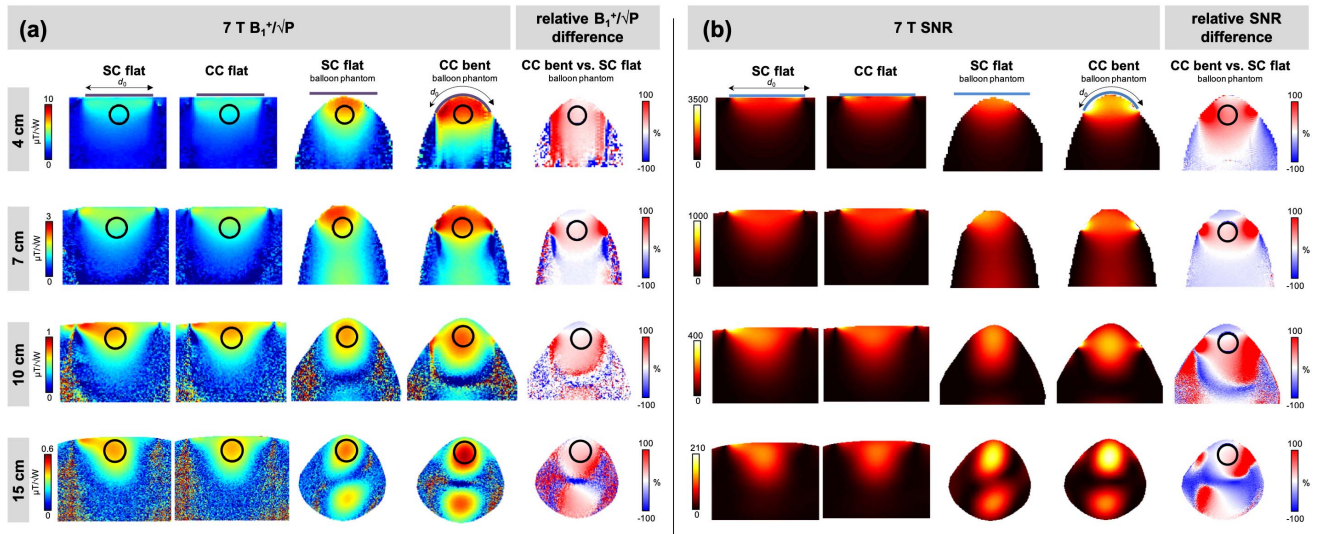


Fig. 11. 7 T MRI results, B_1^+/\sqrt{P} maps (a) and SNR maps (b) in the central sagittal slice for the 4, 7, 10 and 15 cm SC and CC in flat position on a container phantom and the SC in flat and the CC in bent position on a balloon phantom, relative B_1^+/\sqrt{P} and SNR difference maps (CC vs. SC on balloon phantom).

than for flat measurements on the container were required to achieve 90° average flip angle in the ROI ($V_{\text{ref,SC}} = 12.5, 44, 123, 193$ V and $V_{\text{ref,CC}} = 11, 38, 112, 160$ V). CCs in bent configuration showed higher transmit efficiency than the flat SC with a gain in B_1^+/\sqrt{P} of +17.1 %, +14.8 %, +9.1 % and +21.9 % for the 4, 7, 10 and 15 cm CC, respectively (Fig. 11a). 7 T SNR maps demonstrate that, in flat position, the average SNR in a circular ROI is comparable or slightly lower for CCs as compared to SCs (+0.5 %, +1.1 %, -8.1 % and -6.9 % for the 4, 7, 10 and 15 cm CC, respectively), see Fig. 11b. However, when CCs are form-fitted to the balloon and compared to the flat SCs, a considerable SNR gain can be observed (+40.5 %, +18.0 %, +11.1 % and +10.6 % for the 4, 7, 10 and 15 cm CC, respectively), see Fig. 11b.

Standing wave patterns occurring in both B_1^+/\sqrt{P} and SNR maps, which are more pronounced for larger coil sizes, can be explained by the electrical properties and dimensions of the phantom. For a wavelength (≈ 11 cm) smaller than the phantom size and low sample conductivity, resulting in a skin depth larger than the phantom size, the forward and reflected wave can create EM interference patterns. Alternatively, dielectric phantom resonances could be the cause for standing wave patterns [51].

IV. DISCUSSION AND CONCLUSION

In this work, the design concept for multi-turn multi-gap coaxial RF coils is presented. An equivalent circuit is modeled; theoretical solutions for CCs are calculated for five common B_0 field strengths and different coil sizes. Surface current density simulations are performed to analyze the three distinct conductor parts of a CC. SAR simulations conducted for 7 T Tx/Rx CCs and SCs demonstrate similar performance of both coil types. The study focused on a proof-of-concept of employing (MTMG-)CCs in Rx-only mode at 3 T and Tx/Rx mode at 7 T MRI. CCs with 4, 7, 10 and 15 cm coil

diameters were fabricated from commercially available non-magnetic coaxial cables. During bench and MRI tests, they demonstrate robustness upon bending as well as B_1^+/\sqrt{P} and SNR improvement (7 T) or no significant SNR loss (3 T) when form-fitted to a balloon sample as compared to flat standard copper loop coils.

One of the causes for deviations between measured, calculated and simulated f_0 is most likely the limited accuracy of handmade gap construction, where asymmetries and gap length variations might shift f_0 . Also, the equivalent circuit model does not account for stray capacitance at the gaps. The fabricated CC geometries slightly deviate from simulated ones, e.g. the multi-turn CC geometry was modeled as a helical structure and the conductor material was assumed to be solid copper for all coils although some conductors may in reality be braided and/or coated by other materials. Nevertheless, calculated resonance frequencies sufficiently match the measured results, so that the equivalent circuit was deemed valid to be used for finding suitable MTMG-CC designs for a target resonance frequency and desired coil diameter. In the choice of coaxial structures used in this work, an emphasis was put on flexibility and commercial availability of the cable. This comes with advantages, e.g. easier reproducibility and fast prototyping but also with drawbacks, e.g. soldering joints along the loop to re-connect the outer conductors at inner gaps. However, in principle also semi-rigid or rigid coaxial structures (commercial or custom 3D printed) or other elaborate techniques for flexible coaxial structure manufacturing could be used for coil fabrication. In that case, e.g. the cable impedance could be varied in an even larger range and the CC resonance could be more precisely tuned for a given coil diameter. Furthermore, solder joints along the loop could be avoided with customized manual assembling of inner conductor and outer conductor with beforehand introduced gaps, and a separating dielectric.

Clearly, additional active detuning components required for multi-gap coils operating in Rx-only mode impair flexibility, lead to suboptimal coil robustness and increase coil noise. Nevertheless, we believe it is interesting to show the proof-of-concept of fabricating MTMG-CCs for Rx-only use at 3 T and the implications of introducing multiple gaps on the active detuning reliability, not least to ensure patient safety when experimenting with this novel coil design concept. The multi-gap design is certainly more advantageous for Tx/Rx coils where additional active detuning components are not needed. When employed at UHF ≥ 7 T, where standard coils would require many segmenting capacitors, stub segments between gaps in multi-gap CCs become shorter (in contrast to the single-gap coil of same size), yielding homogeneous current distribution on the outer surface of the outer coaxial conductor (see Fig. 7), similar Tx/Rx performance (see Fig. 11) and SAR efficiency (Fig. 8, supplementary Fig. 2¹) compared to rigid segmented copper loops.

The characteristics of single-element (MTMG-)CCs could be more ideally exploited in array configuration: the size-optimized CC elements achieving optimal SNR in the target penetration depth, combined with large FOV coverage of an array would result in a flexible, light-weight coil improving patient comfort and image quality compared to rigid arrays with large variations in sample-coil distance. Also, in array configuration, depending on the application, the single element coil radius may be rather small and therefore single elements not necessarily as strongly bent as demonstrated in this work. Furthermore, in practice, the baseline bending and loading configuration for coil matching can be changed from flat to a certain average bending and a more specific load depending on the anatomical application.

For *in vivo* use of Tx/Rx MTMG-CCs EM simulations are required to estimate the specific absorption rate. These simulations should ideally be based on a finite element method (FEM) solver due to the fine sub-millimeter structures involved, as also employed for EM simulations presented in this work. For heavily populated coil arrays, the computational complexity could potentially become unfeasible to be computed with a FEM solver, due to the sophisticated meshing necessary to resolve the coil structures and a human sample. As demonstrated in this work, CCs could be approximated by standard loops for *H*- and *E*-field simulations, since it was shown here that the current interacting with the sample and neighboring coils (on the outer surface of the outer conductor) is rather uniform and EM simulation results on SAR and transmit efficiency were comparable between SCs and CCs at 7 T. Large CCs > 20 cm not fabricated in this work could be interesting for use as Tx coils at 7 T although other coil types (e.g. dipoles alone or combined with loop coils) might be more advantageous for large penetration depths at UHF [52], [53]. Although a homogeneous current distribution along the *oCo* was targeted in this work (as with most segmented standard coils), it is conceivable that a non-uniform placement of the gaps leading to unbalanced current distribution on the *oCo* [29] could also be exploited at UHF, in analogy to “loopole” designs [54], [55] which combine loop and dipole antenna properties. The 1T1G coil shown in Fig. 7 (see also [38]),

operating far from its self-resonance can cause a similar “loopole”-type current distribution and might yield improved performance compared to a simple loop coil, depending on the coil orientation relative to B_0 [54]. Furthermore, the asymmetric current pattern might be an explanation [55] for improved inter-element decoupling observed in references [29], [38].

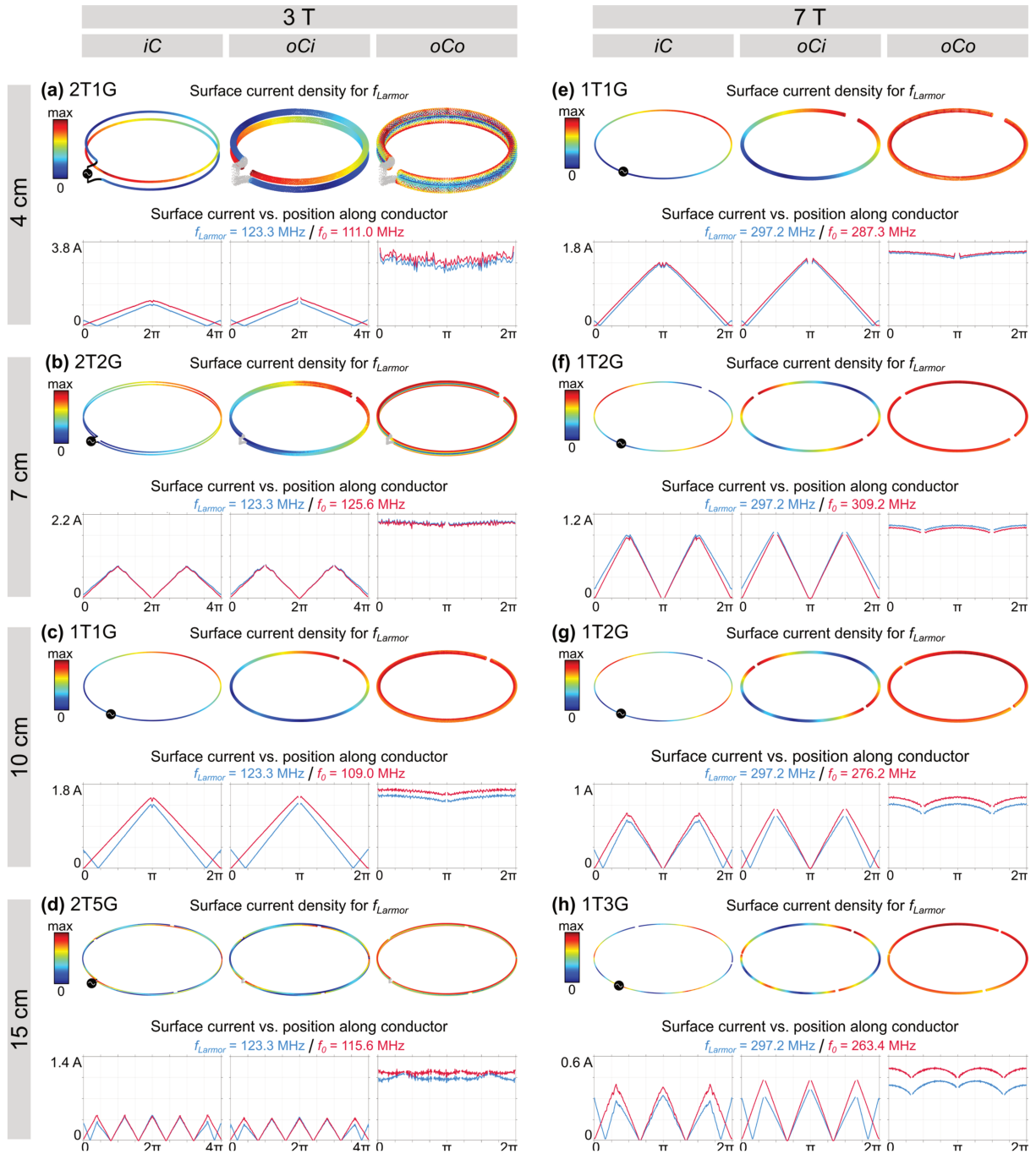
As a future perspective, tracking of the flexible coils using MR-visible materials contained in the outer cable jacket [56] can be envisioned, possibly useful for localized on-coil B_0 shimming or motion correction.

In conclusion, the major asset of MTMG coaxial coils presented in this work is their low weight, flexibility, and the fact that the coil size can be chosen (almost) freely for various B_0 field strengths. Implementing the MTMG principle, the size-restriction of 1T1G-CCs can be overcome, and CC elements can be size-optimized for a wide range of anatomical applications. The high flexibility of CCs especially benefits applications where inter-subject variability is strong (breast, abdomen, joints, heart etc.) and where standard rigid coils would usually be placed far away from the anatomy of interest. Furthermore, the low weight and flexibility allows the fabrication of versatile, “wearable” coils, increasing patient comfort.

REFERENCES

- [1] E. Moser, “Ultra-high-field magnetic resonance: Why and when,” *World J. Radiol.*, vol. 2, no. 1, pp. 37–40, 2010.
- [2] E. Moser, F. Stahlberg, M. E. Ladd, and S. Trattnig, “7-T MR—from research to clinical applications?” *NMR Biomed.*, vol. 25, no. 5, pp. 695–716, May 2012.
- [3] E. Moser, E. Laistler, F. Schmitt, and G. Kontaxis, “Ultra-high field NMR and MRI—the role of magnet technology to increase sensitivity and specificity,” *Frontiers Phys.*, vol. 5, p. 33, Aug. 2017.
- [4] A. Kumar, W. A. Edelstein, and P. A. Bottomley, “Noise figure limits for circular loop MR coils,” *Magn. Reson. Med.*, vol. 61, no. 5, pp. 1201–1209, May 2009.
- [5] A. N. Nnewiwe *et al.*, “Custom-fitted 16-channel bilateral breast coil for bidirectional parallel imaging,” *Magn. Reson. Med.*, vol. 66, no. 1, pp. 281–289, Jul. 2011.
- [6] K. M. Gilbert, J.-G. Belliveau, A. T. Curtis, J. S. Gati, L. M. Klassen, and R. S. Menon, “A conformal transceive array for 7 T neuroimaging,” *Magn. Reson. Med.*, vol. 67, no. 5, pp. 1487–1496, May 2012.
- [7] E. Laistler *et al.*, “*In vivo* MRI of the human finger at 7 T,” *Magn. Reson. Med.*, vol. 79, no. 1, pp. 588–592, Jan. 2018.
- [8] S. Goluch *et al.*, “Proton-decoupled carbon magnetic resonance spectroscopy in human calf muscles at 7 T using a multi-channel radiofrequency coil,” *Sci. Rep.*, vol. 8, no. 1, p. 6211, Dec. 2018.
- [9] W. Kwok, “A volume adjustable four-coil phased array for high resolution MR imaging of the hip,” *Magn. Reson. Mater. Biol., Phys., Med.*, vol. 9, nos. 1–2, pp. 59–64, Oct. 1999.
- [10] G. Adriany *et al.*, “A geometrically adjustable 16-channel transmit/receive transmission line array for improved RF efficiency and parallel imaging performance at 7 Tesla,” *Magn. Reson. Med.*, vol. 59, no. 3, pp. 590–597, Mar. 2008.
- [11] J. A. Nordmeyer-Massner, N. De Zanche, and K. P. Pruessmann, “Mechanically adjustable coil array for wrist MRI,” *Magn. Reson. Med.*, vol. 61, no. 2, pp. 429–438, Feb. 2009.
- [12] B. Wu *et al.*, “Flexible transceiver array for ultrahigh field human MR imaging,” *Magn. Reson. Med.*, vol. 68, no. 4, pp. 1332–1338, Oct. 2012.
- [13] R. Kriegl *et al.*, “Novel inductive decoupling technique for flexible transceiver arrays of monolithic transmission line resonators,” *Magn. Reson. Med.*, vol. 73, no. 4, pp. 1669–1681, Apr. 2015.
- [14] T. Zhang *et al.*, “A semiflexible 64-channel receive-only phased array for pediatric body MRI at 3T,” *Magn. Reson. Med.*, vol. 76, no. 3, pp. 1015–1021, Sep. 2016.
- [15] R. Frass-Kriegl *et al.*, “Flexible 23-channel coil array for high-resolution magnetic resonance imaging at 3 Tesla,” *PLoS ONE*, vol. 13, no. 11, Nov. 2018, Art. no. e0206963.

- [16] S. Hosseinezhadian *et al.*, "A flexible 12-channel transceiver array of transmission line resonators for 7 T MRI," *J. Magn. Reson.*, vol. 296, pp. 47–59, Nov. 2018.
- [17] J. R. Corea *et al.*, "Screen-printed flexible MRI receive coils," *Nature Commun.*, vol. 7, no. 1, Apr. 2016, Art. no. 10839.
- [18] S. A. Winkler *et al.*, "Evaluation of a flexible 12-channel screen-printed pediatric MRI coil," *Radiology*, vol. 291, no. 1, pp. 180–185, 2019.
- [19] J. A. Nordmeyer-Massner, N. De Zanche, and K. P. Pruessmann, "Stretchable coil arrays: Application to knee imaging under varying flexion angles," *Magn. Reson. Med.*, vol. 67, no. 3, pp. 872–879, Mar. 2012.
- [20] A. Port *et al.*, "Towards wearable MR detection: A stretchable wrist array with on-body digitization," in *Proc. 26th Int. Soc. Magn. Reson. Med.*, Paris, France, 2018, p. 17.
- [21] B. Gruber, R. Rehner, E. Laistler, and S. Zink, "Anatomically adaptive coils for MRI—A 6-Channel array for knee imaging at 1.5 Tesla," *Frontiers Phys.*, vol. 8, p. 80, Apr. 2020.
- [22] A. Mehmman *et al.*, "On the bending and stretching of liquid metal receive coils for magnetic resonance imaging," *IEEE Trans. Biomed. Eng.*, vol. 66, no. 6, pp. 1542–1548, Jun. 2019.
- [23] J. A. Malko, E. C. McClees, I. F. Braun, P. C. Davis, and J. C. Hoffman, "A flexible mercury-filled surface coil for MR imaging," *Amer. J. Neuroradiology*, vol. 7, no. 2, pp. 246–247, 1986.
- [24] A. Port *et al.*, "Detector clothes for MRI: A wearable array receiver based on liquid metal in elastic tubes," *Sci. Rep.*, vol. 10, no. 1, p. 8844, Dec. 2020.
- [25] A. Port, R. Luechinger, D. O. Brunner, and K. P. Pruessmann, "Conductive elastomer for wearable RF coils," in *Proc. 28th Int. Soc. Magn. Reson. Med.*, 2020, p. 1137.
- [26] H. J. Zabel, R. Bader, J. Gehrig, and W. J. Lorenz, "High-quality MR imaging with flexible transmission line resonators," *Radiology*, vol. 165, no. 3, pp. 857–859, Dec. 1987.
- [27] N. Haziza, J. Bittoun, and S. Kan, "Multiturn split-conductor transmission-line resonator," *Rev. Sci. Instrum.*, vol. 68, no. 5, pp. 1995–1997, May 1997.
- [28] T. Ruytenberg, A. Webb, and I. Zivkovic, "A flexible five-channel shielded-coaxial-cable (SCC) transceive neck coil for high-resolution carotid imaging at 7T," *Magn. Reson. Med.*, vol. 84, no. 3, pp. 1672–1677, Sep. 2020.
- [29] M. S. M. Mollaei, C. C. Van Leeuwen, A. J. E. Raaijmakers, and C. R. Simovski, "Analysis of high impedance coils both in transmission and reception regimes," *IEEE Access*, vol. 8, pp. 129754–129762, 2020.
- [30] K. Fujimoto *et al.*, "A tight-fit flexible high-impedance coil array for high-resolution imaging of small ex-vivo specimen using a human 7T scanner," in *Proc. 28th Int. Soc. Magn. Reson. Med.*, 2020, p. 4018.
- [31] J.-C. Ginefri *et al.*, "Implanted, inductively-coupled, radiofrequency coils fabricated on flexible polymeric material: Application to *in vivo* rat brain MRI at 7T," *J. Magn. Reson.*, vol. 224, pp. 61–70, Nov. 2012.
- [32] R. Frass-Kriegl *et al.*, "Multi-turn multi-gap transmission line resonators—Concept, design and first implementation at 4.7 T and 7 T," *J. Magn. Reson.*, vol. 273, pp. 65–72, Dec. 2016.
- [33] X. Yang, T. Zheng, Y. Wu, and M. Finnerty, "Coaxial cable magnetic resonance image (MRI) coils," U.S. Patents 9678 180 B2, Jun. 13, 2017.
- [34] B. Zhang, D. K. Sodickson, and M. A. Cloos, "A high-impedance detector-array glove for magnetic resonance imaging of the hand," *Nature Biomed. Eng.*, vol. 2, no. 8, pp. 570–577, Aug. 2018.
- [35] S. E. Zijlema, L. Van Dijk, J. J. W. Legendijk, R. H. N. Tijssen, and C. A. T. Van Den Berg, "A radiolucent and flexible high impedance coil array to improve the imaging performance of a 1.5T MR-linac," in *Proc. 27th Int. Soc. Magn. Reson. Med.*, Montreal, QC, Canada, 2019, p. 1504.
- [36] S.-I. Urayama, B. Zhang, K. Fujimoto, T. Okada, and M. A. Cloos, "A modular 7T highimpedance array for ex-vivo imaging," in *Proc. 27th Int. Soc. Magn. Reson. Med.*, Montreal, QC, Canada, 2019, p. 1541.
- [37] R. S. Stormont *et al.*, "Systems for a radio frequency coil for MR imaging," U.S. Patents 20190277926 A1, Sep. 12, 2019.
- [38] T. Ruytenberg, A. Webb, and I. Zivkovic, "Shielded-coaxial-cable coils as receive and transceive array elements for 7T human MRI," *Magn. Reson. Med.*, vol. 83, no. 3, pp. 1135–1146, Mar. 2020.
- [39] P. Gonord, S. Kan, and A. Leroy-Willig, "Parallel-plate split-conductor surface coil: Analysis and design," *Magn. Reson. Med.*, vol. 6, no. 3, pp. 353–358, Mar. 1988.
- [40] P. Gonord, S. Kan, A. Leroy-Willig, and C. Wary, "Multigap parallel-plate bracelet resonator frequency determination and applications," *Rev. Sci. Instrum.*, vol. 65, no. 11, pp. 3363–3366, 1994.
- [41] S. Serfaty, N. Haziza, L. Darrasse, and S. Kan, "Multi-turn split-conductor transmission-line resonators," *Magn. Reson. Med.*, vol. 38, no. 4, pp. 687–689, Oct. 1997.
- [42] M. D. Harpen, "The theory of shielded loop resonators," *Magn. Reson. Med.*, vol. 32, no. 6, pp. 785–788, Dec. 1994.
- [43] A. Stensgaard, "Optimized design of the shielded-loop resonator," *J. Magn. Reson., Ser. A*, vol. 122, no. 2, pp. 120–125, Oct. 1996.
- [44] J. T. Vaughan, H. P. Hetherington, J. Otu, J. W. Pan, and G. M. Pohost, "High frequency volume coils for clinical NMR imaging and spectroscopy," *Magn. Reson. Med.*, vol. 32, no. 2, pp. 206–218, 1994.
- [45] E. Laistler and E. Moser, "Handy magnetic resonance coils," *Nature Biomed. Eng.*, vol. 2, no. 8, pp. 557–558, Aug. 2018.
- [46] P. K. H. Röschmann, "High-frequency coil system for a magnetic resonance imaging apparatus," U.S. Patents 4746866 A, May 24, 1988.
- [47] J. Mispelter, M. Lupu, and A. Briguet, *NMR Probeheads for Biophysical and Biomedical Experiments: Theoretical Principles and Practical Guidelines*. London, U.K.: Imperial College Press, 2006.
- [48] L. Darrasse and G. Kassab, "Quick measurement of NMR-coil sensitivity with a dual-loop probe," *Rev. Sci. Instrum.*, vol. 64, no. 7, pp. 1841–1844, Jul. 1993.
- [49] S. Chung, D. Kim, E. Breton, and L. Axel, "Rapid B1+ mapping using a preconditioning RF pulse with TurboFLASH readout," *Magn. Reson. Med.*, vol. 64, no. 2, pp. 439–446, Aug. 2010.
- [50] L. Darrasse, "Perspectives with cryogenic RF probes in biomedical MRI," *Biochimie*, vol. 85, no. 9, pp. 915–937, Sep. 2003.
- [51] M. V. Vaidya, C. M. Collins, D. K. Sodickson, R. Brown, G. C. Wiggins, and R. Lattanzi, "Dependence of B1- and B1+ field patterns of surface coils on the electrical properties of the sample and the MR operating frequency," *Concepts Magn. Reson. B, Magn. Reson. Eng.*, vol. 46, no. 1, pp. 25–40, Feb. 2016.
- [52] A. J. E. Raaijmakers, P. R. Luijten, and C. A. T. van den Berg, "Dipole antennas for ultrahigh-field body imaging: A comparison with loop coils," *NMR Biomed.*, vol. 29, no. 9, pp. 1122–1130, Sep. 2016.
- [53] M. A. Ertürk, A. J. E. Raaijmakers, G. Adriany, K. Uğurbil, and G. J. Metzger, "A 16-channel combined loop-dipole transceiver array for 7 Tesla body MRI," *Magn. Reson. Med.*, vol. 77, no. 2, pp. 884–894, 2017.
- [54] K. Lakshmanan, M. Cloos, R. Brown, R. Lattanzi, D. K. Sodickson, and G. C. Wiggins, "The 'loopole' antenna: A hybrid coil combining loop and electric dipole properties for Ultra-High-Field MRI," *Concepts Magn. Reson. B, Magn. Reson. Eng.*, vol. 2020, pp. 1–9, Sep. 2020.
- [55] X. Yan, J. C. Gore, and W. A. Grissom, "Self-decoupled radiofrequency coils for magnetic resonance imaging," *Nature Commun.*, vol. 9, no. 1, p. 3481, Dec. 2018.
- [56] B. Gruber, J. Stockmann, B. Guerin, and L. L. Wald, "Real-time image-based tracking of B0 shim elements in flexible matrix shim arrays for dynamic B0 shimming of the abdomen," in *Proc. 27th Int. Soc. Magn. Reson. Med.*, Montreal, QC, Canada, 2019, p. 1496.



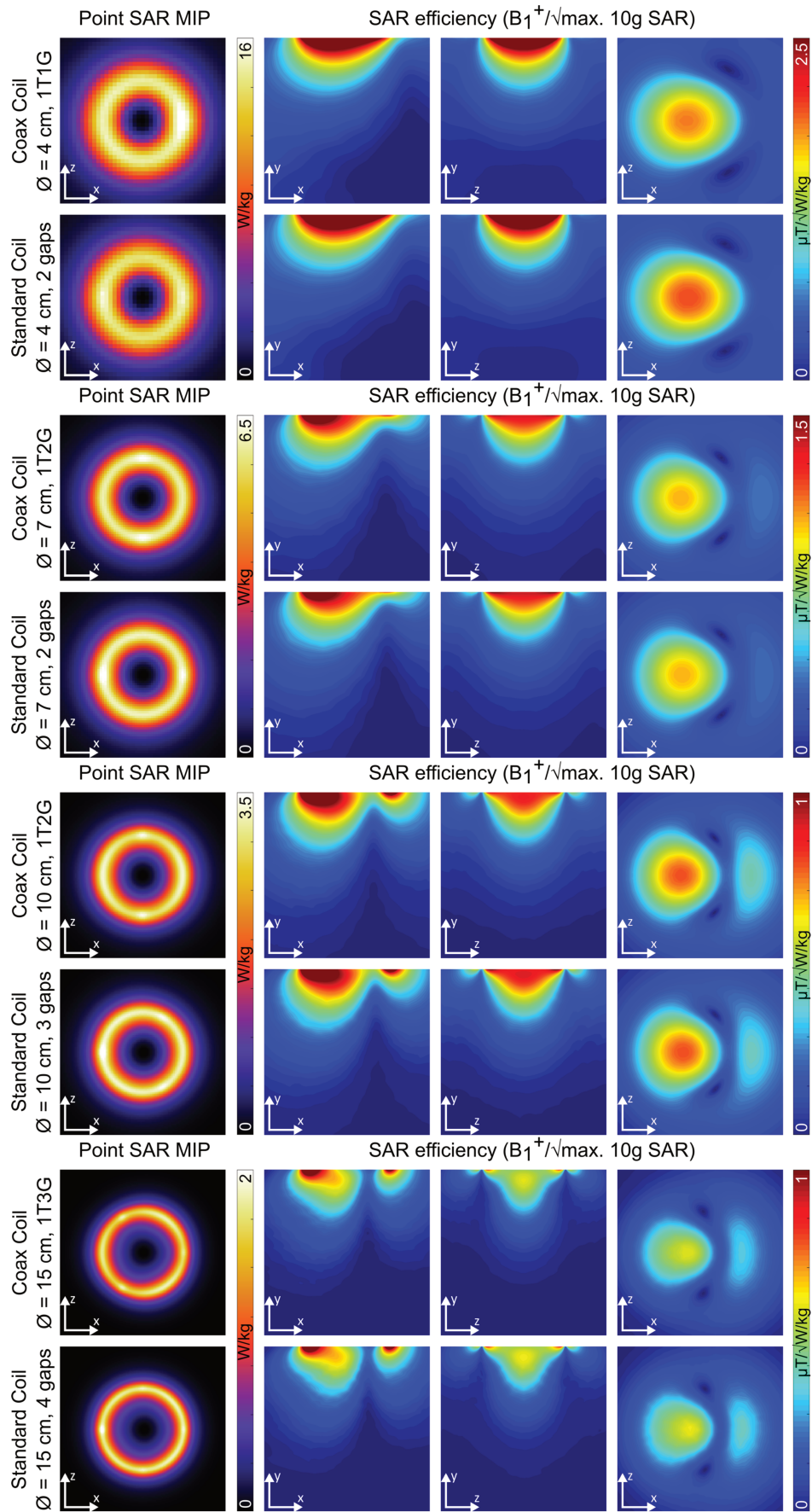
Supplementary Fig. 1: Surface current and surface current density simulation results for all investigated CCs. The surface current densities K at their target Larmor frequencies (f_{Larmor}) are depicted as 3D plots for *iC*, *oCi*, and *oCo*, scaled to their individual maximum. The corresponding surface currents I along the coil winding are shown as line plots for the respective self-resonances (f_0) in blue and f_{Larmor} in red, starting from 0 at the feed point to $n_t \times 2\pi$ in the case of *iC* and *oCi*. For *oCo*, the surface current was integrated over all turns, since this represents the effective current seen at distance from the coil, and the plot only goes to 2π . The feeding port is depicted in black in the *iC* and in case of the MTMG-CCs (a, b, d), connecting structures in *oCi* and *oCo* are depicted in gray. They are necessary to avoid self-intersection between the start and end point. These structures were excluded from surface current evaluation. When operating the CC at f_0 , the surface current at the feed point equals 0, which is generally not the case for other frequencies. For $f_0 < f_{Larmor}$ (a,c,d,e,g,h) the surface current first decreases to 0 before it rises to a local maximum at position $n/n_g \times \pi$. This behavior results in generally lower levels of surface current at f_{Larmor} than at f_0 . Also, an asymmetrical behavior in the first and last coaxial segments is observed. For $f_0 > f_{Larmor}$ (b,f) the surface current starts to rise immediately after the feed point to reach a local maximum at position $n/n_g \times \pi$. At this position, i.e. at an outer gap, the *iC/oCi* surface current level at f_{Larmor} is almost the same as at f_0 , resulting in insignificantly higher *oCo* surface current levels than compared with I at f_0 . An asymmetric behavior in the first and last segments can be observed as well. Further systematic investigation is needed to evaluate whether operation of a CC with a higher self-resonance than the Larmor frequency could bring any benefit or if the optimum in terms of *oCo* surface current amplitude is reached with operation exactly at f_0 for all cases.

SUPPLEMENTARY TABLE I

BENCH MEASUREMENT RESULTS FOR 3 T AND 7 T SCs AND CCs WITH AND WITHOUT INTERFACE FOR DIFFERENT COIL POSITIONS, AND DIFFERENT TUNING AND MATCHING (T+M) CONFIGURATIONS.

d ₀ [cm]	coil, position	3 T – Rx-only										7 T – Tx/Rx									
		coil only					with interface (T+M on flat phantom)			with interface (T+M on balloon phantom)		coil only				with interface (T+M on flat phantom)			with interface (T+M on balloon phantom)		
		Q _u	f _{0,u} [MHz]	Q _i	f _{0,i} [MHz]	Q _u /Q _i	Q _i	S ₁₁ [dB]	Δf _{0,i} [%]	Q _i	S ₁₁ [dB]	Q _u	f _{0,u} [MHz]	Q _i	f _{0,i} [MHz]	Q _u /Q _i	Q _i	S ₁₁ [dB]	Δf _{0,i} [%]	Q _i	S ₁₁ [dB]
4	SC, flat	301	123.1	67	122.2	4	57	-28.0	-	177	-25.4	351	297.4	18	288.1	19	16	-21.3	-	76	-17.0
	CC, flat	211	109.7	73	108.4	3	70	-33.2	-	-	-	220	286.2	23	276.2	10	28	-24.9	-	-	-
	CC, half-bent	223	110.1	134	109.4	2	98	-7.2	+0.4	-	-	225	290.2	37	281.3	6	35	-7.6	+0.6	-	-
	CC, bent	225	109.9	126	109.5	2	100	-7.1	+0.4	136	-17.1	227	291.5	75	282.5	3	41	-4.4	+0.9	65	-22.2
7	SC, flat	390	123.1	27	120.9	14	23	-30.8	-	155	-15.0	261	297.3	9	278.9	28	9	-19.6	-	18	-15.3
	CC, flat	99	119.1	25	115.8	4	30	-20.4	-	-	-	206	298.5	9	280.0	22	14	-21.6	-	-	-
	CC, half-bent	100	120.6	42	117.8	2	46	-6.0	+1.0	-	-	209	302.2	10	282.2	21	15	-23.3	+0.0	-	-
	CC, bent	99	121.8	57	119.8	2	51	-2.9	+1.8	94	-30.1	202	304.9	10	292.9	20	16	-10.7	+1.5	17	-32.7
10	SC, flat	321	123.3	15	119.4	22	13	-27.8	-	63	-26.8	122	297.4	5	261.9	26	4	-18.4	-	8	-15.6
	CC, flat	224	107.9	21	102.0	11	24	-31.8	-	-	-	156	258.5	6	243.8	28	10	-20.4	-	-	-
	CC, half-bent	224	109.0	33	105.0	7	32	-5.9	+1.7	-	-	159	260.5	9	244.6	18	11	-20.6	+0.8	-	-
	CC, bent	217	110.9	40	105.7	5	33	-3.9	+2.1	59	-29.8	169	264.5	10	246.3	17	15	-20.5	-0.8	11	-22.5
15	SC, flat	304	123.3	10	116.7	30	8	-29.2	-	38	-17.1	97	297.3	3	288.9	29	6	-34.0	-	15	-17.9
	CC, flat	65	110.8	11	107.3	6	15	-18.9	-	-	-	97	261.5	6	271.3	17	12	-30.7	-	-	-
	CC, half-bent	69	111.6	12	107.8	6	18	-15.6	+0.2	-	-	102	262.3	5	252.9	20	13	-31.7	-0.1	-	-
	CC, bent	71	113.4	20	110.1	4	21	-8.0	+1.1	45	-35.0	122	265.7	8	257.9	15	13	-21.2	-0.6	12	-24.7

Matching levels (S₁₁ in dB) were determined at f_{Larmor} = 123.2 MHz for 3 T coils and f_{Larmor} = 297.2 MHz for 7 T coils. Δf_{0,i} indicates the deviation from f_{Larmor} in % for the bent and half-bent case.



Supplementary Fig. 2: Point SAR (W/kg) and SAR efficiency ($\mu\text{T}/\sqrt{\text{W/kg}}$) simulation results for all SCs and CCs used at 7 T, with diameters ranging from 4 to 15 cm. Point SAR maximum intensity projections (MIPs) are calculated in the coronal (xz) plane, over the whole sample. SAR efficiency maps are shown for a transversal and sagittal slice through the coil center, and a coronal slice (at a distance of $d_0/4$ from the coil) for CCs and SCs, respectively. It can be observed that the spatial distribution of B_1^+ and SAR is very similar for CCs operated close to their self-resonance and SCs.

4.3 Supplementary studies with flexible coaxial RF coils

4.3.1 Introduction

This section presents additional information on the development and implementation of coaxial RF coils, including single-turn single-gap and multi-turn multi-gap CCs, resulting from a series of supplementary studies. Aspects shown and discussed in the supplementary studies comprise results from analytical calculations, EM simulations, bench tests and MRI. The data was to a majority not presented in the article and partly presented during international and national (French) scientific conferences [221–226]. For data also shown in the article, this chapter allows for a deeper discussion of coaxial coil properties and a more detailed explanation of results and perspectives.

All supplementary studies were grouped into the following categories:

- **Design theory**

Section 4.3.2 first focuses on the experimental validation of the design concept and equivalent circuit model of CCs, comparing calculated and simulated to measured resonance frequency values. A modified boxplot diagram containing details on the CC solutions depending on the diameter range and B_0 field strength is presented. This is followed by a detailed coaxial coil resonance frequency behavior and interface component analysis.

- **1T1G vs. MTMG coaxial coils**

In section 4.3.3, the comparison of same-size 1T1G-CCs and MTMG-CCs at 3 T and at 7 T based on analytical calculations, EM simulations as well as bench (3 T and 7 T) and MR tests (3 T only) is discussed.

- **MR experiments**

Ultimately, in section 4.3.4, relative flip angle maps characterizing the active detuning performance of 3 T SCs and CCs are presented alongside with a more detailed SNR and transmit efficiency analysis (3 and 7 T) of all coils used in *Article I*. Furthermore, MR images of different types of fruit, acquired with 3 T CCs of four different sizes are shown.

4.3.2 Design theory

As mentioned in *Article I*, the novel design concept for flexible MTMG coaxial coils was introduced in analogy to parallel-plate MTMG TLRs fabricated using semi-flexible substrate [41] and was initiated by the increasing recent research interest in flexible coaxial RF coils [55,118,120,121]. The studies summarized below were dedicated to the validation of the proposed equivalent circuit model and to a better understanding of the (MTMG-)CC functioning principle.

4.3.2.1 Validation of the equivalent circuit model

One focus of preliminary studies was the experimental validation of the theoretical circuit, modelled for self-resonance calculations of coaxial coils.

The data collection includes 55 coaxial coils fabricated of 6 different cables (A-F, see Fig. 2, *Article I*), with diameters of 4, 6, 9, 10, 12, 15 or 20 cm and different combinations of turns and gaps ($n_{t,max} = 4$, $n_{g,max} = 8$). Measured self-resonance frequencies (1st resonant mode) range from 17.7 MHz to 631.9 MHz.

The scatter plot in Figure 4.1 visualizes the correlation between bench-measured ($f_{0,meas}$) and theoretically predicted self-resonance frequency values ($f_{0,calc}$, 1st resonant mode). On the bench, all coils were measured using the double-loop probe method [62] in unloaded configuration. Larger absolute deviations between measured and calculated frequencies occur when f_0 increases.

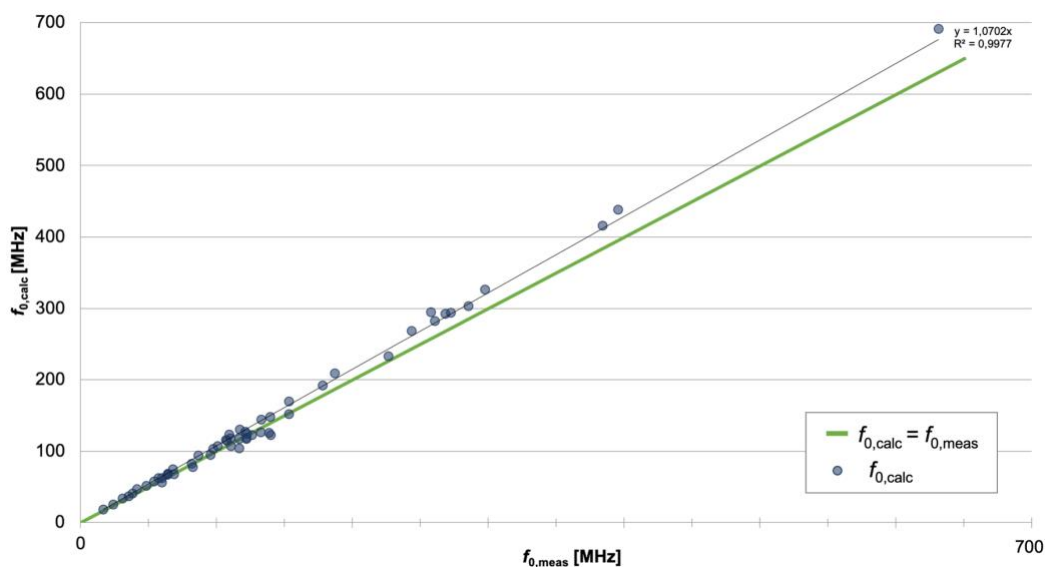


Figure 4.1: Correlation between calculated and measured (unloaded) self-resonance frequencies

Looking at the relative deviation between measured f_0 values and calculated or simulated ones ($\frac{f_{0,calc}}{f_{0,meas}} - 1$ or $\frac{f_{0,sim}}{f_{0,meas}} - 1$ in %) in Figure 4.2, Figure 4.3 and values listed in Table 4.1, it was found that the maximum deviation for calculated values is +13.9 % (10 cm 1T2G coil, cable C) whereas for values determined in EM simulations, the maximum relative deviation is +6.9 % (10 cm 1T2G coil, cable C). The bullet area in Figure 4.2 is proportional to the number of gaps and proportional to the number of turns in Figure 4.3. There was no direct correlation that could be identified between the relative deviation, the number of turns, number of gaps, resonance frequency or cable type. In general, there is a slight tendency towards larger relative deviations between $f_{0,calc}$ and $f_{0,meas}$ with a high number of gaps and/or turns and at high frequencies (≈ 250 MHz and above), where $f_{0,calc}$ tends to be an overestimation of what is measured on the bench. It is evident that one also has to consider initial inaccuracies in the coaxial coil fabrication process as potential source for deviations in resonance frequency. The difficulty of accurate gap fabrication and re-soldering of outer conductors depends on the number of gaps and turns but also on the cable type. When the dielectric material of either the insulation layer between outer and inner conductor or the cable jacket is foamed polyethylene (PE), e.g. as in cable C, which has a much lower melting point than other materials (e.g. polytetrafluoroethylene, PTFE), this complicates soldering of surrounding conductors, and thus, gap construction.

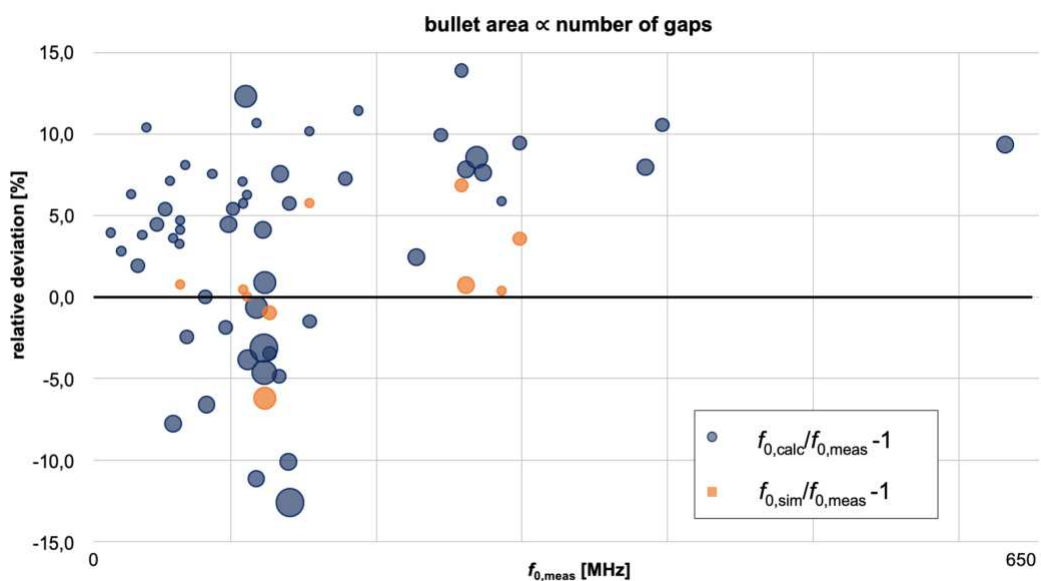


Figure 4.2: Relative deviation between resonance frequency calculations ($f_{0,calc}$) and measurements ($f_{0,meas}$), the bullet area is proportional to the number of gaps (n_g).

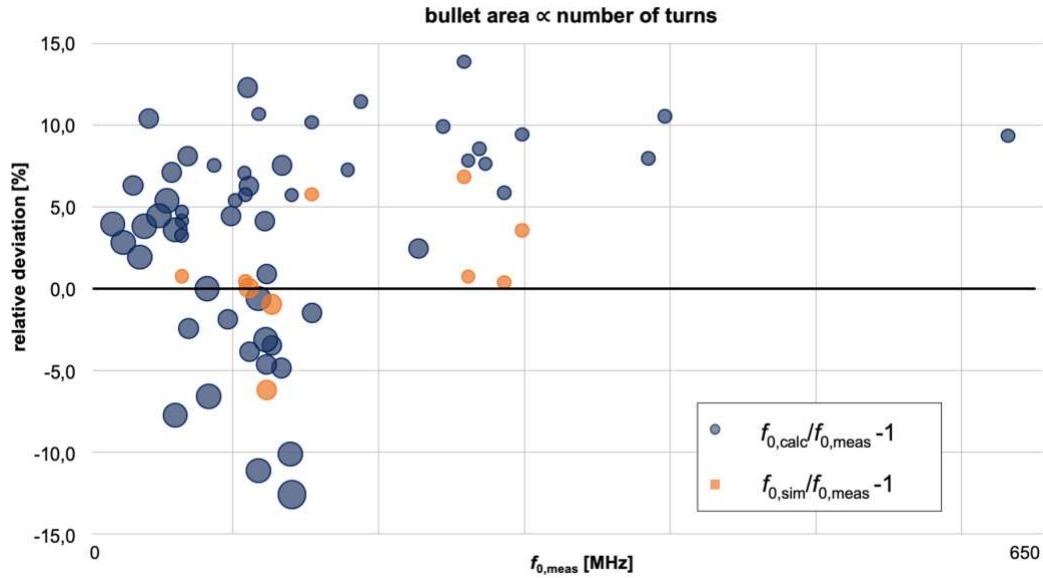


Figure 4.3: Relative deviation between resonance frequency calculations ($f_{0,calc}$) and measurements ($f_{0,meas}$), the bullet area is proportional to the number of turns (n_t).

d_0 [cm]	cable	n_t	n_g	$f_{0,meas}$ [MHz]	$f_{0,calc}$ [MHz]	$f_{0,calc}/f_{0,meas} - 1$ [%]
4	B	1	1	286.2	303.0	5.9
4	D	2	1	111.0	118.0	6.3
4	E	3	1	60.5	62.7	3.6
6	A	1	1	187.8	209.3	11.4
6	A	1	2	396.4	438.3	10.6
6	A	1	3	631.9	691.1	9.4
6	A	2	1	68.9	74.5	8.1
6	A	2	2	154.3	152.0	-1.5
6	A	2	3	227.4	233.0	2.5
6	A	3	1	39.2	40.7	3.8
6	A	3	2	82.4	82.4	0.0
6	A	3	3	139.4	125.3	-10.1
7	E	1	1	154.1	169.8	10.2
7	B	1	2	298.5	326.7	9.4
7	A	2	1	58.1	62.3	7.1
7	A	2	2	133.2	126.7	-4.9
7	E	2	2	126.8	122.4	-3.5
7	A	3	3	117.5	104.4	-11.1
9	A	1	1	117.8	130.4	10.7
9	A	1	2	244.3	268.6	9.9
9	A	1	3	384.9	415.6	8.0
9	A	2	1	42.2	46.6	10.4
9	A	2	2	96.4	94.6	-1.9
9	A	2	3	133.7	143.8	7.6
9	A	3	1	24.8	25.5	2.8

9	A	3	2	49.3	51.5	4.5
9	A	3	3	83.4	77.9	-6.6
10	A	1	1	108.5	114.7	5.8
10	A	1	1	107.9	115.6	7.1
10	C	1	2	258.5	294.4	13.9
10	A	2	3	122.1	127.2	4.1
10	C	3	2	54.9	57.8	5.4
10	A	3	5	117.5	116.8	-0.6
10	A	4	8	140.6	122.9	-12.6
12	A	1	1	87.3	93.9	7.6
12	A	1	2	178.8	191.8	7.3
12	A	1	3	273.3	294.2	7.6
12	A	2	1	31.6	33.6	6.3
12	A	2	2	69.7	68.0	-2.4
12	A	2	3	98.6	103.0	4.5
12	A	3	1	17.7	18.4	4.0
12	A	3	2	36.3	37.0	1.9
12	A	3	3	60.6	55.9	-7.8
15	B	1	1	65.1	67.8	4.1
15	B	1	1	65.1	68.2	4.7
15	A	1	2	140.3	148.4	5.7
15	C	1	3	261.5	282.0	7.8
15	A	2	4	111.5	107.2	-3.8
15	B	2	5	123.2	124.3	0.9
15	A	3	8	122.7	118.9	-3.1
20	C	1	1	64.8	66.9	3.3
20	A	1	2	101.5	107.0	5.4
20	F	1	5	269.2	292.3	8.6
20	C	2	5	110.1	123.7	12.3
20	A	2	6	123.0	117.3	-4.6

Table 4.1: Table listing the relative deviation between resonance frequency calculations ($f_{0,calc}$) and measurements ($f_{0,meas}$), the green color gradient indicates increasing number of turns (n_t) or gaps (n_g) and increasing frequency ($f_{0,meas}$).

In conclusion, the equivalent circuit model presented in *Article I* is reliable enough for resonance frequency predictions to set the parameter range such that computation times in EM simulations can be reduced. For more precise self-resonance frequency determinations, EM simulations are a helpful tool as detailed 3D models of the coaxial coil (material and structure of the conductors and dielectric) lead to simulated frequency values that come closer to the experimentally determined ones (see orange dots in Figure 4.2 and Figure 4.3).

4.3.2.2 Coaxial coil diameter ranges

After having demonstrated the validity of the equivalent circuit model, the calculated coaxial coil diameter range shown in the boxplot figure (Fig. 5) of *Article I* can be modified to contain more detailed information about possible CC solutions. In Figure 4.4 a distinction is made between possible coil diameter ranges for 1T1G-CCs (yellow boxes), 1TMG-CCs (dark blue boxes), MT1G-CCs (orange boxes) and ranges where either MTMG or 1T1G (dark grey boxes) and MTMG or MT1G (light grey boxes) CC solutions can be found. It is shown that for the chosen parameter space (Table I, *Article I*), only a very limited range of small coil diameters can be covered with MT1G solutions. If one would consider also smaller B_0 field strengths, these ranges would increase accordingly. At high field strengths, for large coil diameters, only 1TMG solutions were found. This range would extend to smaller coil sizes for higher B_0 field strengths. It has to be noted that within the ranges where either MTMG- or 1TMG-/MT1G-CC solutions are possible, the coil designer can choose between the solution closest to the target frequency and the easiest to fabricate (low number of gaps) or the one with the least coil losses and highest flexibility (low number of turns and gaps). In *Article I*, a trade-off was found to limit coil losses but still use a flexible coaxial coil with a calculated self-resonance close to the desired Larmor frequency ($\pm 10\%$). At a given resonance frequency (or B_0 field strength) for ^1H imaging (or any other nucleus), compared to a 1T1G-CC, using multiple turns allows for smaller coil diameters, whereas adding gaps allows for larger coil diameters. For a fixed coil diameter, the resonance frequency increases with the number of gaps and decreases with the number of turns.

In conclusion, it is demonstrated, that by enabling more than one turn and/or gap, practically any coil diameter can be chosen, which allows for optimization of the coil size with regard to target penetration depth.

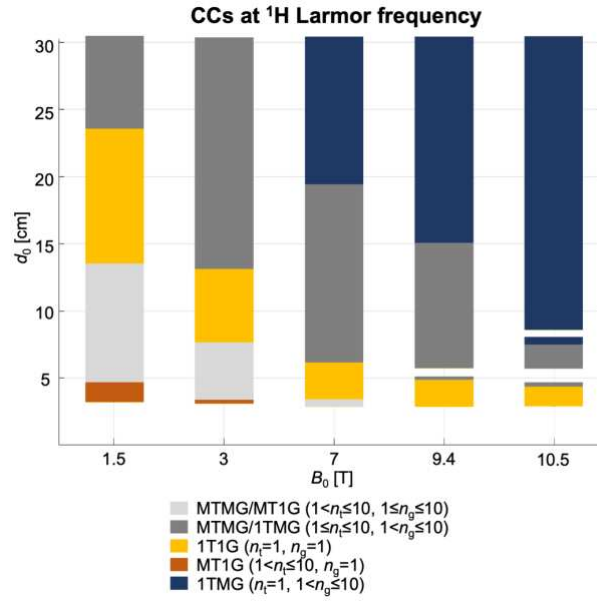


Figure 4.4: Coil diameter range depending on the gaps/turns CC configuration and B_0 field strength

4.3.2.3 Resonance behavior and interface component analysis

Until now, only the self-resonances of CCs as described in *Article I* were considered. For MR experiments with CCs, the coil has to be related to the MR scanner with an interfacing circuitry for tuning, matching and AD for Rx-only coils. For MTMG-CC interface design, the 1T1G-CC interface as described by Zhang *et al.* [55] was used as a starting point. Modifications were made mainly concerning the AD for multi-gap coils as described in *Article I*.

To better understand the resonance frequency behavior of a CC, the self-resonances of a CC alone and resonances of a CC interfaced to the MR scanner using different tuning, matching and AD components have to be explained. First, it has to be noted that the self-resonance frequency of a coaxial coil can be determined assuming a series resonant circuit with impedance $Z_{\text{coil,self,series}}(\omega)$ (Eq. 4.1) only when it is measured inductively via a pick-up loop (as also mentioned in *Article I*, Eq. 4.1). The equivalent circuit schematic for the coaxial coil alone is shown in Fig. 1 of *Article I*.

$$Z_{\text{coil,self,series}}(\omega) = R + Z_{\text{shield}}(\omega) + 2n_g Z_{\text{TL}}(\omega) \quad \text{Eq. 4.1}$$

Eq. 4.2 - Eq. 4.4 describe the coaxial stub impedance Z_{TL} and the outer shield impedance Z_{shield} (assuming lossless stubs and inductors, thus neglecting resistive parts). w_g denotes the width of one gap and l the length of one coaxial stub, depending on the number of turns and gaps.

$$Z_{\text{TL}}(\omega) = iX_{\text{TL}}(\omega) = -iZ_0 \cot\left(\frac{\omega l \sqrt{\epsilon_r}}{c_0}\right) \quad \text{Eq. 4.2}$$

$$l = \frac{n_t d_0 \pi}{2n_g} - w_g \quad \text{Eq. 4.3}$$

$$Z_{\text{shield}}(\omega) = iX_{\text{shield}}(\omega) = in_t^2 \omega \mu_0 \frac{d_0}{2} \left[\ln\left(\frac{8d_0}{d_1}\right) - 2 \right] \quad \text{Eq. 4.4}$$

If the coil's self-resonance frequency is measured connecting the coil to the VNA across the coil port (at the inner conductors, at an inner gap, see *Article I* Fig. 1c), the formula for a parallel resonant circuit has to be considered. The coil's parallel impedance without any tuning or matching components, $Z_{\text{coil,self,parallel}}(\omega)$, is given by Eq. 4.5.

$$Z_{\text{coil,self,parallel}}(\omega) = \frac{1}{\frac{1}{R + Z_{\text{shield}}(\omega) + (n_g - 1)2Z_{\text{TL}}(\omega)} + \frac{1}{2Z_{\text{TL}}(\omega)}} \quad \text{Eq. 4.5}$$

R is the sum of coil (R_c) and sample losses (R_s). One can also write:

$$Z_{\text{coil,self,parallel}}(\omega) = \frac{2Z_{\text{TL}}(\omega) \cdot (R + Z_{\text{shield}}(\omega) + (n_g - 1)2Z_{\text{TL}}(\omega))}{2Z_{\text{TL}}(\omega) + R + Z_{\text{shield}}(\omega) + (n_g - 1)2Z_{\text{TL}}(\omega)} \quad \text{Eq. 4.6}$$

Eq. 4.6 explains the high impedance characteristics of coaxial coils, if ω approaches ω_0 , i.e. $2Z_{\text{TL}}(\omega) + Z_{\text{shield}}(\omega) + (n_g - 1)2Z_{\text{TL}}(\omega) = 0$ and assuming $R = 0$, then $Z_{\text{coil,self,parallel}}(\omega) = \infty$. Realistic values for R are in the tens of Ω range, which can result in $k\Omega$ input impedances of CCs [55].

Multiple self-resonance modes in coaxial coils (1T1G-CCs and MTMG-CCs) can be attributed to the coaxial stub reactance ($X_{\text{TL}}(\omega)$) behavior. The formula for $X_{\text{TL}}(\omega)$ (part of Eq. 4.2) can be rewritten to express the relationship between the wavelength λ , the physical stub length l to the stub reactance:

$$X_{\text{TL}}(\omega) = -Z_0 \cot\left(\frac{\omega l \sqrt{\epsilon_r}}{c_0}\right) = -Z_0 \cot\left(\frac{2\pi l}{\lambda}\right) \quad \text{Eq. 4.7}$$

$$\lambda = \frac{c_0 2\pi}{\sqrt{\epsilon_r} \omega} \quad \text{Eq. 4.8}$$

The cotangent is a periodic function with period π . The $-\cot(x)$ is negative for $n\pi < x < (2n + 1)\frac{\pi}{2}$ and positive for $(2n + 1)\frac{\pi}{2} < x < (n + 1)\pi$. Here, n describes the number of resonant modes ($n = 0, 1, 2, \dots$), where $n = 0$ is the first self-resonance (denoted as f_0). Therefore, the reactive behavior of the open-circuited coaxial stub changes with period $(2n + 1)\frac{\pi}{2}$ from capacitive to inductive, every time

$$\frac{2\pi l}{\lambda} = (2n + 1)\frac{\pi}{2} \text{ and, as a consequence, if } l = (2n + 1)\frac{\lambda}{4}.$$

From this, it can be seen that an open-circuited stub can be modeled as

- a capacitance for stub lengths $n\frac{\lambda}{2} < l < (2n + 1)\frac{\lambda}{4}$ and as
- an inductance for stub lengths $(2n + 1)\frac{\lambda}{4} < l < (n + 1)\frac{\lambda}{2}$.

Figure 4.5 shows the absolute values of the total capacitive impedance ($2Z_{TL}(\omega)$) and inductive impedance ($Z_{shield}(\omega)$) of a 20 cm 1T1G-CC constructed with cable A (see Fig. 2, Article I), over a frequency range from 0 to 800 MHz. This coil example with a rather low first self-resonance due to the large coil diameter was chosen in order to demonstrate the occurrence of multiple self-resonances in the chosen frequency range.

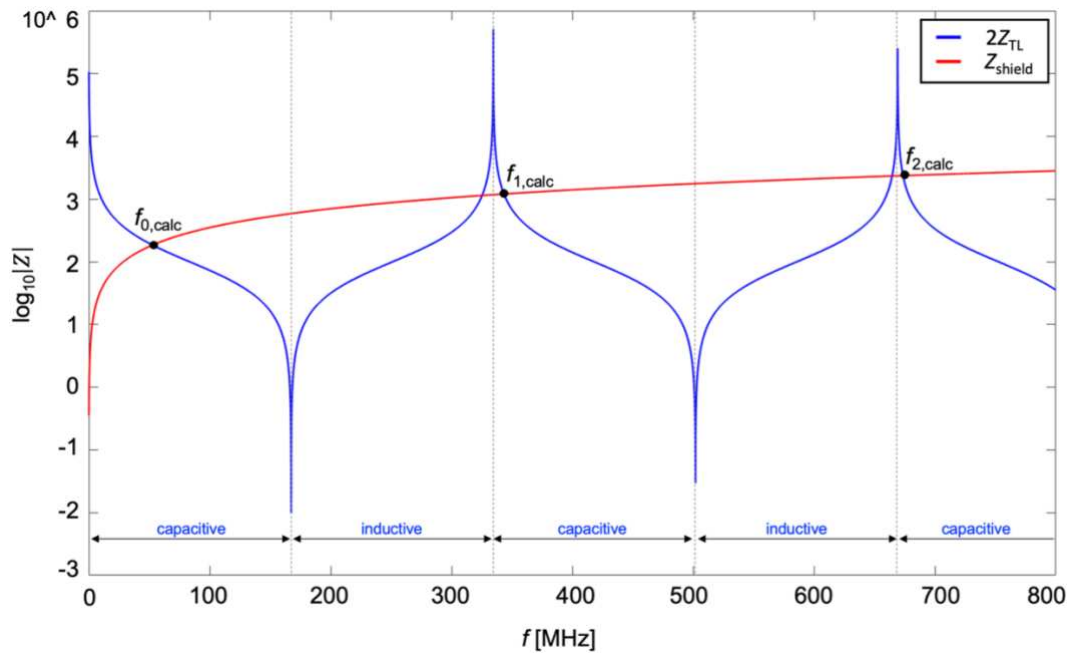


Figure 4.5: Total capacitive impedance ($2Z_{TL}$) and inductive impedance (Z_{shield}) of a 20 cm 1T1G-CC. Resonances occur when the capacitive and inductive parts have same absolute values (i.e. imaginary reactive parts cancel each other out).

Self-resonances occur every time the capacitive and inductive parts have same (absolute) values at intersections of both curves, i.e. when imaginary parts of the impedances cancel each other out. At frequencies where the coaxial stub length equals $(2n + 1) \frac{\lambda}{4}$, the open-circuited coaxial transmission line acts as a series resonant circuit and the impedance is at a minimum (low resistance, i.e. it appears as a short). At frequencies where the coaxial stub length equals $(n + 1) \frac{\lambda}{2}$, the coaxial transmission line acts as a parallel resonant circuit, the impedance is at a maximum (high resistance, i.e. it appears as an open). In between the impedance minima and maxima, the coaxial stub either acts as an inductance or a capacitance, depending on the relation between stub length and wavelength, as detailed in bullet points above and marked in Figure 4.5. As $Z_{\text{shield}}(\omega)$ is proportional to ω and $Z_{\text{TL}}(\omega)$ is a function of $\cot\left(\frac{\omega L \sqrt{\epsilon_r}}{c_0}\right)$, the self-resonances $f_{0,\text{calc}}$, $f_{1,\text{calc}}$ and $f_{2,\text{calc}}$ are not linearly related. In Table 4.2, some examples measured on the bench (inductively with a double pick-up probe with baseline $S_{21} < -80$ dB) are given, together with the respective relative deviation between calculated and measured resonance frequency values.

	cable	d_0 [cm]	n_t	n_g	f_0 [MHz]	$f_{0,\text{calc}}/f_{0,\text{meas}}-1$ [%]	f_1 [MHz]	$f_{1,\text{calc}}/f_{1,\text{meas}}-1$ [%]
meas.	A	12	1	1	88.1	+5.9 %	534.5	+8.6 %
calc.					93.3		580.2	
meas.	A	10	1	1	121.7	-5.8 %	699.0	+0.3 %
calc.					114.7		700.9	
meas.	A	6	3	1	40.3	+0.5 %	435.5	-13.4 %
calc.					40.5		377.0	

Table 4.2: Bench measurement examples for two self-resonance modes of CCs without interfacing circuitry

The modified circuit schematic with additional tuning components L_T and/or C_T used to adjust the coaxial coil's resonance frequency measured at the coil port is shown in Figure 4.6. In the most simple case of a 1T1G-CC, two coaxial stub segments and the outer shield form a parallel resonant circuit together with L_T and/or C_T . This parallel circuit is in series to the matching capacitors. For multi-gap coils, $2(n_g - 1)$ times the number of stubs ($Z_{\text{TL}}(\omega)$) can be seen in series with the outer shield ($Z_{\text{shield}}(\omega)$), which are then in parallel to the coaxial stubs at the coil port ($2Z_{\text{TL}}(\omega)$), again in

parallel to the tuning components (L_T and/or C_T) and in series to matching components.

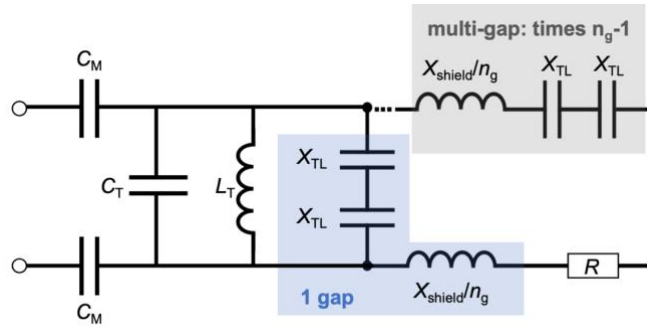


Figure 4.6: Equivalent circuit including tuning and (symmetric) matching components

The impedance formula for the parallel resonant circuit with tuning and matching components $Z_{\text{coil,TM}}(\omega)$ is as follows:

$$\begin{aligned}
 & Z_{\text{coil,TM}}(\omega) \\
 &= \frac{1}{\frac{1}{R + Z_{\text{shield}}(\omega) + (n_g - 1)2Z_{\text{TL}}(\omega)} + \frac{1}{2Z_{\text{TL}}(\omega)} + \frac{1}{Z_{L_T}(\omega)} + \frac{1}{Z_{C_T}(\omega)}} \\
 &+ Z_M(\omega)
 \end{aligned} \tag{Eq. 4.9}$$

The tuning and matching components' impedances (assuming ideal capacitors and inductors, thus neglecting resistive parts) are given by:

$$Z_{L_T}(\omega) = i\omega L_T \tag{Eq. 4.10}$$

$$Z_{C_T}(\omega) = -\frac{i}{\omega C_T} \tag{Eq. 4.11}$$

$$Z_{C_M}(\omega) = -\frac{i}{\omega C_M/2} \tag{Eq. 4.12}$$

To illustrate the effect of tuning components in parallel to the coaxial coil port, exemplary impedance calculations (see Figure 4.7) and consequently the determination of the resonance frequency ($\text{Im}(Z) = 0$ at resonance) were performed for the following coil and interfacing configurations:

1T1G-CC:

- $d_0 = 7 \text{ cm}$
- cable E ($d_1 = 1.17 \text{ mm}$, $Z_0 = 50 \Omega$, $\varepsilon_r = 1.6$)
- $L_T = 300 \text{ nH}$
- $C_T = 4.4 \text{ pF}$
- $R = 10 \Omega$
- $Z_{C_M}(\omega) = 0$

→ CC only, $Z_{\text{coil,self}}(\omega)$

→ parallel tuning inductor L_T across the CC port, $Z_{\text{coil},L_T}(\omega)$

→ parallel tuning capacitor C_T across the CC port, $Z_{\text{coil},C_T}(\omega)$

→ parallel tuning capacitor C_T and inductor L_T across the CC port, $Z_{\text{coil},C_T+L_T}(\omega)$

Inductive fine-tuning components at the coil port are required if for example the coil is too long and therefore the self-resonance lower than an arbitrarily chosen target resonance frequency. In this case, a capacitive imaginary part appears at the target resonance frequency which can be compensated by a tuning inductor L_T parallel to the coil port. Thus, adding a tuning inductor increases the resonance frequency as shown in Figure 4.7. The larger the L_T value, the less the influence on the resonance frequency (Eq. 4.9, Eq. 4.10). If the coil is too short and therefore the self-resonance higher than the arbitrarily chosen resonance frequency, an inductive imaginary part appears which can be compensated by a tuning capacitor (or a tuning capacitor in combination with a tuning inductor) at the coil port. In Figure 4.7 it can be seen that adding only a tuning capacitor at the coil port decreases the resonance frequency. The larger the C_T value, the larger the decrease in resonance frequency (Eq. 4.9, Eq. 4.11). If both, L_T and C_T are used, L_T counteracts the effect of C_T and therefore the resonance frequency is only slightly shifted down in the example shown in Figure 4.7.

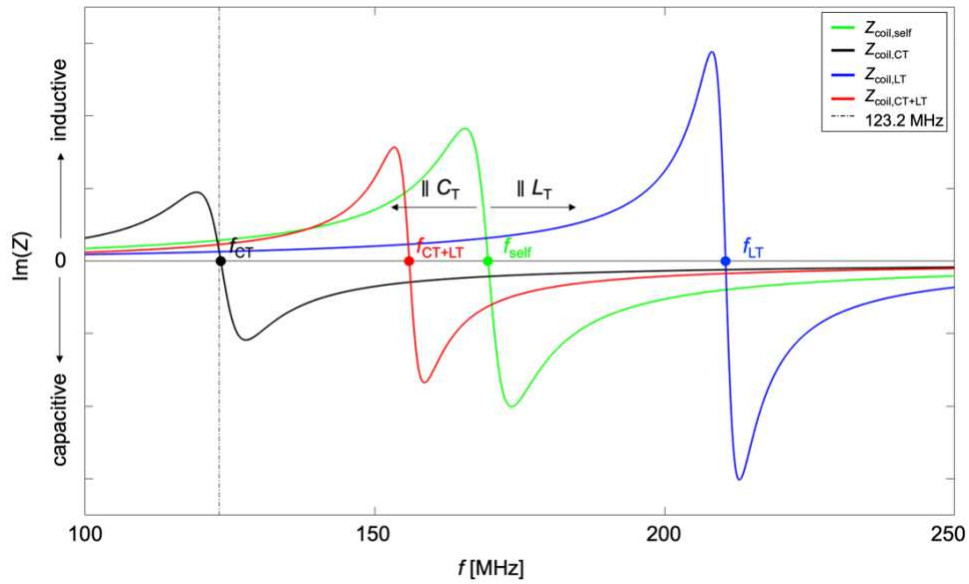


Figure 4.7: Effect of tuning components L_T and/or C_T parallel to the coil port

When plotting the absolute impedance values on a logarithmic scale as shown in Figure 4.8 it can be seen that the series impedance of the CC (according to Eq. 4.1), is at a minimum at resonance, whereas parallel circuits (Eq. 4.9) show an impedance peak at their respective resonance frequencies [227].

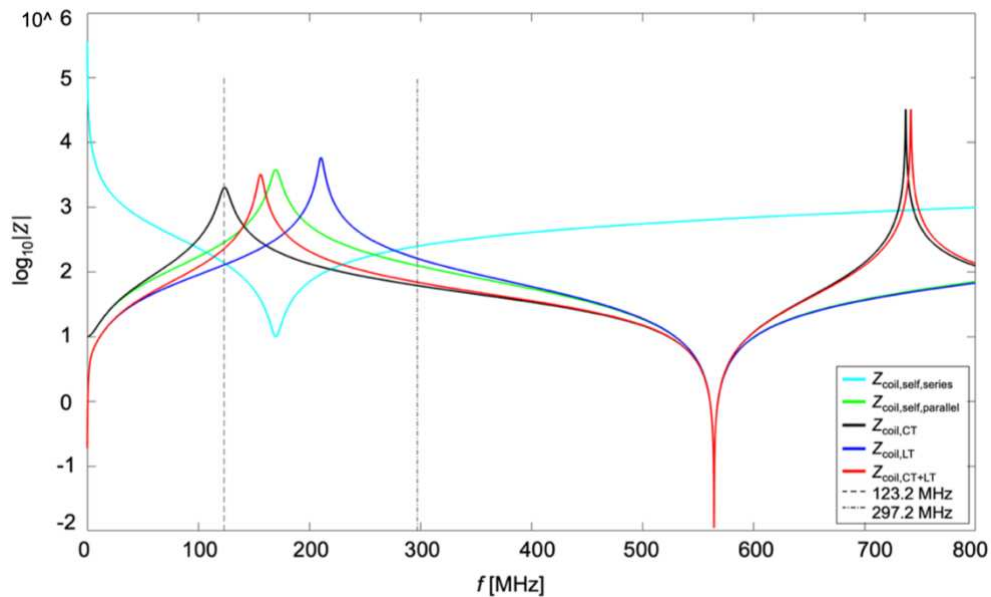


Figure 4.8: Impedance maxima at resonance for parallel resonance circuits ($Z_{\text{coil,self,parallel}}$, $Z_{\text{coil,CT}}$, $Z_{\text{coil,LT}}$, $Z_{\text{coil,CT+LT}}$) and impedance minimum for the series resonance circuit ($Z_{\text{coil,self,series}}$). Another impedance minimum, i.e. resonance dip, occurs at around 580 MHz when the coaxial stub appears as an open circuit which is the case when the stub length equals $(2n + 1) \frac{\lambda}{4}$

While the second self-resonance of this specific CC example lies outside of the plotted frequency range, in case of tuning with a C_T or a $C_T + L_T$ it is visible slightly above 700 MHz.

Also, for multi-gap coils ($n_g > 1$), additional parallel resonances can occur due to inductive tuning components (L_T), following Eq. 4.9. As sketched in Figure 4.6, the coaxial stubs at the coil port form a resonant circuit with L_T and the remaining stubs along the loop form a series resonance circuit. This is the reason why AD components are needed at every gap for Rx-only coils, to eliminate any residual resonance. Still, also with multiple resonances, for the self-resonance of the coaxial coil close to the desired operation frequency (f_L), the trends for resonance frequency fine-tuning (described more in detail for a 1T1G-CC above) apply: the CC resonance seen across the coil port can be tuned down with a C_T and increased with an L_T .

Figure 4.9 shows screenshots of S_{21} measurements carried out with a double pick-up probe [62], for each 7 T CC with a tuning L_T connected across the coil port. To evaluate the influence of tuning components only, the coil port was left open (no 50Ω matching) and coils were measured in unloaded configuration. The measured unloaded frequency shown in Figure 4.9 doesn't match the Larmor frequency as for MRI, the self-resonance is shifted down by loading and adjusted to exactly match the target Larmor frequency (297.2 MHz) in the complete interface configuration with symmetric matching capacitors.

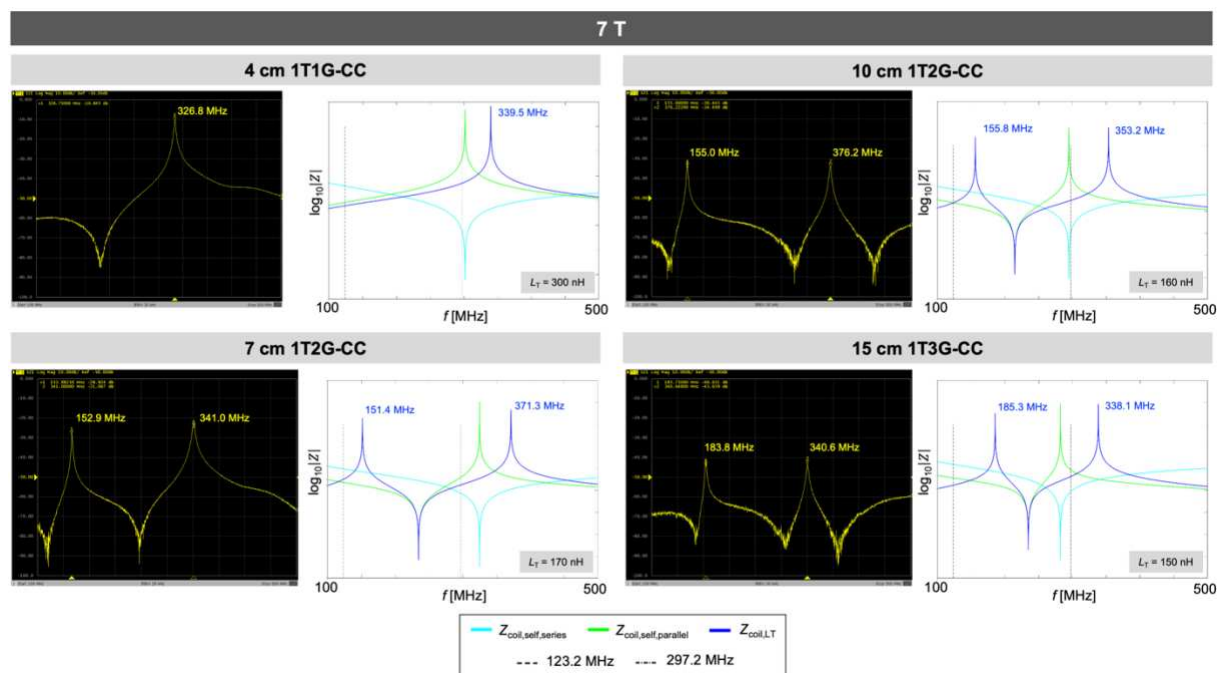


Figure 4.9: S_{21} measurements and impedance calculation results for 7 T CCs in unloaded configuration with a tuning L_T . VNA traces show the S_{21} parameter measured with a double-loop probe; $Z_{\text{coil,self,series}}$ and $Z_{\text{coil,self,parallel}}$ denote the calculated self-resonance of a coaxial coil according to Eq. 4.1 and Eq. 4.5. $Z_{\text{coil,LT}}$ denotes the impedance calculated for a parallel resonance circuit of the coaxial coil with a tuning L_T across the coil port (see also Figure 4.6).

S_{21} measurements and impedance calculation results for 7 T CCs (those constructed in *Article I*) in Figure 4.9 demonstrate the effect of the tuning L_T across the coil port with a single gap (4 cm CC) and multiple gaps (7, 10 and 15 cm CCs). The 4 cm CC shows a resonance only at a frequency slightly above the target f_L . Multi-gap coils have a second resonance appear at a frequency that can be approximated by Eq. 4.9. Differences between measured and calculated resonance frequencies are due to an approximation of the value L_T , the baseline discrepancy between measured and calculated frequency without tuning components and inaccuracies added during the measurement process (e.g. the coil shape being slightly bent).

In 1T1G-CCs, an additional resonance can also occur if the coil is used in Rx-only mode with an AD circuitry at the coil port as used by Zhang *et al.* [55] and described in *Article I*. When the PIN diodes are reverse biased (“off” state), they have a capacitance C_{PIN} , typically 1.8 pF for the diodes used (DH80106-10N, Cobham, Wimborne, UK) that can be seen in parallel across the coil port ($C_{PIN}/2$ for two diodes in series). When a tuning inductor L_T is employed, an additional parallel resonance occurs. Observed additional resonances for single-gap CCs at 3 T were far above the operation frequency (> 380 MHz). The equivalent circuit scheme shown in Figure 4.10 is only accurate for the case of reverse biased PIN diodes. When the diodes are forward biased, they short the inner to the outer coaxial coil conductor, as can be seen in Fig. 3a or Fig. 9a of *Article I*. Therefore, in single-gap coils, the second resonance also vanishes when the diodes are forward biased and, thus, this interface configuration is not prone to become an issue for proper detuning of the CC during RF transmission.

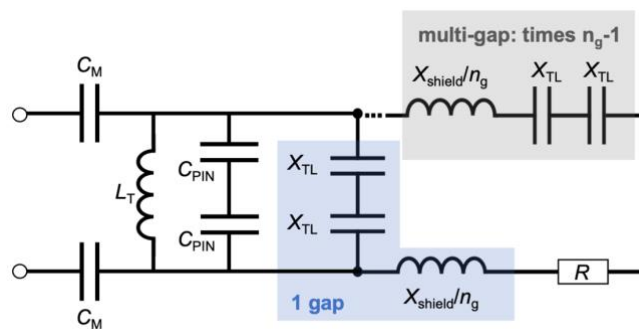


Figure 4.10: Equivalent circuit with two reverse biased PIN diodes (“off” state) and a tuning inductor L_T

In general, for fine-tuning with an L_T , the small added capacitance $C_{PIN}/2$ doesn’t strongly counteract the desired shift to a higher frequency. This is illustrated in Figure

4.11 that shows the frequency response of a 7 and 15 cm MTMG-CC alone (green) and with interface components L_T (blue) and C_{PIN} and L_T (red). In this figure, one can observe additional resonances in the 7 and 15 cm 3 T CCs appear due to their multi-gap structure and as experienced in MR experiments, actively detuning the remaining resonance by an AD circuit at every inner gap is a measure that is indispensable to avoid coupling between the CC and the body coil during RF Tx.

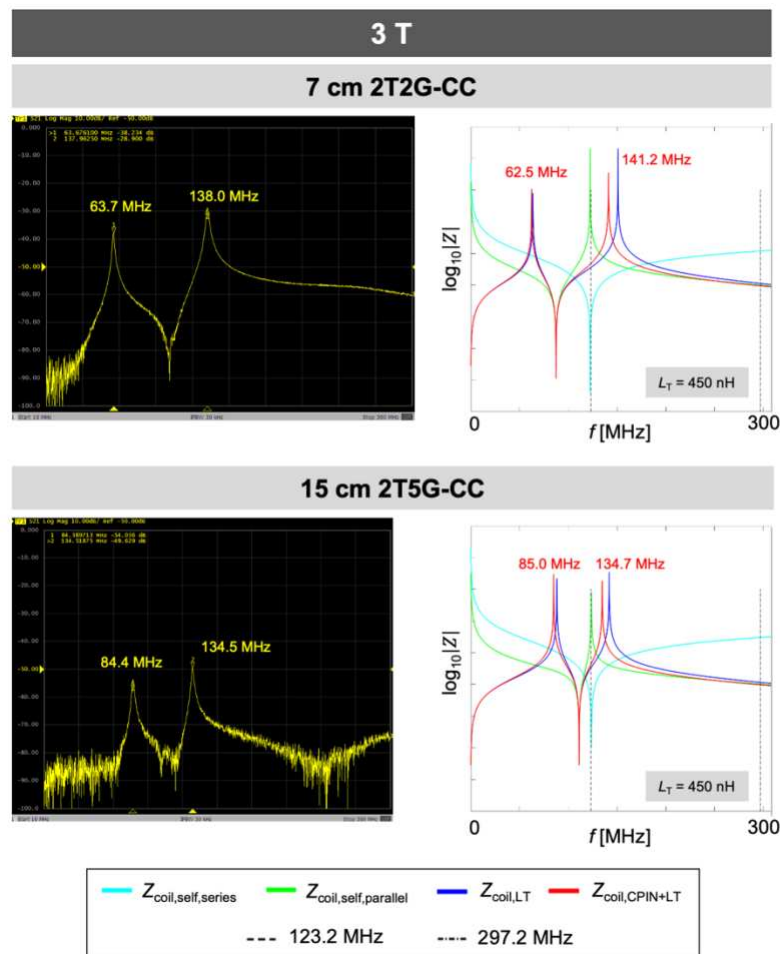


Figure 4.11: 3 T MTMG-CCs' resonance frequency behavior in unloaded coil configuration. VNA traces show the S_{21} parameter measured with a double-loop probe; $Z_{coil,self,series}$ and $Z_{coil,self,parallel}$ denote the calculated self-resonance of a coaxial coil according to Eq. 4.1 and Eq. 4.5. $Z_{coil,LT}$ and $Z_{coil,CPIN+LT}$ denote the impedances calculated for a parallel resonance circuit of the coaxial coil with a tuning L_T with and without two reverse biased PIN diodes across the coil port (see Figure 4.10).

For a given 1T1G-CC with a self-resonance already close to but slightly lower than the target resonance frequency ω , a large tuning inductor value $L_{T,large}$ is needed. $L_{T,large}$ can be decreased to $L_{T,small}$ if a tuning capacitor C_T is employed in parallel to $L_{T,small}$, following Eq. 4.13 and Eq. 4.14. This can be advantageous to reduce the PCB form factor, but one has to trade smaller inductor size (which allows the use of a smaller

interface PCB) for SNR loss, according to preliminary findings published by Obermann *et al.* [216].

$$\begin{aligned} \frac{1}{Z_{L_T, \text{large}}(\omega)} &= \frac{1}{Z_{L_T, \text{small}}(\omega)} + \frac{1}{Z_{C_T}(\omega)} \Leftrightarrow Z_{L_T, \text{large}}(\omega) = \frac{1}{\frac{1}{i\omega L_{T, \text{small}}} + i\omega C_T} \\ &= \frac{1}{i\omega \left(C_T - \frac{1}{\omega^2 L_{T, \text{small}}} \right)} \end{aligned} \quad \text{Eq. 4.13}$$

$$C_T = \frac{1}{\omega^2} \left(\frac{1}{L_{T, \text{small}}} - \frac{1}{L_{T, \text{large}}} \right) = \frac{1}{\omega^2} \left(\frac{L_{T, \text{large}} - L_{T, \text{small}}}{L_{T, \text{large}} \cdot L_{T, \text{small}}} \right) = \frac{1}{\omega^2} \left(\frac{\Delta L_T}{L_{T, \text{large}} \cdot L_{T, \text{small}}} \right) \quad \text{Eq. 4.14}$$

The above-mentioned is illustrated in Figure 4.12. The parameters and tuning configurations used for the exemplary calculations were the following:

1T1G-CC:

- $d_0 = 12 \text{ cm}$
- cable E ($d_1 = 1.17 \text{ mm}$, $Z_0 = 50 \Omega$, $\varepsilon_r = 1.6$)
- $L_{T, \text{large}} = 403 \text{ nH}$
- $L_{T, \text{small}} = 100 \text{ nH}$
- $C_T = 12.6 \text{ pF}$
- $R = 10 \Omega$
- $Z_{C_M}(\omega) = 0$

→ CC only, $Z_{\text{coil, self}}(\omega)$

→ parallel large tuning inductor $L_{T, \text{large}}$ across the CC port, $Z_{\text{coil, LT, large}}(\omega)$

→ parallel small tuning inductor $L_{T, \text{small}}$ and tuning capacitor C_T across the CC port, $Z_{\text{coil, LT, small} + C_T}(\omega)$

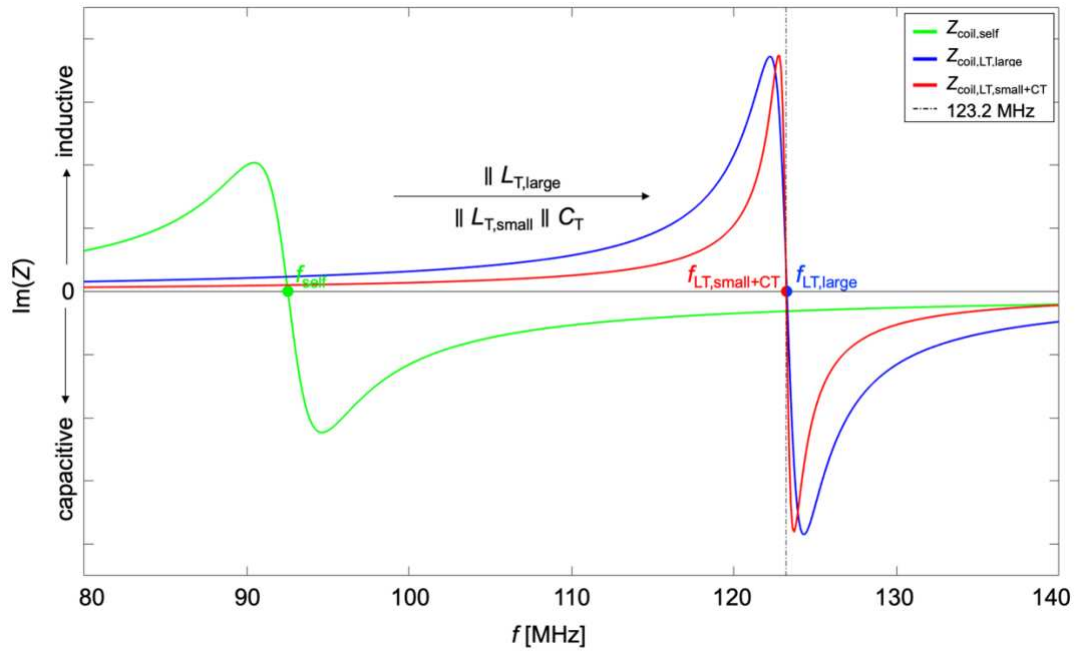


Figure 4.12: Effect of a large tuning inductor $L_{\text{T,large}}$ alone compared to the use of a smaller inductor $L_{\text{T,small}}$ in parallel with C_{T}

4.3.3 1T1G vs. MTMG coaxial coils

In this supplementary study section, the aim was to investigate the difference between the use of coaxial coils with a self-resonance very close to the operation frequency of the MR system, which is the case for the investigated MTMG-CCs in *Article I*, and 1T1G-CCs of same size which have a self-resonance frequency that deviates (more or less) from the Larmor frequency.

4.3.3.1 Comparison of same-size 1T1G- and MTMG-CCs at 3 T

The motivation for using a 1T1G-CC in Rx-only mode at 3 T instead of a MTMG-CC could be easier fabrication, a lower AD component count along the coil than with multi-gap coils (RF chokes at every outer gap, PIN diodes at every inner gap) as well as a lower number of turns and gaps and therefore lower coil noise. Also, an argument for 1T1G-CCs could be that, compared to same-size MTMG-CCs, they are lighter, depending on the cable type slightly more flexible and more robust to bending as the worst case of damaging the coil due to excessive deforming is less likely to occur with only one gap.

The two MTMG-CCs used for 3 T MRI in *Article I*, namely the 7 cm 2T2G-CC and the 15 cm 2T5G-CC were chosen to be compared to same-size 1T1G-CCs in flat position. 1T1G-CCs were fabricated using the same coaxial cable type as used for the respective MTMG-CC fabrication (cable E for the 7 cm coil and cable B for the 15 cm coil). Cable references and properties are given in Fig. 2 of *Article I*.

For 1T1G-CCs, additional analytical calculations to determine the self-resonance frequency and EM simulations to evaluate the surface current density distributions and current amplitude on all three coaxial coil conductors (iC , oCi , oCo , see Fig. 1b of *Article I*) were carried out. Bench measurements and MR experiments were performed with 1T1G-CCs and MTMG-CCs during the same measurement session.

4.3.3.1.1 Analytical calculations and EM simulations

First, analytical calculations of the self-resonance were carried out in MATLAB 2017b (The Mathworks, Inc., Natwick, USA) using the resonance condition described in Eq. 2.70 and Eq. (1)-(3) of *Article I*. For MTMG-CCs, the measured, calculated and simulated frequency values can be taken from Table II in *Article I*. The relative

deviation between measured MTMG self-resonance frequency and the Larmor frequency without PIN diodes or chokes along the coil is -2.8 % (7 cm 2T2G-CC) and 0.0 % (15 cm 2T5G-CC). With AD components along the coil, the resonance frequency is shifted down due to capacitive effects, the relative deviation of the Larmor frequency from measured ones then is +3.4 % (7 cm 2T2G-CC) and +9.7 % (15 cm 2T5G-CC).

1T1G-CCs				
d_0 [cm]	$f_{0,\text{meas}}$ [MHz]	$f_{0,\text{calc}}$ [MHz]	$f_{0,\text{sim}}$ [MHz]	f_L [MHz]
7	154.1	169.8 (+10.2 %)	163.0 (+5.2 %)	123.2 (-20.1 %)
15	65.1	67.8 (+4.1 %)	65.6 (+0.8 %)	123.2 (+89.2 %)

Table 4.3: Results from self-resonance frequency measurements, analytical calculations and EM simulations

As given in Table 4.3, for 1T1G-CCs, the Larmor frequency deviates by -20.1 % (7 cm 1T1G-CC) and +89.2 % (15 cm 1T1G-CC) from the measured unloaded self-resonance frequency. The calculated resonance frequencies deviate more from experimentally determined ones than the simulated ones. This can be explained by a more accurate representation of the coaxial coil properties and structures in 3D EM simulation. The equivalent circuit model is only approximative, neglects the effects of a gap capacitance (possibly slightly lowering f_0) and the characteristic cable impedance was taken from the cable's data sheet but can usually vary by $\pm 2 \Omega$.

EM simulations were performed using CST Studio Suite 2020 (Dassault Systèmes, Paris, France). The simulation and post-processing workflow were executed as described in section II.D of *Article I*. The parameters listed in Table 4.4 were used to model the coaxial coils, according to values given in the data sheets of cable B and E (Fig. 2, *Article I*) and simulation results for 1T1G-CCs were extracted at the Larmor frequency (f_L). The evaluation of surface current amplitude in the outer surface of the outer conductor (oCo) in MTMG-CC and 1T1G-CC simulations at the Larmor frequency is interesting as these are also the cases investigated in MRI experiments. The coils were simulated in unloaded configuration, therefore only the coil noise affects the surface current amplitude.

1T1G-CCs						
d_0 [cm]	d_{iC} [mm]	d_{oCi} [mm]	d_{oCo} [mm]	d_{jacket} [mm]	$\epsilon_{r,\text{dielectric}}$	$\epsilon_{r,\text{jacket}}$
7	0.32	0.91	1.17	1.42	1.6	2.0
15	0.29	0.92	1.12	1.42	2.0	2.0

Table 4.4: EM simulation coaxial coil parameters

As a side note concerning EM simulations, in addition to the skin effect occurring with AC current, it can be mentioned that the proximity effect can be observed in surface current density patterns for single-turn and multi-turn simulations. Examples for the surface current density of a single- and double-turn coil are given in Figure 4.13.

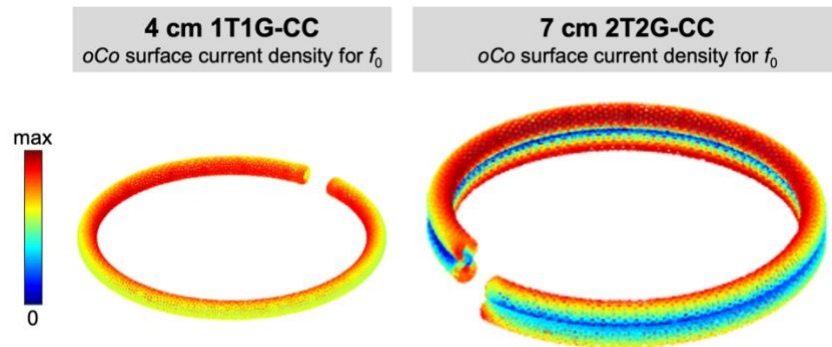


Figure 4.13: Exemplary EM simulations showing the proximity effect on the *oCo* in a single- and double-turn CC.

With a single turn, the opposite coil conductors carry current in opposite direction and therefore the surface current density is increased on the side of the shield pointing towards the coil center rather than the outer side. With multiple turns, the current flows in the same direction on both turns and, therefore the magnetic field of the conductor halves close to each other cancels out and no current flows through that part. The surface current density is concentrated to the most remote path (top, bottom) of each conductor turn.

The analysis of same-size 1T1G and MTMG-CC EM simulation results can be done in terms of surface current density distribution, surface current amplitude, and homogeneity along the *oCo* at the Larmor frequency. 3D plots of the surface current density and line plots for the surface current are shown in Figure 4.14 and Figure 4.15 for the 7 cm and 15 cm 1T1G compared to the respective same-size MTMG-CC configuration. Color maps are always scaled to the maximum surface current density value on the *iC* or *oC* per coil size.

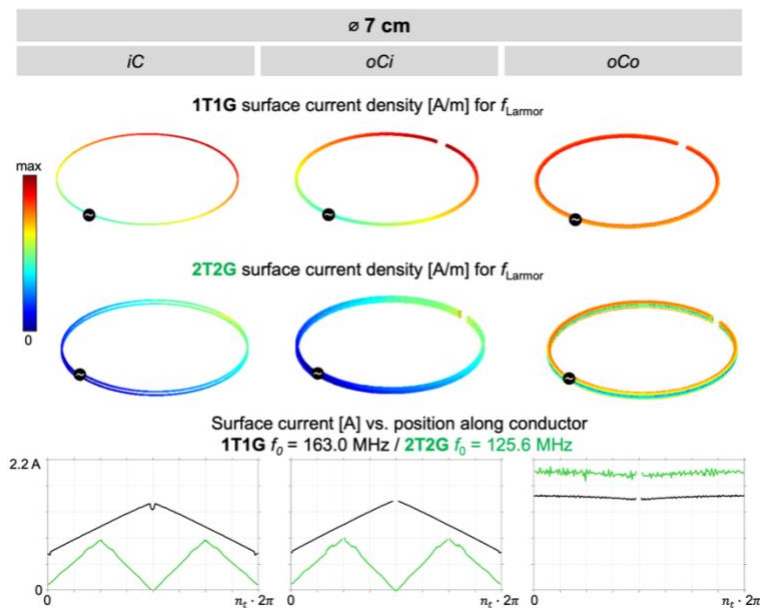


Figure 4.14: Comparison of EM simulation results for the 7 cm 1T1G and 2T2G coaxial coil

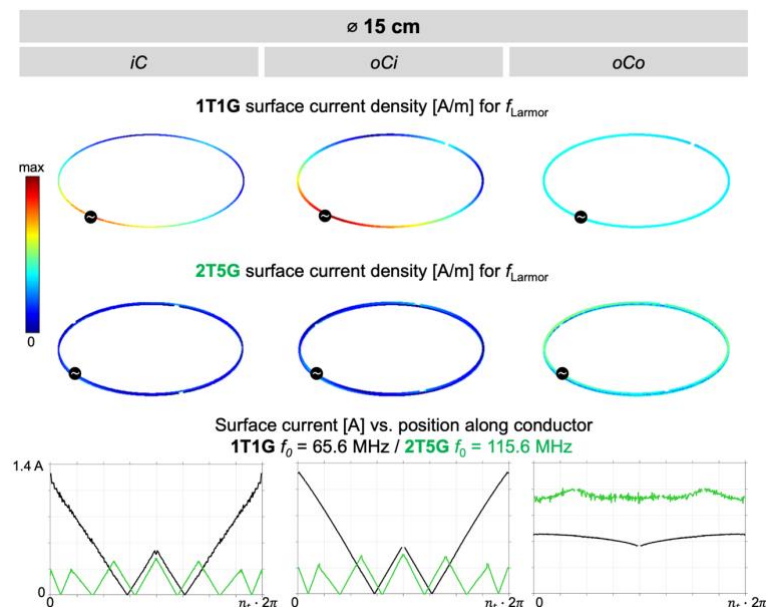


Figure 4.15: Comparison of EM simulation results for the 15 cm 1T1G and 2T5G coaxial coil

The comparison of EM simulation results in Figure 4.14 and Figure 4.15 demonstrates that the mean current amplitude at the *oCo* at the Larmor frequency is higher for the MTMG than for the 1T1G configuration. The approximate mean *oCo* current amplitude values are summarized in Table 4.5.

	mean <i>oCo</i> surface current [A]	
d_0 [cm]	1T1G-CC	MTMG-CC
7	1.5	2.0
15	0.6	1.1

Table 4.5: Mean *oCo* surface current amplitude

The oCo surface current determines the B_1^+ seen at a distance from the coil, thus, following the principle of reciprocity, EM simulation results suggest higher Rx sensitivity for MTMG-CCs than for 1T1G-CCs, considering coil noise only.

4.3.3.1.2 Coil fabrication and bench measurements

The main difference in coil interface design for this study was that for tuning the 7 cm 1T1G-CC to the desired operation frequency of 123.2 MHz, a tuning capacitor C_T in parallel to the tuning inductor L_T (as used for all other coaxial coils in *Article I*), had to be employed as shown in Figure 4.16.

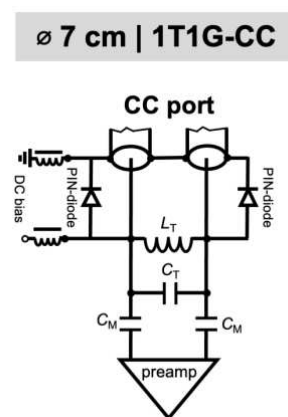


Figure 4.16: Interface schematic with additional tuning capacitor (C_T) as used for the 7 cm 1T1G-CC

The optimal interface configuration would be with the use of an L_T only [216], which is possible if the self-resonance frequency is below the target frequency (f_L). This was the case for all loaded MTMG-CC self-resonance frequency bench measurements in *Article I* (see supplementary Table I) and also for the 15 cm 1T1G-CC (see Table 4.3). With respect to findings in reference [216], the largest possible tuning inductor was chosen that could fit on the small PCB in order to maximize SNR and to keep the resonance frequency shift to a higher frequency at a minimum. C_T was adapted so that the resonance frequency was shifted down to 123.2 MHz.

As can be seen in photographs of the fabricated CCs in Figure 4.17 and Figure 4.18, the 1T1G-CCs are inarguably easier to construct, especially because of the lack of gaps along the loop and the AD components concentrated to the coil port only. For the 15 cm MTMG-CC, the PIN diodes are a major factor, increasing the overall weight of the coil. In terms of flexibility, these specific coils are quite comparable as the coaxial cable is very thin. The advantage of using a 1T1G instead of a MTMG coil could become

more relevant with thicker cables. Even after numerous cases of strong bending, no breaking point along the MTMG coils' conductor, neither at the gaps nor the soldering pads containing PIN diodes and RF chokes was observed.

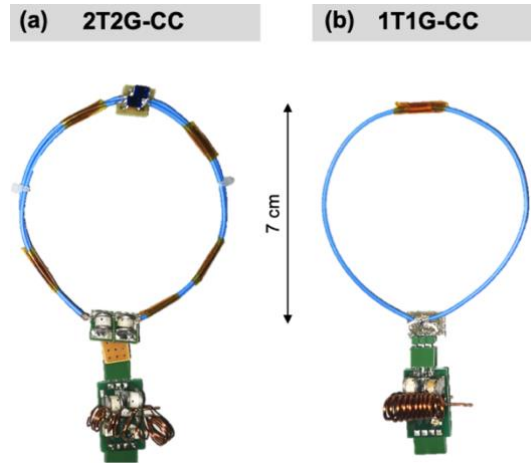


Figure 4.17: Fabricated 2T2G-CC (a) and 1T1G-CC (b) with 7 cm coil diameter and respective (fine-)tuning, matching and active detuning interface.

For the 15 cm 1T1G-CC fabrication, inductive tuning to the Larmor frequency was done with an L_T smaller than the one used for MTMG-CC fabrication as the shift in resonance frequency has to be higher.

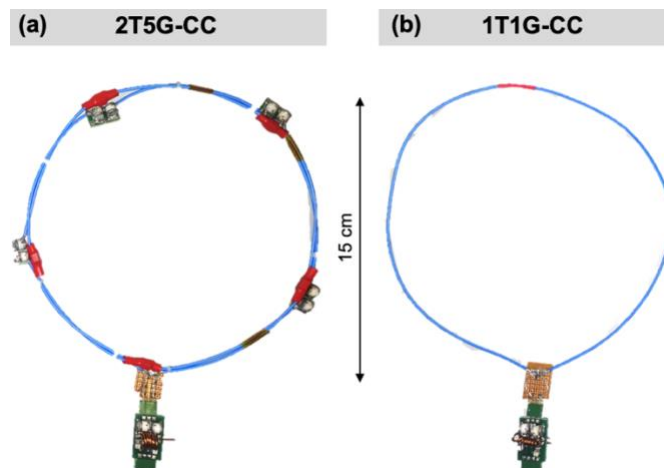


Figure 4.18: Fabricated 2T5G-CC (a) and 1T1G-CC (b) with 15 cm coil diameter and respective (fine-)tuning, matching and active detuning interface.

Bench measurements were carried out using a VNA (E5071C, Agilent, Santa Clara, CA, USA) with the coils in flat position on a 5-l container phantom with a DC conductivity of approximately $\sigma = 0.2$ S/m and dimensions of 24 x 18.5 x 14 cm³.

“Coil only” measurements of the CC without any fine-tuning and matching network at the coil port were carried out with a decoupled double-loop probe [62], with a

baseline S_{21} of approximately -80 dB. Measurements with coil interface were conducted via a 50 Ω coaxial cable connection to the VNA. All bench measurements are summarized in Table 4.6. In addition to the supplementarily fabricated 1T1G-CCs, the MTMG coils also used in *Article I*, were remeasured before MRI. Re-soldering and shortening of connector pins, an exchange of tuning inductors can result in slightly different values for MTMG-CCs than those mentioned in bench tests in *Article I*.

d_0 [cm]	n_t	n_g	coil only					with interface			
			f_u [MHz]	Q_u	f_l [MHz]	Q_l	Q ratio	S_{11} @ f_l [dB]	Q_u	Q_l	Q ratio
7	1	1	154.1	170	148.4	19	8.9	-19.2	70	42	1.7
7	2	2	119.1	95	115.2	24	4.0	-21.4	70	36	1.9
15	1	1	65.1	121	63.0	31	3.9	-31.6	78	26	3.0
15	2	5	112.3	73	108.4	12	6.1	-28.3	52	17	3.1

Table 4.6: Bench measurement results for the 1T1G-CCs and MTMG-CCs without interface (coil only) and with interface

As coil and sample losses are frequency-dependent [24], “coil only” measurements have to be normalized to the Larmor frequency to be comparable for coils of same size.

$$R_c = \frac{L\omega_u}{Q_u} \sqrt{\frac{\omega_L}{\omega_u}} \quad \text{Eq. 4.15}$$

$$R_s = \left(\frac{L\omega_l}{Q_l} - R_c \sqrt{\frac{\omega_l}{\omega_L}} \right) \cdot \left(\frac{\omega_L}{\omega_l} \right)^2 \quad \text{Eq. 4.16}$$

Using Eq. 4.15 and Eq. 4.16, R_c and R_s at the Larmor frequency can be calculated from measurement values, results are given in Table 4.7.

d_0 [cm]	n_t	n_g	coil only				with interface	
			L [nH]	R_c @ f_l [Ω]	R_s @ f_l [Ω]	Q ratio @ f_l (R_s+R_c)/ R_c	R_c @ f_l [Ω]	R_s @ f_l [Ω]
7	1	1	183	0.9	5.5	6.9	2.0	1.4
7	2	2	734	5.9	18.8	4.2	8.1	7.7
15	1	1	469	2.2	16.9	8.8	4.7	9.3
15	2	5	1876	19.0	114.5	7.0	27.9	57.5

Table 4.7: Coil and sample loss calculations for the 1T1G-CCs and MTMG-CCs without interface (coil only) and with interface

Without interface, for “coil only” measurements, it can be observed that coil losses are higher for MTMG coils due to the longer cable length with multiple turns

($R_c \propto \sqrt{\omega} n_t^2$, [24]) and the amount of AD components (PIN diodes, RF chokes) along the loop. Sample noise is also higher for MTMG-CCs as more turns provide higher magnetic coupling to the sample ($R_s \propto \omega^2 n_t^2$, [24]).

The Q ratio with tuning and matching interface is comparable between 1T1G and MTMG coils (see Table 4.6) and respective calculated coil and sample noise (depending on the inductance) are given in Table 4.7. It can be clearly seen that the coil noise is higher for MTMG coils but also sample noise is higher which suggests higher magnetic coupling to the sample with multiple turns.

4.3.3.1.3 MR experiments

SNR maps for all coils shown in Figure 4.19 were calculated from 2D GRE acquisitions in the transversal imaging plane using the following imaging parameters:

- FOV = 290 x 290 mm²
- $T_R/T_E = 50/10$ ms
- 0.6 x 0.6 mm² in-plane resolution
- 6.5 mm slice thickness
- FA = 60°

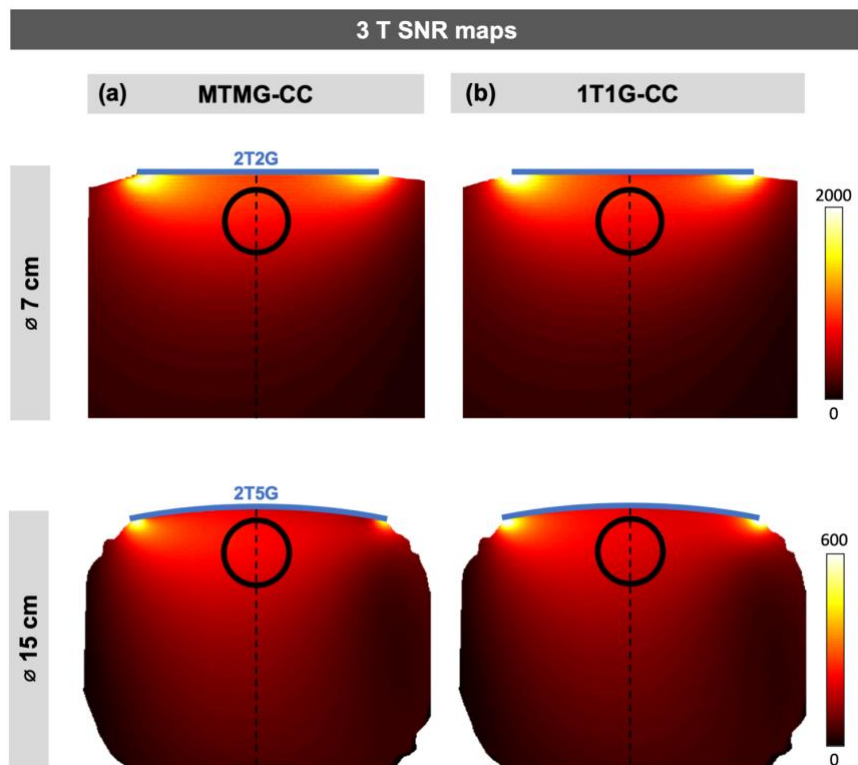


Figure 4.19: SNR maps from 2D GRE images acquired in the central transversal phantom plane at 3 T for MTMG-CCs (a) and 1T1G-CCs (b) of 7 and 15 cm diameter, respectively. The circular ROI and central axis used for SNR evaluation are marked in black.

The average SNR was evaluated in a circular ROI with a diameter of $d_0/4$ and the ROI center located at distance D from the coil center, as depicted in Figure 4.20. D was chosen to be 1.5 or 2.5 cm for the 7 or 15 cm CC, respectively.

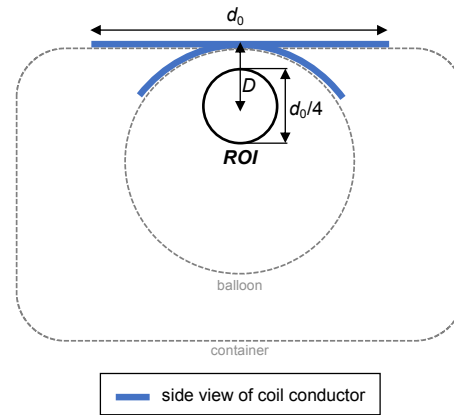


Figure 4.20: ROI position and size used for average SNR evaluation in container or balloon phantoms

In Table 4.8, the average SNR values and the relative SNR difference in the ROI between the MTMG-CC and 1T1G-CC are listed for comparison of 7 and 15 cm coils. It can be seen that the average SNR is slightly higher for the MTMG-CC, more significantly for the 15 cm coil than the 7 cm coil.

d_0 [cm]	Average SNR		relative SNR difference (MTMG vs. 1T1G)
	1T1G-CC	MTMG-CC	
7	715	750	+4.7 %
15	190	211	+10.0 %

Table 4.8: SNR comparison between MTMG-CC and 1T1G-CC

SNR central axis profiles shown in Figure 4.21 (along the dotted line in Figure 4.19) for the 7 cm and 15 cm coaxial coils demonstrate that the 1T1G and MTMG coils perform quite comparably at larger depths (> 1.5 cm for the 7 cm coils and > 10 cm for the 15 cm coils). At smaller depths, the MTMG-CC yields better SNR.

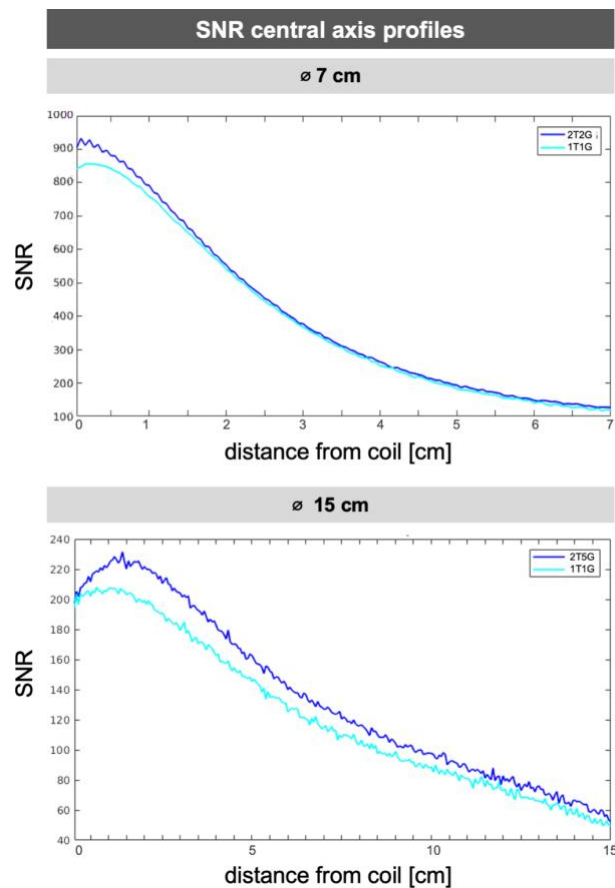


Figure 4.21: SNR central axis profiles, for the 7 cm coaxial coils (top) and the 15 cm coaxial coils (bottom).

To characterize the AD reliability of 1T1G and MTMG coaxial coils, the minimum and maximum values taken from FA difference maps over the whole phantom (with vs. without Rx coil, body coil in Tx/Rx) are given in Table 4.9. Except the minimum value of the 15 cm coils, the relative FA difference values are comparable. Imperfections in phantom alignment in between the scan with Rx coil and the reference scan without the Rx coil or partial volume effects can lead to evaluation inaccuracies.

d_0 [cm]	minimum (phantom) [%]		maximum (phantom) [%]	
	MTMG-CC	1T1G-CC	MTMG-CC	1T1G-CC
7	-12.0	-10.8	+8.5	+8.7
15	-19.5	-9.9	+19.1	+17.9

Table 4.9: Relative FA difference (minimum, maximum) over the whole phantom

4.3.3.1.4 Conclusion

To sum up this section, there are several factors that have to be taken into account when comparing a 1T1G-CC and MTMG-CC of same-size at 3 T MRI.

Concerning fabrication, weight and robustness, one could lean towards the use of the 1T1G-CC if the compromise between flexibility or lightweight and SNR loss is acceptable.

Bench and MRI tests of the two investigated coil pairs (1T1G and MTMG) have demonstrated that different aspects can have an influence on the coil performance. Following EM simulations, it has been shown that the oCo current amplitude at the Larmor frequency is higher for the MTMG configuration than for the 1T1G coil. Bench measurements demonstrated that for MTMG-CCs, PIN diodes and RF chokes increase coil noise (low Q_u). For the 7 cm 1T1G-CC, adding the tuning capacitor C_T might be responsible for an increase in coil noise (due to the interface). Lower SNR performance with a tuning interface consisting of L_T and C_T instead of an L_T only was also shown in a more extensive study in reference [216]. From MRI experiment results it seems that still, in terms of SNR, it is advantageous to employ a coil as close as possible to its self-resonance which is the case for the MTMG-CCs, even if in this case, additional AD components are required along the loop, increasing coil noise and impairing total flexibility in some cases.

4.3.3.2 Comparison of a 10 cm 1T1G- and 1TMG-CC at 7 T

In a sum of publications presenting 1.5 T, 3 T or 7 T 1T1G-CCs [55,119–121,124] and this work on MTMG-CCs, coils with a first self-resonance mode close to the target resonance frequency f_L are employed. In contrast to that, in recent publications by Ruytenberg *et al.* [122,123], a 10 cm 1T1G-CC with a first self-resonance below f_L was used at 7 T in Tx/Rx mode and in array configuration for human neck (carotid), hand and knee imaging. EM simulation results for both CCs (1T1G and 1T2G) in unloaded configuration are shown in *Article I* (Fig. 7) and demonstrated that the 1T1G 10 cm loop has a surface current density maximum at the iC gap (as also shown in [122]) and the current distribution on the oCo is more inhomogeneous than in a 1T2G-CC. The main difference is the lower mean oCo surface current amplitude in a 1T1G-CC as compared to a 1T2G-CC, when simulated at $f_L = 297.2$ MHz.

In the following, the goal was to experimentally validate analytical calculations of the multi-resonance behavior of a 10 cm 1T1G-CC on the bench.

4.3.3.2.1 Analytical calculations and bench measurements

Analytical impedance calculations were carried out in MATLAB 2017b (The Mathworks, Inc., Natwick, USA) for the self-resonances and parallel resonances of a 10 cm 1T1G-CC with and without a tuning capacitor C_T (33 pF) across the coil port and cable type A (cf. *Article I*, Huber+Suhner, K_02252_D-08) as used by Ruytenberg *et al.* [122]. Bench measurements were performed with C_T and two symmetric matching capacitors C_M of 27 pF each. A 5-l container phantom with a DC conductivity of ≈ 0.65 S/m was used for loaded measurements with the coil directly placed on the phantom. First, the unloaded self-resonances (coil only) and the unloaded resonance frequencies with C_T across the coil port were determined with a double pick-up probe (S_{21}). The loaded measurement was done with interface, i.e. C_T and two symmetric C_M , via a 50Ω connection to the VNA (S_{11} measurement).

Calculated resonance frequency values (parallel resonances) are given in Table 4.10. The first calculated self-resonance frequency of a 10 cm 1T1G-CC is closer to the 3 T Larmor frequency than to the desired Larmor frequency of 297.2 MHz (7 T). A second self-resonance appears at around 700 MHz. With a tuning C_T across the coil port, the

calculated first parallel resonance is shifted to 51.4 MHz and the second parallel resonance shifts to 368.9 MHz.

configuration	$f_{0,calc}$ [MHz]	$f_{1,calc}$ [MHz]
self-resonance	114.7	700.9
$\parallel C_T$	51.4	368.9

Table 4.10: Resonance frequency calculations for a 10 cm 1T1G-CC

Bench measurement results in Table 4.11 show good accordance with resonance calculations (Table 4.10). With the coil in loaded configuration and the inclusion of matching capacitors in the interface, S_{11} measurements revealed that the second parallel resonance shifts very close to f_L and the coil is matched, although not to a satisfying level at 297.2 MHz. The matching could be improved with different C_M values or a different phantom (in size and dielectric properties), or by reducing the coupling to the sample by increasing the coil-sample distance. Fine-tuning could be achieved with a variable capacitor instead of or in addition to C_T .

unloaded	$f_{0,meas}$ [MHz]	$Q_{u,0}$	S_{11} [dB]	$f_{1,meas}$ [MHz]	$Q_{u,1}$	S_{11} [dB]
self-resonance	121.7	233	-	699.0	160	-
$\parallel C_T$	44.8	115	-	336.2	85	-
loaded	$f_{0,meas}$ [MHz]	$Q_{l,0}$		$f_{1,meas}$ [MHz]	$Q_{l,1}$	
$\parallel C_T$ + matching	38.5	24	-30.0	297.3	20	-7.5

Table 4.11: Bench measurement results for a 10 cm 1T1G-CC with capacitive tuning and matching

4.3.3.2.2 Conclusion

In this section, the multi-resonance behavior of a 1T1G-CC found in analytical calculations is validated by bench measurements. Results show that for a 10 cm 1T1G-CC with a first self-resonance $f_0 < f_L$, tuning and matching capacitors can be used so that, when measured across the coil port, a parallel resonance (“tuned down” second self-resonance f_1) appears close to the 7 T Larmor frequency of 297.2 MHz and the coil is matched to 50 Ω . Presumably, according to EM simulation results in *Article I* (Fig. 7), it could be advantageous to employ a 10 cm 1T2G-CC instead of a 1T1G-CC at 7 T MRI. The coil performance comparison in loaded EM simulations and MRI is the goal of an on-going study. Suggested future work on EM simulations will be presented in section 6.1.1 and the 10 cm 1T2G-CC could potentially find its application in knee imaging (discussed in 6.2.2).

4.3.4 MR experiments

While in previous sections, also additional CCs to the ones used in *Article I* were fabricated and analyzed, the following sub-sections present results acquired in MRI with the 3 or 7 T MTMG-CCs and SCs described in *Article I*.

4.3.4.1 Active detuning performance of 3 T SCs and CCs

Before 3 T GRE measurements at the Siemens Prisma Fit system were carried out to acquire SNR data shown in *Article I*, the AD performance of both Rx-only SCs and CCs of all sizes (4, 7, 10 and 15 cm) was assessed. For AD characterization, relative FA difference maps were calculated from a FA mapping scan with the Rx coil present vs. the reference scan without coil ($B_{1,coil}/B_{1,ref} - 1$). A Gaussian 2D smoothing filter ($\sigma = 1$) was applied to all relative FA difference maps shown in Figure 4.22.

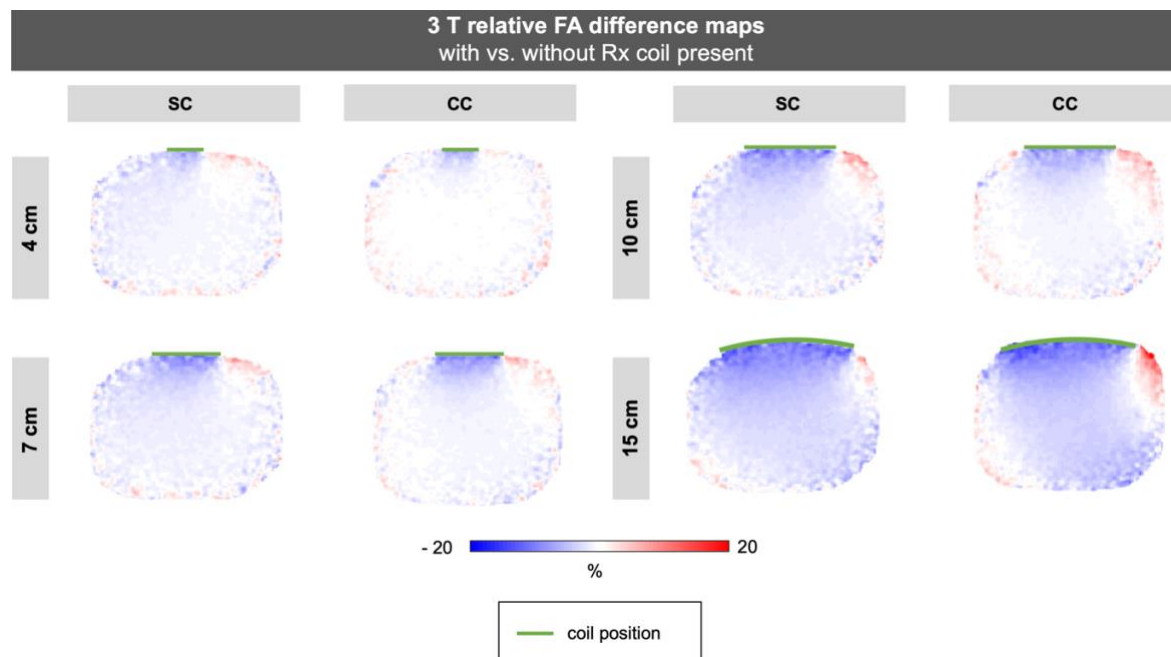


Figure 4.22: Relative FA difference maps calculated from FA maps acquired without and with Rx coil present during MRI with the body coil in Tx/Rx mode.

Each coil was placed directly on the 5-l container sample with a wall thickness of only a few mm. Comparing SCs and CCs of different sizes, the AD performance over the whole phantom is very similar. Too strong coupling between the body coil and the detuned Rx-only coil could lead to image degradations and patient safety risks, i.e. heating due to a not sufficiently decoupled structure creating an E -field when excited

by the RF transmit field. In this study, values between 10 and 20 % maximum relative FA difference over the whole phantom (higher percentage the larger the coil, Figure 4.22) were considered as safe especially as for in-vivo measurements, these coils would need to be embedded in some textile or flexible coil housing, isolating electrical components from the patient and ensuring mechanical robustness. In this case, the coil itself would be placed farther away from the sample. With increasing sample-coil distance given by the textile/housing layer properties, the influence on the FA distribution would decrease. To prevent damage to the patient, in product coils, an additional fuse and passive detuning network (crossed diodes) would be implemented in the Rx coil as supplementary safety measures in case of the malfunction of the AD circuit.

To give some quantitative measure, the minimum and maximum relative FA difference values are listed in Table 4.12. As mentioned before, phantom misalignment in between the reference scan and the scan with Rx coil present as well as partial volume effects may be the reason for inaccuracies in this evaluation.

d_0 [cm]	minimum (phantom) [%]		maximum (phantom) [%]	
	SC	CC	SC	CC
4	-7.3	-8.5	+5.6	+4.1
7	-10.5	-12.3	+6.9	+5.2
10	-9.5	-8.1	+8.9	+7.1
15	-13.1	-16.7	+7.1	+19.4

Table 4.12: Relative FA difference (minimum, maximum) over the whole phantom

4.3.4.2 SNR and transmit efficiency profile analysis

Data presented in SNR and B_1^+/\sqrt{P} (transmit efficiency) maps in *Article I* (Fig. 10 and 11) can be plotted along the central coil axis, aiming for a depth-dependent analysis of the SNR and transmit efficiency depending on the coil type and size, and position on a large container phantom or a balloon phantom.

In Figure 4.23, SNR central axis profiles for 3 T SCs and CCs reveal that in flat position on the container phantom, the SC performs better as compared to the same-size CC, independently of the distance from the coil. Starting at the following depths from the coil conductor, one can consider the SNR as comparable:

- 4 cm coils: ≈ 3 cm (container)
- 7 cm coils: ≈ 4 cm (container)
- 10 cm coils: ≈ 7 cm (container)
- 15 cm coils: ≈ 6 cm (container)

For measurements with a flat SC compared to the CC in bent position on a balloon phantom, at a certain depth, similar or only slightly improved SNR along the central coil axis can be observed:

- 4 cm coils: ≈ 1.2 cm (balloon)
- 7 cm coils: ≈ 1.5 cm (balloon)
- 10 cm coils: ≈ 2.25 cm (balloon)
- 15 cm coils: ≈ 5 cm (balloon)

Standing wave patterns that can be observed in transmit efficiency and SNR profiles in Figure 4.24 and Figure 4.25 for 7 T measurements carried out with large balloon phantoms (and large coils, 10 and 15 cm) occur because of EM wave interferences or dielectric resonances originating from the choice of phantom dimensions and dielectric properties, as mentioned in *Article I*. This conclusion is supported by the fact that the standing wave effect was not observed for container phantom measurements with SCs and CCs in flat position and was independent of the choice of FA mapping technique or reference voltage. The transmit efficiency, i.e. the created B_1^+ field normalized to input power, shown in Figure 4.24 can be compared along the whole coil axis. It can be observed that in flat coil position, the CC and the SC have almost the same B_1^+/\sqrt{P} values close to the sample surface but also at large distances from the coil. The CC bent to the balloon phantom yields slightly lower B_1^+/\sqrt{P} only at superficial depths for some coils: at distances < 0.5 cm, < 1.5 cm, < 0.5 cm from the 7, 10 and 15 cm coils, respectively. Else, the CC bent to the balloon phantom yields higher B_1^+/\sqrt{P} as compared to a flat SC.

As only for flat measurements at 7 T, the same reference voltage was used for the rectangular 500 μ s excitation pulse, only those SNR profiles in Figure 4.25 are truly comparable over the whole central coil axis. For bent measurements, the reference voltage was adjusted for the SC and CC, aiming for 90° average FA in the ROI drawn

in Fig. 11 in *Article I* but outside of the ROI differences in FA might occur, leading to SNR values that can be increased/decreased due to different flip angles and not exclusively due to the coil's Rx sensitivity. In flat position, the 4 and 7 cm SC and CC have very similar SNR values over the whole sample whereas the 10 and 15 cm SC performs slightly better than the CC.

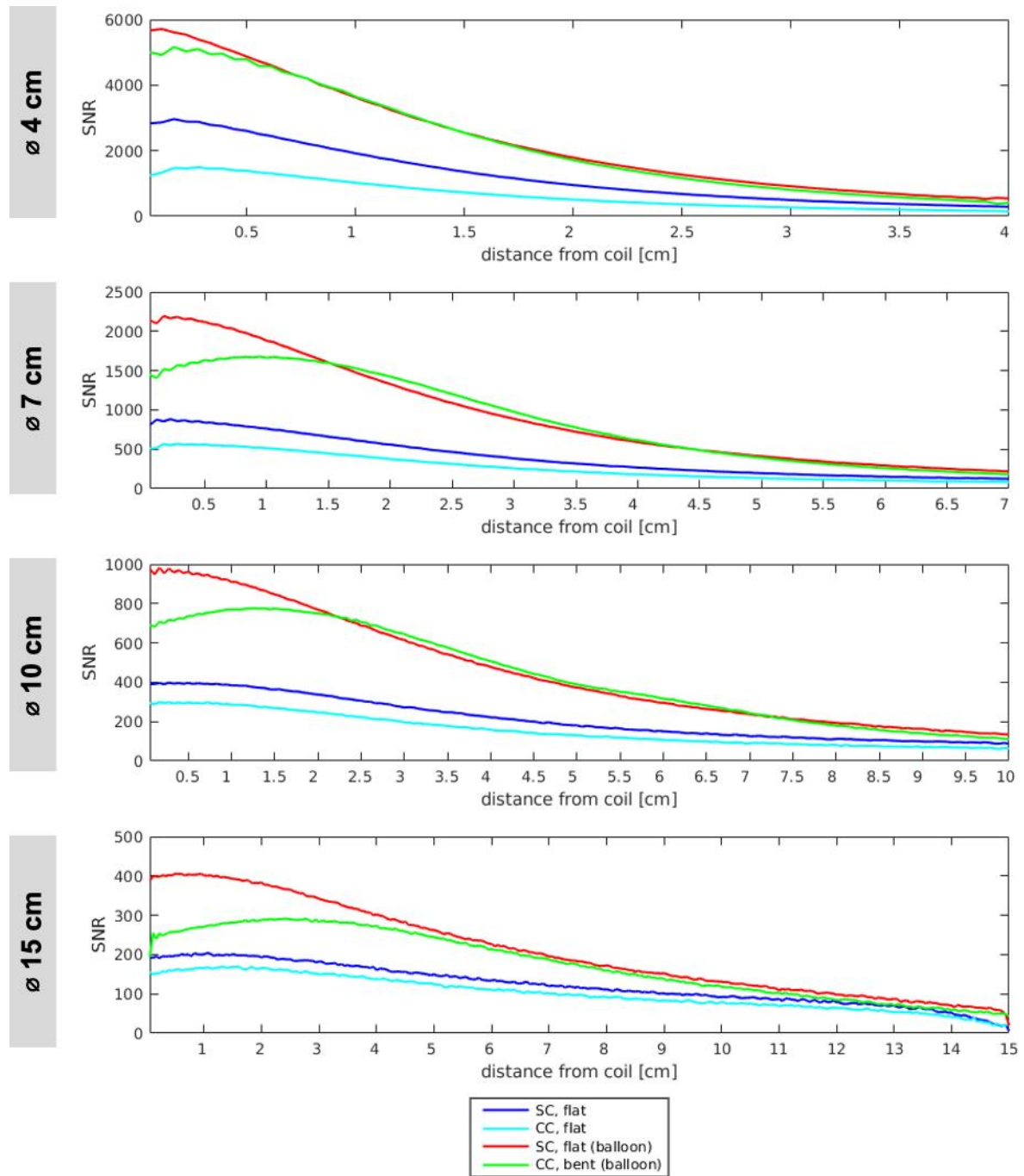


Figure 4.23: SNR along the central coil axis for 3 T SCs and CCs

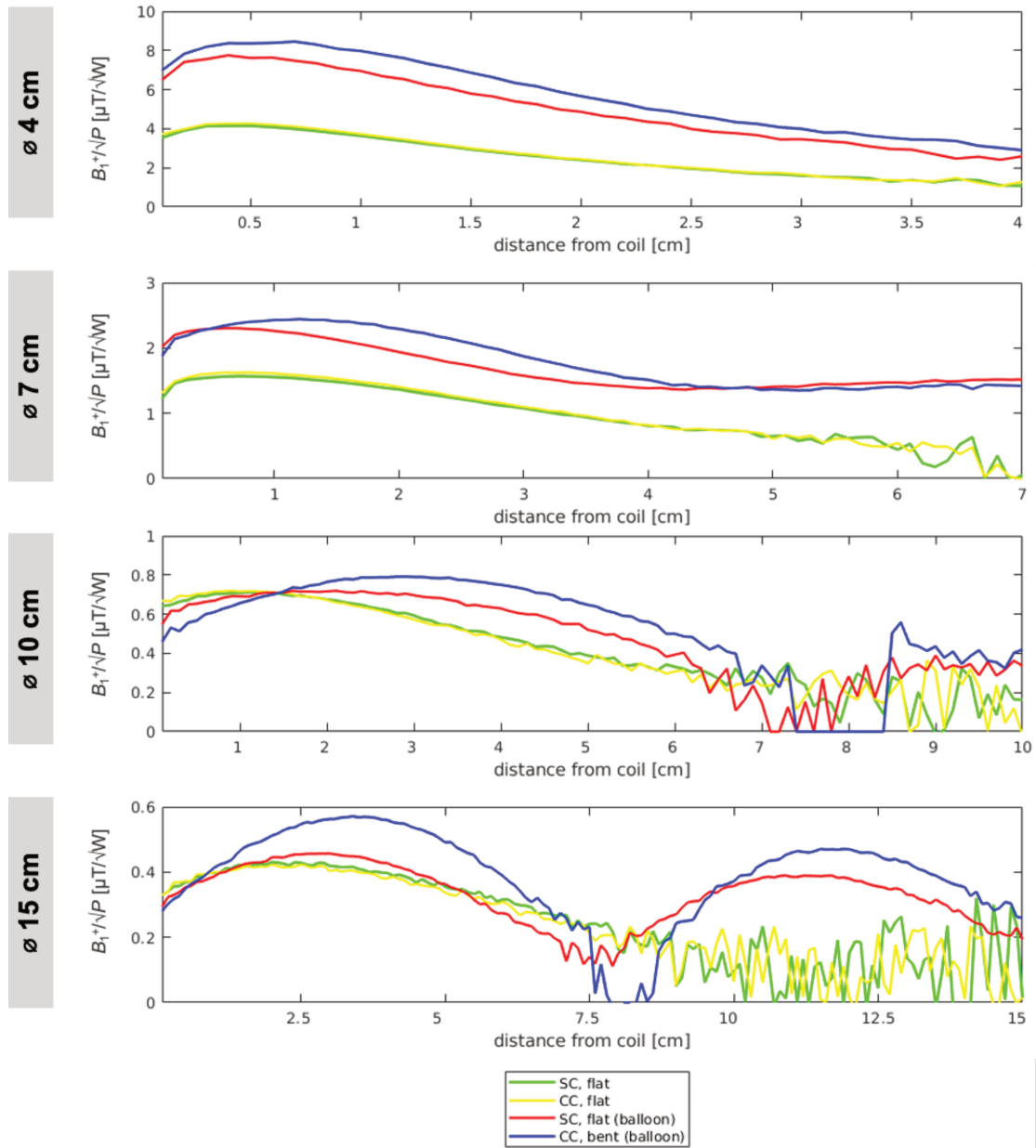


Figure 4.24: Transmit efficiency (B_1^+ / \sqrt{P}) along the central coil axis for 7 T SCs and CCs

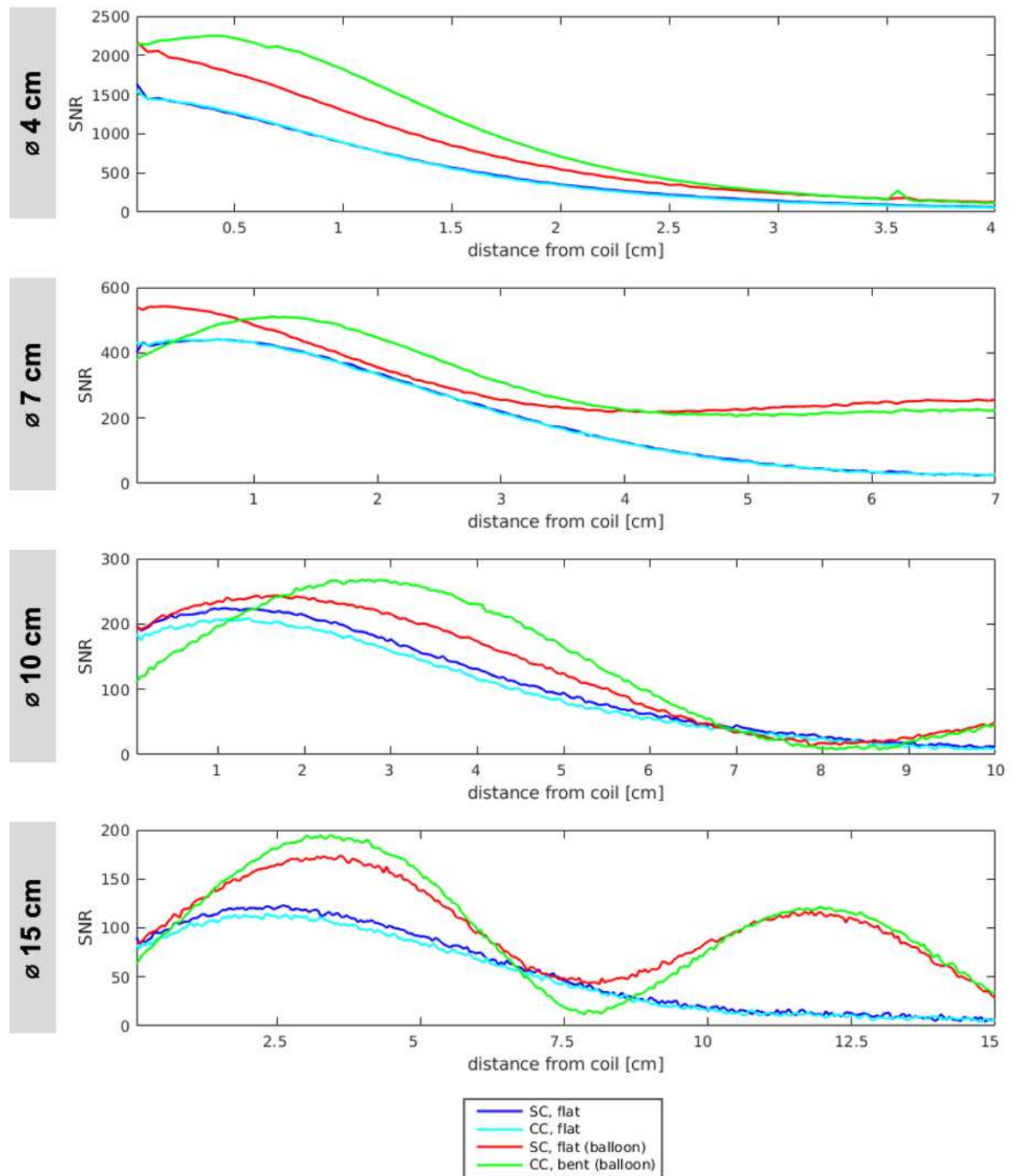


Figure 4.25: SNR along the central coil axis for 7 T SCs and CCs

4.3.4.3 MR imaging with different types of fruit at 3 T

In addition to homogeneous phantom measurements presented in *Article I*, a supplementary study was conducted to assess the coaxial coil functioning and applicability during 3 T MR imaging of different types of fruit.

The aim of the study was to further investigate the robustness and flexibility of CCs and to examine their MRI performance with a different phantom load and bending scenario. For each coaxial coil with diameters ranging from 4 to 15 cm (same coils as shown in Fig. 3a of *Article I*), a fruit was selected that could represent a possible bending scenario similar to the human anatomy:

- 4 cm: kiwi
- 7 cm: pomegranate
- 10 cm: muskmelon
- 15 cm: papaya

As the fruit represents a different load to the coaxial coil than the container or balloon phantom, re-tuning and re-matching of each coil was necessary. Matching levels (reflection coefficients S_{11}) better than -15 dB were reached for all coils. With a single form-fitted coaxial coil element, high resolution MR images were acquired using a Siemens 3 T Prisma Fit system.

All MR experiments were performed with 2D GRE sequences and the following imaging parameters were used:

- $T_R/T_E = 150/10$ ms
- slice thickness: 10 mm
- FA = 60°
- matrix size = 512
- $T_{acq} = 1.18$ min
- FOV = 100 x 100 / 120 x 120 / 140 x 140 / 210 x 210 mm² for experiments with the 4 / 7 / 10 / 15 cm CCs, respectively.
- in-plane resolution = 0.20 x 0.20 / 0.23 x 0.23 / 0.27 x 0.27 / 0.41 x 0.41 mm² for experiments with the 4 / 7 / 10 / 15 cm CCs, respectively.

For the acquisition of a transversal slice of the papaya using the 15 cm 2T5G coaxial coil, some of the above-listed imaging parameters were adapted for better contrast and visibility of structures inside the fruit:

- $T_R/T_E = 20/5.82$ ms
- $FA = 40^\circ$
- $FOV = 200 \times 200$ mm²
- in-plane resolution = 0.39 mm²

The coils were positioned in bent configuration on the fruit, as can be seen in Figure 4.26 - Figure 4.29. Each figure shows a photograph of the respective coil with connected tuning, matching and detuning interface on a fruit as well as the acquired MR images in different imaging planes, showing highly resolved, detailed internal structures of the fruit.

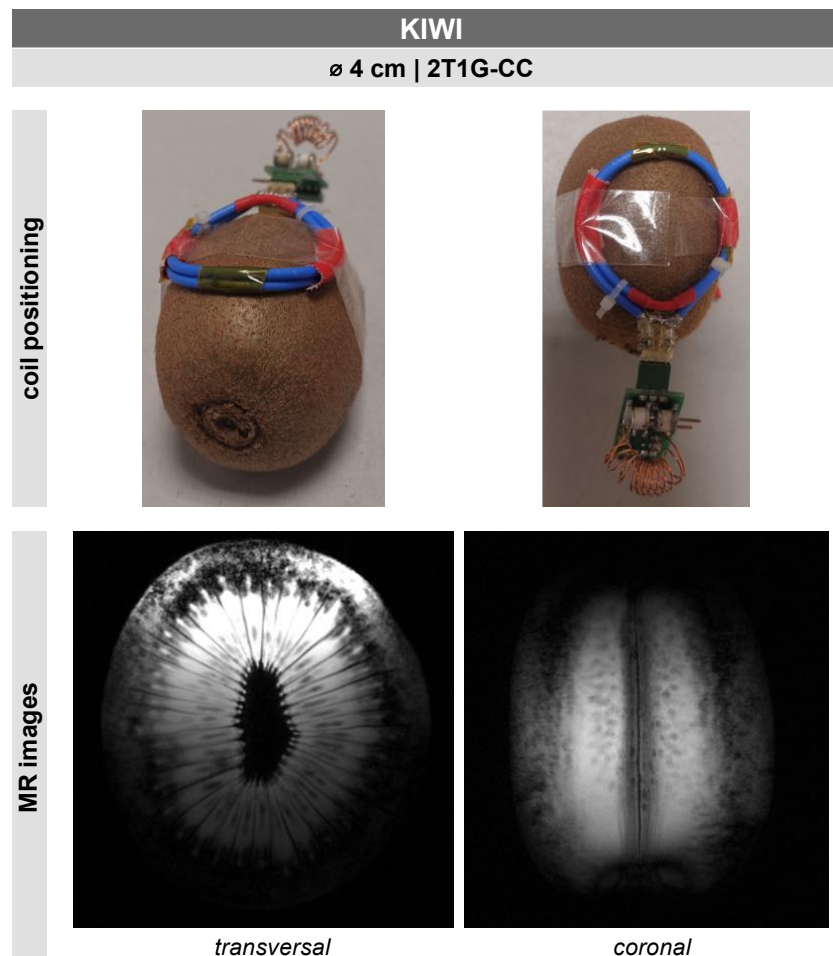


Figure 4.26: MR imaging set-up with a 2T1G-CC positioned on a kiwi and acquired MR images in the transversal and coronal plane (200 μ m isotropic resolution).

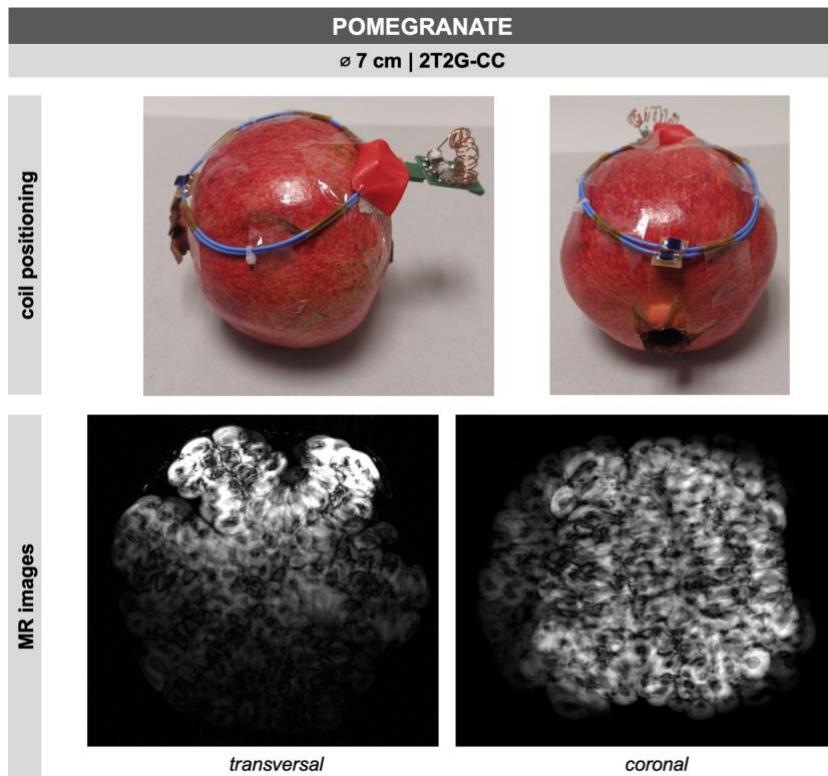


Figure 4.27: MR imaging set-up with a 2T2G-CC positioned on a pomegranate and acquired MR images in the transversal and coronal plane (230 μm isotropic resolution).

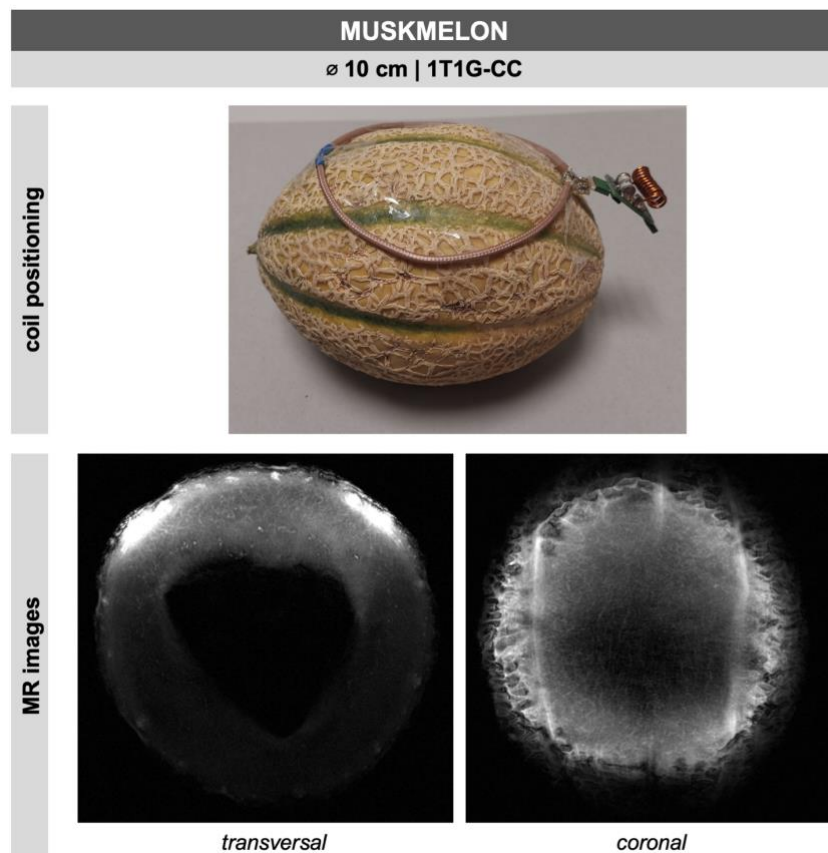


Figure 4.28: MR imaging set-up with a 1T1G-CC positioned on a muskmelon and acquired MR images in the transversal and coronal plane (270 μm isotropic resolution).

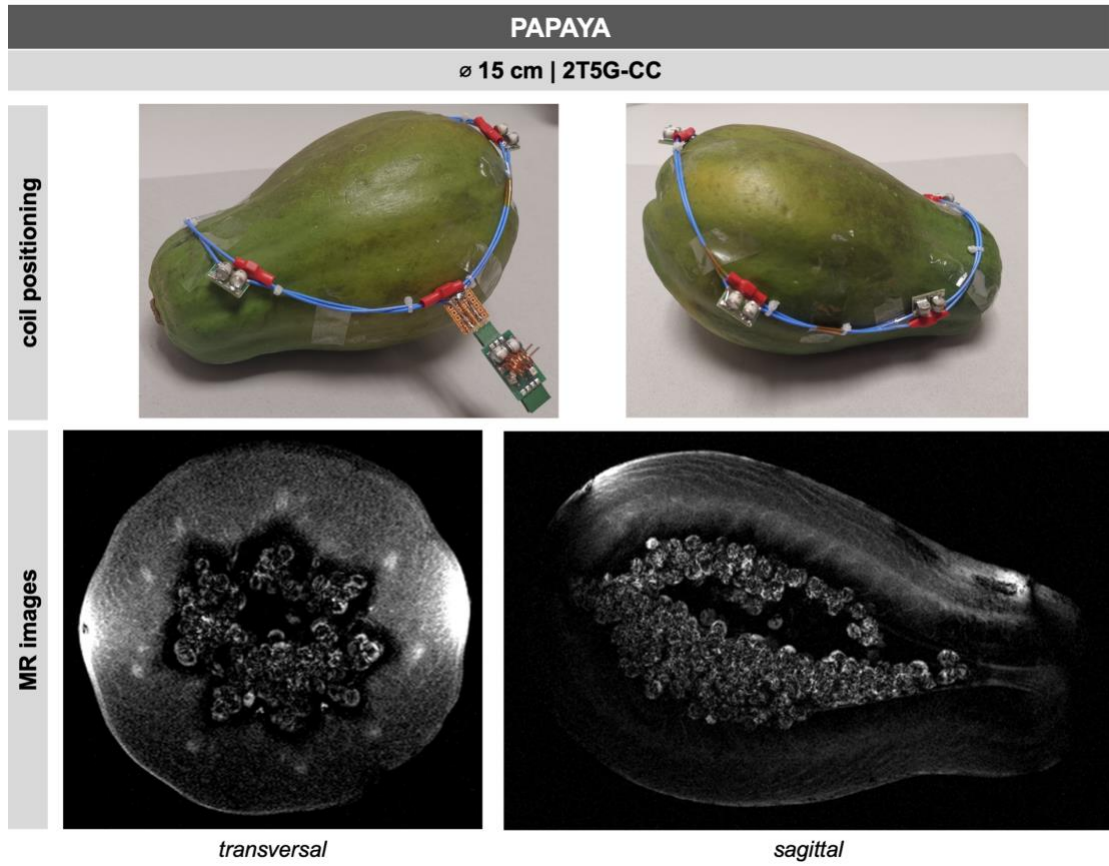


Figure 4.29: MR imaging set-up with a 2T5G-CC positioned on a papaya and acquired MR images in the transversal (390 μm isotropic resolution) and sagittal plane (410 μm isotropic resolution).

5. Study II: Wireless data transmission in MR

5.1 Prelude

Within the MR community, not only the discussions about flexible coil technology but also wireless MRI have increasingly gained interest during the last two decades. Several meetings with international experts in MR hardware and RF coil engineering were initiated, and content concerning wireless MRI was presented during conferences, e.g. already during the annual ISMRM (International Society for Magnetic Resonance in Medicine) conference in 2005, a dedicated virtual ISMRM meeting in 2017 and most recently the ISMRM conference 2020. Publications of the last few years have presented major advancements in the development of wireless power supply, digital wireless signal transmission and wireless control signaling in the MR environment.

The goal of the “perspective” article (*Article II*) was to provide a synthesized summary of the status-quo and to detail promising strategies and challenges encountered in the development of key technologies for wireless MR. This will give an outlook on the feasibility of wireless RF coils in the future, including opinions and ideas of the authors.

5.2 ***Article II: Perspectives in Wireless Radio Frequency Coil Development for Magnetic Resonance Imaging***

This sub-chapter is an exact replica of the article entitled “Perspectives in Wireless Radio Frequency Coil Development for Magnetic Resonance Imaging” [10], published in *Frontiers in Physics*. This work is licensed under a Creative Commons Attribution 4.0 License (<https://creativecommons.org/licenses/by/4.0/>).

Citation information: DOI 10.3389/fphy.2020.00011



Perspectives in Wireless Radio Frequency Coil Development for Magnetic Resonance Imaging

Lena Nohava^{1,2}, Jean-Christophe Ginefri¹, Georges Willoquet¹, Elmar Laistler² and Roberta Frass-Kriegl^{2*}

¹ Université Paris-Saclay, CEA, CNRS, Inserm, BioMaps, Orsay, France, ² Division MR Physics, Center for Medical Physics and Biomedical Engineering, Medical University of Vienna, Vienna, Austria

OPEN ACCESS

Edited by:

Wouter van Elmpt,
Maastricht University, Netherlands

Reviewed by:

Simone Angela S. Winkler,
Weill Cornell Medicine, Cornell
University, United States
Riccardo Lattanzi,
Langone Medical Center, New York
University, United States

*Correspondence:

Roberta Frass-Kriegl
roberta.frass@meduniwien.ac.at

Specialty section:

This article was submitted to
Medical Physics and Imaging,
a section of the journal
Frontiers in Physics

Received: 01 October 2019

Accepted: 09 January 2020

Published: 21 February 2020

Citation:

Nohava L, Ginefri J-C, Willoquet G,
Laistler E and Frass-Kriegl R (2020)
Perspectives in Wireless Radio
Frequency Coil Development for
Magnetic Resonance Imaging.
Front. Phys. 8:11.
doi: 10.3389/fphy.2020.00011

This paper addresses the scientific and technological challenges related to the development of wireless radio frequency (RF) coils for magnetic resonance imaging (MRI) based on published literature together with the authors' interpretation and further considerations. Key requirements and possible strategies for the wireless implementation of three important subsystems, namely the MR receive signal chain, control signaling, and on-coil power supply, are presented and discussed. For RF signals of modern MRI setups (e.g., 3T, 64 RF receive channels), with on-coil digitization and advanced methods for dynamic range ($DR \geq 16$ -bit) and data rate compression, still data rates > 500 Mbps will be required. For wireless high-speed MR data transmission, 60 GHz WiGig and optical wireless communication appear to be suitable strategies; however, on-coil functionality during MRI scans remains to be verified. Besides RF signals, control signals for on-coil components, e.g., active detuning, synchronization to the MR system, and B_0 shimming, have to be managed. Wireless power supply becomes an important issue, especially with a large amount of additional on-coil components. Wireless power transfer systems (> 10 W) seem to be an attractive solution compared to bulky MR-compatible batteries and energy harvesting with low power output. In our opinion, completely wireless RF coils will ultimately become feasible in the future by combining efficient available strategies from recent scientific advances and novel research. Besides ongoing improvement of all three subsystems, innovations are specifically required regarding wireless technologies, MR compatibility, and wireless power supply.

Keywords: magnetic resonance imaging, radio frequency coil, signal transmission, wireless technologies, wireless power

INTRODUCTION

Magnetic resonance imaging (MRI) has become one of the major tools in non-invasive medical diagnostics, providing a multitude of quantitative and functional information with ever-increasing performance. The constant search for improved sensitivity and specificity in MR examinations has coined the trend toward MR scanners with higher static magnetic field strength (B_0) [1, 2] and radio frequency (RF) coil arrays with larger numbers of individual receive elements [3]. Today's

high-end clinical MR scanners have a static magnetic field strength of 3 T (together with first clinical 7 T systems being installed currently) and feature up to 64 receive channels (128 or more in some research units), allowing for shorter examination times using parallel imaging [4, 5]. Typically, the excitation of the nuclear spins is done with a large high-power RF transmit coil—the system body coil—included in the scanner bore, while signal detection is performed with a local receive-only coil array, followed by on-coil preamplification and digitization in either the MR room or the technical cabinet, or rarely, on-coil. Coaxial cables are commonly used to transfer the received RF signal to the image reconstruction unit outside the MR scanner room and to power active electronic devices, such as preamplifiers, typically using DC current running on the coaxial cable's shield, which requires a bias-tee arrangement usually already integrated in commercial scanner hardware and thus avoids supplementary power cables. In addition, single wires carrying DC control signals are routed together with the coaxial cables, e.g., to bias PIN diodes as part of an on-coil switching circuitry. With increasing cabling complexity of modern high field scanners equipped with high-density and/or mechanically flexible receive arrays, the use of a large number of coaxial and wire cables gives rise to several challenges.

One main concern with cabling is the increased patient risk due to local heating phenomena associated to currents induced on the cable shields during RF transmission and fast switching of magnetic field gradients [6–8]. Secondly, as each receive element requires its own set of coaxial cable and wires, adjacent routing of cables may lead to cross talk and increase coupling between receive elements, causing a significant reduction of RF detection sensitivity. Since the coaxial cables are routed within the system body coil, a partial loss of transmit power may also occur, as some of the RF power is dissipated in the coil's cabling rather than in the target patient tissue. Baluns and RF traps [9, 10], conventionally used to reduce the abovementioned electromagnetic issues, make the receive coil heavy, bulky, and potentially intimidating and ill-fitting for patients. Moreover, handling of the coil becomes cumbersome and delicate in a way that the coil installation can occupy a significant fraction of the total exam time. This is of particular concern for applications requiring very long coaxial cables, such as abdominal MRI.

Consequently, the use of coaxial cables is one of the bottlenecks that have to be overcome to develop the next generation of coil arrays with improved sensitivity and less patient risk in high field MRI. Several approaches were proposed for the replacement of coaxial receive cables in MR experiments by optical fibers for analog [11–17] or digital [18–24] MR signal transmission. While the use of optical fibers avoids safety issues and reduces signal interferences, the positioning and handling of the receive coils are still limited by the length, placement, and maximum curvature of the optical fibers.

Fully wireless RF coils could lead to a safer, more cost- and time-efficient receive system for MRI and ultimately enable lightweight, flexible, or even “wearable” coil arrays (e.g., [23–26]), improving patient comfort and supporting the evolution of on-coil sensor integration.

Challenges in the development of wireless RF coils can especially be related to the harsh MR environment as all envisioned devices must be designed to be MR compatible, i.e., not ferro- or strongly para-magnetic. Additionally, all parts must function robustly in the strong static B_0 field and handle coil vibrations, patient movement, bore reflections, and most importantly, gradient and RF fields present during MRI. To this end, some sensitive parts can be covered by Faraday cages. Possible current induction on the devices should be avoided with regard to patient safety, and added on-coil devices, e.g., digitization units or wireless transceivers, must appear transparent during imaging. Also, it is desirable to preserve high linearity and a low system noise figure (<1 dB [27]) even with the inclusion of wireless technologies. Especially for flexible arrays, a reduction of the total amount, size, and weight of on-coil components is crucial.

In this work, we focus on the realizability of completely wireless MR receive arrays by addressing and interrelating different aspects of the MR receive system. The aim is to outline feasible and efficient approaches toward wireless communication in MRI and prospect digital wireless RF devices, highlighting the most promising strategies as well as associated benefits and challenges.

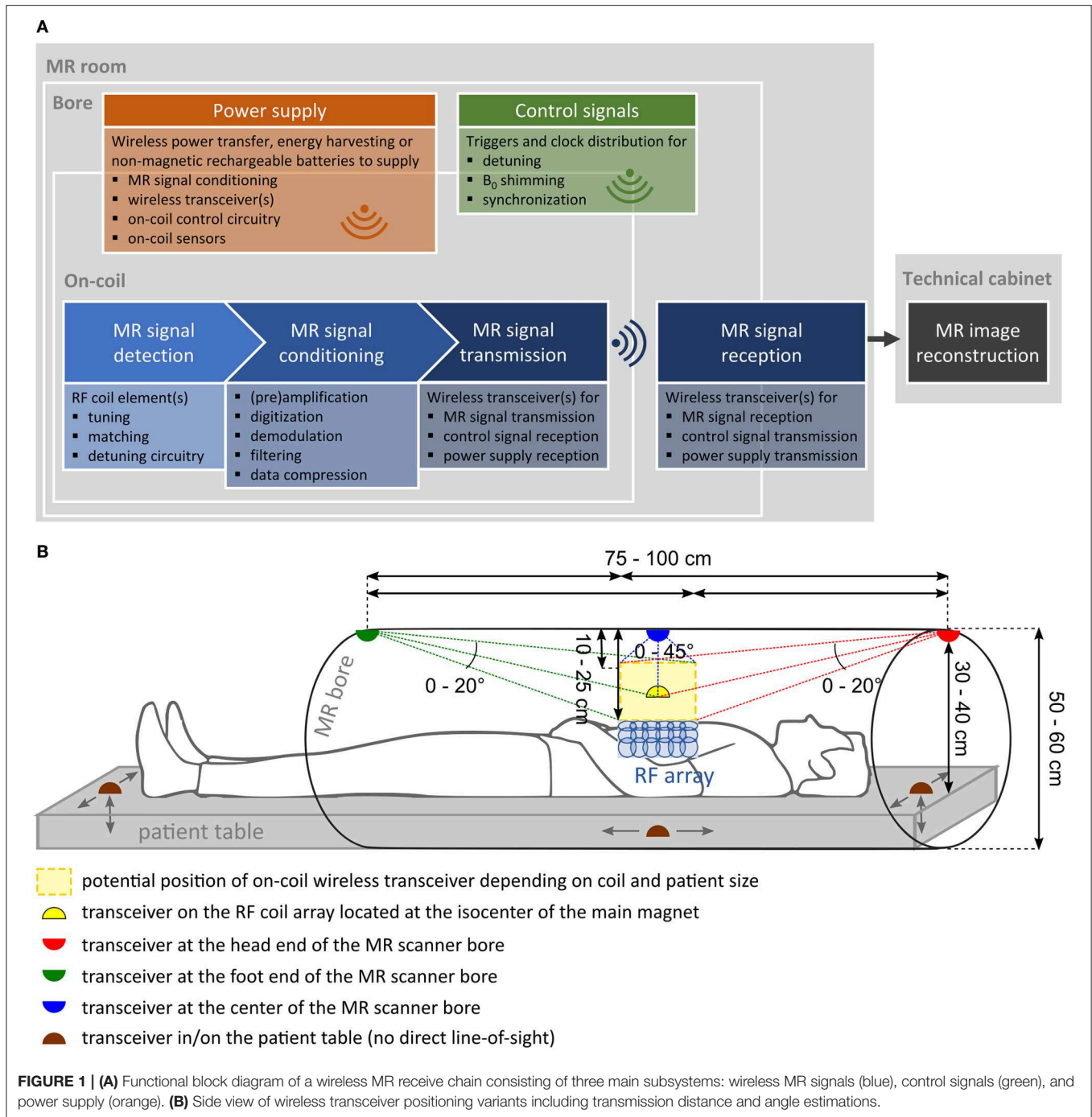
WIRELESS APPROACHES FOR DIFFERENT PARTS OF THE MR RECEIVE SYSTEM

Three subsystems that have to undergo significant changes for wireless MRI were identified: the MR receive signal chain, control signaling, and on-coil power supply. Their functional blocks and respective possible physical location are depicted in **Figure 1A**. Different wireless transceiver positioning variants, estimated transmission distances, and angles are sketched in **Figure 1B**.

In **Figure 2**, the state of the art in wireless RF coil development, listing existing technologies or strategies for each respective subsystem, corresponding to sections “MR Receive Signal Chain”, “Control Signaling”, and “On-Coil Power Supply” in the manuscript, is summarized. Specific requirements that need to be met for each of the functional blocks are included, and benefits of current technology as well as current limitations or challenges encountered in their development are listed. The following general requirements apply to all of the mentioned subsystems and corresponding components: MR compatibility (no impact on MRI or component functioning), patient safety (no heating), linearity, low noise figure, low power consumption, low number of additional components, miniature component size, and minimum weight. For all wireless paths, a reliable, ideally lossless, spatial data transmission (≈ 10 – 100 cm, see **Figure 1B**) is required.

MR Receive Signal Chain

The features of the MR signal directly impact signal conditioning, which comprises (pre)amplification, digitization, analog and/or digital data compression, and filtering. The MR signal is characterized by high signal frequency (the Larmor frequency),



depending on the investigated nucleus and B_0 field strength, typically in the order of 50–300 MHz. Further, the DR easily reaches ~ 90 dB [28]. In extreme cases, especially for high-resolution 3D acquisitions at high B_0 fields, the DR can attain up to ~ 120 dB [29, 30]. To enable proper signal conditioning for various imaging scenarios (frequency, DR, number of receive coil elements, etc.), necessary adaptations for a wireless receive chain imply the relocation of many components inside the MR bore or directly on-coil, e.g., adjustable gain amplifiers, analog-to-digital converters (ADCs), or mixers.

Signal Digitization

The choice of suitable digitization components is a critical task, as there is always a trade-off between achievable conversion rates, bit resolution, power dissipation, cost, and scalability to multi-channel systems. In general, on-coil digitization is advantageous, as it improves signal and phase stability, yielding better image quality, and offers easier scalability to multi-channel systems [18, 19, 31]. For component selection, the main challenges are related to the MR signal properties. Concerning the DR, ADCs should provide high bit resolutions ($\geq DR$ in decibels divided by

function	strategies	specific requirements	main benefits (+) and limitations/challenges (-)	Ref.
<i>Input</i>				
<i>preamplified analog filtered MR signal</i>				
MR signal conditioning				
analog down-conversion	baseband (BB)/intermediate frequency (IF)	<ul style="list-style-type: none"> • mixing with local oscillator (LO) signal on-coil • LO sync. to MR system clock 	<ul style="list-style-type: none"> + lower ADC sampling rate requirement - quadrature (I/Q) mixing necessary for BB conversion - free running LO impaired by gradient inductions 	21, 23, 24, 31, 35
	digitization	<ul style="list-style-type: none"> • sampling of demodulated MR signal (BB/IF) • ADC sampling rate $f_s \geq 2 \cdot f_{max}$ (except undersampling) • high ADC bit resolution (#b \geq DR/6.02) • ADC clock synchronization to MR system clock 	<ul style="list-style-type: none"> + low resulting data rate + easy reconfiguration to other B_0 field strengths by changing LO frequency + availability of low-cost low-speed multi-channel ADCs with high DR + low power consumption + on-coil MR compatibility of ADCs in integrated circuit tested - complexity of circuit design - high amount of on-coil components (using discrete components) 	21, 23, 24, 31, 35
digital data compression	direct (under)sampling without analog down-conversion	<ul style="list-style-type: none"> • integration of dedicated digital signal processing components in-bore/on-coil • synchronization to MR system clock 	<ul style="list-style-type: none"> + on-coil MR compatibility of custom high-speed ADCs with high DR tested + low amount of additional on-coil components (no analog mixing) - high resulting data rate - restriction to application at specific B_0 field strength - questionable MR compatibility of many commercially available ADCs - high cost and restricted availability of high-speed ADCs with high DR - high power consumption 	18-20, 22, 34, 36-39
digital data compression	(dynamic) demodulation/filtering/decimation/DR compression/bit-depth reduction/coil compression	<ul style="list-style-type: none"> • integration of dedicated digital signal processing components in-bore/on-coil • synchronization to MR system clock 	<ul style="list-style-type: none"> + reduced data for wireless transmission with early on-coil data compression + reduced data storage requirements + easier scalability to systems with many Rx channels/additional sensors - use of hardware on-coil still has to be demonstrated - increase in the number/size of on-coil components (e.g. FPGAs) - increase in required on-coil power 	22, 41, 42
<i>Output</i>				
<i>digital (compressed) MR signal</i>				
wireless MR signals				
MR signal transmission	Wi-Fi (2.4 – 60 GHz carriers)	<ul style="list-style-type: none"> • achievable data rate \geq input signal data rate (\rightarrow sets requirements for signal conditioning) 	<ul style="list-style-type: none"> + data rates < 665 Mbps over < 3 m feasible out-of-bore (Wi-Gig dongles) + data rates < 500 Mbps over < 0.65 m feasible in-bore with B_0 only (60 GHz) + low power solutions available (60 GHz) - trade-off between achievable data rate, device size and spatial range - questionable full MR compatibility of wireless transceivers 	43, 44, 51
	optical wireless communication (THz carriers)		<ul style="list-style-type: none"> + small and low power components + high achievable data rate, e.g. > 3Gbps Li-Fi - MR compatibility of suitable components to be tested - direct line-of-sight often required 	56
<i>Output</i>				
<i>wireless MR signal</i>				
wireless control signals				
active detuning	wireless trigger to switch diodes or FETs	<ul style="list-style-type: none"> • synchronization to the MR scanner's Tx/Rx state 	<ul style="list-style-type: none"> + low power FETs available + MR compatibility tested 	59, 60
synchronization	physical clock transmission	<ul style="list-style-type: none"> • phase synchronization of multiple receive channels' and on-coil electronics with the MR system 	<ul style="list-style-type: none"> + only hardware modifications necessary - additional wireless back-channel from MR system to coil required - additional on-coil clocking components required (e.g. PLL) 	34, 61
	software synchronization		<ul style="list-style-type: none"> - often software and hardware modifications necessary - free running on-coil oscillator impaired by gradient inductions - additional wireless channel from coil to MR system needed to send clock information alongside with MR data 	62-65
on-coil B_0 shimming	RF coil as B_0 shim element & Wi-Fi transponder	<ul style="list-style-type: none"> • independency of RF/DC/Wi-Fi operating modes 	<ul style="list-style-type: none"> + no separate Wi-Fi transponder required - shim current must be provided via battery pack/external power supply 	67
wireless power supply				
on-coil power supply	non-magnetic batteries	<ul style="list-style-type: none"> • available power \geq power required by on-coil components 	<ul style="list-style-type: none"> + simple implementation - restricted availability of fully MR compatible batteries - possible image artifacts - trade off between available power capacity and battery size and weight - need for recharging limits scan time 	21, 68, 69
	energy harvesting		<ul style="list-style-type: none"> + uses RF & gradient energy available during MRI scans - low power supply (\approx mW range) 	74-77
	RF WPT	<ul style="list-style-type: none"> • low-power on-coil components 	<ul style="list-style-type: none"> + high power supply (< 13 W) compared to other options + negligible impact on imaging performance demonstrated - low WPT distance (few cm) - dedicated WPT system needed in-bore 	78, 79
	optical WPT	<ul style="list-style-type: none"> • wireless power supply integration on-coil/in-bore 	<ul style="list-style-type: none"> + optical signal immune to RF - MR compatibility of components to be tested - low demonstrated power supply capability (\approx mW range) - direct line-of-sight required - eye-safety depending on optical power and wavelength 	70, 71

FIGURE 2 | Summary of the state of the art in wireless radio frequency (RF) coil development. Existing technologies/strategies for each subsystem (i.e., MR receive signal chain, control signaling, and on-coil power supply) are analyzed listing specific requirements, benefits, as well as limitations or challenges encountered in their current development.

6.02 [28]) to correctly quantize analog MR signal amplitudes. To date, commercially available high-speed ADCs dedicated to MRI are limited to 16-bit [32, 33], insufficient for some imaging scenarios with very high DR. Concerning the sampling rate, one possibility is direct sampling at the Nyquist rate, employing ADCs capable of sampling at high rates greater than twice the Larmor frequency [34]. However, the essential imaging information of the MR signal lies only within a small signal bandwidth (maximum 1–2 MHz), determined by the maximum gradient strength and the field of view (FOV), modulated onto the carrier wave at the Larmor frequency. Therefore, demodulation of the amplified analog RF signal to baseband (around zero frequency) or to an intermediate frequency (IF) by mixing with a local oscillator (LO) signal on-coil before conversion to digital data is possible. This significantly lowers the ADC sampling rate requirement. Analog down-conversion is often used in traditional systems [31, 35] but can also be advantageous for easier system reconfiguration to other B_0 fields and higher power efficiency (<240 mW/channel [21]). This was shown with broadband on-coil receivers for optical fiber transmission of digital signals from two [21] or four [24] wrist coil channels at 1.5–10.5 T. Direct undersampling corresponds to sampling at lower than twice the maximum frequency and digital demodulation at the same time. This technique was applied for single receive elements at 0.18 and 4.7 T [36, 37]. Multi-channel scalable solutions in combination with optical fibers were proposed for in-field receivers with one ADC per coil element at 1.5 and 3 T [18, 19], and four-channel ADCs for MRI up to 2.4 T with an eight-channel coil [38, 39]. Recent research also demonstrated a digital RF front end adaptable for 16 channels and useable from 1.5 to 11.7 T [20, 22]. Direct (under)sampling approaches are useful, as no analog conversion step is needed prior to digitization, and the amount of on-coil components is usually low. However, this technique can be demanding in terms of power consumption (>1 W/channel [20, 22]). Care has to be taken to remove signal ambiguities, e.g., by quadrature (I/Q) demodulation and digitization method-dependent signal filtering. Using I/Q demodulation, the number of components (e.g., amplifiers, ADCs, filters) after the quadrature mixer will be doubled, as there are two separate (I/Q) signal paths. Therefore, especially with discrete components, the form factor and power consumption of the receiver increase. Nevertheless, it can be advantageous to use baseband (I/Q) demodulation, e.g., in an integrated-circuit (IC) design [21, 23], to keep the resulting data rate at a minimum, which can be lower than with IF conversion or direct (under)sampling approaches.

Data Rate

Taken together, the required data rate for wireless transmission depends on the digitization approach and ADC bit resolution for any MR receive system with a specific B_0 field strength, imaging bandwidth, and number of coil elements. Sequence parameters, such as the receive duty cycle (the ratio between acquisition and repetition time), also influence the effective data rate. Estimations of up to 2.6 Gbps, assuming two coil elements at 1.5 T with direct sampling (130 Msps, 20-bit, 50% receive duty cycle) or 64 coil elements at 7 T with baseband sampling of a high bandwidth

signal (2 Msps, 20-bit I/Q, 50% receive duty cycle), reveal that these high resulting data rates are difficult to handle with current wireless technologies, as will be detailed in section “Wireless Transmission Technologies and Protocols”.

An evident remedy against high data rate and storage requirements is data compression, which can be realized in the analog domain by means of down-conversion before digitization as described above and/or in the digital domain, which requires dedicated signal processing units on-coil (e.g., a field-programmable gate array (FPGA) and digital frequency synthesizer [40]). Digital strategies for DR compression and coil-wise demodulation can be combined to efficiently reduce the data size to one-third of the original amount [41]. Nonetheless, with digital compression directly after digitization, the number of components and, therefore, also the power needed on-coil will increase [22, 42].

To give an estimate for the minimum data rate requirement, we take a modern clinical MRI setup at 3 T with 64 RF receive elements as a reference. In this case, a data rate of at least 512 Mbps would be desirable, assuming moderate signal bandwidth (500 ksps minimum sampling rate), average DR of around 90 dB (covered by 16-bit I/Q ADCs), 50% receive duty cycle, and baseband demodulation to keep the resulting data rate and component power consumption low. Our estimation is in line with other published values [43, 44], only differing in terms of assumed ADC bit resolution, receive duty cycle, or number of receive elements.

Wireless Transmission Technologies and Protocols

Wireless transmission setups have been investigated for their usability in MRI, testing only the wireless link with “synthetic” MR image data without RF coil or signal conditioning components. Except early work on analog wireless MR signal transmission with carriers in the low gigahertz range (<3 GHz [45–47]), research was mostly oriented toward digital wireless MR signal transceivers following IEEE Wi-Fi standards. For digital wireless communication in MRI, apart from achievable data rate and power consumption, lossless spatial transmission is an important criterion. First MR data transfer tests based on the 802.11b [48] or 802.11n [49] standards revealed that long range (>10 m) comes at the cost of low achievable data rates as well as large and power-consuming antennas. These approaches are clearly impractical for wireless MRI. More recent attempts were conducted with higher carriers in the 5 GHz band (802.11ac Wi-Fi protocol), showing reliable in-bore operation of client and router antennae during an MRI scan at data rates around 90 Mbps [44]. This Wi-Fi approach is interesting as small client routers, used in most portable devices nowadays, are available, providing sufficient spatial range for MRI. Efficient data throughput could be improved up to 350 Mbps, suitable for low-channel and low-bandwidth MRI. However, power consumption for only one transmitter antenna can exceed 1 W [50], which can be problematic with limited wireless on-coil power supply, as explained in section “On-Coil Power Supply”. Aiming for enhanced data rate capability and reduced power consumption, subsequent work focused on even higher carriers—60 GHz “WiGig” links—included in the

802.11ad Wi-Fi protocol. At 1.5 T, without the presence of RF pulses or gradients, data rates up to 500 Mbps over 10–65 cm were achieved using a miniature transceiver that can achieve up to 2.5 Gbps with only 14 mW DC power per wireless transmitter [43]. Recently, out-of-bore experiments with shielded WiGig dongles [51] have shown transmission rates of 187–665 Mbps over 3–5.5 m distance. This Wi-Fi standard meets our estimated minimum data rate requirement for a modern clinical MRI setup and is therefore viable for wireless coil arrays. Also, the shorter spatial transmission range of one of the presented 60 GHz links [43] is sufficient for some transceiver positioning variants (see **Figure 1B**).

Optical wireless communication (OWC) [52, 53] with visible, infrared, or ultraviolet light carriers (i.e., several 100 THz) could be an attractive alternative to Wi-Fi with distinct benefits [54]: large license-free bandwidth, small and low-power components, immunity to electromagnetic interference, and the possibility for integration into available illumination infrastructure; moreover, OWC can operate well below light intensities considered dangerous for the human eye. Data rates over 3 Gb/s in visible light communication have been shown using a single LED [55]. An MR-compatible OWC front end has been tested for 2 m analog positron emission tomography detector signal transmission [56], but the technology has not yet been exploited for MR signals. Unlike Wi-Fi, high-speed OWC mostly requires a direct line of sight between transceivers, although some systems can even communicate via diffuse light reflections [57]. Suitable components for Li-Fi (Light-Fidelity, i.e., high-speed optical wireless networking [58]) in MRI still remain to be identified and tested on-coil in future studies.

Authors' Opinion on a Wireless MR Receive Signal Chain

Wireless digital MR signal transmission appears feasible with current Wi-Fi strategies under the condition that appropriate measures for data rate reduction prior to wireless transmission are implemented on-coil, e.g., analog baseband demodulation, if possible even combined with further digital data compression methods. Wi-Fi protocol-dependent or component-related drawbacks, e.g., the trade-off between achievable data rate, spatial transmission range, and required power as well as questionable full MR compatibility, restrict the usability of today's Wi-Fi technologies. WiGig (60 GHz) seems to be a promising strategy because of high data rate capability, sufficient transmission range, and low power consumption, although full functioning of WiGig hardware on-coil during an MR scan and the effect on image quality still have to be examined. Also, the final interfacing of the chosen wireless (WiGig) transceiver to a digital RF coil still has to be demonstrated and can be challenging, as it requires the smooth interaction of various on-coil components. So far, Wi-Fi technology benefited from rapid development pushed by the portable device industry; therefore, we think that the implementation of future high-performance Wi-Fi transceivers in RF coils is an aspect to be followed up by the research community. Alternatively, OWC strategies could be investigated for wireless MR signal transmission. With OWC, the wireless transmission of uncompressed, directly digitized MR signals

could be envisioned, which is advantageous with respect to miniaturized device size and low system complexity but is questionable concerning a limited on-coil power budget.

Control Signaling

Striving for full removal of coil cabling, a bidirectional wireless link is indispensable as signals must be sent not only from the coil to the MR scanner but also from the scanner control unit to the coil, mainly for triggering, synchronization, and in some cases, control of B_0 shimming.

Active Detuning

Trigger signals need to be distributed to the coil electronics, e.g., to bias PIN diodes for detuning receive coils during RF transmission. Wireless detuning triggers transmitted via a 418 MHz antenna during an MRI scan at 1.5 T have been investigated [59], involving power-efficient replacement of PIN diodes by field-effect transistors (FETs) [60]. Presumably, these trigger signals could also be applied to activate power-consuming components (preamplifiers, ADCs) only during signal reception.

Synchronization

A stable clock, phase-synchronous with the MRI, controlling on-coil electronics (such as ADC or down-conversion), is critical. Clock jitter, which decreases the effective number of ADC bits and creates image artifacts, must be limited. For synchronization of MR unit and in-bore receivers, one method is to physically transmit the MRI master clock to the receiver, which has been demonstrated with 1.6, 2.4, and 3.5 GHz carriers [34, 61]. This requires additional on-coil clocking electronics (e.g., a phase-locked loop, PLL) and a wireless back channel from the MR unit to the coil. In contrast, on-coil clock generators can be used but are particularly impaired by gradient induction; therefore, free-running oscillator information has to be sent to the MR system alongside sampled data to detect and correct for frequency and phase errors as well as time offsets, i.e., to synchronize the two clocks by software. This often requires both additional hardware and software in the wireless receive system [62–65].

On-Coil B_0 Shimming

Several MRI applications benefit from localized on-coil B_0 shimming with DC currents on the RF coil elements compensating for B_0 inhomogeneities [66]. High shim currents themselves cannot be wirelessly transmitted but can be wirelessly controlled, which has been successfully demonstrated by 2.4 GHz Wi-Fi communication [67], using the RF coil itself as a wireless transponder.

Authors' Opinion on Wireless Control Signaling

Overall, less stringent requirements concerning data rate and DR apply to wireless control signals, but correct timing and reliable, simultaneous operation to other wireless paths, especially the MR signal transmission, play a crucial role. Wireless control of active detuning and on-coil B_0 shimming circuits is feasible with existing technologies and has been implemented during an MRI scan in combination with a wired or battery power supply and MR signal transmission via coaxial cables. Solutions

for the synchronization of LO signals or ADC sampling clocks to the MR system clock, crucial to avoid image artifacts and signal degradation, were presented but not demonstrated with a realistic wireless MR receive chain yet because implementation in practice seems challenging. Patient movement and coil vibrations can become an issue for synchronization, but to date, physical system clock transmission via a wireless back-channel appears to be a quite robust solution for wireless MRI. The long-term stability of the external reference clock might be combined with further clock correction in post-processing. Also, a possibility for software synchronization with a free-running oscillator might be included in any case as a fallback strategy if the physical clock transmission fails.

On-Coil Power Supply

The electric power required on-coil is of major concern for wireless RF coil development. In wired coils, generally only components for preamplification and detuning (plus B_0 shimming in some applications) have to be supplied with DC power. In contrast, wireless digital MR signal transmission will add on-coil power requirements for ADCs, potential down-conversion, and wireless transceivers. In this case, the power budget can easily exceed 1–2 W per channel, especially with high-speed ADCs. Power requirements scale with the number of receive channels and depend on multiplexing strategies, i.e., if one ADC and/or wireless transceiver is used for one or multiple coil element(s). For a 64-channel coil and one direct sampling ADC per channel, the power requirement could thus exceed 100 W, which is not feasible with current wireless power supply strategies in MRI as detailed below. Therefore, the first step to implement power supply for wireless coils is to reduce power consumption. Realizable low-power solutions for digitization, detuning, and wireless transceivers have been investigated in studies cited above [21, 43, 60] and could be further improved employing passive components whenever possible, e.g., passive mixers for down-conversion. Assuming a low power consumption in the range of hundreds of milliwatts per receive channel, for arrays up to 64 channels, this still results in on-coil power requirements of tens of watts.

Batteries

The use of non-magnetic rechargeable batteries could be envisioned, although available battery power capacities are limited, and as a consequence, the need for recharging limits scan time. Li-ion batteries (e.g., 5,000 mAh, 7.2 V [21]) or, more specifically, Lithium-ion polymer batteries, e.g., used for motion sensors (250 mAh, 3.7 V, $6.5 \times 18 \times 25 \text{ mm}^3$ [68, 69]), themselves are generally non-magnetic. However, care must be taken because voltage conversion circuits often include ferrite core transformers not suitable for use in MRI. Typically, an increase in power capacity means bigger battery pack size (e.g., 6,000 mAh, 3.7 V, $5.8 \times 58 \times 138 \text{ mm}^3$ [69]), and it is therefore obvious that with higher channel count, battery power supply becomes cumbersome and suboptimal for use in-bore or on-coil with limited space.

Wireless Power Transfer

Optical wireless power transfer (WPT) has been suggested for recharging medical implants (<10 mW [70]) or portable devices [71] and could be used in analogy to power-over-fiber approaches previously employed in MRI [12, 72]. To satisfy the power budget for an MR receiver array, it is likely that multiple free-space lasers with high optical powers in combination with efficient photodetectors would be required, possibly resulting in solutions that—depending on optical powers and wavelengths—are not eye-safe [73] and would require sophisticated alignment mechanisms.

For MRI, WPT in the RF range and energy harvesting have been investigated as attractive alternatives. The latter converts energy from electromagnetic fields present during an MR examination, namely the transmit RF field (tens of kilowatts) and gradient fields, into DC power, using inductive coupling in resonant “harvesting” loops [74–77]. Harvesting loops rely on induction at the Larmor frequency, and thus, to avoid system interferences, the size and placement of the loops cannot be chosen freely; further, variations in harvested power depending on the imaging sequence have to be taken into account, which limits the achievable power supply (tens of milliwatts). RF WPT implies the construction of a dedicated system consisting of primary (e.g., in the patient table) and secondary (close to the receive coil) loops for the sole purpose of power delivery by inductive coupling. Byron et al. [78, 79] propose an MR-compatible WPT system operating at 10 MHz transferring up to 13 W over a few centimeters’ distance in a 1.5 T system.

Authors’ Opinion on Wireless On-Coil Power Supply

The analysis of existing approaches for wireless on-coil power supply leads us to the conclusion that this aspect is still a bottleneck, currently preventing completely wireless MRI. Limitations due to available on-coil power reappear in every subsystem, e.g., concerning the choice of digitization components, analog/digital compression steps, and wireless transceivers. To overcome this bottleneck, ideally, solutions should be found to reduce the total power consumption per wireless MR channel to around 200 mW, so that a 13 W RF WPT system would be sufficient to supply DC power for a 64-channel coil array. Further advances in wireless power development are also desirable to increase available on-coil power budget and therefore alleviate related restrictions. Batteries are currently the only solution for a simple implementation of on-coil power supply, but considering weight, size, and uncertain MR compatibility in some cases, this approach should not remain the only accessible strategy in the future. Out of the other existing strategies, we believe that RF WPT is currently the most sophisticated and promising wireless power supply solution for receive arrays including electronics, as it is capable of supplying a high amount of DC power with negligible impact on MRI performance. A drawback of RF WPT is that the developed system is not yet optimized for on-coil (secondary loop) or in-bore (primary loop) integration. Power transfer distance should ideally be increased and system size and complexity reduced to yield an easily reproducible and efficient WPT solution. Perhaps, another alternative DC power source in MRI

might be a technology based on the magnetoelectric effect, using a piezoelectric material between magnetostrictive layers [80]. However, this technology has not been adapted for MRI conditions yet and will, as we believe, rather be suitable for power delivery in the milliwatt range, similar to existing harvesting techniques, as it is now employed for medical implant charging.

DISCUSSION AND CONCLUSION

In this paper, we summarized the status quo of wireless RF coil development and analyzed existing strategies for the adaptation of the three subsystems of wireless RF coils: the MR receive signal chain, control signaling, and on-coil power supply. We reviewed the benefits of current technology as well as technological challenges or limitations encountered in their development and suggest some future directives.

Over the last years, considerable progress has been made investigating wireless MR and control signal transmission. Feasible strategies exist for on-coil digitization, wireless in-bore signal transmission, cordless active detuning, synchronization to the MR system, and B_0 shim control. However, regarding the numerous requirements for a complete removal of coil cabling in high-density coil arrays, there is still a need for improvement. Solutions described in this work have limitations concerning data rate capabilities and spatial transmission distance as well as power consumption and device size. In addition, full MR compatibility is often questionable. Despite required innovations, we think that future work should focus on the first demonstration of a complete bidirectional wireless MR and control signal chain. This implies the connection of an RF coil with on-coil digitization to a suitable wireless transceiver and the inclusion of wireless active detuning and synchronization circuitry on-coil (leaving out B_0 shimming in a first step, reserved for some specific applications). An important aspect is to thoroughly test this assembly under realistic MRI scan conditions, i.e., with B_0 , RF, and gradient fields present and patient movement or coil vibrations possibly impairing component functioning, especially wireless links, and MRI performance. For a proof of concept, only a low number of RF receive elements could be targeted to

circumvent high system complexity and high demands in terms of system miniaturization, required data rate, and on-coil power.

Already with low channel counts, wireless on-coil power supply seems to be the main bottleneck, currently preventing fully wireless MRI. Other than bulky rechargeable batteries, no easily accessible WPT technology exists. We believe that reduction of on-coil component power consumption will be achieved and more efficient technologies for WPT will be developed that can be more easily integrated in existing MR systems.

In conclusion, based on our investigations of the state of the art, we predict that completely wireless RF coils will be feasible in the future. Their final implementation will require the combination of already-available technologies and the investigation of alternative promising strategies. Ultimately, with innovations especially required for wireless technologies (e.g., OWC for MRI), MR-compatible components, as well as wireless power supply, efficient solutions for each of the subsystems could be assembled. The realization of wireless RF coils would lead to a significant improvement in coil usability, image quality, patient safety, and comfort.

In the future, wireless RF coils could also follow the trend of additional sensor integration, providing a multitude of complementary information during MRI, e.g., patient motion [81, 82], to further improve image quality and physiological monitoring. While wireless sensor data transmission often relaxes data rate constraints, efficient power supply and reliable data transmission still have to be ensured.

AUTHOR CONTRIBUTIONS

RF-K initiated the work. LN, RF-K, EL, and J-CG contributed to the literature search. LN, RF-K, and EL generated the figures. All authors contributed to writing and proofreading the manuscript.

FUNDING

This work was funded by the Austrian/French FWF (Austrian Science Fund)/ANR grant, No. I-3618 BRACOIL, and the Austrian/French OeAD WTZ grant FR 03/2018.

REFERENCES

- Moser E. Ultra-high-field magnetic resonance: why and when? *World J Radiol.* (2010) 2:37–40. doi: 10.4329/wjr.v2.i1.37
- Moser E, Laistler E, Schmitt F, Kontaxis G. Ultra-high field NMR and MRI—the role of magnet technology to increase sensitivity and specificity. *Front Phys.* (2017) 5:33. doi: 10.3389/fphy.2017.00033
- Roemer PB, Edelstein WA, Hayes CE, Souza SP, Mueller OM. The NMR phased array. *Magn Reson Med.* (1990) 16:192–225. doi: 10.1002/mrm.1910160203
- Sodickson DK, Manning WJ. Simultaneous acquisition of spatial harmonics (SMASH): fast imaging with radiofrequency coil arrays. *Magn Reson Med.* (1997) 38:591–603. doi: 10.1002/mrm.1910380414
- Pruessmann KP, Weiger M, Scheidegger MB, Boesiger P. SENSE: sensitivity encoding for fast MRI. *Magn Reson Med.* (1999) 42:952–62.
- Konings MK, Bartels LW, Smits HFM, Bakker CJG. Heating around intravascular guidewires by resonating RF waves. *J Magn Reson Imaging.* (2000) 12:79–85. doi: 10.1002/1522-2586(200007)12:1<79::aid-jmri9>3.0.co;2-t
- Armenean C, Perrin E, Armenean M, Beuf O, Pilleul F, Saint-Jalmes H. RF-induced temperature elevation along metallic wires in clinical magnetic resonance imaging: influence of diameter and length. *Magn Reson Med.* (2004) 52:1200–6. doi: 10.1002/mrm.20246
- International Electrotechnical Commission (IEC). *International Standards. Medical Electrical Equipment – Part 2-33: Particular Requirements for the Basic Safety and Essential Performance of Magnetic Resonance Equipment for Medical Diagnosis (IEC-60601-2-33).* 3.1. Geneva (2013).
- Peterson DM, Beck BL, Duensing GR, Fitzsimmons JR. Common mode signal rejection methods for MRI: reduction of cable shield currents for high static magnetic field systems. *Concepts Magn Reson Part B Magn Reson Eng.* (2003) 19:1–8. doi: 10.1002/cmr.b.10090
- Seeber DA, Jevtic J, Menon A. Floating shield current suppression trap. *Concepts Magn Reson Part B Magn Reson Eng.* (2004) 21:26–31. doi: 10.1002/cmr.b.20008

11. Yuan J, Wei J, Shen GX. A 4-channel coil array interconnection by analog direct modulation optical link for 1.5-T MRI. *IEEE Trans Med Imaging*. (2008) 27:1432–8. doi: 10.1109/TMI.2008.922186
12. Memis OG, Eryaman Y, Aytur O, Atalar E. Miniaturized fiber-optic transmission system for MRI signals. *Magn Reson Med*. (2008) 59:165–73. doi: 10.1002/mrm.21462
13. Fandrey S, Weiss S, Müller J. A novel active MR probe using a miniaturized optical link for a 1.5-T MRI scanner. *Magn Reson Med*. (2012) 67:148–55. doi: 10.1002/mrm.23002
14. Koste GP, Nielsen MC, Tolliver TR, Frey RL, Watkins RD. Optical MR receive coil array interconnect. In: *Proceedings of the International Society for Magnetic Resonance in Medicine 13*. Miami Beach (2005). p. 411.
15. Biber S, Baureis P, Bollenbeck J, Höcht P, Fischer H. Analog optical transmission of 4 MRI receive channels with high dynamic range over one single optical fiber. In: *Proceedings of the International Society for Magnetic Resonance in Medicine 16*. Toronto (2008). p. 1120.
16. Demir T, Delabarre L, Akin B, Adriany G, Ugurbil K, Atalar E. Optical transmission system for high field systems. In: *Proceedings of the International Society for Magnetic Resonance in Medicine 19*. Montréal (2011). p. 1865.
17. Du C, Yuan J, Shen GX. Comparison of FP, VCSEL and DFB laser diode in optical transmission for MR RF coil array. In: *Proceedings of the International Society for Magnetic Resonance in Medicine 15*. Berlin (2007). p. 1041.
18. Possanzini C, Van Liere P, Roeven H, Den Boef J, Saylor C, Van Eggermond J, et al. Scalability and channel independency of the digital broadband dStream architecture. In: *Proceedings of the International Society for Magnetic Resonance in Medicine 19*. Montréal (2011). p. 5103.
19. Possanzini C, Harvey PR, Ham K, Hoogeveen R. *The Digital Revolution in MRI With dStream Architecture*. (2016) Available online at: <http://clinical.netforum.healthcare.philips.com/global/Explore/White-Papers/MRI/Ingenia-dStream-architecture-the-digital-revolution-in-MRI> (accessed September 2, 2019).
20. Reber J, Marjanovic J, Brunner DO, Port A, Pruessmann KP. Scalable, in-bore array receiver platform for MRI. In: *Proceedings of the International Society for Magnetic Resonance in Medicine 24*. Singapore (2016). p. 2170.
21. Sporrer B, Wu L, Bettini L, Vogt C, Reber J, Marjanovic J, et al. A fully integrated dual-channel on-coil CMOS receiver for array coils in 1.5–10.5 T MRI. *IEEE Trans Biomed Circuits Syst*. (2017) 11:1245–55. doi: 10.1109/TBCAS.2017.2764443
22. Reber J, Marjanovic J, Brunner DO, Port A, Schmid T, Dietrich BE, et al. An in-bore receiver for magnetic resonance imaging. *IEEE Trans Med Imaging*. (2019). doi: 10.1109/TMI.2019.2939090. [Epub ahead of print].
23. Sporrer B, Bettini L, Vogt C, Mehmman A, Reber J, Marjanovic J, et al. Integrated CMOS receiver for wearable coil arrays in MRI applications. In: *Design, Automation & Test in Europe Conference & Exhibition (DATE)*. (2015) p. 1689–94. doi: 10.7873/DATE.2015.1152
24. Port A, Reber J, Vogt C, Marjanovic J, Sporrer B, Wu L, et al. Towards wearable MR detection: a stretchable wrist array with on-body digitization. In: *Proceedings of the International Society for Magnetic Resonance in Medicine 26*. Paris (2018). p. 17.
25. Frass-Kriegl R, Navarro de Lara LI, Pichler M, Sieg J, Moser E, Windischberger C, et al. Flexible 23-channel coil array for high-resolution magnetic resonance imaging at 3 Tesla. *PLoS ONE*. (2018) 13:e0206963. doi: 10.1371/journal.pone.0206963
26. Mehmman A, Varga M, Vogt C, Port A, Reber J, Marjanovic J, et al. On the bending and stretching of liquid metal receive coils for magnetic resonance imaging. *IEEE Trans Biomed Eng*. (2019) 66:1542–8. doi: 10.1109/TBME.2018.2875436
27. De Zanche N. MR receive chain. In: *Proceedings of the International Society for Magnetic Resonance in Medicine 27*. Montréal (2019).
28. Gabr RE, Schär M, Edelstein AD, Kraitchman DL, Bottomley PA, Edelstein WA. MRI dynamic range and its compatibility with signal transmission media. *J Magn Reson*. (2009) 2:137–45. doi: 10.1016/j.jmr.2009.01.037
29. Behin R, Bishop J, Henkelman RM. Dynamic range requirements for MRI. *Concepts Magn Reson Part B Magn Reson Eng*. (2005) 26:28–35. doi: 10.1002/cmr.b.20042
30. Yuan J, Wei J, Du C, Shen GX. Investigation of dynamic range requirement for MRI signal transmission by optical fiber link. In: *Proceedings of the International Society for Magnetic Resonance in Medicine 15*. Berlin (2007). p. 995.
31. Hashimoto S, Kose K, Haishi T. Comparison of analog and digital transceiver systems for MR imaging. *Magn Reson Med Sci*. (2014) 13:285–91. doi: 10.2463/mrms.2013-0114
32. Texas Instruments. *Magnetic resonance Imaging (MRI)*. Available online at: http://www.ti.com/solution/mri_magnetic_resonance_imaging (accessed September 3, 2019).
33. ADI's *Magnetic Resonance Imaging (MRI) Solutions*. Available online at: https://www.analog.com/media/cn/technical-documentation/apm-pdf/adi-mri-solution_en.pdf (accessed September 3, 2019).
34. Sekiguchi T, Akita K, Nakanishi T, Kato S, Adachi K, Okamoto K. Development of digital wireless transceiver for a MRI coil with clock synchronization. In: *Proceedings of the International Society for Magnetic Resonance in Medicine 17*. Honolulu (2009). p. 3048.
35. Bollenbeck J, Vester M, Oppelt R, Kroeckel H, Schnell W. A high performance multi-channel RF receiver for magnet resonance imaging systems. In: *Proceedings of the International Society for Magnetic Resonance in Medicine 13*. Miami Beach (2005). p. 860.
36. Giovannetti G, Hartwig V, Viti V, Gaeta G, Francesconi R, Landini L, et al. Application of undersampling technique for the design of an NMR signals digital receiver. *Concepts Magn Reson Part B Magn Reson Eng*. (2006) 29:107–14. doi: 10.1002/cmr.b.20065
37. Pérez P, Santos A, Vaquero JJ. Potential use of the undersampling technique in the acquisition of nuclear magnetic resonance signals. *Magn Reson Mater Phys Biol Med*. (2001) 13:109–17. doi: 10.1016/S1352-8661(01)00137-5
38. Tang W, Sun H, Wang W. A digital receiver module with direct data acquisition for magnetic resonance imaging systems. *Rev Sci Instrum*. (2012) 83:104701. doi: 10.1063/1.4755089
39. Tang W, Wang W, Liu W, Ma Y, Tang X, Xiao L, et al. A home-built digital optical MRI console using high-speed serial links. *Magn Reson Med*. (2015) 74:578–88. doi: 10.1002/mrm.25403
40. De Zanche N. MRI technology: circuits and challenges for receiver coil hardware. In: Iniewski K, editor. *Medical Imaging: Principles, Detectors, and Electronics*. Hoboken, NJ: John Wiley & Sons, Inc. (2009). p. 285–301.
41. Jutras JD, Fallone BG, De Zanche N. Efficient multichannel coil data compression: a prospective study for distributed detection in wireless high-density arrays. *Concepts Magn Reson Part B Magn Reson Eng*. (2011) 39:64–77. doi: 10.1002/cmr.b.20191
42. Marjanovic J, Reber J, Brunner DO, Engel M, Kasper L, Dietrich BE, et al. A reconfigurable platform for magnetic resonance data acquisition and processing. *IEEE Trans Med Imaging*. (2019). doi: 10.1109/TMI.2019.2944696. [Epub ahead of print].
43. Aggarwal K, Joshi KR, Rajavi Y, Taghivand M, Pauly JM, Poon ASY, et al. A millimeter-wave digital link for wireless MRI. *IEEE Trans Med Imaging*. (2017) 36:574–83. doi: 10.1109/TMI.2016.2622251
44. Vassos C, Robb F, Vasanaawala S, Pauly J, Scott G. Characterization of In-Bore 802.11ac Wi-Fi performance. In: *Proceedings of the International Society for Magnetic Resonance in Medicine 27*. Montréal (2019). p. 1543.
45. Scott G, Yu K. Wireless transponders for RF coils: systems issues. In: *Proceedings of the International Society for Magnetic Resonance in Medicine 13*. Miami Beach (2005). p. 330.
46. Heid O, Vester M, Cork P, Hulbert P, Huish DW. Cutting the cord - wireless coils for MRI. In: *Proceedings of the International Society for Magnetic Resonance in Medicine 17*. Honolulu (2009). p. 100.
47. Riffe MJ, Heilman JA, Gudino N, Griswold MA. Using on-board microprocessors to control a wireless MR receiver array. In: *Proceedings of the International Society for Magnetic Resonance in Medicine 17*. Honolulu (2009). p. 2936.
48. Wei J, Liu Z, Chai Z, Yuan J, Lian J, Shen GX. A realization of digital wireless transmission for MRI signals based on 802.11b. *J Magn Reson*. (2007) 186:358–63. doi: 10.1016/j.jmr.2007.03.003
49. Shen GX, Wei J, Pang Y. Design of digital wireless transmission for 64 channel array using IEEE 802.11n. In: *Proceedings of the International Society for Magnetic Resonance in Medicine 16*. Toronto (2008). p. 1121.
50. Saha SK, Deshpande P, Inamdar PP, Sheshadri RK, Koutsonikolas D. Power-throughput tradeoffs of 802.11n/ac in smartphones. In: *2015 IEEE Conference*

- on *Computer Communications (INFOCOM)*. Kowloon (2015). p. 100–8. doi: 10.1109/INFOCOM.2015.7218372
51. Ko Y, Bi W, Felder J, Shah NJ. Wireless digital data transfer based on WiGig/IEEE 802.11ad with self-shielded antenna gain enhancement for MRI. In: *Proceedings of the International Society for Magnetic Resonance in Medicine 27*. Montréal (2019). p. 1537.
 52. Barry JR. *Wireless Infrared Communications*. Norwell, MA: Kluwer Academic Publishers (1994).
 53. Chu T-S, Gans M. High speed infrared local wireless communication. *IEEE Commun Mag.* (1987) 25:4–10. doi: 10.1109/MCOM.1987.1093675
 54. Hou R, Chen Y, Wu J, Zhang H. A brief survey of optical wireless communication. In: *13th Australasian Symposium on Parallel and Distributed Computing (AusPDC 2015)*. Sydney (2015) p. 41–50.
 55. Tsonev D, Chun H, Rajbhandari S, McKendry JJD, Videv S, Gu E, et al. A 3-Gb/s single-LED OFDM-based wireless VLC link using a gallium nitride μ LED. *IEEE Photonics Technol Lett.* (2014) 26:637–40. doi: 10.1109/LPT.2013.2297621
 56. Konstantinou G, Ali W, Chil R, Cossu G, Ciaramella E, Vaquero J. Experimental demonstration of an optical wireless MRI compatible PET/SPECT insert front-end. In: *2016 IEEE Nuclear Science Symposium, Medical Imaging Conference and Room-Temperature Semiconductor Detector Workshop (NSS/MIC/RTSD)*. Strasbourg (2016). p. 1–4. doi: 10.1109/NSSMIC.2016.8069524
 57. Lu Z, Tian P, Fu H, Montes J, Huang X, Chen H, et al. Experimental demonstration of non-line-of-sight visible light communication with different reflecting materials using a GaN-based micro-LED and modified IEEE 802.11ac. *AIP Adv.* (2018) 8:105017. doi: 10.1063/1.5048942
 58. Tsonev D, Videv S, Haas H. Light fidelity (Li-Fi): towards all-optical networking. In: *Proceedings SPIE 9007, Broadband Access Communication Technologies VIII, 900702*. San Francisco, CA (2014). doi: 10.1117/12.2044649
 59. Lu JY, Robb F, Pauly J, Scott G. Wireless Q-spoiling of Receive Coils at 1.5T MRI. In: *Proceedings of the International Society for Magnetic Resonance in Medicine 25*. Honolulu (2017). p. 4297.
 60. Lu JY, Grafendorfer T, Zhang T, Vasanaawala S, Robb F, Pauly JM, et al. Depletion-mode GaN HEMT Q-spoil switches for MRI coils. *IEEE Trans Med Imaging.* (2016) 35:2558–67. doi: 10.1109/TMI.2016.2586053
 61. Lu JY, Grafendorfer T, Robb F, Winkler S, Vasanaawala S, Pauly JM, et al. Clock transmission methods for wireless MRI: a study on clock jitter and impact on data sampling. In: *Proceedings of the International Society for Magnetic Resonance in Medicine 27*. Montréal (2019). p. 1542.
 62. Scott G, Robb F, Pauly J, Stang P. Software synchronization of independent receivers by transmit phase tracking. In: *Proceedings of the International Society for Magnetic Resonance in Medicine 25*. Honolulu (2017). p. 4311.
 63. Reykowski A, Redder P, Calderon Rico R, Wynn T, Ortiz T, Dowling G, et al. High precision wireless clock recovery for on-coil MRI receivers using round-trip carrier phase tracking. In: *Proceedings of the International Society for Magnetic Resonance in Medicine 26*. Paris (2018). p. 27.
 64. Scott G, Vasanaawala S, Robb F, Stang P, Pauly J. Pilot tone software synchronization for wireless MRI receivers. In: *Proceedings of the International Society for Magnetic Resonance in Medicine 26*. Paris (2018). p. 25.
 65. Reber J, Marjanovic J, Schildknecht C, Brunner DO, Pruessmann KP. Correction of gradient induced clock phase modulation for in-bore sampling receivers. In: *Proceedings of the International Society for Magnetic Resonance in Medicine 25*. Honolulu (2017). p. 1056.
 66. Truong T-K, Darnell D, Song AW. Integrated RF/shim coil array for parallel reception and localized B0 shimming in the human brain. *Neuroimage.* (2014) 103:235–40. doi: 10.1016/j.neuroimage.2014.09.052
 67. Darnell D, Cuthbertson J, Robb F, Song AW, Truong TK. Integrated radio-frequency/wireless coil design for simultaneous MR image acquisition and wireless communication. *Magn Reson Med.* (2019) 81:2176–83. doi: 10.1002/mrm.27513
 68. Chen B, Weber N, Odille F, Large-Dessale C, Delmas A, Bonnemains L, et al. Design and validation of a novel MR-compatible sensor for respiratory motion modeling and correction. *IEEE Trans Biomed Eng.* (2017) 64:123–33. doi: 10.1109/TBME.2016.2549272
 69. PowerStream. Available online at: <https://www.powerstream.com/non-magnetic-lipo.htm> (accessed November 30, 2019).
 70. Saha A, Iqbal S, Karmaker M, Fairrose Zinnat S, Tanseer Ali M. A wireless optical power system for medical implants using low power near-IR laser. In: *2017 39th Annual International Conference of the IEEE Engineering in Medicine and Biology Society (EMBC)*. Seogwipo (2017). doi: 10.1109/EMBC.2017.8037238
 71. Wi-Charge. *The Future of Power*. Available online at: <https://wi-charge.com/> (accessed September 26, 2019).
 72. Werthen JG, Cohen MJ, Wu T-C, Widjaja S. Electrically isolated power delivery for MRI applications. In: *Proceedings of the International Society for Magnetic Resonance in Medicine 14*. Seattle (2006). p. 1353.
 73. International Electrotechnical Commission (IEC). *International Standard IEC 60825-1:2014. Safety of Laser Products - Part 1: Equipment Classification and Requirements 3*. Geneva (2014).
 74. Riffe MJ, Heilman JA, Griswold MA. Power scavenging circuit for wireless DC power. In: *Proceedings of the International Society for Magnetic Resonance in Medicine 15*. Berlin (2007). p. 3278.
 75. Höflin J, Fischer E, Hennig J, Korvink JG. Energy Harvesting towards autonomous MRI detection. In: *Proceedings of the International Society for Magnetic Resonance in Medicine 21*. Salt Lake City (2013). p. 728.
 76. Middelstaedt L, Foerster S, Doebbelin R, Lindemann A. Power electronics for an energy harvesting concept applied to magnetic resonance tomography. In: *Progress in Electromagnetics Research Symposium*. Prague (2015). p. 1419–23.
 77. Byron K, Robb F, Vasanaawala S, Pauly J, Scott G. Harvesting power wirelessly from MRI scanners. In: *Proceedings of the International Society for Magnetic Resonance in Medicine 27*. Montréal (2019). p. 1535.
 78. Byron K, Robb F, Stang P, Vasanaawala S, Pauly J, Scott G. An RF-gated wireless power transfer system for wireless MRI receive arrays. *Concepts Magn Reson Part B Magn Reson Eng.* (2017) 47B:e21360. doi: 10.1002/cmr.b.21360
 79. Byron K, Winkler SA, Robb F, Vasanaawala S, Pauly J, Scott G. An MRI compatible RF MEMs controlled wireless power transfer system. *IEEE Trans Microw Theory Tech.* (2019) 67:1717–26. doi: 10.1109/TMTT.2019.2902554
 80. Rizzo G, Loyau V, Nocua R, Lourme JC, Lefevre E. Potentiality of magnetolectric composites for wireless power transmission in medical implants. In: *13th International Symposium on Medical Information and Communication Technology (ISMICT)*. Oslo (2019). p. 1–4. doi: 10.1109/ISMICT.2019.8743873
 81. Schildknecht CM, Brunner DO, Schmid T, Reber J, Marjanovic J, Pruessmann KP. Wireless motion tracking with short-wave radiofrequency. In: *Proceedings of the International Society for Magnetic Resonance in Medicine 27*. Montréal (2019). p. 66.
 82. van Niekerk A, van der Kouwe A, Meintjes E. Toward “plug and play” prospective motion correction for MRI by combining observations of the time varying gradient and static vector fields. *Magn Reson Med.* (2019) 82:1214–28. doi: 10.1002/mrm.27790

Conflict of Interest: The authors declare that the research was conducted in the absence of any commercial or financial relationships that could be construed as a potential conflict of interest.

Copyright © 2020 Nohava, Ginefri, Willoquet, Laistler and Frass-Kriegl. This is an open-access article distributed under the terms of the Creative Commons Attribution License (CC BY). The use, distribution or reproduction in other forums is permitted, provided the original author(s) and the copyright owner(s) are credited and that the original publication in this journal is cited, in accordance with accepted academic practice. No use, distribution or reproduction is permitted which does not comply with these terms.

5.3 Supplementary studies: MR compatible optical wireless data transmission

5.3.1 Introduction

The theoretical possibility of employing an optical wireless communication approach for high-rate data transfer in wireless RF receiver arrays in the future was discussed in *Article II*. The motivation for supplementary studies was therefore to explore the feasibility of OWC in MR and to put a focus on the development of an OWC module.

The first goal was to employ OWC data transmissions where less stringent performance requirements (e.g., data rates) than for MR signals apply. In section 5.3.2, the prototype development of a custom-built optical wireless transceiver module and preliminary test results are described. The OWC module targets the in-bore optical wireless transmission of motion sensor data at a minimum rate of approximately 1 Mbps per sensor.

To further evaluate different light propagation scenarios inside the MR scanner bore, in section 5.3.3, a simulation study for different use cases is presented.

Finally, a test procedure to be followed to ensure full functioning of the envisioned OWC transmission system in the MR environment has been established. This summary of tests is presented in section 5.3.4, which could be the guideline for device performance, MR compatibility, and safety tests in the future.

5.3.2 Development of an OWC module prototype

5.3.2.1 Motivation

As discussed in *Article II*, the on-coil digitization and wireless transmission of high data rate signals is challenging. In order to alleviate data rate and digitization requirements for the development of a first prototype managing the optical wireless signal transmission in the MR, already digitized motion sensor signals were the target for preliminary tests. An MR compatible accelerometer for respiratory motion sensing, short “MARMOT”, as described by Chen *et al.* [11], was chosen to be a suitable example for a wearable sensor that could benefit from a wireless signal data transmission chain whilst providing relaxed requirements in terms of data rate (≈ 1 MBd) for the OWC prototype development.

The current set-up for the acquisition and transmission of different sensor data via long optical fibers to a real-time signal analyzer and event controller (SAEC), used by the IADI laboratory in Nancy (France), is sketched in Figure 5.1. Furthermore, the example of a MARMOT [11,214] is shown which is typically connected to the SAEC via two separate optical fibers to allow for bi-directional communication between SAEC and each motion sensor. For in-bore use, a non-magnetic battery and housing cover are placed on top of the PCB.

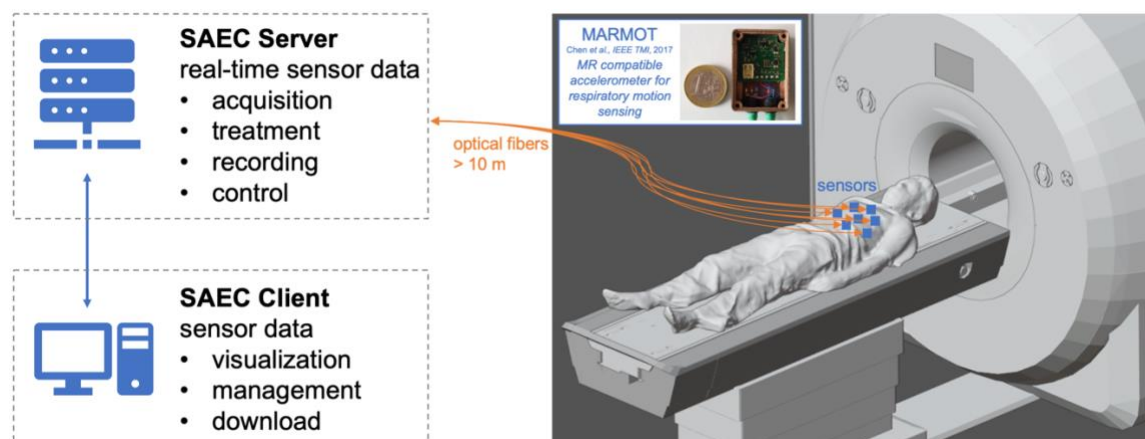


Figure 5.1: Current set-up for acquiring motion sensor data in the MR with optical fibers transmitting the signals to a real-time signal analyzer and event controller (SAEC). MR compatible accelerometer for respiratory motion sensing (MARMOT) photo courtesy of [11].

Each MARMOT contains a 3-axis accelerometer, 3-axis gyroscope, and 3-axis Hall sensor, sampling at 1 kHz. An asynchronous serial communication protocol (one start bit, one stop bit, no parity bit) is used for digital optical fiber data transmission of the motion data to the SAEC at a rate of approximately 1 MBd (921600 Bd). The data rate is set to 1 MBd in order to retrieve the data in real-time from the sensor and accommodate all other tasks, e.g. of the microcontroller, within one sensor time-sampling interval (1 ms), and to stay within data rate limitations of common serial to USB conversion cables as used for interfacing to the SAEC server after optical-electrical signal conversion. The bidirectional optical fiber link is used to activate sensor data transmission, starting by the sensor's identity, and to set the sensor in standby mode or transmit data of only some of the integrated measurement units (Hall sensor or gyroscope and accelerometer). One or multiple MARMOT's accelerometer data can be employed for retrospective motion correction, e.g. using a reconstruction-based method implemented in the so-called GRICS algorithm (generalized reconstruction by inversion of coupled systems, [228]). The MARMOT provides an alternative to pneumatic belts and is interesting as it can improve patient comfort and facilitate or accelerate the set-up process on the patient. A single MARMOT sensor which is placed close to the anatomy of interest can yield similar motion modelling and correction performance as with a pneumatic belt [11].

To further improve motion sensor handling, the goal is to replace the long optical fiber bundles, which can become especially cumbersome with a multitude of sensors, by an optical wireless transmission set-up. For OWC module prototype development, achieving the required data rate of 1 Mbps (or 1 MBd) for one MARMOT, a sufficient spatial transmission distance of at least ≈ 1 m and the conception of a general PCB layout were the primary goals. MR compatibility of the used components was a requirement that was considered during component selection but for the final implementation of OWC modules in the MR bore, parts of the current set-up will have to be replaced by a completely non-magnetic equivalent. Therefore, until now, preliminary tests were only conducted outside of the MR scanner.

5.3.2.2 OWC module design

The aim was to first characterize the performance of a designed OWC module consisting of an optical transmitter and receiver and surrounding Tx and Rx circuitry at a very basic level, as shown in Figure 5.2. As bidirectional (half-duplex) communication is targeted for the motion sensors, each module should be equipped with Rx and Tx components, i.e. PD(s) and LEDs, in the final version. For first tests, instead of directly interfacing the modules to a MARMOT output, a single-board computer (Raspberry Pi) was connected to each OWC module via its general-purpose input/output (GPIO) pins. The Raspberry Pi (RasPi) model 2B+ was used for all tests. Thus, in a first step, the RasPi takes over the TTL (transistor-transistor logic) signal generation, power supply and control functions which could later be replaced by the MARMOT itself, a battery and a microcontroller integrated on the OWC module.

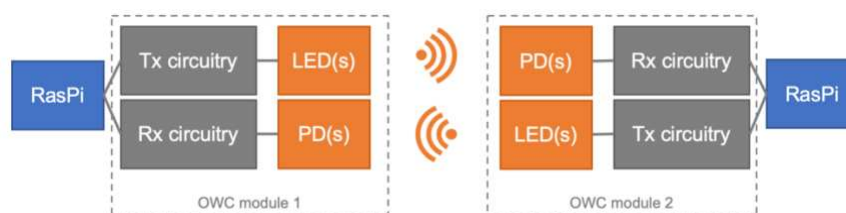


Figure 5.2: OWC module overview

The main components used in each OWC module, indispensable for the data link functioning are sketched in a simplified manner in Figure 5.3. Components are divided into the signal source and acquisition system, the Tx and Rx circuitry and optical transmitter(s) and receiver(s). Furthermore, the Rx signal at different stages, the Tx signal at the output of the RasPi as well as power supply and control signals, e.g. the comparator reference voltage CV_{Ref} , are indicated. On the bench, these signals were measured using an oscilloscope, and the different colors used to mark signal paths in Figure 5.3 correspond to the color code used for oscilloscope traces.

The full circuitry is shown in Figure 5.4. The circuit and PCB layout have been developed by Georges Willoquet at the BioMaps laboratory (Université Paris-Saclay). A list of main active components required to construct this OWC card can be found in the appendix of this thesis.

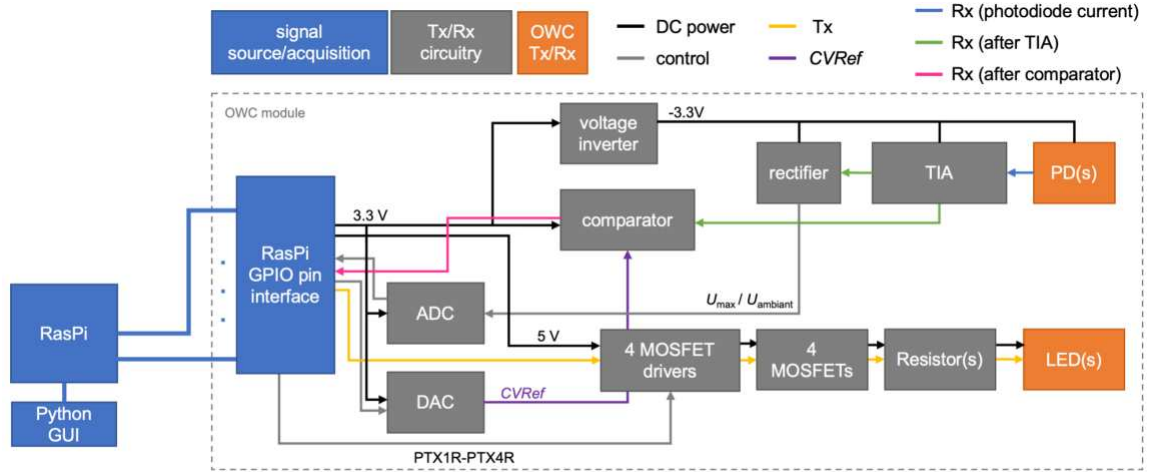


Figure 5.3: General schematic of components used in the OWC module

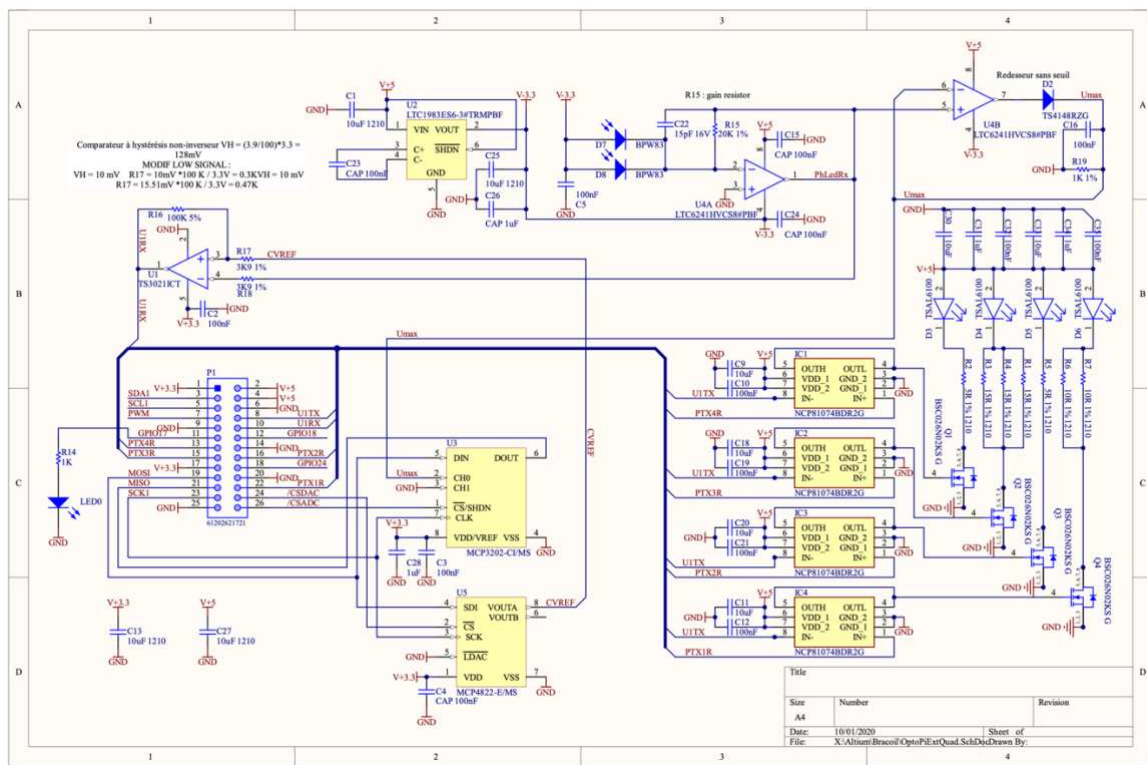


Figure 5.4: Circuit schematic of the fabricated OWC module prototype

5.3.2.3 Component description

In the following, a short overview and explanation of the main components used in the OWC module prototype is given.

RasPi GPIO pin interface

The transmit signal (U1TX, Figure 5.4) which can be arbitrary serial TTL data (byte arrays) controlled via a Python (v.3.7.4) graphical use interface (GUI) running on the RasPi is located at pin #8. The control signals (PTX1R-PTX4R, Figure 5.4) for the MOSFET (metal-oxide-semiconductor field-effect transistor) drivers are located on pin #13, 15, 16 and 22. The received signal (U1RX, Figure 5.4) is fed to pin #10. Further GPIO pins provide DC power and are used for interfacing to the DAC and ADC.

LED power adaptation

Different combinations of resistors (R1-R7, Figure 5.4) in series with the LEDs, determining the drive LED current, can be selected by a switching logic implemented by four high-speed MOSFET drivers (controlled by signals PTX1R-PTX4R) each in series to a MOSFET. With different resistor values, this results in theoretically 2^4 possible LED power combinations. As for preliminary tests, the limiting resistor was set to the same value for all 4 LEDs (5Ω) this results in 4 possible total LED power levels given in Table 5.1, depending on the number of active LEDs. The forward current determined by the resistors is approximately $3 \text{ V} / 5 \Omega = 600 \text{ mA}$ for each LED. With a voltage of $\approx 1.9 \text{ V}$ at each LED, this results in a total LED power of either 1.14, 2.28, 3.42 or 4.56 W for 1, 2, 3 or 4 active LEDs, respectively.

P_{LED}	PTX1R	PTX2R	PTX3R	PTX4R	$P_{\text{LED}\#1}$ [W]	$P_{\text{LED}\#2}$ [W]	$P_{\text{LED}\#3}$ [W]	$P_{\text{LED}\#4}$ [W]	$P_{\text{tot,LED}}$ [W]
1	0	0	0	1	0	0	0	1.14	1.14
5	0	1	0	1	0	1.14	0	1.14	2.28
7	0	1	1	1	0	1.14	1.14	1.14	3.42
15	1	1	1	1	1.14	1.14	1.14	1.14	4.56

Table 5.1: LED power levels ($P_{\text{tot,LED}}$) depending on the combination of resistors. P_{LED} denotes the value out of 2^4 possible combinations that was entered in the Python GUI (see Figure 5.6).

Optical transmitter and receiver

Concerning LED(s) and PDs, apart from a short rise/fall time to ensure fast switching response, the peak wavelength and spectral sensitivity has to be matched between LED and PD, i.e. they should have the same band pass characteristics. The PD ideally has a large radiant photosensitive area but usually there is a trade-off between speed and the size of the photosensitive area since the PD's capacitance increases with size. The reason why the PD is reverse biased (-3.3 V), i.e. operated in photoconductive

mode, is to increase the width of the depletion layer, therefore reduce the junction capacitance and as a consequence achieve faster response times.

During initial tests with a VLC system based on four white phosphorus LEDs as suggested in reference [229], insufficient data rates < 600 kbps (< 300 kbps using Manchester encoding) for the targeted purpose and transmission distances < 40 cm were achieved at high optical output powers that were perceived as very bright for the human eye. Furthermore, a strong influence from ambient light and board reflections on the data transfer as well as fast LED heating was observed during continuous operation [230]. For the OWC module version presented in this thesis, optical components operating in the near-IR light range were used. Four TSAL6100 LEDs with a peak wavelength of 940 nm and an angle of half intensity of $\pm 10^\circ$ were used as transmitters and could be driven individually, as indicated in the schematic in Figure 5.4. No eye-safety concerns apply for this type of infrared LED [231]. The optical receivers were two BPW83 PDs connected in parallel, with a large radiant sensitive area of 7.5 mm^2 each and angular sensitivity ($\pm 65^\circ$ angle of half sensitivity). Also, a daylight filter was part of the PDs, matched with 870 nm to 950 nm emitters. Short rise/fall times of the optical components (15 ns for the LED, 100 ns for the PD) let us expect to achieve high data rates. The rise time of PDs is higher than for the LEDs, therefore the system's modulation frequency will be limited by the optical Rx chain. According to Eq. 3.6 and Eq. 3.8 it can be calculated that the system rise/fall time is dominated by the PD and neglecting the influence of surrounding Rx and Tx circuitry, with NRZ OOK encoding, theoretically a bit rate of ≈ 7 Mbps would be achievable. In practice, rise/fall times of amplifier and comparator will reduce the achievable switching speed.

Transimpedance amplifier (TIA)

A transimpedance amplifier consisting of a CMOS operational amplifier (op amp), a feedback resistor (R_{gain} , $R15 = 20 \text{ k}\Omega$ in Figure 5.4) which determines the gain and a capacitor (C22) to ensure stability and low-pass filter the signal is used to convert the small PD current to a usable voltage signal. The TIA is suitable because it increases both gain and speed with the feedback resistor as compared to the use of a simple resistor for current-voltage conversion.

Rectifier

The rectifier can be used to extract the values of dark current (PD current without any incident light) or current due to ambient light (U_{ambient}) as well as the maximum signal voltage (U_{max}), in order to correctly set the reference voltage $CVRef$ fed to the comparator. $CVRef$ needs to be above the signal minimum U_{ambient} at approximately half the maximum signal amplitude U_{max} after the TIA. It can be calibrated depending on the ambient light conditions, LED power used and the Tx/Rx distance before data transmission, each time the set-up is modified. For preliminary tests, $CVRef$ was manually set via the Python GUI or could be read via the ADC as described below.

Comparator

The comparator takes the value set for $CVRef$ as an input and interprets analog voltage levels below $CVRef$ as a binary digital output “0” and voltages above $CVRef$ as “1”. Therefore, the comparator filters dark or ambient current and sets the output signal to levels between 0 and 3.3 V.

The Rx signal after the TIA is inverted as the PD is reverse biased but the comparator re-inverts it again so that the received signal levels are equal to the transmitted ones.

Analog-to-digital converter and digital-to-analog converter

A 12-bit ADC and DAC (digital-to-analog converter) were placed on the OWC modules, as described in [232], to read analog input voltages (U_{ambient} and U_{max}) and set analog voltages ($CVRef$) via digital control in the Python GUI. $CVRef$ can be set to a voltage at the DAC output between 0 V and the internal 2.048 V reference (by default). The bit resolution determines the number of possible voltage level discretization steps (2^{12}) of $CVRef$. The ADC is not automatically used but can be employed to read U_{ambient} and U_{max} which has been implemented in the Python GUI via a “Read ADC” button (see Figure 5.6). As a consequence, the operator is able to determine the value that has to be set for $CVRef$ (e.g. at $U_{\text{max}} - U_{\text{ambient}} / 2$).

5.3.2.4 Experimental validation

On the bench, the test set up consisted of two monitors, each one connected to a RasPi, and an oscilloscope to measure the signal amplitudes of transmitted and received bit sequences as well as $CVRef$. The fabricated OWC modules each connected to a RasPi

are shown in Figure 5.5. Whereas for preliminary tests, a dedicated Tx and Rx board was used, the optical transmitter and receiver could be mounted on both modules to carry out bidirectional tests.

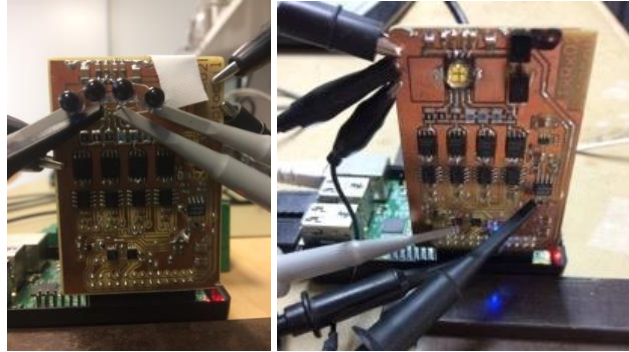


Figure 5.5: Transmitter (left) and receiver OWC card (right). The LEDs surrounded by a ball lens mounted on the Rx board are not used and could be replaced by IR LEDs (shown on the left side) for bidirectional tests.

A Python GUI depicted in Figure 5.6 was running on the RasPi to establish a TTL serial communication link and modify the following OWC parameters:

- LED intensity (LED power) P_{LED}
- Comparator reference voltage (CV_{Ref})
- Baud rate (equal to bits per second with NRZ OOK)
- Data string (byte array) to be sent and number of successive transmissions

The Python code used can be found in this GitHub repository: https://github.com/Inohav/owc_tests.

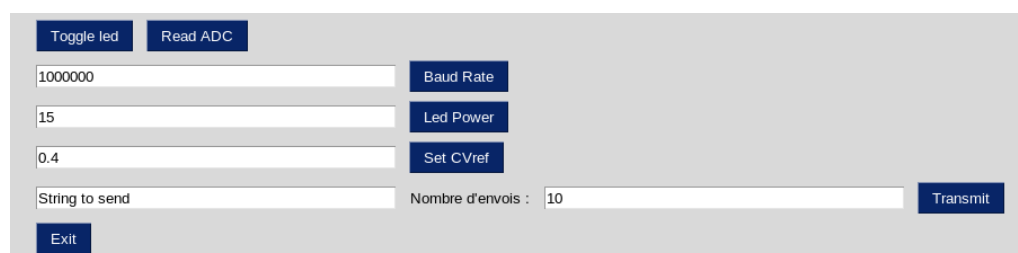


Figure 5.6: Python GUI

Manually adjustable parameters are the Rx gain by using different values of R_{gain} in the TIA or the spatial distance d between modules. The general approach followed during module tests was to determine the maximum achievable Baud rate for a module with fixed Rx gain, testing different transmission distances at different LED

power by steadily adjusting $CVRef$. After several iterations of optimizing the Rx gain, the OWC module configuration described above and shown in Figure 5.4 was found to be capable of transmitting data at a rate of 2 MBd over a small and large transmission distance (0.3 - 1.5 m) using a LOS between modules and simple NRZ OOK. Selected test results are detailed in the following.

The test result summary in Table 5.2 is voluntarily restricted to the most important cases of successful and power-efficient data transmissions (test 1 and 2), and examples demonstrating the upper data rate limit for this OWC module configuration using NRZ OOK (tests 3-5).

test	# LEDs	P_{LED} [W]	distance [m]	data rate [MBd]	message	status	Figure
1	1	1.14	0.3	2	"Hello world"	OK	5.7
2	2	2.28	1.5	2	"Hello world"	OK	5.8
3	4	4.56	1.5	2	"Hello world"	OK	5.9
4	4	4.56	1.5	2.5	"Hello world"	failed	5.10
5	4	4.56	1.5	2.4	"UUUUSSSSSS"	OK	5.11

Table 5.2: OWC module test result summary

Figure 5.7 and Figure 5.8 show the oscilloscope traces recorded during successful data transmissions at a rate of 2 MBd with the minimum number of active LEDs needed for a reliable OWC link over 0.3 and 1.5 m (test 1 and 2, see Table 5.2). These tests revealed that the number of active LEDs and resulting received signal amplitude needs to be adjusted so that the average variation of the signal amplitude was still accommodated within the threshold below or above $CVRef$. It should be noted that when using a high number of LEDs at low transmission distances, the mean received signal amplitude was higher than the maximum value that could be set for $CVRef$ (2.048 V), making reception impossible. Anyway, operation with the lowest possible number of LEDs is the desired operation mode in terms of power-efficiency. With one or two LEDs in test 1 or 2, the $CVRef$ limits were sufficient ($CVRef \approx 1$ V) which is ensured by the optimal choice of Rx gain. In oscilloscope screenshots, yellow traces show the Tx signal, green traces show the Rx signal after the TIA and pink traces show the Rx signal after the comparator. $CVRef$ is shown with a purple trace. The time offset between transmitted (yellow) and received signal (pink) is mainly due to the receive

components' rise/fall time (PD and TIA). This means that the delay is introduced by the time it takes the received signal after the TIA (green) to reach $CVRef$.

test	# of active LEDs	distance [m]	data rate [MBd]	message	status
1	1	0.3	2	"Hello world"	OK

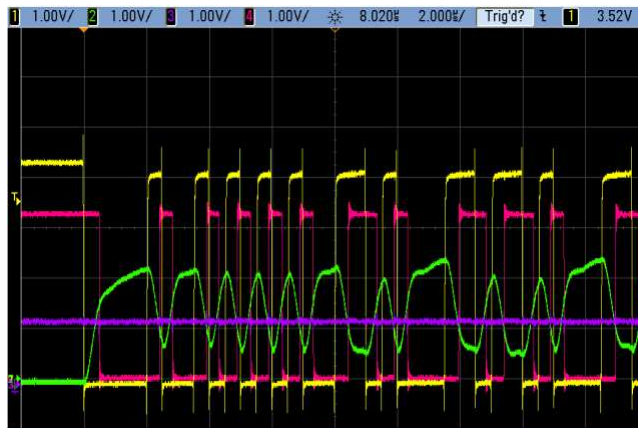


Figure 5.7: OWC test 1, 2 μ s / division

test	# of active LEDs	distance [m]	data rate [MBd]	message	status
2	2	1.5	2	"Hello world"	OK

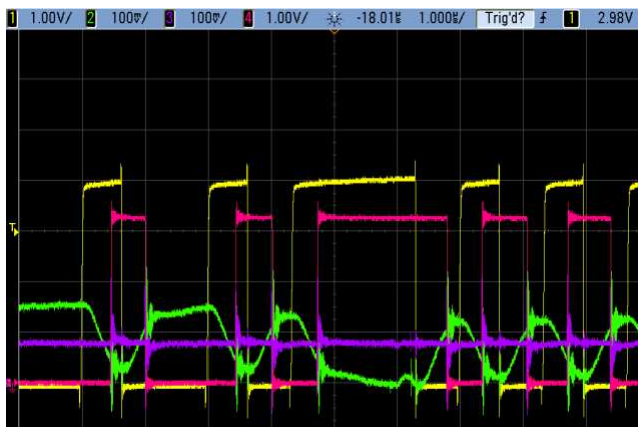


Figure 5.8: OWC test 2, 1 μ s / division

Further, tests concerning data transmission at rates ≥ 2 MBd are shown in Figure 5.9- Figure 5.11 for the same transmission distance and number of active LEDs but different transmitted messages (tests 3-5) to discuss effects occurring at high data rates using OOK. Test 3 (Figure 5.9) presents the baseline measure indicating that the OWC was still reliably working over 1.5 m at 2 MBd with 4 active LEDs, sending "Hello world". Note the higher received signal amplitude as compared to previous tests due to the use of 4 LEDs.

test	# of active LEDs	distance [m]	data rate [MBd]	message	status
3	4	1.5	2	"Hello world"	OK

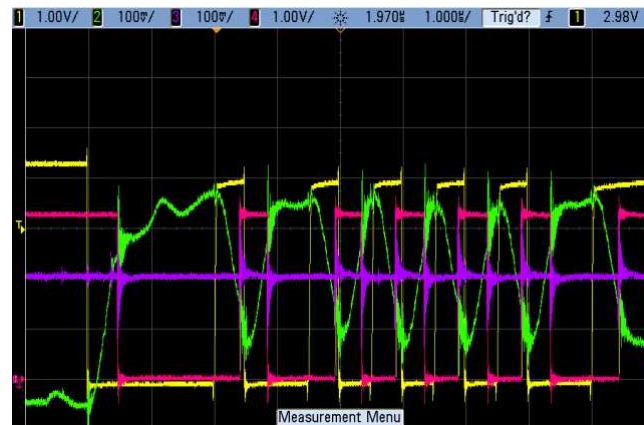


Figure 5.9: OWC test 3, $1 \mu\text{s}$ / division

At a higher rate of 2.5 MBd using OOK and transmitting the message "Hello world" which contains a longer series of successive binary "1"s or "0"s as shown in Figure 5.10, the Rx side cannot determine the exact number of successive bits which often leads to erroneous signal decoding. A remedy to circumvent this issue would be the use of Manchester encoding which in turn limits the effective bit rate to half of the bit rate achievable with OOK (see Figure 3.6, Eq. 3.7). A data rate reduced to around 1 MBd would still be sufficient for the transmission of one MARMOT's signals and yield a more reliable data transmission as the clock information is contained in the bit sequence. Spikes occurring in the received signals and $CVRef$, impairing the correct assignment of "0"s or "1"s in the comparator in some cases could possibly be solved by signal filtering or a change in PD.

test	# of active LEDs	distance [m]	data rate [MBd]	message	status
4	4	1.5	2.5	"Hello world"	failed

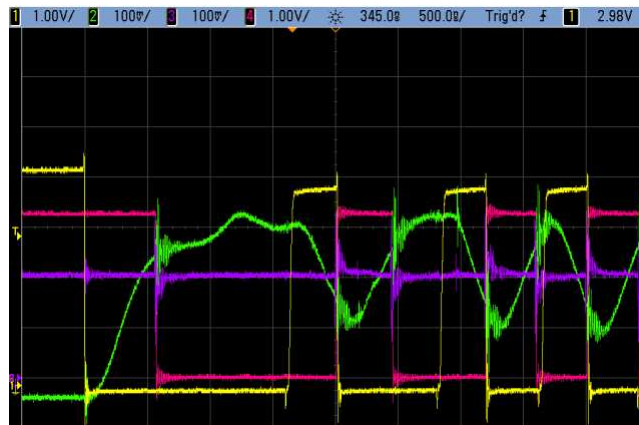


Figure 5.10: OWC test 4, 500 ns / division

When transmitting a message consisting only of "U" and "S", a maximum of two successive "0"s or "1"s appears in the binary sequence which allows reliable transmission also at a higher data rate, e.g. 2.4 MBd as shown in Figure 5.11. However, this example cannot be considered as the most general case, and as found for the message "Hello world" and other random messages, the upper limit for reliable repeated transmission therefore has to be assumed at 2 MBd.

test	# of active LEDs	distance [m]	data rate [MBd]	message	status
5	4	1.5	2.4	"UUUUUSSSSSS"	OK



Figure 5.11: OWC test 5, 500 ns / division

The power consumption is 1.14 W on average per LED (full duty cycle). With a bi-directional link module, power for the transmit and receive part is required on the same card and the power consumption of surrounding Tx and Rx circuitry has to be taken into account as well. Assuming a duty cycle of 50 % for optical components,

which is a correct approximation for long continuous data transmissions, the two LEDs dissipate 1.14 W in total. The power consumption for optical detectors, surrounding Tx and Rx circuitry was estimated according to average values given in data sheets, resulting in a total of 2.58 W of which the power dissipation in resistors and MOSFET drivers are the main factors (1.8 W and 0.7 W, respectively). The resulting estimation for the total power consumption of an OWC transceiver prototype with 2 active LEDs is ≈ 3.72 W. This estimation was verified on the bench, with the RasPi and launched Python GUI consuming 1.55 W and data transmission at approximately 50 % of the time. It was found that the theoretically calculated value for OWC module power consumption was an overestimation by only 20 mW. With a Lithium-Polymer battery of reasonable size for on-patient use, usually a power capacity of 2.5 Ah (3.7 V) can be reached. For the total power estimation, this results in a battery runtime of ≈ 2.5 h with continuous data transmission (for the OWC module only, excluding the RasPi).

5.3.2.5 Conclusion

Preliminary tests revealed that short (0.3 m) and long (1.5 m) range OWC is possible with the designed prototype modules. The maximum achievable data rate for reliable transmission is 2 MBd. This performance would even allow for the optical wireless transmission of the multiplexed signals of two MARMOTs. Long and short possible transmission distances accommodate different OWC module positioning scenarios in the MR bore (see Figure 1B, *Article II*).

An advantage of this OWC module configuration is the operation with optical transmitters producing light in the near-IR range, which is invisible for the human eye. The transmitters can therefore be operated at high powers while not being perceived as “too bright”. For the IR detector, ambient light in the visible range has no influence on the data link performance as a daylight blocking filter is integrated in the PD housing.

Possible improvements and directions of future work mainly concerning the adaptation of the OWC module for in bore use and the minimization of power consumption will be discussed in section 6.1.2.

5.3.3 OWC module use case simulation study

For the future employment of custom-built or modified commercial non-magnetic OWC (or Li-Fi) modules it is interesting to simulate different use cases of such an OWC data transmission set-up in the MR bore. Scanner dimensions, subject positioning and interference in the LOS as well as OWC module restrictions e.g. beam angle and maximum transmission distance can become a bottleneck for successful optical wireless transmission in the bore. The aim is to show here that for a generic OWC module, with wise choice of OWC module positioning and alignment mechanisms, the LOS is provided.

To this end, optical FOV simulations were performed with the open-source 3D modelling and rendering software package Blender (v.2.83.1) [233]. OWC module characteristics were assumed to be those of one product developed at the Fraunhofer Institute for Photonic Microsystems (100 Mbps Li-Fi HotSpot, [234]) operating with LEDs in the near-infrared light spectrum. This module was tested out-of-bore but contained too many ferromagnetic parts to be placed in-bore while still ensuring reliable functioning of the 100 Mbps data link and patient safety.

5.3.3.1 Module specifications

Assumed module characteristics are summarized in the following for two identical OWC transceivers, i.e. capable of bidirectional communication with Rx and Tx circuitry (LEDs and PDs) on each side:

- data rate: ≈ 100 Mbps
- Ethernet connection to PC via CAT5 cable
- power consumption/module: ≈ 5 W
- dimensions: $\approx 10 \times 10 \times 6$ cm³
- maximum spatial transmission distance: ≈ 5 m
- 2 m spot size in 5 m distance from the module $\rightarrow \approx 22.6^\circ$ beam divergence

This module was chosen as an example for simulations because its dimensions are reasonable, e.g. also for a custom-built module with multiple integrated transmitters, receivers and battery power supply. Also, beam angle characteristics are ideal to accommodate different positioning variants and should also be aimed for with

custom-built OWC modules. Further, due to the high achievable data rate of up to 100 Mbps, in case the OWC module could be modified to be completely non-magnetic, the simulated OWC module set-up could be employed for the on-coil transmission of digital MR signals, e.g. with 4 Rx-channels sampled at 1.5 MSps with a 16-bit ADC (results in 96 Mbps at 100 % duty cycle). Another possibility would be to use the optical wireless transceiver to send out sensor data from the scanner bore, e.g. ECG, pulse oximeter, patient motion, temperature or E - and B - field data.

5.3.3.2 General set-up in the MR scanner

With a required line-of-sight between OWC modules, one option is to place one optical transceiver centered at the top of the, back end of the scanner bore. The other optical transceiver should be integrated on-coil to limit cabling between the digital coil or sensor output and the on-coil OWC module's electronics. Figure 5.12 shows an exemplary module set-up inside the bore, assuming perfect alignment between the two optical wireless transceivers. OWC modules are represented by yellow cuboids with the above-mentioned dimensions and the MR scanner model used is the Siemens Magnetom Skyra 3 T (70 cm bore diameter, 163 cm magnet length, [235]). Here, the distance between OWC modules is approximately 105 cm.

Of course, another possibility would be the placement of one optical transceiver at the center of the bore, directly above the on-coil transceiver. However, no issues for the maintenance of a LOS are expected for this scenario, unlike with scenarios as shown in Figure 5.12 where the subject's head could move in the LOS.

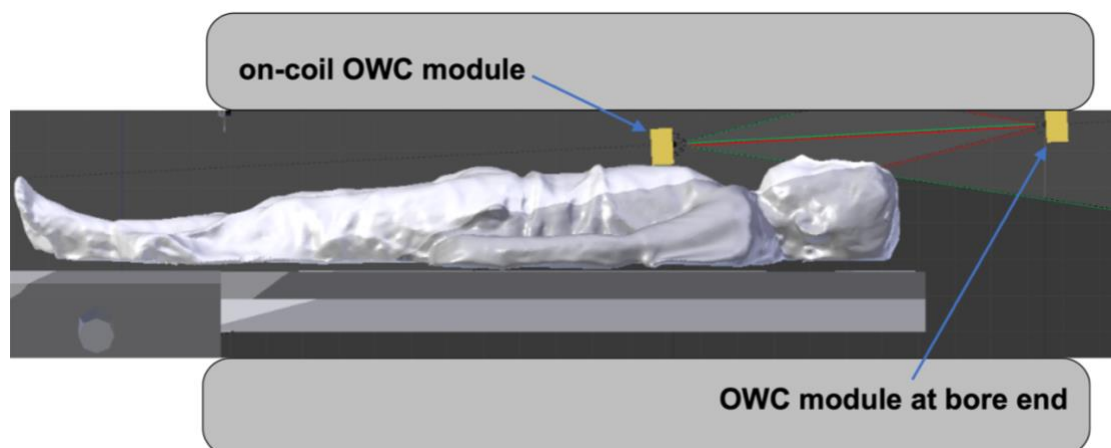


Figure 5.12: General OWC module set-up inside the MR bore

5.3.3.3 Alignment of OWC modules

Using flexible RF coils in combination with an on-coil OWC module, every time the coil is positioned on the patient lying on the patient bed, the on-coil transceiver has to be carefully aligned to be in the line-of-sight of the OWC module at the bore end when the patient is moved inside the scanner and the coil positioned around the iso-center. With rigid coils, e.g. knee birdcage coils, the optimal position of the on-coil OWC module can be set during initial tests and fixed (e.g. on the coil housing) for all following experiments.

One possible method to ensure alignment between modules is to integrate an additional laser pointer in one of the OWC modules, in analogy to the laser cross used for coil positioning in common clinical MR scanners. For the case shown in Figure 5.13, the on-coil module would be adjustable by screws or other mechanisms and equipped with the positioning laser. With the coil including the OWC module positioned on the patient, the laser and module direction should point to a pre-set marking on the scanner housing (e.g. at the center of the display on the front side of the scanner), hence ensuring correct alignment between on-coil OWC module and the second module at the bore end when the patient (including coil and optical wireless transceiver) is moved inside the scanner bore. This alignment strategy seems feasible for flexible coils placed at the center of the body, e.g. for abdomen or thorax examinations, but will be more difficult to implement for coils used at joints at the side of the body or extremities, e.g. the elbow or ankle.

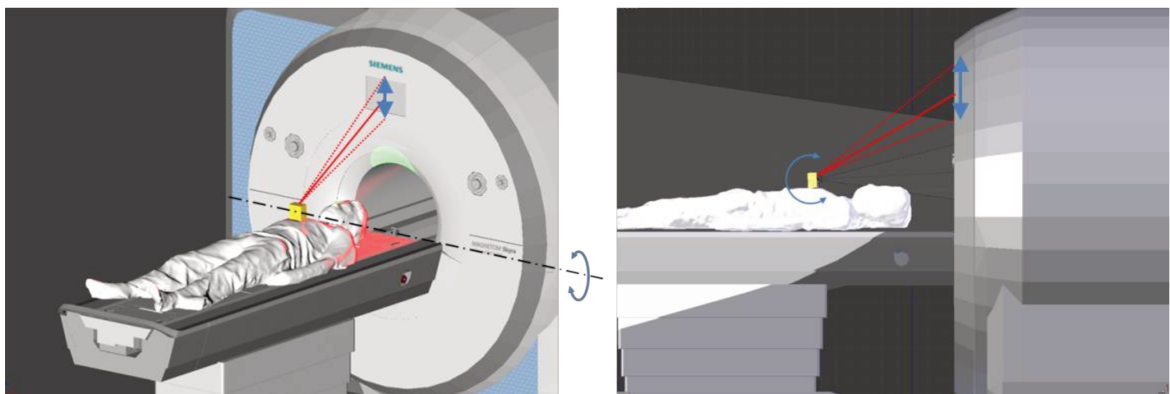


Figure 5.13: Pre MR-examination OWC module alignment with a positioning laser

As can be seen in Figure 5.14, the large beam angle of 22° can compensate slight misalignments between receivers due to breathing motion or patient movement to a certain degree ($\pm 11^\circ$).

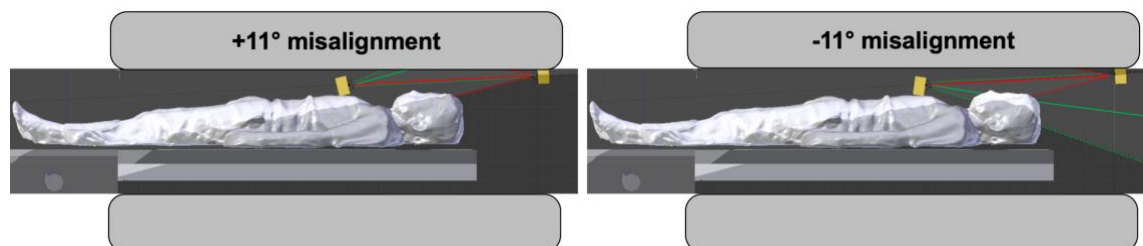


Figure 5.14: Misalignment limits

5.3.3.4 Optical field-of-view simulation for different use cases

In Figure 5.15 and Figure 5.16, the optical FOV for different use cases, i.e. head or feet first examination with a male or female subject, with OWC inside the bore was studied. The following simulations show the FOV of the on-coil OWC module with a green light beam and the FOV of the OWC module placed at the bore end with a red light beam. For breast or thorax MR examinations, usually the patient would be placed head first inside the MR scanner. When examining women, e.g. for MR mammography in supine position, one of the concerns could be that the breast is an obstacle in the LOS between OWC modules. As can be observed in Figure 5.15, for the simulated subject size (male, female) and an ideal placement of the OWC transceiver at the highest point of the chest, the red light beam always hits the front side of the on-coil OWC module and, thus, a LOS is provided.

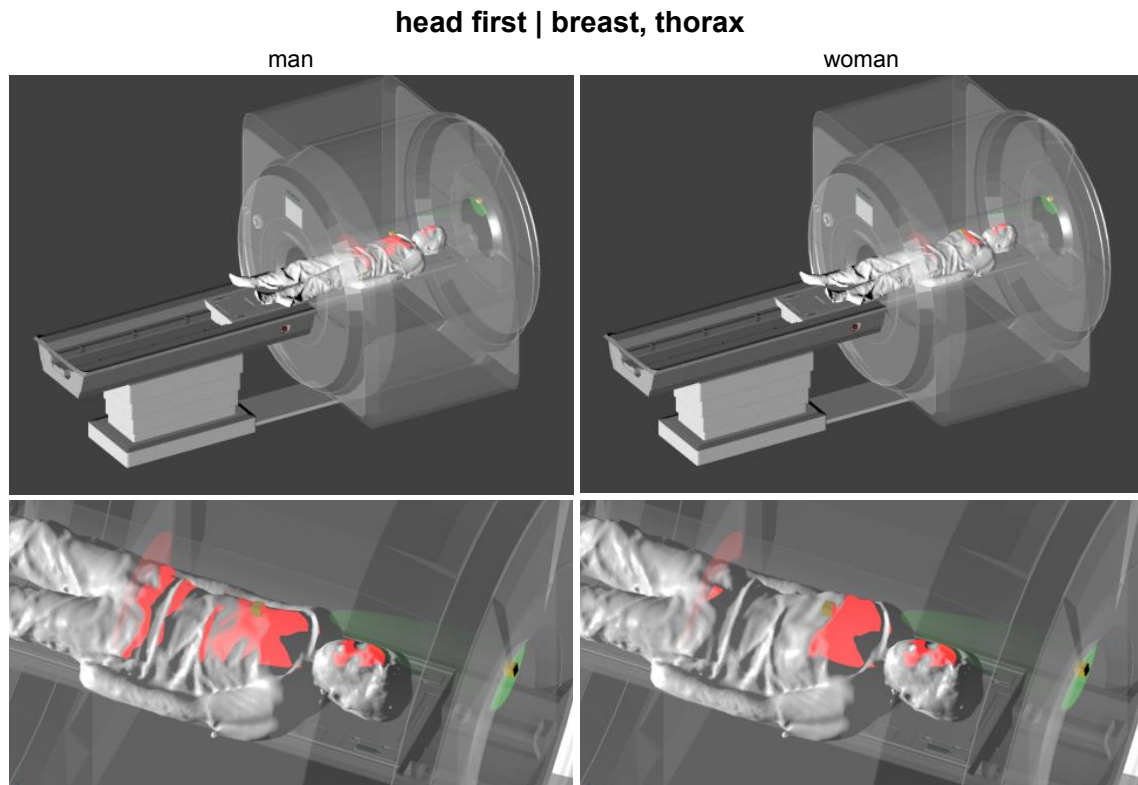


Figure 5.15: Optical FOV simulation for head first MR examinations

Same applies to a feet first imaging set-up, e.g. for knee imaging, as shown in Figure 5.16. No obstacles in the line of-sight for the simulated subject dimensions and OWC module characteristics are to be expected.

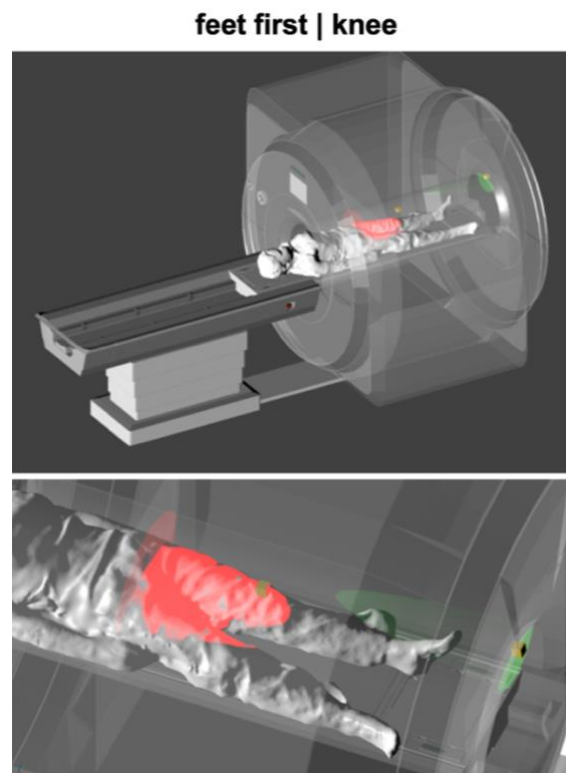


Figure 5.16: Optical FOV for a feet first MR examination

From what is shown in optical FOV studies in this section, for the presented standard cases of patient positioning and ideal transceiver positioning on-body, the LOS between modules is maintained for head and feet first examinations for both men and women. In reality, with suboptimal transceiver positioning, large patients or unexpected patient movements of the head or the limbs, the LOS and therefore the data transfer can be interrupted. Also, different OWC module characteristics, e.g. a more directive beam, shorter transmission distance or sensitivity to bore reflections will have an influence on the effective data transmission.

5.3.4 OWC module test summary

For future OWC module investigations, the aim is to either use a non-magnetic modified version of a commercially available OWC (or Li-Fi) module or a custom-built module in-bore. This section provides a list of possible tests to perform divided into 3 categories:

MR compatibility	device performance	patient safety
------------------	--------------------	----------------

Table 5.3: OWC module test categories

At first, full MR compatibility has to be ensured and device performance thoroughly tested with varying set-ups. For in vivo use, the aspect of patient safety is non-negligible. The color code in Table 5.3 will be used to relate listed tests to one of the above-mentioned categories.

OWC module tests have to be conducted in two different configurations: (1) outside of the MR scanner, e.g. in a separate room, to confirm MR compatibility, device functioning and rule out basic patient safety concerns, and (2) inside the MR bore where the OWC module should be used in its final implementation on-coil and could suffer from the influence of the B_0 , B_1 and gradient fields.

5.3.4.1 Outside of the MR scanner

The general test set-up outside the MR scanner could consist of 2 OWC modules, e.g. connected to a PC via Ethernet (non-magnetic RJ45 plugs) or to a single-board computer (e.g. Raspberry Pi) while they are battery-powered or equipped with a cabled power supply. A network performance test software that could be used is iPerf3 [236], reporting bandwidth and data package loss with random test data or specific files that can be transmitted. The two modules have to be placed on a LOS between tables or any other planar surface, together with some distance and angle measurement devices. All tests would be carried out with ambient light, ideally comparable to that in an MR scanner room. Furthermore, a mock-up scanner bore with characteristics similar to the inside of the MR bore (paint, texture) could be used for all tests, especially to test the influence of reflections on the OWC link. One would start with mechanical tests and a verification of the MR compatibility (attraction to strong Neodymium magnet) of all used parts:

1.	Test attraction to strong Neodymium magnet of parts accessible with housing around PCB (screws, connectors for data or power inlet, lenses or optical transmitter/receiver) and the housing itself.
2.	Test attraction to strong Neodymium magnet of parts inside the housing of the OWC module (PCB, control circuits, amplifiers, optical transmitters and receivers etc.).

Table 5.4: MR compatibility tests outside of the MR scanner

Baseline performance tests outside of the MR scanner are important to judge whether the OWC characteristics are sufficient for the targeted application (e.g. required data rate and transmission distance). Also, this measurement data will later serve as a reference to determine the influence of the presence of a strong B_0 field, gradients and an RF field on the data link performance.

1.	Bidirectional data transfer capability (e.g. iPerf3: change server and client mode)?
2.	Maximum achievable data rate and data loss depending on distance and angle (change in horizontal alignment) between OWC modules?
3.	Simulated breath hold (stable OWC set-up) vs. simulated free-breathing (up-down movement of one OWC module, change in vertical alignment between modules) and effect on maximum achievable data rate and data losses?
4.	Sensitivity to reflection: wrap reflective (white, comparable to scanner bore surface) or light-absorbing (black) material around receiver part: effect on maximum achievable data rate and data losses?
5.	Sensitivity to shading of area near the receiver due to objects in the optical path (e.g. head coil): effect on maximum achievable data rate and data losses?
6.	Sensitivity to changes in ambient light: effect on maximum achievable data rate and data losses?
7.	Power consumption of modules in standby mode (no data Tx) and during data transfer (at maximum data rate)?

Table 5.5: OWC module performance tests outside of the MR scanner

The following aspects concerning patient safety could already be taken into consideration during tests outside the MR scanner:

1.	Weight of on-coil OWC module?
2.	OWC module heating during ≈ 30 min. operation (assuming that this is the average scan duration) at the maximum achievable data rate and in standby (no data Tx) mode? Fiber-optic probes could be used to measure the temperature at the OWC module surface.
3.	Laser class of optical transmitter? [209]

Table 5.6: OWC module patient safety tests outside of the MR scanner

5.3.4.2 Inside the MR bore

For setting up the OWC modules inside the MR scanner, a construction has to be built to fix one of the optical transceivers at the end of the scanner bore. The second optical transceiver could be placed on the patient bed or on top of a phantom. For data link performance tests, the modules could be connected to a PC, e.g. via long non-magnetic Ethernet cables. For in-bore tests, either power outlets in the MRI room or ideally, a non-magnetic power solution (e.g. rechargeable batteries) could be used.

Here, tests on MR compatibility and device performance go hand-in-hand as robust device functioning in the MR is desired and ideally, at the same time, image quality stays unaffected by the placement of the OWC module inside the bore.

The functioning of in-bore electronics can suffer from voltage created due to the Hall effect in semi-conductors in the B_0 field. Also, eddy currents can be induced in conductors either by movement of the device in the B_0 field or gradient switching and the RF transmit and gradient field can lead to heating of the device or high induced currents (e.g. on conductive loops formed on the PCB) due to the high RF power which could possibly damage device electronics. MR image artefacts can originate from B_0 distortions (magnetic susceptibility artefacts) or gradient field distortions due to eddy currents. If active components produce EM fields or traces and components on a PCB produce a resonance near the Larmor frequency this can lead to RF-induced artifacts or increased image noise.

Inside the MR scanner, tests on the effect of reflection (cf. test 4 in 5.3.4.1) could be carried out comparing the device performance with the bare scanner bore surface and the bore surface being shielded by light-absorbing material.

1.	B_0 field only: force or torque on the modules due to strong static magnetic field? + gradients: instability due to bore/patient bed vibrations?
2.	B_0 mapping with and without the in-bore OWC module placed on a phantom to rule out susceptibility artefacts.
3.	B_0 field only: repeat basic device performance tests 1-7 (cf. 5.3.4.1).
4.	B_0 field + gradients: repeat basic device performance tests 1-7 (cf. 5.3.4.1)
5.	B_0 field + gradients: heating of modules and cables? Fiber-optic temperature sensors could be used to assess possible heating close to the in-bore OWC module or along cables.
6.	B_0 + gradients + RF transmit field: phantom-imaging test to evaluate effect on B_1 and MR image quality of the OWC module in-bore (e.g. FA mapping [64] with and without OWC module present using the body coil in Tx/Rx mode, acquisition of standard GRE image).
7.	B_0 + gradients + RF transmit field: repeat basic device performance tests 1-7 (cf. 5.3.4.1)
8.	B_0 + gradients + RF transmit field: heating of OWC modules and cables during image acquisition? Fiber-optic temperature sensors or MR thermometry could be used to assess possible heating inside the phantom and close to the OWC module or along cables.

Table 5.7: OWC module tests in the MR bore

5.3.4.3 In vivo use

The list above covers a basic set of tests that would be carried out to examine robust performance, MR compatibility and safety of the device for research purposes. For future use during in vivo experiments or even the commercialization of such OWC modules, more rigorous, systematic tests would have to be conducted. The following

standards concerning medical devices exist and criteria set in these directives have to be strictly followed and all applicable requirements would have to be fulfilled:

- IEC 60601-1 (Medical electrical equipment - Part 1: General requirements for basic safety and essential performance) [220]
- IEC 60601-2-33 (Medical electrical equipment - Part 2-33: Particular requirements for the basic safety and essential performance of magnetic resonance equipment for medical diagnosis) [65]
- ISO 14971 (Medical devices - Application of risk management to medical devices) [237]

The IEC 60825 series of standards concerns the safety of laser products and the following additional standards applicable for general laser safety and free space optical communication could become relevant for an OWC device in the MR environment that uses one or multiple lasers for signal transmission:

- IEC 60825-1 (Safety of laser products - Part 1: Equipment classification and requirements) [209]
- IEC 60825-12 (Safety of laser products - Part 12: Safety of free space optical communication systems used for transmission of information) [210]

In this section, a list covering different aspects for OWC tests concerning device functioning, MR compatibility, patient safety and considerations for in-vivo use is proposed. It will serve as a guideline for tests with non-magnetic OWC modules in the future.

6. Outlook and Conclusion

6.1 Future work

The presented work on flexible lightweight coaxial coils, the perspectives of wireless RF coils, as well as the development of an optical wireless communication module reveals several aspects that can be considered for future work. In the following, some ideas for further investigations and possible improvements are suggested.

6.1.1 Flexible coaxial coils

The comparison between 1T1G and MTMG coaxial coils shown only for some cases at 3 and 7 T calls for a more systematic and in-depth study of the difference between employing a coil with a self-resonance close to the target Larmor frequency versus a coil with a self-resonance that is either lower or higher than the Larmor frequency.

One possibility would be the simulation of a 1T1G coaxial coil of a certain diameter at various resonance frequencies (below and above self-resonance). Then, for each simulated frequency, a suitable MTMG configuration with a self-resonance as close as possible to the specific frequency could be found and simulated as well. This would allow for a pairwise comparison of an MTMG operated at self-resonance and an a 1T1G operated off-self-resonance.

Another approach for a comparison using a larger parameter space would be the simulation of a single-turn coaxial coil of defined size and a number of gaps ranging from 1 to 6 for example. The resonance frequency increases with the number of gaps and each coil could be simulated at its respective self-resonance frequency f_0 as well as frequencies above and below f_0 , e.g. in an interval spanned by values of $f_{\text{sim}}/f_0 = [0.2; 5]$. All comparisons could be done based on the analysis of surface current amplitude and homogeneity on the O_{co} , the transmit efficiency, and local SAR.

Furthermore, the design of a coaxial coil which is dual-tuned, i.e. suitable for operation at different operation frequencies or nuclei is interesting. One could evaluate whether there exists one coaxial coil geometry which, when operated at two or more different frequencies, yields high O_{co} currents, transmit efficiency and low local SAR. Tuning and matching could be achieved using different interface configurations giving rise to the appearance of a second resonance, e.g. with a tuning inductor L_T and a multi-gap coil, as discussed in section 4.3.2.3. The coil port for each

separate frequency-dependent Tx/Rx path could be located at different gap positions. For this purpose, but also more generally, tuning and matching components should also be integrated in EM simulations to account for losses in the coil interface.

Array configurations with coaxial coils could be interesting as high SNR of small flexible surface coils may be exploited over an extended FOV. Studies could focus on the investigation of the parallel imaging and parallel transmission performance of such an array. Possible applications for arrays with large coaxial coil diameters at 7 T that could be constructed using multi-gap coaxial elements, are cardiac, knee or calf imaging targeting proton-only or multi-nuclear acquisitions. In preliminary tests with coaxial coil arrays, the overlap decoupling was found to be optimal for same overlap distances as measured for SCs [119]. For receive-only arrays, reversed preamplifier decoupling and the broadband resonance destruction could lead to better decoupling performance than for SCs [55]. For transceiver arrays, it has also been shown that coupling between elements is lower between CCs and that CCs are more stable to variations in the phantom load [56]. This will require a more detailed investigation depending on the number of coil turns and gaps as well as interfacing circuitry used to construct the array.

Another aspect especially important for flexible coaxial Tx/Rx arrays dedicated to in vivo imaging at 7 T is the investigation of local and global SAR using EM simulations and different bending scenarios of the coil as the superposition of E fields is influenced by the coil position.

6.1.2 Wireless data transmission in MR

The described OWC prototype development is the first step towards the goal of an MR compatible OWC system. In order to achieve a fully MR compatible OWC module solution, some parts will have to be exchanged by a suitable non-magnetic version. Further, components that did not show significant attraction to a strong Neodymium magnet on the bench should in a next step be tested in MR phantom imaging.

First of all, the RasPi is not suitable for use inside the MR bore and therefore, it is necessary to move all control operations now handled by the RasPi to a

microcontroller integrated on the PCB. While the PCB now holds only the optical components and surrounding circuitry, the options are either the design of an extension card or a complete redesign which could also aim for a miniaturization of the whole card. Another major aspect is power supply which is currently realized via the RasPi. It would need to be replaced by a non-magnetic rechargeable battery for example. The optical components did not show strong attraction to the Neodymium magnet except the leads of the IR LED used. Maybe, if shortened enough and mounted directly on PCB, the remaining ferromagnetic parts will be sufficiently minimized and the influence on MRI negligible. Else, the optical transmitter will have to be exchanged e.g. using a surface-mount LED or a customized option.

Improvements are possible concerning the manual adaptations necessary for setting the reference voltage and LED power. This calls for automation of the control of these parameters. This could be done by an automatic gain control circuit to adapt the received voltage amplitude depending on the distance between the transmitter and receiver or the used transmitter power. Another possibility to accommodate for transmission distance variations is software-based, i.e. programming the microcontroller in a way that it measures the dark current and maximum received amplitude before actual data transmission and automatically sets the adequate CV_{Ref} from these values. Further, future software implementations could use random bit sequences and bit error detection via checksum comparison to test the reliability of the OWC link.

In the current OWC version, power consumption is rather high as all LEDs are driven with high currents to ensure data transmission also over a large distance. Therefore, as soon as the above-mentioned primary goal of implementing a fully MR compatible module is achieved, the focus will be put on finding a module configuration with minimum power requirements to prolong battery runtime. The modifiable parameters are the number of optical transmitters and receivers used for example. Also, the LED drive current can be reduced depending on the required optical power for reliable OWC over a certain free-space distance.

OWC module tests in a mock-up scanner and in MRI can be performed according to the test summary in section 5.3.4. As the initial motivation for the OWC development

is the motion sensor signal transmission, the final MR compatible and power-optimized module version can be interfaced to a MARMOT motion sensor shown in Figure 5.1. The wireless link performance should then be characterized during a realistic imaging set-up with retrospective motion correction based on accelerometer data acquired via the OWC link.

A long-term perspective is the investigation on how to scale up the achievable data rate for potential use of the OWC prototype for MR data transmission. Most probably, this will require faster switching optical circuitry, for example employing VCSEL and APD technology. Furthermore, alignment mechanisms to direct the focused laser beam to a receiver or receiver array will have to be studied.

The ultimate goal for the future of MR receive coils and coil arrays would be to merge flexible technology and wireless signal transmission developments.

In the larger context of the future implementation of flexible wireless Rx coils, all different parts of the receive system need to be considered: wireless MR data transmission, wireless on-coil power supply and wireless control signals. Wireless data Tx in MRI is feasible with current Wi-Fi standards that support high data rates for high channel counts but still, the need for demodulation and data compression before wireless transmission is evident. Maybe one could even envision the use of optical wireless links in MRI supporting data rates in the Gbps range. Some promising strategies for wireless control signaling have been published and synchronization is feasible but challenging. Wireless power transfer by RF seems to be the most promising option to obtain DC power on-coil but requires a lot of additional hardware in the MR. The remaining main challenges are related to finding fully MR compatible digitization and power components, and wireless transceivers. High power requirements can quickly become a bottleneck in getting rid of the cord. According to the knowledge of the author, a completely wireless Rx chain consisting of a digital coil interfaced to a wireless transceiver, which is wirelessly powered and controlled, even for a single element, has not been demonstrated yet.

6.2 Potential applications

Various imaginable applications for flexible wireless RF coil designs exist. Pushing aside the very challenging aspect of wireless data transmission in a first step, still, multiple applications would benefit from the development of lightweight flexible wired RF coils. With the development of suitable solutions for wireless MR data transmission, sensor data transmission and power supply, these could also be integrated gradually. In the following, two potential fields of application are presented where the implementation of flexible RF coils in the form of coaxial coils could have a considerable impact on a large number of examinations in the clinic and a broad mass of patients in the future.

6.2.1 MR mammography

According to the World Health Organization, breast cancer is the most common carcinoma in women, impacting 2.1 million women each year and also causes the greatest number of cancer-related deaths among women [238]. The biggest risk factors are age, family history and genetic factors. Nowadays, X-ray based mammography to assess the breast tissue and potentially detect carcinoma is recommended at a rather high age (40-50 years) as it employs ionizing radiation. Also, the conventional X-ray mammography procedure is often described as painful. Although it is not yet common practice to rely on MRI for routine breast cancer screenings, the trend points towards preferring MR mammography for several reasons:

As MR mammography doesn't rely on ionizing radiation, this could lead to a paradigm shift so that also younger patients could routinely be screened for breast cancer prevention, i.e. to find breast cancer at the earliest possible stage where the chance of recovery is the best. MR-mammography has proven to be the best method for early detection of breast cancer, both in women with increased risk of breast cancer and in women with normal risk [239].

MR mammography has the highest sensitivity of all examination modalities in the detection of breast cancer and can distinguish most reliably between benign and malignant tumors [240]. MR mammography finds 90 % of all breast carcinomas, X-ray mammography or ultrasound only 38 % and many carcinomas (45 %) are only

found with MR mammography, but not with X-ray mammography or sonography [241].

Dense glandular tissue reduces sensitivity by about 20 % in X-ray mammography, but there is no disadvantage in MR mammography. Half of all women have "dense glandular tissue" and benefit particularly from MR mammography [242].

For a long time, high costs related to long examination times were an argument against the general acceptance of MR mammography for breast cancer prevention. To reduce costs, leading breast experts are working on the development of abbreviated examination protocols [243].

Currently, MR mammography is performed with a coil integrated in two rigid cup-shaped molds and the patient in face-down (prone) position. Depending on the breast size, the coil loading can be suboptimal, e.g. for small breasts, which leads to SNR penalty. For large breasts, the positioning is complicated and in general, the imaging position is uncomfortable for the patient. This underlines the need for technological advances for improved patient comfort and image quality.

A versatile solution would be the development of a flexible lightweight coil vest that could be worn like a sports bra, with integrated flexible RF coil elements and miniaturized on-coil electronics. Using coaxial coil elements, the total weight of a coil array consisting of up to 32 channels could be kept very low (approximately 1.5 kg as discussed in section 3.2.3.1). The main benefits of the design of such a coil for MR mammography can be summarized as follows:

- one size-fits-all approach: ideal form-fitting of highly sensitive flexible surface coils to the tissue of interest for a variety of breast sizes.
- imaging in supine position: increase in patient comfort.

A challenge related to this MR mammography approach in supine patient position is motion management. Presumably, the influence of breathing motion on the image quality will be more prominent than with imaging in prone position. This could be addressed by real-time or retrospective motion correction, e.g. using wireless motion sensors on-coil in the future.

6.2.2 Knee imaging

A second possible application is knee imaging. Knee injuries can involve different parts of the joint, i.e. the tendons, ligaments, cartilage, bones, and muscles which can be efficiently resolved in MRI, especially at UHF. This application has already been targeted in some publications demonstrating the use of flexible transceiver [122] and stretchable receive-only [134,138] coil arrays at 3 or 7 T. A knee array constructed out of single-turn double-gap coaxial elements with a diameter of approximately 10 cm could probably yield improved sensitivity compared to an array fabricated of single-turn single-gap coaxial elements [122]. This hypothesis is based on the results from this work demonstrating that the simulated surface current at the outer surface of the outer coaxial conductor is higher and more homogeneous for the 1T2G coil (see Fig. 7, *Article I*). The “loopole”-like asymmetric surface current density distribution in a 1T1G-CC might be advantageous for better inter-element decoupling but as demonstrated in reference [244], the transmit and receive performance could strongly depend on the coil orientation relative to the B_0 field direction. The verification of this hypothesis on the bench and in MRI could be realized in future work. Again, the advantage of form-fitting knee coil design compared to a conventional array is improved sensitivity and patient comfort. Further, a flexible knee coil enables the flexion of the joint from one static image acquisition to the other and allows for kinematic knee imaging [134].

6.3 General conclusion

In conclusion, this thesis work presents the development and implementation of flexible RF coils based on coaxial transmission line resonator technology for 3 T MRI in receive-only and 7 T MRI in transmit/receive mode. The design concept relies on the extension to multiple coaxial cable turns and/or gaps enabling the construction of form-fitting coils of optimal size for a target penetration depth depending on the anatomical application. The flexible design yields optimal coil sensitivity and transmit efficiency when conformed to a bent shape and can be exploited in array configuration in the future.

This work also includes a comprehensive review of the perspectives in wireless radio frequency coil development for MRI and gives an outlook on the future implementation of a custom-built optical wireless communication system in the MR environment.

Appendix

Optical wireless communication module: list of main components

component	description	schematic ref.	footprint	#
TSAL6100	IR emitter 940 nm	D3, D4, D5, D6	FP-6_544-5259_08- 4-MFG	4
BPW83	Photosensitive Diode	D7, D8	PIN2	2
NCP81074BDR2G	Integrated Circuit	IC1, IC2, IC3, IC4	SOIC127P600X175- 8N	4
BSC026N02KS G	N-Channel OptiMOS 2 Power-Transistor, 20 V VDS, 100 A ID, -55 to 150 degC, PG-TDSON-8-1	Q1, Q2, Q3, Q4	INF-PG-TDSON-8- 1_V	4
TS3021ICT	Rail-to-Rail High-Speed Comparator, 1.8 to 5 V, 5-Pin SC70 (SOT323)	U1	STM-SC70-5_L	1
LTC1983ES6-3#TRMPBF	100 mA Regulated Charge-Pump Inverter, 3 to 5.5 V Vin, -3 V Vout, 6-pin SOT23 (S6-6), Pb-Free	U2	LT-S6-6-TSOT-23_N	1
MCP3202-CI/MS	2.7V Dual Channel 12-Bit A/D Converter with SPI Serial Interface, 8-Pin MSOP	U3	MSOP-MS8_N	1
LTC6241HVCS8#PBF	Dual Channel, Low Noise, CMOS Operational Amplifier, RRO, 18 MHz Typical GBW, 10 V/us Typical SR, 2.8 to 12 V, 8-Pin SOIC (S8-8)	U4	LT-S8-8_M	1
MCP4822-E/MS	12-Bit DACs with Internal VREF and SPI Interface, 8-Pin MSOP	U5	MSOP-MS8_L	1
TS4148RZG	High Speed Switching Diode, 150 mW, 1 V, 2-Pin SMD (0603)	D2	TWS-0603_L	1

List of Figures

Figure 1.1: Thesis structure overview. The chart shows a “chronology” axis, spanning over all 6 thesis chapters. Chapter content is then classified along the “specificity” axis, ranging from general to the most detailed explanations and studies.	6
Figure 2.1: Illustration of the Zeeman splitting effect and corresponding potential energy of the spins aligned parallel or antiparallel to the B_0 field.	10
Figure 2.2: (a) Equilibrium magnetization M_0 in the laboratory frame, spins precess around the z-direction (which is also the B_0 direction), (b) illustration of tilted magnetization towards the transverse plane in the rotating frame during B_1 transmission.	13
Figure 2.3: Time variation of the (a) longitudinal and (b) transversal magnetization component during spin relaxation.	14
Figure 2.4: Free induction decay.	16
Figure 2.5: Slice selection and spatial encoding in MRI.	18
Figure 2.6: k-space and image domain, adapted from [16].	20
Figure 2.7: Spin echo sequence diagram, adapted from [17].	21
Figure 2.8: Gradient echo formation, adapted from [17].	21
Figure 2.9: MR receive bandwidth depending on the gradient strength and FOV, adapted from [18].	22
Figure 2.10: Analog-to-digital conversion.	23
Figure 2.11: Basic representation of an RF coil forming either a series (a) or parallel RLC circuit (b)	31
Figure 2.12: Impedance plots (magnitude, real and imaginary part) for a series (a) and parallel RLC (b).	32
Figure 2.13: Current distribution in a non-segmented (a) and capacitively segmented (b) loop coil ..	34
Figure 2.14: Unbalanced (a) and balanced (b) capacitive matching.	36
Figure 2.15: Volume coils (birdcage and solenoid) and surface coil.	36
Figure 2.16: Receive-only standard loop coil.	39
Figure 2.17: Parallel plate and coaxial transmission line resonators. The coil port is indicated for coaxial TLRs as this structure will be explained more in detail, using an equivalent circuit scheme, in the next figure (Figure 2.18).	40
Figure 2.18: Schematic representation of a 1-gap, 2-gap and 3-gap coaxial TLR with corresponding equivalent circuit diagram.	42
Figure 2.19: Decoupling techniques for coil arrays: overlap and preamplifier decoupling.	43
Figure 2.20: Basic schematic of a T/R switch, adapted from [30].	45
Figure 2.21: Trap balun and floating cable trap for common mode current suppression.	47
Figure 2.22: 2-port network.	48
Figure 2.23: Comparison between FDTD and FEM mesh and example of multi-turn CC port modelling in CST.	54

Figure 3.1: Schematic representation of analog optical fiber or optical wireless transmission strategies: (a) direct modulation or (b) external modulation. Additional filtering and amplification stages that might be necessary for signal conditioning are not shown. T+M...tune & match, AD...active detuning, E/O...electro-optical, MZM...Mach-Zehnder modulator (E/O converter), OWC...optical wireless communication.	69
Figure 3.2: Schematic representation of digital optical fiber or optical wireless transmission strategies: (a) direct digitization or (b) analog down-conversion. Additional filtering and amplification stages that might be necessary for signal conditioning are not shown. T+M...tune & match, AD...active detuning, LO... local oscillator, E/O...electro-optical, OWC...optical wireless communication.	71
Figure 3.3: Wireless MR signal Rx chain overview	75
Figure 3.4: The electromagnetic spectrum. Note that the axis is not proportional.	78
Figure 3.5: Required technologies for optical wireless networking, adapted from [178,197]	79
Figure 3.6: Encoding schemes	80
Figure 3.7: LED and laser functioning principle based on spontaneous and stimulated light emission	81
Figure 3.8: LED vs. laser linearity and output power depending on drive current, adapted from [202]	85
Figure 3.9: Photodiode functioning principle based on optical absorption	86
Figure 4.1: Correlation between calculated and measured (unloaded) self-resonance frequencies ..	114
Figure 4.2: Relative deviation between resonance frequency calculations ($f_{0,calc}$) and measurements ($f_{0,meas}$), the bullet area is proportional to the number of gaps(n_g).....	115
Figure 4.3: Relative deviation between resonance frequency calculations ($f_{0,calc}$) and measurements ($f_{0,meas}$), the bullet area is proportional to the number of turns (n_t).	116
Figure 4.4: Coil diameter range depending on the gaps/turns CC configuration and B_0 field strength	119
Figure 4.5: Total capacitive impedance ($2Z_{TL}$) and inductive impedance (Z_{shield}) of a 20 cm 1T1G-CC. Resonances occur when the capacitive and inductive parts have same absolute values (i.e. imaginary reactive parts cancel each other out).....	121
Figure 4.6: Equivalent circuit including tuning and (symmetric) matching components.....	123
Figure 4.7: Effect of tuning components L_T and/or C_T parallel to the coil port	125
Figure 4.8: Impedance maxima at resonance for parallel resonance circuits ($Z_{coil,self,parallel}$, $Z_{coil,CT}$, $Z_{coil,LT}$, $Z_{coil,CT+LT}$) and impedance minimum for the series resonance circuit ($Z_{coil,self,series}$). Another impedance minimum, i.e. resonance dip, occurs at around 580 MHz when the coaxial stub appears as an open circuit which is the case when the stub length equals $2n + 1\lambda/4$	125
Figure 4.9: S_{21} measurements and impedance calculation results for 7 T CCs in unloaded configuration with a tuning L_T . VNA traces show the S_{21} parameter measured with a double-loop probe; $Z_{coil,self,series}$ and $Z_{coil,self,parallel}$ denote the calculated self-resonance of a coaxial coil according to	

Eq. 4.1 and Eq. 4.5. $Z_{\text{coil,LT}}$ denotes the impedance calculated for a parallel resonance circuit of the coaxial coil with a tuning L_T across the coil port (see also Figure 4.6).....	126
Figure 4.10: Equivalent circuit with two reverse biased PIN diodes (“off” state) and a tuning inductor L_T	127
Figure 4.11: 3 T MTMG-CCs’ resonance frequency behavior in unloaded coil configuration. VNA traces show the S_{21} parameter measured with a double-loop probe; $Z_{\text{coil,self,series}}$ and $Z_{\text{coil,self,parallel}}$ denote the calculated self-resonance of a coaxial coil according to Eq. 4.1 and Eq. 4.5. $Z_{\text{coil,LT}}$ and $Z_{\text{coil,CPIN+LT}}$ denote the impedances calculated for a parallel resonance circuit of the coaxial coil with a tuning L_T with and without two reverse biased PIN diodes across the coil port (see Figure 4.10).....	128
Figure 4.12: Effect of a large tuning inductor $L_{T,\text{large}}$ alone compared to the use of a smaller inductor $L_{T,\text{small}}$ in parallel with C_T	130
Figure 4.13: Exemplary EM simulations showing the proximity effect on the oCo in a single- and double-turn CC.....	133
Figure 4.14: Comparison of EM simulation results for the 7 cm 1T1G and 2T2G coaxial coil.....	134
Figure 4.15: Comparison of EM simulation results for the 15 cm 1T1G and 2T5G coaxial coil.....	134
Figure 4.16: Interface schematic with additional tuning capacitor (C_T) as used for the 7 cm 1T1G-CC.....	135
Figure 4.17: Fabricated 2T2G-CC (a) and 1T1G-CC (b) with 7 cm coil diameter and respective (fine-)tuning, matching and active detuning interface.....	136
Figure 4.18: Fabricated 2T5G-CC (a) and 1T1G-CC (b) with 15 cm coil diameter and respective (fine-)tuning, matching and active detuning interface.....	136
Figure 4.19: SNR maps from 2D GRE images acquired in the central transversal phantom plane at 3 T for MTMG-CCs (a) and 1T1G-CCs (b) of 7 and 15 cm diameter, respectively. The circular ROI and central axis used for SNR evaluation are marked in black.	138
Figure 4.20: ROI position and size used for average SNR evaluation in container or balloon phantoms.....	139
Figure 4.21: SNR central axis profiles, for the 7 cm coaxial coils (top) and the 15 cm coaxial coils (bottom).....	140
Figure 4.22: Relative FA difference maps calculated from FA maps acquired without and with Rx coil present during MRI with the body coil in Tx/Rx mode.....	144
Figure 4.23: SNR along the central coil axis for 3 T SCs and CCs.....	147
Figure 4.24: Transmit efficiency ($B1 +/P$) along the central coil axis for 7 T SCs and CCs.....	148
Figure 4.25: SNR along the central coil axis for 7 T SCs and CCs.....	149
Figure 4.26: MR imaging set-up with a 2T1G-CC positioned on a kiwi and acquired MR images in the transversal and coronal plane ($200 \mu\text{m}$ isotropic resolution).....	151
Figure 4.27: MR imaging set-up with a 2T2G-CC positioned on a pomegranate and acquired MR images in the transversal and coronal plane ($230 \mu\text{m}$ isotropic resolution).	152
Figure 4.28: MR imaging set-up with a 1T1G-CC positioned on a muskmelon and acquired MR images in the transversal and coronal plane ($270 \mu\text{m}$ isotropic resolution).	152

Figure 4.29: MR imaging set-up with a 2T5G-CC positioned on a papaya and acquired MR images in the transversal ($390\ \mu\text{m}$ isotropic resolution) and sagittal plane ($410\ \mu\text{m}$ isotropic resolution).....	153
Figure 5.1: Current set-up for acquiring motion sensor data in the MR with optical fibers transmitting the signals to a real-time signal analyzer and event controller (SAEC). MR compatible accelerometer for respiratory motion sensing (MARMOT) photo courtesy of [10].	168
Figure 5.2: OWC module overview.....	170
Figure 5.3: General schematic of components used in the OWC module	171
Figure 5.4: Circuit schematic of the fabricated OWC module prototype	171
Figure 5.5: Transmitter (left) and receiver OWC card (right). The LEDs surrounded by a ball lens mounted on the Rx board are not used and could be replaced by IR LEDs (shown on the left side) for bidirectional tests.	175
Figure 5.6: Python GUI	175
Figure 5.7: OWC test 1, $2\ \mu\text{s}$ / division	177
Figure 5.8: OWC test 2, $1\ \mu\text{s}$ / division	177
Figure 5.9: OWC test 3, $1\ \mu\text{s}$ / division	178
Figure 5.10: OWC test 4, $500\ \text{ns}$ / division.....	179
Figure 5.11: OWC test 5, $500\ \text{ns}$ / division.....	179
Figure 5.12: General OWC module set-up inside the MR bore	182
Figure 5.13: Pre MR-examination OWC module alignment with a positioning laser	183
Figure 5.14: Misalignment limits.....	184
Figure 5.15: Optical FOV simulation for head first MR examinations.....	185
Figure 5.16: Optical FOV for a feet first MR examination.....	185

List of Tables

Table 2.1: NMR relevant nuclei.....	9
Table 2.2: Main components of an MRI system.....	16
Table 2.3: Scaling rules for the Q factor, RF sensitivity factor and SNR	29
Table 2.4: Excerpt from the SAR limits set for the “normal operating mode” in the IEC standard, [61].	51
Table 3.1: Alternative MR signal transmission methods, adapted from [135], RIN... relative intensity noise, NF...noise figure, LED...light-emitting diode, RCLED...Resonant Cavity LEDs, MIMO... multiple input multiple output, Wi-Fi...Wireless Fidelity, Li-Fi...Light Fidelity	68
Table 3.2: Non-magnetic ADC examples, LVDS...low voltage differential signaling.....	73
Table 3.3: Typical characteristics comparison between an LED and a semiconductor laser	82
Table 4.1: Table listing the relative deviation between resonance frequency calculations ($f_{0,calc}$) and measurements ($f_{0,meas}$), the green color gradient indicates increasing number of turns (n_t) or gaps (n_g) and increasing frequency ($f_{0,meas}$).....	117
Table 4.2: Bench measurement examples for two self-resonance modes of CCs without interfacing circuitry	122
Table 4.3: Results from self-resonance frequency measurements, analytical calculations and EM simulations.....	132
Table 4.4: EM simulation coaxial coil parameters	132
Table 4.5: Mean oCo surface current amplitude.....	134
Table 4.6: Bench measurement results for the 1T1G-CCs and MTMG-CCs without interface (coil only) and with interface.....	137
Table 4.7: Coil and sample loss calculations for the 1T1G-CCs and MTMG-CCs without interface (coil only) and with interface	137
Table 4.8: SNR comparison between MTMG-CC and 1T1G-CC.....	139
Table 4.9: Relative FA difference (minimum, maximum) over the whole phantom	140
Table 4.10: Resonance frequency calculations for a 10 cm 1T1G-CC.....	143
Table 4.11: Bench measurement results for a 10 cm 1T1G-CC with capacitive tuning and matching.....	143
Table 4.12: Relative FA difference (minimum, maximum) over the whole phantom	145
Table 5.1: LED power levels ($P_{tot,LED}$) depending on the combination of resistors. P_{LED} denotes the value out of 2^4 possible combinations that was entered in the Python GUI (see Figure 5.6).	172
Table 5.2: OWC module test result summary.....	176
Table 5.3: OWC module test categories	187
Table 5.4: MR compatibility tests outside of the MR scanner	188
Table 5.5: OWC module performance tests outside of the MR scanner	188
Table 5.6: OWC module patient safety tests outside of the MR scanner.....	189
Table 5.7: OWC module tests in the MR bore.....	190

Bibliography

1. Moser E, Meyerspeer M, Fischmeister FPS, Grabner G, Bauer H, Trattnig S. Windows on the Human body - in Vivo High-Field Magnetic Resonance Research and Applications in Medicine and Psychology. *Sensors* (2010) **10**:5724–5757. doi:10.3390/s100605724
2. Moser E. Ultra-high-field magnetic resonance: Why and when? *World J Radiol* (2010) **2**:37–40. doi:10.4329/wjr.v2.i1.37
3. Moser E, Stahlberg F, Ladd ME, Trattnig S. 7-T MR-from research to clinical applications? *NMR Biomed* (2012) **25**:695–716. doi:10.1002/nbm.1794
4. Roemer PB, Edelstein WA, Hayes CE, Souza SP, Mueller OM. The NMR Phased Array. *Magn Reson Med* (1990) **16**:192–225. doi:10.1109/ICCOMM.2010.5509053
5. Pruessmann KP, Weiger M, Scheidegger MB, Boesiger P. SENSE: sensitivity encoding for fast MRI. *Magn Reson Med* (1999) **42**:952–962. doi:10.1002/(SICI)1522-2594(199911)42:5<952::AID-MRM16>3.0.CO;2-S
6. Pruessmann KP. Encoding and reconstruction in parallel MRI. *NMR Biomed* (2006) **19**:288–299. doi:10.1002/nbm.1042
7. Sodickson DK, Manning WJ. Simultaneous acquisition of spatial harmonics (SMASH): Fast imaging with radiofrequency coil arrays. *Magn Reson Med* (1997) **38**:591–603. doi:10.1002/mrm.1910380414
8. Katscher U, Börnert P, Leussler C, van den Brink JS. Transmit SENSE. *Magn Reson Med* (2003) **49**:144–150. doi:10.1002/mrm.10353
9. Nohava L, Czerny R, Roat S, Obermann M, Kuehne A, Frass-Kriegel R, Felblinger J, Ginefri J-C, Laistler E. Flexible multi-turn multi-gap coaxial RF coils: design concept and implementation for Magnetic Resonance Imaging at 3 and 7 Tesla. *IEEE Trans Med Imaging* (2021) doi:10.1109/TMI.2021.3051390. Epub ahead of print.
10. Nohava L, Ginefri J-C, Willoquet G, Laistler E, Frass-Kriegel R. Perspectives in Wireless Radio Frequency Coil Development for Magnetic Resonance Imaging. *Front Phys* (2020) **8**:11. doi:10.3389/fphy.2020.00011
11. Chen B, Weber N, Odille F, Large-Dessale C, Delmas A, Bonnemains L, Felblinger J. Design and validation of a novel MR-compatible sensor for respiratory motion modeling and correction. *IEEE Trans Biomed Eng* (2017) **64**:123–133. doi:10.1109/TBME.2016.2549272
12. Haacke EM, Brown RW, Thompson MR, Venkatesan R. *Magnetic Resonance Imaging Physical Principles and Sequence Design*. 1st ed. New York: John Wiley & Sons (1999).
13. Lipton ML. *Totally Accessible MRI*. New York: Springer (2008). doi:10.1007/978-0-387-48896-7
14. Reiser MF, Semmler W, Hricak H. *Magnetic Resonance Tomography*. Springer-Verlag Berlin Heidelberg (2008). doi:10.1007/b135693

15. De Graaf RA. *In Vivo NMR Spectroscopy: principles and techniques*. 3rd ed. John Wiley & Sons Ltd (2019). doi:10.1002/9781119382461
16. Moser E, Laistler E, Schmitt F, Kontaxis G. Ultra-High Field NMR and MRI—The Role of Magnet Technology to Increase Sensitivity and Specificity. *Front Phys* (2017) **5**:33. doi:10.3389/fphy.2017.00033
17. Paschal CB, Morris HD. K-Space in the Clinic. *J Magn Reson Imaging* (2004) **19**:145–159. doi:10.1002/jmri.10451
18. Siemens Healthcare GmbH. *Magnets, Spins, and Resonances: An introduction to the basics of Magnetic Resonance*. Erlangen (2015). Available at: <https://www.magnetomworld.siemens-healthineers.com/publications/mr-basics> [Accessed September 23, 2020]
19. MRI Physics: MRI Image Formation Parameters, SNR, and Artifacts. Available at: <http://xrayphysics.com/mri.html> [Accessed September 13, 2020]
20. Hoult DI. The principle of reciprocity in signal strength calculations - A mathematical guide. *Concepts Magn Reson* (2000) **12**:173–187. doi:10.1002/1099-0534(2000)12:4<173::AID-CMR1>3.0.CO;2-Q
21. Hoult DI, Richards RE. The Signal-to-Noise Ratio of the Nuclear Magnetic Resonance Experiment. *J Magn Reson* (1976) **24**:71–85. doi:10.1016/0022-2364(76)90233-X
22. De Zanche N. MR Receive Chain. in *Proc. Intl. Soc. Mag. Reson. Med. 27* (2019).
23. Fujita H, Zheng T, Yang X, Finnerty MJ, Handa S. RF Surface Receive Array Coils: The Art of an LC Circuit. *J Magn Reson Imaging* (2013) **38**:12–25. doi:10.1002/jmri.24159
24. Darrasse L, Ginefri J-C. Perspectives with cryogenic RF probes in biomedical MRI. *Biochimie* (2003) **85**: doi:10.1016/j.biochi.2003.09.016
25. IT'IS foundation. Tissue properties data base. Available at: <https://itis.swiss/virtual-population/tissue-properties/database/dielectric-properties/> [Accessed September 25, 2020]
26. Hoult DI, Lauterbur PC. The sensitivity of the zeugmatographic experiment involving human samples. *J Magn Reson* (1979) **34**:425–433. doi:10.1016/0022-2364(79)90019-2
27. Edelstein WA, Foster TH, Schenck JF. The relative sensitivity of surface coils to deep lying tissues. in *Proceedings of the 4th Annual Meeting, Society of Magnetic Resonance (1985)*, 964–965.
28. Roemer P, Edelstein WA. Ultimate sensitivity limits of surface coils. in *Proceedings of the SMRM 6th Annual Meeting (1987)*, 410.
29. Chen CN, Hoult DI. *Biomedical magnetic resonance technology*. Bristol: Adam Hilger (1989).
30. Kumar A, Edelstein WA, Bottomley PA. Noise figure limits for circular loop MR coils. *Magn Reson Med* (2009) **61**:1201–1209. doi:10.1002/mrm.21948

31. Behin R, Bishop J, Henkelman RM. Dynamic range requirements for MRI. *Concepts Magn Reson Part B Magn Reson Eng* (2005) **26**:28–35. doi:10.1002/cmr.b.20042
32. Gabr RE, Schär M, Edelstein AD, Kraitchman DL, Bottomley PA, Edelstein WA. MRI dynamic range and its compatibility with signal transmission media. *J Magn Reson* (2009) **2**:137–145. doi:10.1016/j.jmr.2009.01.037
33. Vaidya M V., Collins CM, Sodickson DK, Brown R, Wiggins GC, Lattanzi R. Dependence of B1- and B1+ field patterns of surface coils on the electrical properties of the sample and the MR operating frequency. *Concepts Magn Reson Part B Magn Reson Eng* (2016) **46**:25–40. doi:10.1002/cmr.b.21319
34. Mispelter J, Lupu M, Briguët A. *NMR Probeheads for Biophysical and Biomedical Experiments: Theoretical Principles and Practical Guidelines*. 2nd ed. London: Imperial College Press (2015). doi:10.1142/p759
35. Hayes CE, Edelstein WA, Schenck JF, Mueller OM, Eash M. An Efficient, Highly Homogeneous Radiofrequency Coil for Whole-Body NMR Imaging at 1.5 T. *J Magn Reson* (1985) **63**:622–628. doi:10.1016/0022-2364(85)90257-4
36. Glover G, Hayes C, Pelc N, Edelstein W, Mueller O, Hart H, Hardy C, O'Donnell M, Barber W. Comparison of linear and circular polarization for magnetic resonance imaging. *J Magn Reson* (1985) **64**:255–270. doi:10.1016/0022-2364(85)90349-X
37. Laistler E, Dymerska B, Sieg J, Goluch S, Frass-Kriegl R, Kuehne A, Moser E. In vivo MRI of the human finger at 7 T. *Magn Reson Med* (2018) **79**:588–592. doi:10.1002/mrm.26645
38. Gonord P, Kan S, Leroy-Willig A. Parallel-plate split-conductor surface coil: Analysis and design. *Magn Reson Med* (1988) **6**:353–358. doi:10.1002/mrm.1910060313
39. Gonord P, Kan S, Leroy-Willig A, Wary C. Multigap parallel-plate bracelet resonator frequency determination and applications. *Rev Sci Instrum* (1994) **65**:353–358. doi:10.1063/1.1144573
40. Serfaty S, Haziza N, Darrasse L, Kan S. Multi-Turn Split-Conductor Transmission-Line Resonators. *Magn Reson Med* (1997) **38**:687–689. doi:10.1002/mrm.1910380424
41. Frass-Kriegl R, Laistler E, Hosseinezhadian S, Schmid AI, Moser E, Poirier-Quinot M, Darrasse L, Ginefri J-C. Multi-turn multi-gap transmission line resonators - Concept, design and first implementation at 4.7T and 7T. *J Magn Reson* (2016) **273**:65–72. doi:10.1016/j.jmr.2016.10.008
42. Hosseinezhadian S, Frass-Kriegl R, Goluch-Roat S, Pichler M, Sieg J, Vít M, Poirier-Quinot M, Darrasse L, Moser E, Ginefri J-C, et al. A flexible 12-channel transceiver array of transmission line resonators for 7 T MRI. *J Magn Reson* (2018) **296**:47–59. doi:https://doi.org/10.1016/j.jmr.2018.08.013
43. Kriegl R, Ginefri JC, Poirier-Quinot M, Darrasse L, Goluch S, Kuehne A, Moser E, Laistler E. Novel inductive decoupling technique for flexible transceiver arrays of monolithic transmission line resonators. *Magn Reson Med* (2015) **73**:1669–1681. doi:10.1002/mrm.25260

44. Woytasik M, Ginefri JC, Raynaud JS, Poirier-Quinot M, Dufour-Gergam E, Grandchamp JP, Girard O, Robert P, Gilles JP, Martincic E, et al. Characterization of flexible RF microcoils dedicated to local MRI. *Microsyst Technol* (2007) **13**:1575–1580. doi:10.1007/s00542-006-0277-x
45. Couty M, Woytasik M, Ginefri JC, Rubin A, Martincic E, Poirier-Quinot M, Darrasse L, Boumezbeur F, Lethimonnier F, Tatoulian M, et al. Fabrication and packaging of flexible polymeric microantennae for in vivo magnetic resonance imaging. *Polymers (Basel)* (2012) **4**:656–673. doi:10.3390/polym4010656
46. Ginefri J-C, Rubin A, Tatoulian M, Woytasik M, Boumezbeur F, Djemaï B, Poirier-Quinot M, Lethimonnier F, Darrasse L, Dufour-Gergam E. Implanted, inductively-coupled, radiofrequency coils fabricated on flexible polymeric material: Application to in vivo rat brain MRI at 7T. *J Magn Reson* (2012) **224**:61–70. doi:https://doi.org/10.1016/j.jmr.2012.09.003
47. Ginefri JC, Poirier-Quinot M, Girard O, Darrasse L. Technical aspects: Development, manufacture and installation of a cryo-cooled HTS coil system for high-resolution in-vivo imaging of the mouse at 1.5 T. *Methods* (2007) **43**:54–67. doi:10.1016/j.ymeth.2007.03.011
48. Libby L. Special Aspects of Balanced Shielded Loops. *Proc IRE* (1945) **34**:641–646. doi:10.1109/JRPROC.1946.230887
49. Stensgaard A. Optimized Design of the Shielded-Loop Resonator. *J Magn Reson Ser A* (1996) **122**:120–125. doi:10.1006/jmra.1996.0187
50. Harpen MD. The theory of shielded loop resonators. *Magn Reson Med* (1994) **32**:785–788. doi:10.1002/mrm.1910320615
51. Haziza N, Bittoun J, Kan S. Multiturn split-conductor transmission-line resonator. *Rev Sci Instrum* (1997) **68**:1995–1997. doi:10.1063/1.1148115
52. Zabel HJ, Bader R, Gehrig J, Lorenz WJ. High-quality MR imaging with flexible transmission line resonators. *Radiology* (1987) **165**:857–859. doi:10.1148/radiology.165.3.3685365
53. Thomas EM, Heebl JD, Pfeiffer C, Grbic A. A power link study of wireless non-radiative power transfer systems using resonant shielded loops. *IEEE Trans Circuits Syst I Regul Pap* (2012) **59**:2125–2136. doi:10.1109/TCSI.2012.2185295
54. Tierney BB, Grbic A. Planar Shielded-Loop Resonators. *IEEE Trans Antennas Propag* (2014) **62**:3310–3320. doi:10.1109/TAP.2014.2314305
55. Zhang B, Sodickson DK, Cloos MA. A high-impedance detector-array glove for magnetic resonance imaging of the hand. *Nat Biomed Eng* (2018) **2**:570–577. doi:10.1038/s41551-018-0233-y
56. Mollaei MSM, Van Leeuwen CC, Raaijmakers AJE, Simovski CR. Analysis of High Impedance Coils Both in Transmission and Reception Regimes. *IEEE Access* (2020) **8**:129754–129762. doi:10.1109/ACCESS.2020.3009367
57. Röschmann Peter K H. High-Frequency Coil System for a Magnetic Resonance Imaging

- Apparatus. US Patent 4746866. (1988)
58. Yang X, Zheng T, Wu Y, Finnerty M. Coaxial cable magnetic resonance image (MRI) coils. US Patent US9678180B2. (2017)
 59. Kriegl R. A flexible coil array for high resolution magnetic resonance imaging at 7 Tesla. PhD thesis. Université Paris Sud - Paris XI & Medizinische Universität Wien. (2014) Available at: <https://tel.archives-ouvertes.fr/tel-01127308> [Accessed September 27, 2020]
 60. Friis HT. Noise Figures of Radio Receivers. *Proc IRE* (1944) **32**:419–422. doi:10.1109/JRPROC.1944.232049
 61. Seeber DA, Jevtic J, Menon A. Floating shield current suppression trap. *Concepts Magn Reson Part B Magn Reson Eng* (2004) **21**:26–31. doi:10.1002/cmr.b.20008
 62. Darrasse L, Kassab G. Quick measurement of NMR-coil sensitivity with a dual-loop probe. *Rev Sci Instrum* (1993) **64**:1841–1844. doi:10.1063/1.1144020
 63. Ginefri J-C, Durand E, Darrasse L. Quick measurement of nuclear magnetic resonance coil sensitivity with a single-loop probe. *Rev Sci Instrum* (1999) **70**:4730–4731. doi:10.1063/1.1150142
 64. Chung S, Kim D, Breton E, Axel L. Rapid B1+ mapping using a preconditioning RF pulse with TurboFLASH readout. *Magn Reson Med* (2010) **64**:439–446. doi:10.1002/mrm.22423
 65. International Electrotechnical Commission (IEC). *Medical electrical equipment - Part 2-33: Particular requirements for the basic safety and essential performance of magnetic resonance equipment for medical diagnosis (IEC 60601-2-33:2010+AMD1:2013+AMD2:2015 CSV)*. 3.2. Geneva (2015). doi:10.1109/IEEESTD.2007.4288250
 66. Pennes HH. Analysis of Tissue and Arterial Blood Temperatures in the Resting Human Forearm. *J Appl Physiol* (1948) **1**:93–122. doi:10.1152/jappl.1948.1.2.93
 67. Collins CM, Liu W, Schreiber W, Yang QX, Smith MB. Central brightening due to constructive interference with, without, and despite dielectric resonance. *J Magn Reson Imaging* (2005) **21**:192–196. doi:10.1002/jmri.20245
 68. Yee KS. Numerical solution of initial boundary value problems involving Maxwell's equations in isotropic media. *Antennas Propagation, IEEE Trans* (1966) **14**:302–307. doi:10.1109/TAP.1966.1138693
 69. Coggon JH. Electromagnetic and Electrical Modelling by the Finite Element Method. *GEOPHYSICS* (1971) **36**:132–155. doi:10.1190/1.1440151
 70. Christ A, Kainz W, Hahn EG, Honegger K, Zefferer M, Neufeld E, Rascher W, Janka R, Bautz W, Chen J, et al. The Virtual Family—development of surface-based anatomical models of two adults and two children for dosimetric simulations. *Phys Med Biol* (2010) **55**:N23–N38. doi:10.1088/0031-9155/55/2/N01
 71. Kozlov M, Turner R. Fast MRI coil analysis based on 3-D electromagnetic and RF circuit co-simulation. *J Magn Reson* (2009) **200**:147–152. doi:10.1016/j.jmr.2009.06.005

72. Goluch S. A design and development procedure for transceive radio frequency coils in ultra-high field magnetic resonance. PhD thesis. Medizinische Universität Wien. (2015) Available at: <https://repositorium.meduniwien.ac.at/obvumwhs/content/titleinfo/1714930?query=goluch> [Accessed September 28, 2020]
73. Godfrey A, Hetherington V, Shum H, Bonato P, Lovell NH, Stuart S. From A to Z: Wearable technology explained. *Maturitas* (2018) **113**:40–47. doi:10.1016/j.maturitas.2018.04.012
74. Schneegass S, Amft O. *Smart Textiles Fundamentals, Design, and Interaction*. Springer International Publishing (2017). doi:10.1007/978-3-319-50124-6
75. Van Langenhove L, Hertleer C. Smart clothing: a new life. *Int J Cloth Sci Technol* (2004) **16**:63–72. doi:10.1108/09556220410520360
76. Mehmman A, Vogt C, Varga M, Port A, Reber J, Marjanovic J, Pruessmann KP, Sporrer B, Huang Q, Troster G. Automatic Resonance Frequency Retuning of Stretchable Liquid Metal Receive Coil for Magnetic Resonance Imaging. *IEEE Trans Med Imaging* (2019) **38**:1420–1426. doi:10.1109/TMI.2018.2873317
77. Wilson JIB, Mather RR. “Photovoltaic energy harvesting for intelligent textiles,” in *Electronic Textiles: Smart Fabrics and Wearable Technology* (Elsevier Ltd), 155–171. doi:10.1016/B978-0-08-100201-8.00009-6
78. Waqar S, Wang L, John S. “Piezoelectric energy harvesting from intelligent textiles,” in *Electronic Textiles: Smart Fabrics and Wearable Technology* (Elsevier Ltd), 173–197. doi:10.1016/B978-0-08-100201-8.00010-2
79. Boehm A, Yu X, Neu W, Leonhardt S, Teichmann D. A Novel 12-Lead ECG T-Shirt with Active Electrodes. *Electronics* (2016) **5**:75. doi:10.3390/electronics5040075
80. Fukuma N, Hasumi E, Fujiu K, Waki K, Toyooka T, Komuro I, Ohe K. Feasibility of a T-Shirt-Type Wearable Electrocardiography Monitor for Detection of Covert Atrial Fibrillation in Young Healthy Adults. *Sci Rep* (2019) **9**:11768. doi:10.1038/s41598-019-48267-1
81. Clarius Mobile Health. Available at: <https://clarius.com> [Accessed September 8, 2020]
82. Portable MRI - Hyperfine. Available at: <https://www.hyperfine.io/portable-mri> [Accessed September 8, 2020]
83. Cooley CZ, Stockmann JP, Witzel T, LaPierre C, Mareyam A, Jia F, Zaitsev M, Wenhui Y, Zheng W, Stang P, et al. Design and implementation of a low-cost, tabletop MRI scanner for education and research prototyping. *J Magn Reson* (2020) **310**:106625. doi:10.1016/j.jmr.2019.106625
84. Sarracanie M, Salameh N. Low-Field MRI: How Low Can We Go? A Fresh View on an Old Debate. *Front Phys* (2020) **8**:172. doi:10.3389/fphy.2020.00172
85. Vogt C, Reber J, Waltisberg D, Büthe L, Marjanovic J, Münzenrieder N, Pruessmann KP, Tröster G. A wearable Bluetooth LE sensor for patient monitoring during MRI scans. in *Annu Int Conf IEEE Eng Med Biol Soc*, 4975–4978. doi:10.1109/EMBC.2016.7591844

86. van Niekerk A, van der Kouwe A, Meintjes E. Toward “plug and play” prospective motion correction for MRI by combining observations of the time varying gradient and static vector fields. *Magn Reson Med* (2019) **82**:1214–1228. doi:10.1002/mrm.27790
87. Clément J, Gruetter R, Ipek Ö. A combined 32-channel receive-loops/8-channel transmit-dipoles coil array for whole-brain MR imaging at 7T. *Magn Reson Med* (2019) **82**:1229–1241. doi:10.1002/mrm.27808
88. Gilbert KM, Belliveau J-G, Curtis AT, Gati JS, Klassen LM, Menon RS. A conformal transceive array for 7 T neuroimaging. *Magn Reson Med* (2012) **67**:1487–1496. doi:10.1002/mrm.23124
89. Nnewihe AN, Grafendorfer T, Daniel BL, Calderon P, Alley MT, Robb F, Hargreaves BA. Custom-fitted 16-channel bilateral breast coil for bidirectional parallel imaging. *Magn Reson Med* (2011) **66**:281–289. doi:10.1002/mrm.22771
90. Goluch S, Kuehne A, Meyerspeer M, Kriegl R, Schmid AI, Fiedler GB, Herrmann T, Mallow J, Hong SM, Cho ZH, et al. A form-fitted three channel ³¹P, two channel ¹H transceiver coil array for calf muscle studies at 7 T. *Magn Reson Med* (2015) **73**:2376–2389. doi:10.1002/mrm.25339
91. Goluch S, Frass-Kriegl R, Meyerspeer M, Pichler M, Sieg J, Gajdošík M, Krššák M, Laistler E. Proton-decoupled carbon magnetic resonance spectroscopy in human calf muscles at 7 T using a multi-channel radiofrequency coil. *Sci Rep* (2018) **8**:6211. doi:10.1038/s41598-018-24423-x
92. Gerges T, Semet V, Lombard P, Gaillard S, Cabrera M, Lambert SA. 3D Plastronics for Smartly Integrated Magnetic Resonance Imaging Coils. *Front Phys* (2020) **8**:240. doi:10.3389/fphy.2020.00240
93. Kwok WE, Lo KK, Seo G, Totterman SMS. A volume adjustable four-coil phased array for high resolution MR imaging of the hip. *Magn Reson Mater Physics, Biol Med* (1999) **9**:59–64. doi:10.1007/BF02634593
94. Hardy CJ, Giaquinto RO, Piel JE, Rohling KW, Marinelli L, Blezek DJ, Fiveland EW, Darrow RD, Foo TKF. 128-Channel body MRI with a flexible high-density receiver-coil array. *J Magn Reson Imaging* (2008) **28**:1219–1225. doi:10.1002/jmri.21463
95. Adriany G, Van de Moortele P-F, Ritter J, Moeller S, Auerbach EJ, Akgün C, Snyder CJ, Vaughan T, Uğurbil K. A geometrically adjustable 16-channel transmit/receive transmission line array for improved RF efficiency and parallel imaging performance at 7 Tesla. *Magn Reson Med* (2008) **59**:590–597. doi:10.1002/mrm.21488
96. Nordmeyer-Massner JA, De Zanche N, Pruessmann KP. Mechanically adjustable coil array for wrist MRI. *Magn Reson Med* (2009) **61**:429–438. doi:10.1002/mrm.21868
97. Mager D, Peter A, Tin L Del, Fischer E, Smith PJ, Hennig J, Korvink JG. An MRI receiver coil produced by inkjet printing directly on to a flexible substrate. *IEEE Trans Med Imaging* (2010) **29**:482–487. doi:10.1109/TMI.2009.2036996
98. Wu B, Zhang X, Wang C, Li Y, Pang Y, Lu J, Xu D, Majumdar S, Nelson SJ, Vigneron DB. Flexible transceiver array for ultrahigh field human MR imaging. *Magn Reson Med* (2012) **68**:1332–

1338. doi:10.1002/mrm.24121
99. Zhang T, Grafendorfer T, Cheng JY, Ning P, Rainey B, Giancola M, Ortman S, Robb FJ, Calderon PD, Hargreaves BA, et al. A semiflexible 64-channel receive-only phased array for pediatric body MRI at 3T. *Magn Reson Med* (2016) **76**:1015–1021. doi:10.1002/mrm.25999
 100. Hancu I, Fiveland E, Park K, Giaquinto RO, Rohling K, Wiesinger F. Flexible, 31-Channel breast coil for enhanced parallel imaging performance at 3T. *Magn Reson Med* (2016) **75**:897–905. doi:10.1002/mrm.25655
 101. Corea JR, Flynn AM, Lechêne B, Scott G, Reed GD, Shin PJ, Lustig M, Arias AC. Screen-printed flexible MRI receive coils. *Nat Commun* (2016) **7**:10839. doi:10.1038/ncomms10839
 102. Winkler SA, Corea J, Lechene B, O'Brien K, Bonanni JR, Robb F, Scott G, Pauly J, Lustig M, Arias AC, et al. First clinical pilot study using screen-printed flexible MRI receive coils for pediatric applications. in *Proc. Intl. Soc. Mag. Reson. Med. 26 (2018)*, 21.
 103. Winkler SA, Corea J, Lechêne B, O'Brien K, Bonanni JR, Chaudhari A, Alley M, Taviani V, Grafendorfer T, Robb F, et al. Evaluation of a Flexible 12-Channel Screen-printed Pediatric MRI Coil. *Radiology* (2019) **291**:180–185. doi:10.1148/radiol.2019181883
 104. Frass-Kriegl R, Navarro de Lara LI, Pichler M, Sieg J, Moser E, Windischberger C, Laistler E. Flexible 23-channel coil array for high-resolution magnetic resonance imaging at 3 Tesla. *PLoS One* (2018) **13**:e0206963. doi:10.1371/journal.pone.0206963
 105. Lopez Rios N, Foias A, Lodygensky G, Dehaes M, Cohen-Adad J. Size-adaptable 13-channel receive array for brain MRI in human neonates at 3 T. *NMR Biomed* (2018) **31**:e3944. doi:10.1002/nbm.3944
 106. Zhang B, Brown R, Cloos M, Lattanzi R, Sodickson D, Wiggins G. Size-adaptable “Trellis” structure for tailored MRI coil arrays. *Magn Reson Med* (2019) **81**:3406–3415. doi:10.1002/mrm.27637
 107. Iwasawa K, Otake Y, Habara H, Kato K, Ochi H. Prototype investigation for a size adaptable RF receiver coil capable of various body parts and sizes. in *Proc. Intl. Soc. Mag. Reson. Med. 27 (2019)*, 1499.
 108. GE Healthcare. AIR technology. Available at: <https://www.gehealthcare.com/products/magnetic-resonance-imaging/air-technology> [Accessed September 10, 2020]
 109. Rossman P, Stormont R, Lindsay S, Robb F, Savitskij D, Stanley D, Huston J, Kaufmann T, Mcgee K. Characterization of a new ultra-flexible, low profile RF receive coil technology. in *Proc. Intl. Soc. Mag. Reson. Med. 25 (2017)*, 0763.
 110. Vasanawala SS, Stormont R, Lindsay S, Grafendorfer T, Cheng JY, Pauly JM, Lustig M, Scott G, Guzman JX, Taracila V, et al. Development and Clinical Implementation of Very Light Weight and Highly Flexible AIR Technology Arrays. in *Proc. Intl. Soc. Mag. Reson. Med. 25 (2017)*, 0755.
 111. Stormont R, Robb F, Lindsey S, Chu D, Vlachos F, Taracila V, Chirayath D, Grafendorfer T, Guzman J, Vasanawala S, et al. Reimagining Flexible Coil Technology. Available at:

- <https://www3.gehealthcare.com/~media/documents/us-global/products/magnetic-resonance-imaging/signa fall 2016/tech trends/air technology coil.pdf> [Accessed September 10, 2020]
112. Stormont RS, Lindsay SA, Taracila V, Mustafa G, M. Malik N, Robb FJL, Chu D. Systems for a radio frequency coil for MR imaging. US Patent US20190277926A1. (2019)
 113. McGee KP, Stormont RS, Lindsay SA, Taracila V, Savitskij D, Robb F, Witte RJ, Kaufmann TJ, Huston J, Riederer SJ, et al. Characterization and evaluation of a flexible MRI receive coil array for radiation therapy MR treatment planning using highly decoupled RF circuits. *Phys Med Biol* (2018) **63**:08NT02. doi:10.1088/1361-6560/aab691
 114. Cozzini C, Bobb C, Engström M, Kaushik S, Molthen R, Rettmann D, Goruganti V, Chiang W-Y, Wiesinger F. A light-weight, flexible head and neck coil design for a patient-friendly MR-only Radiation Therapy workflow. in *Proc. Intl. Soc. Mag. Reson. Med. 27 (2019)*, 1548.
 115. Boskamp E, Taracila V, Lindsay S, Stormont R, Biswas R, Statum S, Aldas S, Barraza C, Robb F, Chung CB, et al. Highly Flexible, Light Weight 24 Channel 3T Bilateral Brachial Plexus Array Worn as a Close Fitting Variable Size Vest. in *Proc. Intl. Soc. Mag. Reson. Med. 26 (2018)*, 19.
 116. Stickle Y-J, Konrad Follante C, Giancola M, Robb F, Taracila V, Franko B, Blahnik H, Stormont RS. A Novel Ultra-Flexible High-Resolution 50-Channel RF Coil for Prostate, Rectal and Pelvis Imaging. in *Proc. Intl. Soc. Mag. Reson. Med. 27 (2019)*, 1547.
 117. Cogswell PM, Trzasko JD, Campeau NG, Gray EM, Rossman PJ, Kang D, Bernstein MA, McGee KP, Robb FJ, Stormont RS, et al. Comparison of AIR Coil Technology to Conventional Head Coils for Neuro Imaging. in *Proc. Intl. Soc. Mag. Reson. Med. 27 (2019)*, 2970.
 118. Laistler E, Moser E. Handy magnetic resonance coils. *Nat Biomed Eng* (2018) **2**:557–558. doi:10.1038/s41551-018-0278-y
 119. Obermann M, Nohava L, Goluch-Roat S, Pichler M, Sieg J, Felblinger J, Ginefri J-C, Laistler E. Ultra-flexible and light-weight 3-channel coaxial transmission line resonator receive-only coil array for 3T. in *Proc. Intl. Soc. Mag. Reson. Med. 27 (2019)*, 1558.
 120. Zijlema SE, Van Dijk L, Lagendijk JJW, Tijssen RHN, Van Den Berg CAT. A radiolucent and flexible high impedance coil array to improve the imaging performance of a 1.5T MR-linac. in *Proc. Intl. Soc. Mag. Reson. Med. 27 (2019)*, 1504.
 121. Urayama S-I, Zhang B, Fujimoto K, Okada T, Cloos MA. A modular 7T high-impedance array for ex-vivo imaging. in *Proc. Intl. Soc. Mag. Reson. Med. 27 (2019)*, 1541.
 122. Ruytenberg T, Webb A, Zivkovic I. Shielded-coaxial-cable coils as receive and transceive array elements for 7T human MRI. *Magn Reson Med* (2020) **83**:1135–1146. doi:10.1002/mrm.27964
 123. Ruytenberg T, Webb A, Zivkovic I. A flexible five-channel shielded-coaxial-cable (SCC) transceive neck coil for high-resolution carotid imaging at 7T. *Magn Reson Med* (2020) **84**:1672–1677. doi:10.1002/mrm.28215
 124. Fujimoto K, Zhang B, Urayama S-I, Shima A, Sawamoto N, Takahashi R, Okada T, Cloos MA. A

- tight-fit flexible high-impedance coil array for high-resolution imaging of small ex-vivo specimen using a human 7T scanner. in *Proc. Intl. Soc. Mag. Reson. Med.* 28 (2020), 4018.
125. Zhang D, Rahmat-Samii Y. Cadaver Measurement Results Using Ultra-flexible Electro-textile MRI RF Coil. in *2019 IEEE International Symposium on Antennas and Propagation and USNC-URSI Radio Science Meeting*, 21–22. doi:10.1109/APUSNCURSINRSM.2019.8888516
 126. Nordmeyer-Massner JA, De Zanche N, Pruessmann KP. Stretchable coil arrays: Application to knee imaging under varying flexion angles. *Magn Reson Med* (2012) **67**:872–879. doi:10.1002/mrm.23240
 127. Port A, Reber J, Vogt C, Marjanovic J, Sporrer B, Wu L, Mehmman A, Brunner DO, Burger T, Troester G, et al. Towards wearable MR detection: A stretchable wrist array with on-body digitization. in *Proc. Intl. Soc. Mag. Reson. Med.* 26 (2018), 17.
 128. Agir BK, Bayrambas B, Yegin K, Ozturk Isik E. Wearable and stretchable surface breast coil. in *Proc. Intl. Soc. Mag. Reson. Med.* 27 (2019), 1501.
 129. Vincent J, Rispoli J. Two-Channel, Stretchable, and Flexible Breast Coil Array. in *Proc. Intl. Soc. Mag. Reson. Med.* 28 (2020), 4275.
 130. Vincent JM, Rispoli J V. Conductive Thread-Based Stretchable and Flexible Radiofrequency Coils for Magnetic Resonance Imaging. *IEEE Trans Biomed Eng* (2020) **67**:2187–2193. doi:10.1109/TBME.2019.2956682
 131. Gruber B, Rehner R, Laistler E, Zink S. Anatomically Adaptive Coils for MRI – A 6-Channel array for knee Imaging at 1.5 Tesla. *Front Phys* (2020) **8**:80. doi:10.3389/fphy.2020.00080
 132. Malko JA, Mcclees EC, Braun IF, Davis PC, Hoffman JC. A Flexible Mercury-Filled Surface Coil for MR Imaging. *AJNR Am J Neuroradiol* (1986) **7**:246–247.
 133. Rousseau J, Lecouffe P, Marchandise X. A new, fully versatile surface coil for MRI. *Magn Reson Imaging* (1990) **8**:517–523. doi:10.1016/0730-725x(90)90061-6
 134. Port A, Luechinger R, Albisetti L, Varga M, Marjanovic J, Reber J, Brunner DO, Pruessmann KP. Detector clothes for MRI: A wearable array receiver based on liquid metal in elastic tubes. *Sci Rep* (2020) **10**:8844. doi:10.1038/s41598-020-65634-5
 135. Port A, Albisetti L, Varga M, Marjanovic J, Reber J, Brunner DO, Pruessmann KP. Liquid metal in stretchable tubes: A wearable 4-channel knee array. in *Proc. Intl. Soc. Mag. Reson. Med.* 27 (2019), 1114.
 136. Varga M, Mehmman A, Marjanovic J, Reber J, Vogt C, Pruessmann KP, Tröster G. Adsorbed Eutectic GaIn Structures on a Neoprene Foam for Stretchable MRI Coils. *Adv Mater* (2017) **29**:1703744. doi:10.1002/adma.201703744
 137. Mehmman A, Varga M, Vogt C, Port A, Reber J, Marjanovic J, Pruessmann KP, Tröster G. On the Bending and Stretching of Liquid Metal Receive Coils for Magnetic Resonance Imaging. *IEEE Trans Biomed Eng* (2019) **66**:1542–1548. doi:10.1109/TBME.2018.2875436
 138. Port A, Luechinger R, Brunner DO, Pruessmann KP. Conductive Elastomer for Wearable RF

- Coils. in *Proc. Intl. Soc. Mag. Reson. Med. 28 (2020)*, 1137.
139. De Zanche N. *MRI Technology: Circuits and Challenges for Receiver Coil Hardware.*, ed. K. Iniewski Hoboken, New Jersey, USA: John Wiley & Sons, Inc. (2009).
 140. Yuan J, Wei J, Shen GX. A direct modulated optical link for MRI RF receive coil interconnection. *J Magn Reson (2007)* 130–138. doi:10.1016/j.jmr.2007.08.016
 141. Yuan J, Wei J, Du C, Shen GX. Investigation of dynamic range requirement for MRI signal transmission by optical fiber link. *Proc. Intl. Soc. Mag. Reson. Med. 15 (2007)*, 995.
 142. Yuan J, Wei J, Shen GX. A 4-channel coil array interconnection by analog direct modulation optical link for 1.5-T MRI. *IEEE Trans Med Imaging (2008)* 27:1432–1438. doi:10.1109/TMI.2008.922186
 143. Memis OG, Eryaman Y, Aytur O, Atalar E. Miniaturized fiber-optic transmission system for MRI signals. *Magn Reson Med (2008)* 59:165–173. doi:10.1002/mrm.21462
 144. Du C, Yuan J, Shen GX. Comparison of FP, VCSEL and DFB laser diode in optical transmission for MR RF coil array. *Proc. Intl. Soc. Mag. Reson. Med. 15 (2007)*, 1041.
 145. Fandrey S, Weiss S, Müller J. A novel active MR probe using a miniaturized optical link for a 1.5-T MRI scanner. *Magn Reson Med (2012)* 67:148–155. doi:10.1002/mrm.23002
 146. Biber S, Baureis P, Bollenbeck J, Höcht P, Fischer H. Analog Optical Transmission of 4 MRI Receive Channels with high Dynamic Range over one Single Optical Fiber. in *Proc. Intl. Soc. Mag. Reson. Med. 16 (2008)*, 1120.
 147. Koste GP, Nielsen MC, Tolliver TR, Frey RL, Watkins RD. Optical MR Receive Coil Array Interconnect. *Proc. Intl. Soc. Mag. Reson. Med. 13 (2005)*, 411.
 148. Aydé R, Gaborit G, Jarrige P, Duvillaret L, Sablong R, Perrier AL, Beuf O. Potentialities of an electro-optic crystal fed by nuclear magnetic resonant resonant coil for remote and low-invasive magnetic field characterization. *IEEE Sens J (2013)* 13:1274–1280. doi:10.1109/JSEN.2012.2230623
 149. Aydé R, Gaborit G, Dahdah J, Duvillaret L, Courjal N, Guyot C, Sablong R, Perrier AL, Beuf O. Unbiased electro-optic waveguide as a sensitive nuclear magnetic resonance sensor. *IEEE Photonics Technol Lett (2014)* 26:1266–1269. doi:10.1109/LPT.2014.2321099
 150. Pockels FCA. *Lehrbuch der Kristallogoptik*. Leipzig und Berlin: B.G. Teubner (1906).
 151. Demir T, Delabarre L, Akin B, Adriany G, Ugurbil K, Atalar E. Optical Transmission System for High Field Systems. *Proc. Intl. Soc. Mag. Reson. Med. 19 (2011)*, 1865.
 152. Saniour I, Aydé R, Perrier AL, Gaborit G, Duvillaret L, Sablong R, Beuf O. Active optical-based detuning circuit for receiver endoluminal coil. *Biomed Phys Eng Express (2017)* 3:025002. doi:10.1088/2057-1976/aa5db0
 153. Possanzini C, Van Liere P, Roeven H, Den Boef J, Saylor C, Van Eggermond J, Harvey P, Moore E. Scalability and channel independency of the digital broadband dStream architecture. *Proc.*

- Intl. Soc. Mag. Reson. Med.* 19 (2011), 5103.
154. Possanzini C, Harvey PR, Ham K, Hoogeveen R. The digital revolution in MRI with dStream architecture. (2016) Available at: <http://clinical.netforum.healthcare.philips.com/global/Explore/White-Papers/MRI/Ingenia-dStream-architecture-the-digital-revolution-in-MRI> [Accessed September 2, 2019]
 155. Sporrer B, Wu L, Bettini L, Vogt C, Reber J, Marjanovic J, Burger T, Brunner DO, Pruessmann KP, Tröster G, et al. A Fully Integrated Dual-Channel On-Coil CMOS Receiver for Array Coils in 1.5–10.5 T MRI. *IEEE Trans Biomed Circuits Syst* (2017) **11**:1245–1255. doi:10.1109/TBCAS.2017.2764443
 156. Reber J, Marjanovic J, Brunner DO, Port A, Schmid T, Dietrich BE, Moser U, Barmet C, Pruessmann KP. An In-Bore Receiver for Magnetic Resonance Imaging. *IEEE Trans Med Imaging* (2020) **39**:997–1007. doi:10.1109/TMI.2019.2939090
 157. Sporrer B. Integrated Broadband Receivers for Magnetic Resonance Imaging. PhD thesis. ETH Zürich. (2017) doi:10.3929/ethz-b-000221997
 158. Valkama M, Pirskanen J, Renfors M. Signal processing challenges for applying software radio principles in future wireless terminals: An overview. *Int J Commun Syst* (2002) **15**:741–769. doi:10.1002/dac.561
 159. ADS52J65. 8-channel 16-bit 125-MSPS analog-to-digital converter (ADC) with JESD204B interface. Available at: <https://www.ti.com/product/ADS52J65> [Accessed September 9, 2020]
 160. AD9656. Quad, 16-Bit, 125 MSPS JESD204B 1.8 V Analog-to-Digital Converter. Available at: <https://www.analog.com/en/products/ad9656.html> [Accessed September 9, 2020]
 161. ADS5263. Quad-Channel, 16-Bit, 100-MSPS Analog-to-Digital Converter (ADC). Available at: <https://www.ti.com/product/ADS5263> [Accessed September 9, 2020]
 162. Jutras JD, Fallone BG, De Zanche N. Efficient multichannel coil data compression: A prospective study for distributed detection in wireless high-density arrays. *Concepts Magn Reson Part B Magn Reson Eng* (2011) **39**:64–77. doi:10.1002/cmr.b.20191
 163. Buehrer M, Pruessmann KP, Boesiger P, Kozerke S. Array compression for MRI with large coil arrays. *Magn Reson Med* (2007) **57**:1131–1139. doi:10.1002/mrm.21237
 164. Marjanovic J, Reber J, Brunner DO, Engel M, Kasper L, Dietrich BE, Vionnet L, Pruessmann KP. A Reconfigurable Platform for Magnetic Resonance Data Acquisition and Processing. *IEEE Trans Med Imaging* (2020) **39**:1138–1148. doi:10.1109/TMI.2019.2944696
 165. Aggarwal K, Joshi KR, Rajavi Y, Taghivand M, Pauly JM, Poon ASY, Scott G. A Millimeter-Wave Digital Link for Wireless MRI. *IEEE Trans Med Imaging* (2017) **36**:574–583. doi:10.1109/TMI.2016.2622251
 166. Vogt CM. Design Concepts and Validation of In-field MRI Electronics. ETH Zürich. (2017) doi:10.3929/ethz-b-000246692
 167. Tang W, Wang W, Liu W, Ma Y, Tang X, Xiao L, Gao JH. A home-built digital optical MRI console

- using high-speed serial links. *Magn Reson Med* (2015) **74**:578–88. doi:10.1002/mrm.25403
168. Firecomms. Medical Imaging Solutions. Available at: https://www.firecomms.com/contentFiles/files/Medical_Imaging-compressed.pdf [Accessed September 13, 2020]
 169. molex. SMI Non-Magnetic Transceiver. Available at: https://www.molex.com/molex/products/part-detail/fiber_optic_adapte/1061085500 [Accessed September 13, 2020]
 170. Bulumulla SB, Fiveland E, Park KJ, Foo TK, Hardy CJ. Inductively coupled wireless RF coil arrays. *Magn Reson Imaging* (2015) **33**:351–357. doi:10.1016/j.mri.2014.12.004
 171. Slobozhanyuk AP, Poddubny AN, Raaijmakers AJE, Van Den Berg CAT, Kozachenko A V., Dubrovina IA, Melchakova I V., Kivshar YS, Belov PA. Enhancement of Magnetic Resonance Imaging with Metasurfaces. *Adv Mater* (2016) **28**:1832–1838. doi:10.1002/adma.201504270
 172. Shchelokova A, Solomakha G, Brui E, Mikhailovskaya A, Melchakova I, Andreychenko A. Wireless coil as a portable and practical alternative to a dedicated transceive coil for extremities MRI at 1.5T. in *Proc. Intl. Soc. Mag. Reson. Med. 27 (2019)*, 0273.
 173. Boskamp EB. Wireless RF module for an MR imaging system. US Patent US20030206019A1. (2003)
 174. Heid O, Vester M, Cork P, Hulbert P, Huish DW. Cutting the cord - wireless coils for MRI. in *Proc. Intl. Soc. Mag. Reson. Med. 17 (2009)*, 100.
 175. Martius S, Heid O, Vester M, Biber S, Nistler J. Wireless local coil signal transmission using a parametric upconverter. in *Proc. Intl. Soc. Mag. Reson. Med. 17 (2009)*, 2934.
 176. Scott G, Yu K. Wireless Transponders for RF Coils: Systems Issues. in *Proc. Intl. Soc. Mag. Reson. Med. 13 (2005)*, 330.
 177. Riffe MJ. Wireless MRI Detector Arrays: Technology & Clinical Applications. PhD thesis. Case Western Reserve University. Cleveland, Ohio, USA. (2014)
 178. De Zanche N, Luechinger R, Blaettler D, Jaeger S, Mudra R, Keller E, Pruessmann K. Compatibility study for concurrent bluetooth wireless transmission and MR imaging. in *Proceedings of the European Society for Magnetic Resonance in Medicine and Biology (2004)* (Copenhagen, DK), 449.
 179. Konstantinou G, Ali W, Chil R, Cossu G, Ciaramella E, Vaquero JJ. Experimental demonstration of an optical wireless MRI compatible PET/SPECT insert front-end. in *IEEE Nuclear Science Symposium, Medical Imaging Conference and Room-Temperature Semiconductor Detector Workshop (2016)*, 1–4. doi:10.1109/NSSMIC.2016.8069524
 180. Refai HH. Comparative study of the performance of analog fiber optic links versus free-space optical links. *Opt Eng* (2006) **45**:025003. doi:10.1117/1.2174623
 181. Hou R, Chen Y, Wu J, Zhang H. A Brief Survey of Optical Wireless Communication. *13th Australas Symp Parallel Distrib Comput (AusPDC 2015)* (2015) **163**:41–50.

182. Haas H, Elmirghani J, White I. Optical wireless communication. *Philos Trans R Soc A Math Phys Eng Sci* (2020) **378**: doi:10.1098/rsta.2020.0051
183. Haas H, Yin L, Wang Y, Chen C. What is LiFi? *J Light Technol* (2016) **34**:1533–1544. doi:10.1109/JLT.2015.2510021
184. Haas H. LiFi is a paradigm-shifting 5G technology. *Rev Phys* (2018) **3**:26–31. doi:10.1016/j.revip.2017.10.001
185. Gao Z, Dai L, Gao X, Shakir MZ, Wang Z. “Fronthaul design for mmWave massive MIMO,” in *mmWave Massive MIMO: A Paradigm for 5G (2017)* (Elsevier Inc.), 289–312. doi:10.1016/B978-0-12-804418-6.00012-1
186. Chowdhury MZ, Hossan MT, Islam A, Jang YM. A Comparative Survey of Optical Wireless Technologies: Architectures and Applications. *IEEE Access* (2018) **6**:9819–9840. doi:10.1109/ACCESS.2018.2792419
187. Khalaf K, Vidojkovic V, Long JR, Wambacq P. *Low-Power Millimeter Wave Transmitters for High Data Rate Applications*. Springer Nature Switzerland AG (2019). doi:10.1007/978-3-030-16653-3
188. Faulwaßer M, Deicke F, Schneider T. 10 Gbit/s bidirectional optical wireless communication module for docking devices. in *2014 IEEE Globecom Workshops*, 512–517. doi:10.1109/GLOCOMW.2014.7063483
189. Milovančev D, Jukić T, Steindl B, Hofbauer M, Enne R, Schneider-Hornstein K, Zimmermann H. Optical wireless communication with monolithic avalanche photodiode receivers. in *2017 IEEE Photonics Conference (IPC)*, 25–26. doi:10.1109/IPCon.2017.8115989
190. Brandl P, Schidl S, Zimmermann H. PIN Photodiode Optoelectronic Integrated Receiver Used for 3-Gb/s Free-Space Optical Communication. *IEEE J Sel Top Quantum Electron* (2014) **20**:391–400. doi:10.1109/JSTQE.2014.2336539
191. Islim MS, Ferreira RX, He X, Xie E, Videv S, Viola S, Watson S, Bamiedakis N, Penty R V., White IH, et al. Towards 10 Gb/s orthogonal frequency division multiplexing-based visible light communication using a GaN violet micro-LED. *Photonics Res* (2017) **5**:A35. doi:10.1364/prj.5.000a35
192. Tsonev D, Videv S, Haas H. Towards a 100 Gb/s visible light wireless access network. *Opt Express* (2015) **23**:1627–1637. doi:10.1364/OE.23.001627
193. He X, Xie E, Islim MS, Purwita AA, McKendry JJD, Gu E, Haas H, Dawson MD. 1 Gbps free-space deep-ultraviolet communications based on III-nitride micro-LEDs emitting at 262 nm. *Photonics Res* (2019) **7**:B41. doi:10.1364/prj.7.000b41
194. High-speed Internet using your lights with LiFi - Signify Company Website. trulifi. Available at: <https://www.signify.com/global/innovation/trulifi> [Accessed September 16, 2020]
195. pureLiFi - Connectivity is evolving. Light becomes data. Available at: <https://purelifi.com> [Accessed September 16, 2020]

196. Li-Fi - Optical Communication - Fraunhofer IPMS. Available at: <https://www.ipms.fraunhofer.de/en/research-development/wireless-microsystems/LiFi.html> [Accessed September 16, 2020]
197. Light Fidelity (LiFi) Internet Service Provider Company - Oledcomm. Available at: <https://www.oledcomm.net> [Accessed September 16, 2020]
198. KORUZA. Light-speed networking. Available at: <http://www.koruza.net> [Accessed September 16, 2020]
199. RONJA. Twibright Labs. Available at: <http://ronja.twibright.com> [Accessed September 16, 2020]
200. Bulumulla SB. Optical link for transmitting data through air from a plurality of receiver coils in a Magnetic Resonance Imaging system. US Patent US7173426. (2007)
201. Tsonev D, Videv S, Haas H. Light Fidelity (Li-Fi): Towards All-Optical Networking. (2014) **9007:1** – 10. doi:10.1117/12.2044649
202. Chun H, Rajbhandari S, Faulkner G, Tsonev D, Xie E, McKendry JJD, Gu E, Dawson MD, O'Brien DC, Haas H. LED based wavelength division multiplexed 10 Gb/s visible light communications. *J Light Technol* (2016) **34**:3047–3052. doi:10.1109/JLT.2016.2554145
203. Mana SM, Hellwig P, Hilt J, Berenguer PW, Jungnickel V. Experiments in Non-Line-of-Sight Li-Fi Channels. in *2019 Global LIFI Congress (GLC)*, 1–6. doi:10.1109/GLC.2019.8864131
204. Agrawal GP. *Fiber-optic communication systems*. John Wiley & Sons, Inc. (2002). doi:10.1002/0471221147
205. Schubert EF. *Light-emitting diodes*. 2nd ed. Cambridge University Press (2006). doi:10.1017/CBO9780511790546
206. Massa Nick. Fundamentals of Photonics. Fiber Optic Telecommunication. Springfield, MA, USA (2000). Available at: <https://spie.org/publications/fundamentals-of-photonics-modules> [Accessed September 17, 2020]
207. Hamamatsu. Opto-Semiconductor Handbook. Available at: https://www.hamamatsu-news.de/hamamatsu_optosemiconductor_handbook/82/ [Accessed September 24, 2020]
208. Elgala H, Mesleh R, Haas H. Indoor optical wireless communication: potential and state-of-the-art. *IEEE Commun Mag* (2011) **49**:56–62. doi:10.1109/MCOM.2011.6011734
209. International Electrotechnical Commission (IEC). *Safety of laser products - Part 1: Equipment classification and requirements (IEC 60825-1)*. 3rd ed. Geneva (2014).
210. International Electrotechnical Commission (IEC). *Safety of laser products - Part 12: Safety of free space optical communication systems used for transmission of information (IEC 60825-12)*. 2nd ed. Geneva (2019).
211. Rockwell DA, Mecherle GS. Optical wireless: low-cost, broadband, optical access. Available at:

- http://www.fsona.com/tech/white_papers/optical_wireless.pdf [Accessed September 17, 2020]
212. Reber J, Marjanovic J, Brunner DO, Port A, Schmid T, Dietrich BE, Moser U, Christoph B, Pruessmann KP. An In-bore Receiver for Magnetic Resonance Imaging. *IEEE Trans Med Imaging* (2020) **39**:997–1007. doi:10.1109/TMI.2019.2939090
 213. Lu JY, Grafendorfer T, Zhang T, Vasanaawala S, Robb F, Pauly JM, Scott GC. Depletion-Mode GaN HEMT Q-Spoil Switches for MRI Coils. *IEEE Trans Med Imaging* (2016) **35**:2558–2567. doi:10.1109/TMI.2016.2586053
 214. Weber N. Mise en oeuvre d'un module multicateurs pour l'imagerie par résonance magnétique (IRM). Master thesis. Université de Lorraine. (2013)
 215. SIEMENS Healthineers. 4-Channel Flex Coils. Available at: <https://www.siemens-healthineers.com/magnetic-resonance-imaging/options-and-upgrades/coils/4-channel-flex-coils/features#00106154> [Accessed September 18, 2020]
 216. Obermann M, Nohava L, Czerny R, Frass-Kriegl R, Roat S, Pichler M, Felblinger J, Ginefri J-C, Laistler E. Optimization and miniaturization of Rx-only coaxial coil interfacing. in *Proc. Intl. Soc. Mag. Reson. Med. 28 (2020)*, 4042.
 217. Karasan E, Taracila V, Robb F, Lustig M. The Very RF Hungry Caterpillar Trap (Highly Flexible, Distributed System of Toroid Cable Traps). in *Proc. Intl. Soc. Mag. Reson. Med. 28 (2020)*, 4050.
 218. Yan X, Gore JC. A highly-miniaturized inverted cable trap. in *Proc. Intl. Soc. Mag. Reson. Med. 27 (2019)*, 1583.
 219. Delfino JG, Krainak DM, Flesher SA, Miller DL. MRI-related FDA adverse event reports: A 10-yr review. *Med Phys* (2019) **46**:5562–5571. doi:10.1002/mp.13768
 220. International Electrotechnical Commission (IEC). *Medical electrical equipment - Part 1: General requirements for basic safety and essential performance (IEC 60601-1:2005+AMD1:2012+AMD2:2020 CSV)*. 3.2. Geneva (2020).
 221. Nohava L, Czerny R, Obermann M, Pichler M, Frass-Kriegl R, Felblinger J, Ginefri J-C, Laistler E. Flexible multi-turn multi-gap coaxial RF coils (MTMG-CCs): design concept and bench validation. in *Proc. Intl. Soc. Mag. Reson. Med. 27 (2019)*, 565.
 222. Czerny R, Nohava L, Frass-Kriegl R, Felblinger J, Ginefri J-C, Laistler E. Flexible multi-turn multi-gap coaxial RF coils: enabling a large range of coil sizes. in *Proc. Intl. Soc. Mag. Reson. Med. 27 (2019)*, 1550.
 223. Nohava L, Czerny R, Obermann M, Pichler M, Frass-Kriegl R, Felblinger J, Ginefri J-C, Laistler E. Antennes RF coaxiales multitours et multifentes: conception et validation expérimentale. in *4th congress of the SFRMBM (Société Française de Résonance Magnétique en Biologie et Médecine), 2019*
 224. Nohava L, Czerny R, Obermann M, Pichler M, Frass-Kriegl R, Felblinger J, Ginefri J-C, Laistler E. Flexible multi-turn multi-gap coaxial coils: investigation of size- and shape-adaptation for different anatomical targets at 1.5, 3 and 7 Tesla. *Magn Reson Mater Physics, Biol Med* (2019)

32:82. doi:10.1007/s10334-019-00753-3

225. Nohava L, Czerny R, Obermann M, Felblinger J, Frass-Kriegl R, Ginefri J-C, Laistler E. Flexible receive-only coaxial coils with multiple turns and gaps for 3 T MRI. in *Proc. Intl. Soc. Mag. Reson. Med. 28 (2020)*, 750.
226. Nohava L, Czerny R, Obermann M, Felblinger J, Frass-Kriegl R, Ginefri J-C, Laistler E. Flexible transmit/receive multi-gap coaxial coils for 7 T MRI. in *Proc. Intl. Soc. Mag. Reson. Med. 28 (2020)*, 4273.
227. Pozar David M. *Microwave Engineering*. 4th ed. Hoboken, NJ: John Wiley & Sons, Inc. (2011).
228. Odille F, Vuissoz PA, Marie PY, Felblinger J. Generalized reconstruction by inversion of coupled systems (GRICS) applied to free-breathing MRI. *Magn Reson Med (2008)* **60**:146–157. doi:10.1002/mrm.21623
229. Böcker A, Eklind V, Hansson D, Holgersson P, Nolkrantz J, Severinson A. An implementation of a visible light communication system based on LEDs. Bachelor thesis. Chalmers University of Technology. Gothenburg, Sweden. (2015)
230. Recker S. MR-compatible Optical Wireless Communication System. Bachelor thesis. Medizinische Universität Wien & Universität Wien. (2019)
231. Vishay Semiconductors. Eye Safety Risk Assessment of Infrared Emitting Diodes According IEC 62471 (based on CIE S009). Available at: <https://www.vishay.com/docs/81935/eyesafe.pdf> [Accessed September 17, 2020]
232. ADCDAC Pi with Python. Available at: <https://www.abelectronics.co.uk/kb/article/15/adcdac-pi-with-python> [Accessed September 1, 2020]
233. Blender. (2020) Available at: <https://www.blender.org> [Accessed August 28, 2020]
234. Fraunhofer IPMS. Li-Fi HotSpot – Long-Distance Data Transmission. (2020) Available at: <https://www.ipms.fraunhofer.de/en/research-development/wireless-microsystems/LiFi/lifi-hotspot.html> [Accessed August 20, 2020]
235. SIEMENS Healthineers. MAGNETOM Skyra. (2020) Available at: https://www.siemens-healthineers.com/magnetic-resonance-imaging/3t-mri-scanner/magnetom-skyra#TECHNICAL_DETAILS [Accessed August 20, 2020]
236. iPerf - The ultimate speed test tool for TCP, UDP and SCTP. Available at: <https://iperf.fr> [Accessed August 31, 2020]
237. International Organization for Standardization (ISO). *Medical devices — Application of risk management to medical devices (ISO 14971:2019)*. 3rd ed. (2019).
238. World Health Organization. Breast Cancer. (2020) Available at: <https://www.who.int/cancer/prevention/diagnosis-screening/breast-cancer/en/> [Accessed September 29, 2020]

239. Saadatmand S, Geuzinge HA, Rutgers EJT, Mann RM, de Roy van Zuidewijn DBW, Zonderland HM, Tollenaar RAEM, Lobbes MBI, Ausems MGEM, van 't Riet M, et al. MRI versus mammography for breast cancer screening in women with familial risk (FaMRisc): a multicentre, randomised, controlled trial. *Lancet Oncol* (2019) **20**:1136–1147. doi:10.1016/S1470-2045(19)30275-X
240. Mann RM, Cho N, Moy L. Breast MRI: State of the Art. *Radiology* (2019) **292**:520–536. doi:10.1148/radiol.2019182947
241. Riedl CC, Luft N, Bernhart C, Weber M, Bernathova M, Tea M-KM, Rudas M, Singer CF, Helbich TH. Triple-Modality Screening Trial for Familial Breast Cancer Underlines the Importance of Magnetic Resonance Imaging and Questions the Role of Mammography and Ultrasound Regardless of Patient Mutation Status, Age, and Breast Density. *J Clin Oncol* (2015) **33**:1128–1135. doi:10.1200/JCO.2014.56.8626
242. Price ER, Hargreaves J, Lipson JA, Sickles EA, Brenner RJ, Lindfors KK, Joe BN, Leung JWT, Feig SA, Bassett LW, et al. The California Breast Density Information Group: A Collaborative Response to the Issues of Breast Density, Breast Cancer Risk, and Breast Density Notification Legislation. *Radiology* (2013) **269**:887–892. doi:10.1148/radiol.13131217
243. Kuhl CK. Abbreviated Magnetic Resonance Imaging (MRI) for Breast Cancer Screening: Rationale, Concept, and Transfer to Clinical Practice. *Annu Rev Med* (2019) **70**:501–519. doi:10.1146/annurev-med-121417-100403
244. Lakshmanan K, Cloos M, Brown R, Lattanzi R, Sodickson DK, Wiggins GC. The “Loopole” Antenna: A Hybrid Coil Combining Loop and Electric Dipole Properties for Ultra-High-Field MRI. *Concepts Magn Reson Part B, Magn Reson Eng* (2020) 8886543. doi:10.1155/2020/8886543

Curriculum Vitae

Lena NOHAVA

lena.nohava@gmail.com

orcid.org/0000-0003-1676-6513

Personal information

Nationality: Austrian

Date and place of birth: June 11, 1993 in Oberpullendorf, Austria

Research focus

MR hardware engineering | innovative RF coils for (ultra-)high field MRI
electromagnetic simulations | RF safety | parallel transmission pulse design

Professional record

PhD fellow

10/2017 – 12/2020

BioMaps (former IR4M) laboratory, Université Paris-Saclay, Orsay, France, project work in collaboration with the RF Lab at the CMPBME, Medical University of Vienna, Vienna, Austria

- lightweight flexible radio frequency coils for 3 and 7 Tesla MRI
- wearable MR technology (a flexible coil vest for MR mammography)
- (optical) wireless data transmission in the MR environment

Master thesis internship

10/2016 – 06/2017

RF Lab at the CMPBME, Medical University of Vienna, Vienna, Austria

Internship

08/2015 – 09/2015

RF Lab at the CMPBME, Medical University of Vienna, Vienna, Austria

Education

Université Paris-Saclay, Orsay, France & Medical University of Vienna, Vienna, Austria

10/2017 – 12/2020

PhD studies “Medical Physics and Imaging” at the Université Paris-Saclay, registered as visiting student at the Medical University of Vienna. Thesis: “*Concepts for Wearable Technology in MR: Lightweight Flexible Radio Frequency Coils and Optical Wireless Communication*”

University of Vienna, Vienna, Austria

10/2012 – 08/2017

Diploma studies, teacher training in Physics and French, focus on MR Physics, passed with distinction. Thesis: “*A parallel transmission pulse design framework for 7 T MRI with physical constraints and SAR minimization*”

Bundesrealgymnasium Gröhrmühlgasse, Wiener Neustadt, Austria

09/2003 – 05/2011

High school graduation, passed with distinction

International

Paris, France

10/2017 – 12/2020

PhD studies, Orsay, France

01/2012 – 06/2012

French linguistics and civilization courses (CCFS, Fondation Robert de Sorbon)

08/2011 – 08/2012

Au-pair year

Nice, France

01/2016 – 07/2016

Erasmus semester, Université Sophia Antipolis

Language skills

German (native), English (C2), French (C2), Spanish (A2)

Awards and scholarships

2020

ISMRM Educational Stipend, virtual meeting

2019

ISMRM Educational Stipend & **SFRMBM** stipend, Montréal, Canada

ISMRM Magna Cum Laude merit award, Montréal, Canada

2018

ISMRM New Entrant Stipend, Paris, France

2017

MESR (Ministère de l'Enseignement Supérieur et de la Recherche) PhD funding for 3 years, Orsay, France

2016

Erasmus+ scholarship, Nice, France

2013, 2014, 2016

Excellent performance scholarship, University of Vienna, Austria

Memberships

2020

IEEE Student Member

Société Française de Résonance Magnétique en Biologie et Médecine (SFRMBM)

Young Scientist Association (YSA) of the Medical University of Vienna

International Society for Magnetic Resonance in Medicine (ISMRM)

European Society for Magnetic Resonance in Medicine and Biology (ESMRMB)

List of publications

Lena NOHAVA | 2016-2020

2 peer-reviewed journal articles
11 peer-reviewed conference proceedings

Peer-reviewed journal articles

1. **Nohava L**, Ginefri J-C, Willoquet G, Laistler E, Frass-Kriegl R. Perspectives in Wireless Radio Frequency Coil Development for Magnetic Resonance Imaging. *Front Phys* (2020) 8:11. doi:10.3389/fphy.2020.00011
2. **Nohava L**, Czerny R, Roat S, Obermann M, Kuehne A, Frass-Kriegl R, Felblinger J, Ginefri J-C, Laistler E. Flexible multi-turn multi-gap coaxial RF coils: design concept and implementation for Magnetic Resonance Imaging at 3 and 7 Tesla. *IEEE Trans Med Imaging* (2021) doi:10.1109/TMI.2021.3051390. Epub ahead of print.

Peer-reviewed conference proceedings

1. **Nohava L**, Czerny R, Obermann M, Felblinger J, Frass-Kriegl R, Ginefri JC, Laistler E. *Flexible transmit/receive multi-gap coaxial coils for 7 T MRI*. Proceedings of the ISMRM, 2020, virtual conference. (*digital poster presentation*)
2. **Nohava L**, Czerny R, Obermann M, Felblinger J, Frass-Kriegl R, Ginefri JC, Laistler E. *Flexible receive-only coaxial coils with multiple turns and gaps for 3 T MRI*. Proceedings of the ISMRM, 2020, virtual conference. (*oral presentation*)
3. Obermann M, **Nohava L**, Czerny R, Frass-Kriegl R, Roat S, Pichler M, Felblinger J, Ginefri JC, Laistler E. *Optimization and miniaturization of Rx-only coaxial coil interfacing*. Proceedings of the ISMRM, 2020, virtual conference. (*digital poster presentation*)
4. **Nohava L**, Czerny R, Obermann M, Pichler M, Felblinger J, Frass-Kriegl R, Ginefri JC, Laistler E. *Flexible multi-turn multi-gap coaxial coils: investigation of size- and shape-adaptation for different anatomical targets at 1.5, 3 and 7 Tesla*. Proceedings of the ESMRMB, 2019, Rotterdam, Netherlands. (*power pitch + traditional poster presentation*)
5. Czerny R, **Nohava L**, Frass-Kriegl R, Felblinger J, Ginefri JC, Laistler E. *Flexible multi-turn multi-gap coaxial RF coils: enabling a large range of coil sizes*. Proceedings of the ISMRM, 2019, Montréal, Canada. (*digital poster presentation*)
6. Obermann M, **Nohava L**, Goluch-Roat S, Pichler M, Sieg J, Felblinger J, Ginefri JC, Laistler E. *Ultra-flexible and light-weight 3-channel coaxial transmission line resonator receive-only coil array for 3T*. Proceedings of the ISMRM, 2019, Montréal, Canada. (*digital poster presentation*)

7. **Nohava L**, Czerny R, Obermann M, Pichler M, Frass-Kriegl R, Felblinger J, Ginefri J-C, Laistler E. *Flexible multi-turn multi-gap coaxial RF coils (MTMG-CCs): design concept and bench validation*. Proceedings of the ISMRM, 2019, Montréal, Canada. (ISMRM Magna Cum Laude award, power pitch + digital poster presentation)
8. **Nohava L**, Czerny R, Obermann M, Pichler M, Frass-Kriegl R, Felblinger J, Ginefri J-C, Laistler E. *Antennes RF coaxiales multitours et multifentes: conception et validation experimentale*. 4th congress of the SFRMBM, 2019, Strasbourg, France. (traditional poster presentation)
9. Rund A, Aigner CS, **Nohava L**, Frass-Kriegl R, Laistler E, Kunisch K, and Stollberger R. *Optimal control based design of parallel transmission RF pulses with minimum local SAR*. Proceedings of the ISMRM/ESMRMB, 2018, Paris, France. (digital poster presentation)
10. **Nohava L**, Kuehne A, Aigner CS, Rund A, Moser E, Laistler E, and Frass-Kriegl R. *Evaluation of RF pulses for 8-channel pTx systems at 7T with respect to hardware constraints and the trade-off between local 10g SAR and excitation accuracy*. Proceedings of the ESMRMB, 2017, Barcelona, Spain. (oral presentation)
11. **Nohava L**, Navarro de Lara LI, Moser E, Laistler E, and Kriegl R. *Influence of the active detuning inductance in a receive-only surface coil on the transmit field homogeneity of a birdcage resonator*. Proceedings of the ESMRMB, 2016, Vienna, Austria. (traditional poster presentation)

Invited talks

Frass-Kriegl R & **Nohava L**, *Options for Wireless MR Data Transmission*. Educational talk, ISMRM, 2020, virtual conference. (co-presenter)

Titre : Concepts pour l'instrumentation portable en IRM : Développement d'antennes radiofréquences légères et flexibles et d'un système de transmission optique sans fil

Mots clés : Imagerie Résonance Magnétique (IRM), haut champ, radiofréquence (RF), flexible, transmission sans fil, instrumentation portable

Résumé : Ce projet doctoral a été réalisé au laboratoire BioMaps de l'Université Paris-Saclay et au CMP-BME de l'Université Médicale de Vienne.

Afin d'améliorer la valeur diagnostique de l'IRM, il est souhaitable de réduire les durées d'acquisition, d'avoir une prise en charge plus efficace des patients et une meilleure qualité des images. Dans ce but, une instrumentation portable avec un matériel optimisé permettrait de réduire le poids, d'augmenter la flexibilité et de transmettre sans fil les signaux RMN, améliorant ainsi la sensibilité, le confort, la sécurité et la facilité d'utilisation de ces dispositifs. Dans ce contexte, nous avons étudié des antennes RF souples à câbles coaxiaux basées sur le principe des résonateurs à lignes à transmission. Ces résonateurs, pouvant posséder plusieurs tours et/ou plusieurs fentes, permettent d'optimiser la taille de l'antenne RF en fonction de l'application visée.

Le concept a d'abord été étudiée in silico. De nombreux prototypes ont été construits et leurs performances ont été testées sur table et en IRM à 3 et 7 T. Les antennes coaxiales ont révélé avoir des performances robustes à la déformation, ne dégradent pas le TAS et peuvent améliorer le RSB et l'efficacité de transmission lorsqu'elles sont conformées au relief de la zone imagée. En parallèle, nous avons mené une étude approfondie des technologies de transmission sans fil en IRM. Un premier prototype de communication optique sans fil pour la transmission de données de capteurs de mouvements a été réalisé et testé.

Les antennes coaxiales portables que nous avons étudiées offrent une alternative intéressante aux antennes standard en raison de leur faible poids et de leur flexibilité.

Title : Concepts for Wearable Technology in MR: Lightweight Flexible Radio Frequency Coils and Optical Wireless Communication

Keywords : Magnetic Resonance Imaging (MRI), radio frequency (RF), high field, flexible, wireless transmission, wearable technology

Abstract : This PhD thesis work was conducted at the BioMaps laboratory at the Université Paris-Saclay and the Center for Medical Physics and Biomedical Engineering (CMPBME) at the Medical University of Vienna.

To improve diagnostic value in MRI, shorter acquisitions, more efficient patient handling and improved image quality are needed. Wearable technology with optimized hardware reduces weight, increases flexibility, and could be wireless, thereby improving sensitivity, comfort, safety, and usability.

In this work, flexible self-resonant coaxial transmission line resonators were investigated. Coaxial coils with multiple turns and gaps enable size optimization depending on the target application.

The design was first studied in silico. Numerous prototypes were constructed, and their performance was tested on the bench and in 3 and 7 T MRI. Coaxial coils were shown to be robust against bending, have no SAR penalty and improve SNR and transmit efficiency when form-fitted.

A review of wireless MR, associated hardware developments and data transmission technology is given. An optical wireless communication module for sensor data transmission was demonstrated experimentally.

Wearable coaxial coils offer an attractive alternative to standard coils due to low weight and flexibility. With wireless motion sensors diagnostic value in e.g. breast, knee, or cardiac MRI could be increased.